



**HAL**  
open science

# Controlled synthesis of bimetallic Fe-Ni/SiO<sub>2</sub> catalysts for furfural hydrogenation: evidencing the roles of Fe and Ni

Dichao Shi

► **To cite this version:**

Dichao Shi. Controlled synthesis of bimetallic Fe-Ni/SiO<sub>2</sub> catalysts for furfural hydrogenation: evidencing the roles of Fe and Ni. Catalysis. Ecole Centrale de Lille, 2019. English. NNT: 2019ECLI0010. tel-03252323

**HAL Id: tel-03252323**

**<https://theses.hal.science/tel-03252323v1>**

Submitted on 7 Jun 2021

**HAL** is a multi-disciplinary open access archive for the deposit and dissemination of scientific research documents, whether they are published or not. The documents may come from teaching and research institutions in France or abroad, or from public or private research centers.

L'archive ouverte pluridisciplinaire **HAL**, est destinée au dépôt et à la diffusion de documents scientifiques de niveau recherche, publiés ou non, émanant des établissements d'enseignement et de recherche français ou étrangers, des laboratoires publics ou privés.

CENTRALE LILLE

**THESE**

Présentée en vue

d'obtenir le grade de

**DOCTEUR**

En

Spécialité: Molécules et Matière Condensée

Par

**Dichao SHI**

DOCTORAT DELIVRE PAR CENTRALE LILLE

---

**CONTROLLED SYNTHESIS OF BIMETALLIC Fe-Ni/SiO<sub>2</sub> CATALYSTS FOR FURFURAL  
HYDROGENATION: EVIDENCING THE ROLES OF Fe AND Ni**

---

**SYNTHESE CONTROLEE DE CATALYSEURS BIMETALLIQUES Fe-Ni/SiO<sub>2</sub> POUR  
L'HYDROGENATION DU FURFURAL: MISE EN EVIDENCE DES ROLES DE Fe ET Ni**

---

Soutenance le 16 Septembre 2019 devant le jury d'examen:

*Président :* **Mme Anne PONCHEL**, Professeur, Université d'Artois

*Rapporteurs:* **Mme Karine PHILIPPOT**, Directeur de Recherche, CNRS-LCC

**Mme Karine VIGIER DE OLIVEIRA**, Professeur, Université de Poitiers

*Examineurs:* **M. Laurent DELANNOY**, Maître de Conférences, Sorbonne Université

**Mme Dorothée LAURENTI**, Chargée de Recherche, CNRS-IRCELYON

*Directeur:* **M. Eric MARCEAU**, Maître de Conférences, Université de Lille

*Co-directeur:* **M. Sébastien PAUL**, Professeur, Ecole Centrale de Lille

*Invité:* **M. Robert WOJCIESZAK**, Chargé de Recherche, CNRS-UCCS

Thèse préparée dans le Laboratoire UCCS

Ecole Doctorale SMRE 104 (UCCS)



## ACKNOWLEDGEMENTS

I would like to thank the CSC-GEC (Chinese Scholarship Council-Groupe des Ecoles Centrale) PhD scholarship program, and the French National Research Agency (ANR), through the NobleFreeCat project (ANR-17-CE07-0022), for their support.

I would like to express my heartfelt gratitude to my supervisors Dr. Eric Marceau and Prof. Sébastien Paul. This thesis has been completed under the care and guidance of my supervisors. They have helped me with valuable instructions and suggestions during all the stages of my three years' PhD study in UCCS. I am deeply impressed by their profound knowledge, rigorous and conscientious scientific attitude. A high tribute shall also be paid to Dr. Robert Wojcieszak, who gave me valuable advices and help for the catalytic tests and during the thesis writing.

I would also like to thank the jury members of my thesis, Dr. Karine Philippot, Prof. Karine Vigier de Oliveira, Dr. Laurent Delannoy, Dr. Dorothée Laurenti and Prof. Anne Ponchel, for the reading and the examination of this manuscript.

I am also deeply indebted to all the other lecturers and engineers in catalysts characterization and catalytic tests, such as Joelle Thuriot-Roukos (ICP and XRF), Jean-Charles Morin (ATR-IR), Olivier Gardoll (TPR), Maya Marinova (STEM-EELS), Anne-Sophie Mamede and Pardis Simon (XPS), Svetlana Heyte (SPR/GC-MS), Pascal Roussel and Laurence Burylo (*in situ* XRD), Achraf Sadier (catalyst deactivation) at UCCS, Lorenzo Stievano and Moulay T. Sougrati (Mössbauer spectroscopy) at ICGM (Montpellier), Valérie Briois and Camille La Fontaine (*in situ* XAS) at Synchrotron SOLEIL, Neil P. Young, Qifeng Yang and P. A. J. Bagot (TEM) at the University of Oxford. In addition, thanks to the REALCAT platform for providing the high-throughput equipment for catalysis.

I also owe my sincere gratitude to my friends and colleagues who gave me help both in my research work and in my life, such as Shuo Chen, Bang Gu, Xiang Yu, Yuanshuang Zheng, Dan Wu, Hua Liu, Xiu Liu, Nisrine Hammi, Bakytzhan Yeskendir, Carmen Ciotonea, Jeremy Dhainaut, and other colleagues.

Finally, my thanks would go to my beloved girlfriend Li Zhang and my parents for their loving considerations and great confidence in me through all these years.



**CONTENT**

RESUME.....	I
ABSTRACT .....	VII
General introduction.....	1
References .....	8
Chapter I Bibliographical study .....	11
I.1. Fe-Ni systems as catalysts for hydrogenation reactions .....	13
I.1.1. Methanation reactions .....	14
I.1.2. Fischer-Tropsch synthesis .....	20
I.1.3. Hydrogenation of organic molecules .....	22
I.1.4. Hydrodeoxygenation of organic molecules .....	26
I.1.5. Hydroconversion of furfural and 5-hydroxymethyl furfural .....	28
I.1.6. Conclusions .....	37
I.2. Formation, structure, size and composition of Fe-Ni nanoparticles .....	38
I.2.1. Preparation methods.....	38
I.2.1.1. Incipient wetness impregnation .....	38
I.2.1.2. Sol-gel method .....	42
I.2.1.3. Deposition-precipitation .....	43
I.2.2. Reducibility of the oxidic phases to Fe-Ni nanoparticles .....	45
I.2.3. Influence of the Ni content on the nanoparticles structure .....	54
I.3. Conclusions.....	55
References .....	57
Chapter II Methods: characterization techniques and catalytic test .....	63
II.1. Chemical analysis .....	65
II.1.1. Inductively Coupled Plasma Optical Emission Spectroscopy (ICP-OES) .....	65
II.1.2. X-ray fluorescence (XRF) .....	66
II.1.3. X-ray Photoelectron Spectroscopy (XPS) .....	67
II.2. Textural and morphological properties .....	67
II.2.1. Nitrogen physisorption .....	67
II.2.2. <i>In-situ</i> / X-ray diffraction (XRD) .....	69
II.2.3. (High Resolution) Transmission Electron Microscopy ((HR)TEM).....	70
II.2.4. HAADF/EDX-EELS .....	71
II.2.5. Temperature-programmed reduction (TPR) .....	73

II.3. Spectroscopic techniques.....	73
II.3.1. Attenuated Total Reflection Infrared spectroscopy (ATR-IR).....	73
II.3.2. Mössbauer spectroscopy (MössS) .....	74
II.3.3. X-ray absorption spectroscopy (XAS) .....	77
II.3.4. Chemometric analysis of X-ray absorption spectra.....	79
II.4. Catalytic tests.....	81
II.4.1. Materials .....	81
II.4.2. Experimental set-up .....	81
II.4.2.1. SPR system presentation .....	81
II.4.2.2. Description of catalysts activation in H <sub>2</sub> .....	83
II.4.2.3. Description of the experimental protocol .....	83
II.4.3. Analytical methods .....	84
References .....	86
Chapter III Study of the deposition-precipitation and reduction processes for Fe-Ni/SiO <sub>2</sub> catalysts .....	89
III.1. Introduction .....	91
III.2. Choice of the experimental parameters for deposition-precipitation and drying	92
III.2.1. Choice of the reactants and strategy .....	92
III.2.2. Description of the preparation procedure .....	93
III.2.3. Influence of drying on the solids prepared by DPU .....	95
III.3. Characterization of Fe-Ni/SiO <sub>2</sub> samples after drying.....	95
III.3.1. Speciation of the metal ions .....	95
III.3.2. Evolution and composition of the phases deposited during DPU: the Fe <sub>50</sub> Ni <sub>50</sub> /SiO <sub>2</sub> solid .....	99
III.3.3. Nature and composition of the phases deposited during DPU: the Fe <sub>x</sub> Ni <sub>(100-x)</sub> /SiO <sub>2</sub> series.....	103
III.3.4. Conclusions .....	105
III.4. The process of reduction for Fe-Ni/SiO <sub>2</sub> solids prepared by DPU .....	105
III.4.1. Speciation of the metals: the Fe <sub>50</sub> Ni <sub>50</sub> /SiO <sub>2</sub> solid.....	105
III.4.2. Reducibility of the metals across the Fe <sub>x</sub> Ni <sub>(100-x)</sub> /SiO <sub>2</sub> series, and composition of the Fe-Ni metal nanoparticles .....	117
III.5. Conclusions .....	127
References .....	129

Chapter IV Characterization of Fe-Ni/SiO <sub>2</sub> nanoparticles after pre-reduction and during reductive activation .....	133
IV.1. Introduction .....	135
IV.2. Characterization of the Fe-Ni nanoparticles on system Fe <sub>50</sub> Ni <sub>50</sub> /SiO <sub>2</sub> .....	135
IV.3. Characterization of the Fe-Ni nanoparticles across the Fe-Ni/SiO <sub>2</sub> series.....	137
IV.4. Evolution of the nanoparticles upon activation in H <sub>2</sub> .....	145
IV.5. Conclusions .....	150
References .....	151
Chapter V Catalytic performances of the Fe-Ni/SiO <sub>2</sub> catalysts in the hydrogenation of furfural.....	153
V.1. Introduction .....	155
V.2. Choice of the solvent and reaction pathways for the hydrogenation of furfural	155
V.3. Choice of the experimental conditions for the hydrogenation of furfural.....	158
V.3.1. Choice of temperature and hydrogen pressure .....	158
V.3.2. Choice of the ratio between furfural and the catalyst mass.....	159
V.4. Description of the set-up .....	160
V.5. Catalytic results .....	162
V.6. Comparison with catalysts prepared by impregnation and DP .....	172
V.6.1. Comparison of reducibility .....	173
V.6.2. Comparison of particle size and structure .....	174
V.6.3 Comparison of catalytic activity .....	179
V.7. Conclusions .....	185
References .....	186
General conclusions and perspectives.....	189
Scientific production .....	195





## RESUME

Le fer Fe et le nickel Ni sont deux métaux non nobles qui peuvent être utilisés pour l'hydrogénation des molécules organiques. Alors que Ni monométallique est connu pour son activité mais aussi pour favoriser des réactions secondaires non désirées, les catalyseurs bimétalliques Fe-Ni ont été mentionnés dans la littérature comme présentant des propriétés intéressantes pour la catalyse d'hydrogénation, en phase gaz comme en phase liquide, en termes à la fois d'activité et de sélectivité: vitesses de réaction plus élevées que sur Ni pour l'hydrogénation des liaisons C=C, C=O et C≡N; sélectivité plus élevée pour l'hydrogénation des liaisons C≡C ou de fonctions polaires, avec peu de réactions secondaires d'hydrogénation totale, d'ouverture de cycle ou d'hydrogénolyse; une sélectivité démontrée pour l'hydrogénation de fonctions oxygénées en alcools; inhibition de l'hydrogénation des cycles aromatiques. Trois types d'explications ont été proposés pour expliquer les spécificités des catalyseurs Fe-Ni:

1) *quantité et nature des espèces adsorbées*: la quantité de H<sub>2</sub> adsorbé et dissocié ne serait pas assez élevée sur les systèmes Fe-Ni pour promouvoir l'hydroconversion profonde des molécules. Ceci s'accroît lorsque la proportion de Fe augmente, conduisant à une diminution de l'activité. De plus, un changement dans le mode d'adsorption des molécules organiques comparé au Ni désavantagerait la formation d'intermédiaires menant à des produits de décarbonylation, d'ouverture de cycle ou d'hydrogénation des cycles.

2) *effets électroniques globaux*: existence d'un transfert de charge de Fe vers Ni, résultant en l'attraction d'atomes d'oxygène par le Fe déficient en électrons, ce qui pourrait contribuer à affaiblir ou à activer les liaisons CO;

3) *sites de surface*: des sites acides de Lewis apparaissent avec l'introduction de Fe (éventuellement des ions non réduits), et ceux-ci pourraient attirer et activer les liaisons CO à travers des interactions avec la paire électronique de l'atome d'oxygène.

Cependant, dans la littérature, les catalyseurs supportés Fe-Ni sont souvent préparés par co-imprégnation, une procédure qui peut conduire à un faible contrôle de la composition, de la structure et de la taille des particules bimétalliques (cette dernière pouvant aller de 2 à 30 nm). Ceci rend difficile l'établissement d'un lien entre composition des nanoparticules Fe-Ni (en particulier, composition de surface), et activité en catalyse d'hydrogénation, car tous ces paramètres peuvent potentiellement être pris en compte pour expliquer les résultats. Le but de cette thèse est donc de préparer des nanoparticules bimétalliques Fe-Ni supportées sur SiO<sub>2</sub>, de structure, de taille et de composition homogènes, afin de mettre en évidence les interactions

entre les deux métaux, et de relier la présence de Fe et de Ni, dans les particules et à leur surface, aux performances des catalyseurs en catalyse d'hydrogénation.

Le furfural, une molécule bio-sourcée importante commercialement, a été choisi pour évaluer la capacité en hydrogénation de ces catalyseurs. Le furfural possède un cycle furanique et une fonction aldéhyde. Il est produit industriellement depuis des décennies à partir de déchets lignocellulosiques, par déshydratation du xylose, un pentose présent dans l'hémicellulose, catalysée par les acides. La présente thèse explore en particulier l'utilisation des catalyseurs Fe-Ni pour la formation sélective de l'alcool furfurylique, un intermédiaire dans la production de molécules en chimie fine et de fibres synthétiques.

La caractérisation des catalyseurs Fe-Ni a été effectuée en utilisant des techniques avancées, telles que la spectroscopie d'absorption X en mode Quick-SAX, la spectroscopie Mössbauer, toutes deux en mode *in situ*, et la microscopie électronique en champ sombre couplée à la spectroscopie des pertes d'énergie à haute résolution, pour l'étude des profils de concentration en Fe et en Ni au sein de nanoparticules Fe-Ni individuelles.

La méthode choisie pour préparer les catalyseurs Fe-Ni/SiO<sub>2</sub> sur la silice Sipernat-50 est le dépôt-précipitation à l'urée. A 80°C, la décomposition de l'urée en milieu aqueux provoque une augmentation homogène du pH dans la suspension, qui entraîne la précipitation de phases hydroxydes métalliques sur la silice, ou la formation de phases silicates. Cette méthode a été utilisée avec succès dans la littérature pour préparer de façon contrôlée des catalyseurs Ni/SiO<sub>2</sub>. Afin d'éviter la précipitation séparée à bas pH de phases contenant Fe(III) (goethite ou hydrohonnite), les sulfates de Fe(II) et Ni(II) ont été sélectionnés comme sels précurseurs, et la synthèse entière a été menée sous un gaz inerte, Ar, pour enlever toute source d'oxydation. Néanmoins, les ions fer s'oxydent en Fe(III) pendant le séchage et le stockage (spectroscopie d'absorption X, spectroscopie Mössbauer), sans conséquence toutefois sur la formation ultérieure des nanoparticules Fe-Ni.

La diffraction des rayons X, la spectroscopie d'absorption X et la spectroscopie infrarouge en mode ATR montrent qu'après 22h, à un pH de 5,3, le dépôt-précipitation résulte en la formation d'un phyllosilicate 1:1 faiblement cristallisé contenant des ions Fe(III) et Ni(II), avec un excès de Ni comparé aux proportions des métaux en solution. La diffraction des rayons X *in situ*, la spectroscopie d'absorption X *in situ* appliquée simultanément aux seuils K de Fe et de Ni et couplée à une analyse chimométrique, la spectroscopie Mössbauer *in situ* et la réduction en température programmée montrent que les nanoparticules d'alliage Fe-Ni se forment au travers de trois étapes de réduction entre 275 et 700 °C: (1) réduction des ions Fe(III) en Fe(II) dans la phase phyllosilicate; (2) destruction de la phase phyllosilicate et réduction de Ni(II) en

Ni(0), qui provoque la réduction progressive des ions Fe(II) à l'état métallique et la formation de particules bimétalliques cubique faces centrées (cfc) riches en Ni; (3) achèvement de la réduction des ions Fe(II), et migration de Fe(0) vers le coeur des nanoparticules Fe-Ni cfc. En termes de température de réduction, la réductibilité du catalyseur est maximale pour les formulations contenant une proportion molaire de 60-75 % Ni. Ni augmente la réductibilité de Fe, mais trop de Ni conduit à un phyllosilicate mieux organisé qui est plus difficile à réduire.

La composition du coeur cristallisé des nanoparticules bimétalliques Fe-Ni peut être évaluée pendant et après réduction sous H<sub>2</sub> selon une loi linéaire de Végard. Les proportions molaires de Fe et Ni ont été comparées avec des résultats de fluorescence X et de spectroscopie de photoélectrons X. En dépit de leurs différences (techniques sondant le volume ou la surface, composition globale ou composition de domaines cristallisés), les trois méthodes donnent des résultats cohérents. Dans tous les cas étudiés, davantage de Ni se dépose par rapport aux proportions initiales en solution, et Fe s'insère progressivement dans le coeur cristallisé des nanoparticules Fe-Ni en fin d'étape de réduction. La teneur massique totale en métaux, déduite de la réduction en température programmée, est comprise entre 40 et 50%.

La taille et la composition des particules cfc Fe-Ni ont été caractérisées par HRTEM-EELS après réduction à 700 °C, pour six formulations: Fe<sub>65</sub>Ni<sub>35</sub>, Fe<sub>45</sub>Ni<sub>55</sub>, Fe<sub>31</sub>Ni<sub>69</sub>, Fe<sub>27</sub>Ni<sub>73</sub>, Fe<sub>16</sub>Ni<sub>84</sub>, Fe<sub>8</sub>Ni<sub>92</sub>. Dans tous les cas, la distribution en taille est étroite, dans l'intervalle 4-7 nm, et les dispersions métalliques sont proches de 20%. Les valeurs des tailles moyennes de particules sont cohérentes avec celles calculées à partir des diffractogrammes de rayons X en utilisant l'équation de Scherrer. Les valeurs de composition en Fe et Ni des coeurs des nanoparticules sont également cohérentes avec les compositions déterminées par diffraction des rayons X, fluorescence X et spectroscopie de photoélectrons X. La distribution de composition globale mesurée sur des particules individuelles présente un faible écart-type, de seulement 8 at%.

Après exposition à l'air, la microscopie en champ sombre couplée à la spectroscopie en pertes d'énergie à haute résolution révèle que sur tous les catalyseurs, les nanoparticules Fe-Ni présentent une morphologie coeur-coquille, avec un alliage Fe-Ni dans le coeur, et des phases plus riches en Fe dans une couche oxydée d'1 nm d'épaisseur. Cette couche peut se développer de façon asymétrique et pas sur tout le pourtour de la particule. Cet excès de Fe superficiel, aussi observé par spectroscopie Mössbauer après réduction, peut provenir de la réduction tardive de ce métal durant la formation des nanoparticules.

La spectroscopie d'absorption X *in situ* couplée à une analyse chimométrique montre que pendant une activation sous H<sub>2</sub>, les deux métaux présents dans la couche oxydée après exposition à l'air sont réduits, et la plus grande part reste associée à l'état métallique dans les

coeurs cfc. Les ions  $\text{Fe}^{3+}$  de la couche oxydée se réduisent d'abord en  $\text{Fe}^{2+}$ . Les ions  $\text{Ni}^{2+}$  se réduisent ensuite à l'état métallique, ce qui provoque la réduction de  $\text{Fe}^{2+}$  à l'état métallique, comme cela a été le cas, dans des phases différentes, pendant le processus de réduction initial. Plus il y a de Ni dans les particules, plus basse est la température de réduction de Fe. En dépit de la présence d'un excès de Fe dans la couche oxydée, le Fe ne se réduit pas séparément et ne forme pas de particules indépendantes. On peut donc supposer qu'après activation sous  $\text{H}_2$ , les nanoparticules Fe-Ni restent entourées d'une couche plus riche en Fe que le cœur des particules.

Les six catalyseurs Fe-Ni/ $\text{SiO}_2$  mentionnés plus haut, et un catalyseur Ni/ $\text{SiO}_2$  de référence préparé selon la même procédure, ont été testés dans l'hydrogénation du furfural en phase liquide à 150 °C sous 20 bar de  $\text{H}_2$ , après activation sous  $\text{H}_2$  à 400 °C pour réduire la couche oxydée. L'hydrogénation du furfural a été testée au moyen d'un réacteur de criblage sous pression (SPR) équipé de 24 réacteurs batch en parallèle, en acier inoxydable, de 6 mL chacun. Les solvants organiques peu polaires, comme le n-heptane, le chlorobenzène et le dichloroéthane, étant connus pour promouvoir l'hydrodésoxygénation du furfural en méthylfurane, et les alcools favorisant plutôt l'hydrogénation de la fonction aldéhyde, l'isopropanol a été choisi comme solvant, ce qui permet de limiter les réactions secondaires d'acétalisation du furfural par rapport à un alcool primaire.

Pour les catalyseurs les plus riches en Fe ( $\text{Fe}_{65}\text{Ni}_{35}/\text{SiO}_2$  et  $\text{Fe}_{45}\text{Ni}_{55}/\text{SiO}_2$ ), les bilans carbone sont toujours inférieurs à 90%. Ceci peut être expliqué par la faible consommation du furfural et par une concentration restant élevée dans le milieu réactionnel, résultant en l'adsorption du furfural à la surface des catalyseurs. De plus, des produits de dégradation non détectés par chromatographie peuvent aussi être responsables de ces faibles bilans carbone. Des bilans carbone supérieurs à 95% sont en revanche obtenus dans la plupart des tests lorsque la proportion en Ni dans les catalyseurs bimétalliques augmente.

La vitesse de consommation de furfural par hydrogénation augmente avec la proportion de Ni dans le catalyseur. Les catalyseurs Fe-Ni contenant une proportion molaire de 60-75 % Ni favorisent l'hydrogénation de la fonction aldéhyde et fournissent le rendement le plus élevé en alcool furfurylique (0,43 - 0,45 mmol, par rapport à une quantité initiale de furfural de 0,56 mmol). Une proportion plus élevée de Ni favorise progressivement les réactions secondaires d'étherification avec le solvant isopropanol, d'hydrogénolyse en méthylfurane, et finalement d'hydrogénation du cycle furanique, qui domine nettement la réactivité du catalyseur monométallique au Ni. Le méthylfurane ne devient jamais le produit majoritaire parce qu'il est consommé par cette réaction qui mène au méthyl-tétrahydrofurane.

Etant donné que cette série de catalyseurs Fe-Ni a été préparée avec des tailles de particules petites et homogènes, des distributions en taille étroites, et un faible intervalle de composition chimique, et que par ailleurs des couches superficielles riches en Fe ont été détectées en périphérie des nanoparticules, l'activité catalytique peut être expliquée par l'hypothèse selon laquelle les surfaces riches en Fe des nanoparticules favorisent l'adsorption du groupe carbonyle et repoussent le cycle furanique. Une analyse quantitative des produits secondaires et tertiaires montre que davantage de nickel dans, et sans doute à la surface des particules, promeut *a contrario* l'hydrogénolyse et l'hydrogénation du cycle furanique. La formation d'éthers, aussi favorisée par les catalyseurs riches en Ni, peut être expliquée par la présence d'ions  $\text{Ni}^{2+}$  résiduels restant non réduits dans des phases silicate, et agissant en sites acides de Lewis.

Cette tendance est comparée à celle obtenue avec des catalyseurs Fe-Ni/SiO<sub>2</sub> préparés par co-imprégnation de nitrates de Fe(III) et Ni(II), qui diffèrent des catalyseurs préparés par dépôt-précipitation par leur distribution en taille de particules plus large (jusqu'à 15 nm) et leur dispersion métallique plus faible. Pour ces catalyseurs, les proportions atomiques en Fe et Ni sont proches des proportions nominales, et dans l'échantillon étudié par microscopie électronique en transmission, la composition des nanoparticules individuelles correspond aussi à la composition nominale, avec un faible écart-type. Comme cela a été trouvé pour les catalyseurs préparés par dépôt-précipitation, après exposition à l'air, les alliages Fe-Ni présentent une morphologie cœur-coquille avec des phases riches en Fe dans la couche oxydée. La réductibilité des catalyseurs préparés par imprégnation est plus élevée que celle des catalyseurs préparés par dépôt-précipitation. Le test des catalyseurs Fe-Ni/SiO<sub>2</sub> préparés par co-imprégnation, pré-réduits à 700 °C, et activés à 400 °C avant réaction, montre qu'en augmentant la proportion de Ni, la vitesse de consommation du furfural et le rendement en alcool furfurylique augmentent. Comme cela était le cas pour les catalyseurs préparés par dépôt-précipitation, le catalyseur Fe-Ni/SiO<sub>2</sub> contenant une proportion atomique de 75 % Ni favorise l'hydrogénation de la fonction aldéhyde et fournit le rendement le plus élevé en alcool furfurylique (0.44 mmol).

La comparaison des six catalyseurs Fe-Ni/SiO<sub>2</sub> préparés par dépôt-précipitation et étudiés dans cette thèse est facilitée par l'homogénéité des nanoparticules Fe-Ni en structure, taille et composition globale. Les spécificités des catalyseurs Fe<sub>31</sub>Ni<sub>69</sub>/SiO<sub>2</sub> et Fe<sub>27</sub>Ni<sub>73</sub>/SiO<sub>2</sub> quant à leur sélectivité et à leur rendement élevés en alcool furfurylique sont expliquées, d'une part, par une réductibilité optimale, et, d'autre part, par la présence majoritaire du Fe oxophile et par un rapport Fe/Ni adéquat à la surface des particules, qu'on peut supposer favoriser l'adsorption du

furfural par le groupe aldéhyde et non par le cycle furanique, et affaiblir les propriétés hydrogénantes du Ni, au moins par un effet de dilution.

**ABSTRACT**

Iron (Fe) and nickel (Ni) are two non-noble metals that can be used for the hydrogenation of organic molecules. Whereas monometallic Ni is known to favor unwanted side-reactions of hydrogenolysis and ring opening, bimetallic Fe-Ni catalysts have been reported to exhibit interesting properties for the selective hydrogenation of oxygenated functions. However, these catalysts are often prepared by co-impregnation, which is a procedure that may lead to a poor control of the bimetallic particle composition, structure and size. This has made it difficult to link the composition of Fe-Ni nanoparticles and catalytic activities. The purpose of this PhD is to prepare SiO<sub>2</sub>-supported Fe-Ni bimetallic nanoparticles of homogeneous structure, size and composition, and to evidence the interplay between the two metals, in order to unambiguously link the presence of Fe and Ni within the particles and at their surface with their catalytic performances. Furfural, a bio-sourced molecule of commercial importance, which holds a furan ring and an aldehyde group, has been chosen to evaluate the hydrogenation ability of these catalysts, especially toward the selective formation of furfuryl alcohol.

Deposition-precipitation with urea has been selected as the method to prepare the Fe-Ni/SiO<sub>2</sub> catalysts. In order to avoid the separate precipitation of Fe(III)-containing phases at low pH, Fe(II) and Ni(II) sulfates have been selected as precursor salts, and the whole synthesis has been carried out under inert gas Ar, to remove any source of oxidation. Iron ions nevertheless oxidize to Fe(III) during drying and storage, though without consequence on the ulterior formation of the Fe-Ni nanoparticles. Deposition-precipitation results in the formation of a poorly crystalline (Fe(III),Ni(II))-containing 1:1 phyllosilicate, with an excess of Ni compared with the metal proportions in solution. *In situ* X-ray diffraction, X-ray absorption spectroscopy, Mössbauer spectroscopy and temperature-programmed reduction show that Fe-Ni alloyed nanoparticles form upon three stages of reduction between 275 and 700 °C: (1) reduction of Fe(III) ions to Fe(II) in the phyllosilicate phase; (2) destruction of the phyllosilicate phase and reduction of Ni(II) to Ni(0), which triggers the progressive reduction of Fe(II) ions to the metallic state and the formation of face-centred cubic (*fcc*) Ni-rich bimetallic particles; (3) completion of the reduction of Fe(II) ions and migration to the core of the Fe-Ni nanoparticles. In terms of reduction temperature, the reducibility of the catalyst is maximum for formulations containing a molar proportion of 60-75 at% Ni. Ni increases the reducibility of Fe, but too much Ni leads to a more organized phyllosilicate that is more difficult to reduce.

The particles size and composition of the *fcc* Fe-Ni nanoparticles have been characterized by HRTEM-EELS-EDX after reduction at 700 °C for six Fe-Ni formulations: Fe<sub>65</sub>Ni<sub>35</sub>, Fe<sub>45</sub>Ni<sub>55</sub>,



Fe<sub>31</sub>Ni<sub>69</sub>, Fe<sub>27</sub>Ni<sub>73</sub>, Fe<sub>16</sub>Ni<sub>84</sub>, Fe<sub>8</sub>Ni<sub>92</sub>. In all cases, the size distribution of the nanoparticles is narrow, in the 4-7 nm range, and metal dispersions are close to 20%. The global composition measured on individual particles exhibits a small standard deviation of only 8 at%. Upon exposure to air, the nanoparticles possess a core-shell structure, with an outer oxidic shell enriched in Fe. This excess of Fe, also observed by Mössbauer spectroscopy, may derive from the late reduction of this metal during the formation of the nanoparticles. *In situ* X-ray absorption spectroscopy shows that upon an activation under H<sub>2</sub>, Ni reduction triggers the reduction of Fe to the metallic state.

The six Fe-Ni/SiO<sub>2</sub> catalysts have been tested in the liquid phase hydrogenation of furfural at 150 °C under 20 bar of H<sub>2</sub>, after activation in H<sub>2</sub> at 400 °C to reduce the oxidic shell. The furfural consumption rate increases with the Ni content. Fe-Ni catalysts containing a molar proportion of 60-75 Ni at% provide the highest yield of furfuryl alcohol. This tendency is confirmed using Fe-Ni/SiO<sub>2</sub> catalysts prepared by co-impregnation of Fe(III) and Ni(II) nitrates, which differ from the catalysts prepared by deposition-precipitation by their broader particle size distribution (up to 15 nm) and lower metal dispersion. More Ni progressively favors the consumption of furfuryl alcohol via three parallel secondary reactions: etherification with the isopropanol solvent, possibly catalyzed by metal ions that remain unreduced after activation; hydrogenolysis of the C-O bond yielding 2-methylfuran; and hydrogenation of the furan ring, which dominates the reactivity of the monometallic Ni/SiO<sub>2</sub> catalyst.

The comparison between the six Fe-Ni/SiO<sub>2</sub> catalysts is facilitated by the homogeneity of the Fe-Ni nanoparticles in structure, size and global composition. The specificities of the Fe<sub>31</sub>Ni<sub>69</sub>/SiO<sub>2</sub> and Fe<sub>27</sub>Ni<sub>73</sub>/SiO<sub>2</sub> catalysts with respect to their high selectivity and yield in furfuryl alcohol are explained on the one hand by an optimum reducibility, on the other hand by the major presence of oxophilic Fe and by an adequate Fe/Ni balance at the surface of the particles, which presumably favor the adsorption of furfural via the aldehyde group and not via the furan ring, and tone down the hydrogenating properties of Ni, at least by a dilution effect.

# General introduction



In a context of increasing energy demand and use of fossil fuels, biomass-derived molecules represent sustainable carbon sources for the production of fuels and chemicals [1, 2]. Biomass can be broadly classified into two categories: first-generation and second-generation biomass [3]. First-generation biomass is based on edible resources, such as carbohydrates and vegetal oils. Second-generation biomass consists of lignocellulose, which is most of the time a waste from agriculture or forests exploitation, and contains cellulose, hemicellulose and lignin. Heterogeneous catalysts are required to allow the transformation of first- or second-generation biomass to valuable biosourced molecules. In particular, the production of alcohols or hydrocarbons involves catalytic hydrogenation, hydrogenolysis and hydrodeoxygenation reactions, as shown in Figure 1.

Among these biosourced molecules, furfural is an aldehyde belonging to the family of the furanic compounds. It has been produced industrially for decades from lignocellulosic wastes, by the acid-catalyzed dehydration of xylose, a pentose present in hemicellulose. Furfural is the precursor for furan-based chemicals and solvents such as furyl (e.g., furanones and furans), furfuryl (e.g., furfuryl alcohol and furfuryl acetate), furoyl (e.g., 2-furoyl chloride and furoylglycine), and furfurylidene compounds used in the chemical industry (Figure 2).

Furfural yields fuel additives such as 2-methylfuran by hydrodeoxygenation or decarbonylation [5] or, by selective hydrogenation, furfuryl alcohol [6], a significant chemical which is widely involved in the production of fine chemicals, rubbers and corrosion resistant glass fibers. Hydrogenation catalysts that are selective for the hydrogenation of the unsaturated C=O bond of furfural should be preferred for the production of furfuryl alcohol, to keep the furan ring intact and avoid the cleavage of the side-group. However, the selective hydrogenation of the C=O bond is still a challenge because the hydrogenation of the C=C bonds is usually more likely to occur [7]. The search for selective hydrogenation catalysts is thus still an important question.

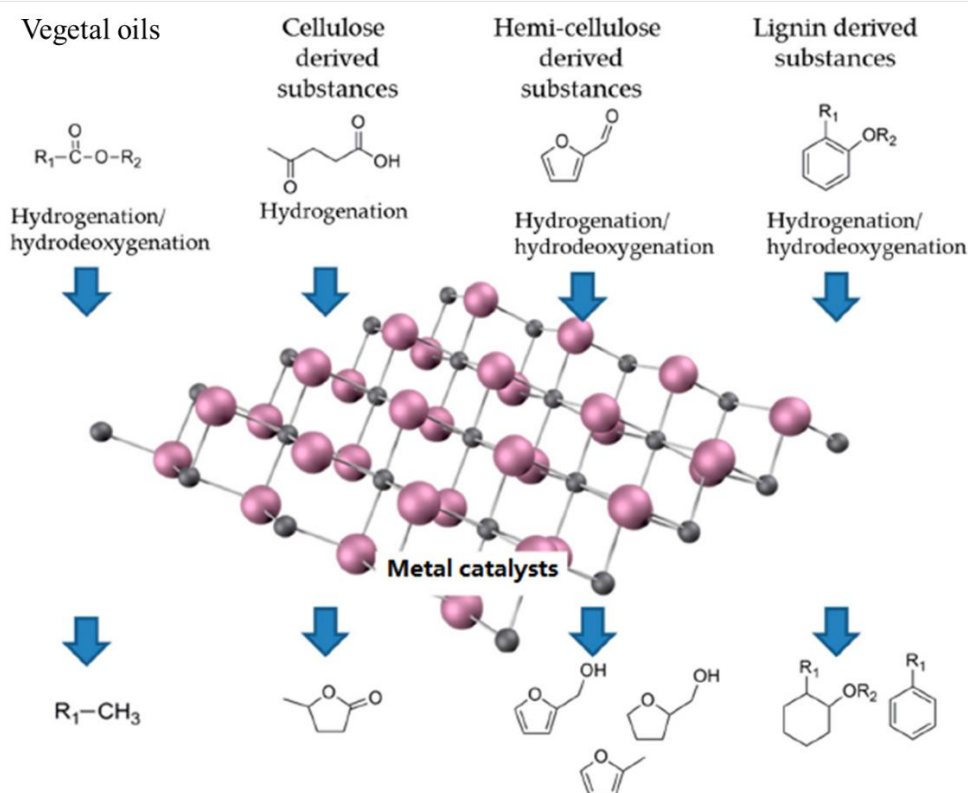


**Figure 1.** Examples of reactions involving bio-sourced molecules, metal-based catalysts and  $H_2$ . Reprinted from ref. 3. Copyright 2018 MDPI

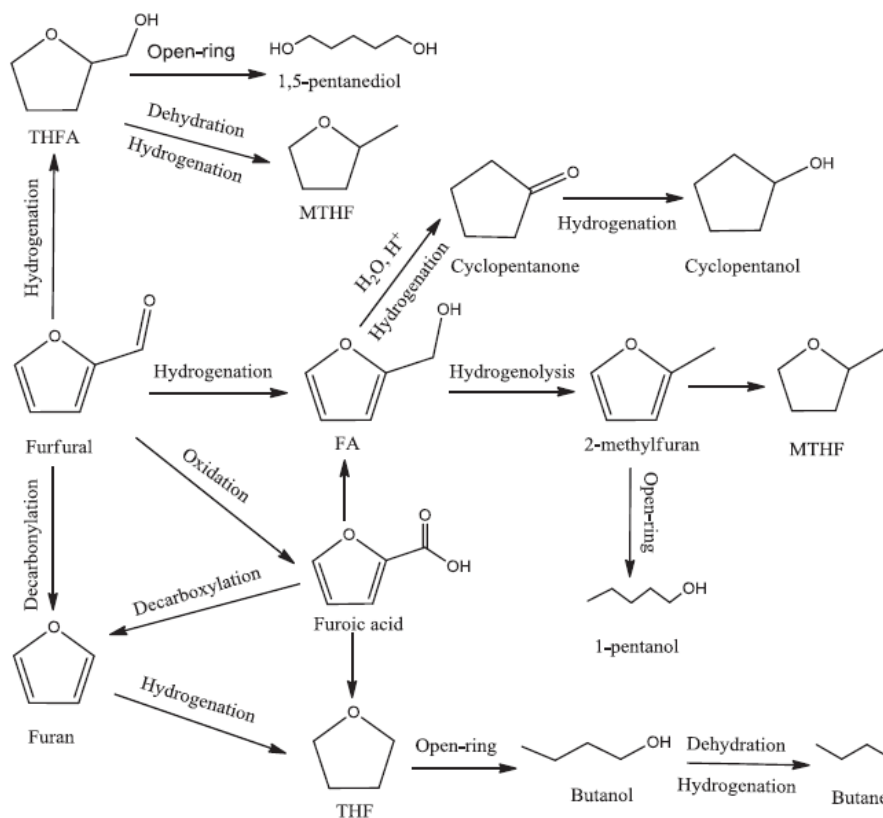


**Figure 2.** Conversion of furfural to value-added chemicals and biofuels [4]. Copyright 2014 Elsevier

Compared with noble metals, non-noble metals such as Fe, Co, Ni and Cu are attractive systems for the catalytic hydrogenation of organic molecules because of their low cost. Among them, Fe is the least active and deactivates easily. Cobalt is the most expensive. Cu usually exhibits a low activity due to the difficulty to have it highly dispersed on a support. In contrast, metallic nickel Ni is known to be an effective catalyst for various reactions, such as the reforming of methane [8], or the hydrogenation of organic molecules [9, 10]. Raney nickel, a fine-grained solid composed mostly of nickel and derived from a nickel-aluminium alloy, is used as a catalyst in organic chemistry, at the laboratory and in the industry [11]. However, one of the most important drawbacks of Raney nickel is its pyrophoricity, because of which it should be handled under an inert atmosphere. Furthermore, deactivation due to the formation of nickel nitride or carbide, or by carbonaceous deposits, is another disadvantage of nickel [12]. Finally, in terms of selectivity, a major problem with Ni-based catalysts is that they may not be selective in the hydrogenation of oxygenated functions, because of their activity in the hydrogenation of C=C bonds and aromatic rings, and in deoxygenation reactions [7, 13].

The addition of a second metal as a promoter has been effectively used to optimize the properties of monometallic Ni catalysts. Bimetallic catalysts often exhibit unique properties, via a synergetic or bi-functional effect, which differ from those of the parent metals and offer the opportunity to design catalysts with an improved activity and selectivity that exceed those achievable with monometallic nickel. The size of bimetallic particles, their composition and their distribution on the support are known to strongly affect the catalytic properties. Therefore, optimizing the size of nanoparticles, the structure of the active sites and the distribution on the support is highly important. Consequently, the preparation method selected for bimetallic catalysts has a critical influence on the performance obtained in hydrogenation reactions [14-16]. The traditional methods used to synthesize bimetallic catalysts include incipient wetness impregnation [17], sol-gel route [18] and deposition-precipitation [19].

Iron has been studied as a promoter of nickel due to its abundance and its effective enhancement of catalytic performances. For instance, Chieffi and co-workers [20] have prepared Fe-Ni bimetallic catalysts which displayed considerable catalytic activity for the

hydrogenation of biosourced aldehydes and monosaccharides (furfural, glucose) to attractive products such as furfuryl alcohol and sorbitol. The product selectivity in the hydrogenation of furfural, as studied by Sitthisa and co-workers [5], is drastically shifted from furan and CO to 2-methylfuran by adding Fe to Ni-based catalysts, but adding Fe species can also help to produce large amounts of furfuryl alcohol.

However, standard preparation methods for Fe-Ni bimetallic catalysts, such as impregnation, yield metal particles of different size or composition [21, 22]. Moreover, both Fe and Ni are prone to oxidation, which raises the question of metals segregation and re-alloying upon exposure to air and subsequent reduction. As a consequence, owing to a lack of control of the nature of the individual nanoparticles (alloyed vs. segregated metals, disparities in metal content), no firm conclusion can currently link the formulation and the properties of Fe-Ni systems, leading to difficulties to reproduce and correlate the best catalytic results to precise Fe and Ni proportions [23-25].

Considering the high potential of Fe-Ni catalysts and the current limits described above, the objective of this thesis is to understand: (i) if, and how, well-defined alloyed Fe-Ni nanoparticles can be prepared over a whole series of Fe/Ni ratios, as uniform as possible in terms of structure, size and composition; and (ii) the consequences on the conversion of furfural and selectivity to furfuryl alcohol. Two different synthesis methods, deposition-precipitation and incipient wetness impregnation, have been chosen to investigate the effect of the preparation mode on the nature and properties of bimetallic Fe-Ni nanoparticles. Given the difficulty to distinguish by classical methods (X-ray diffraction, transmission electron microscopy) two metals with close electron numbers, a combination of classical and advanced *ex situ* and *in situ* characterization techniques (HRTEM-HAADF, X-ray absorption spectroscopy, Mössbauer spectroscopy) will be implemented to evaluate the interplay between Fe and Ni and the structural changes during the catalyst synthesis, initial reduction, exposure to O<sub>2</sub> and subsequent activation in H<sub>2</sub>. The final objective of this thesis will be to correlate the bulk and surface characteristics of Fe-Ni nanoparticles with their catalytic properties in furfural hydrogenation.

In Chapter I, a bibliographical study will sum up the properties of supported Fe-Ni nanoparticles in catalytic hydrogenation, and the factors influencing the preparation of Fe-Ni bimetallic catalysts. In Chapter II, techniques used to characterize and test the catalysts will be described. Chapter III will investigate the process of deposition-precipitation for the preparation of Fe-Ni/SiO<sub>2</sub> catalysts and the interplay between the two metals, using a combination of *in situ* characterization techniques, such as X-ray diffraction, X-ray absorption spectroscopy and Mössbauer spectroscopy. Chapter IV will discuss the bulk and surface composition of Fe-Ni nanoparticles along the different stages before catalytic test. Chapter V will analyze the catalytic performances of this series of catalysts in the hydrogenation of furfural, and compare them with catalysts prepared by co-impregnation. The dissertation will be completed by a final conclusion.



## References

- [1] W. Yu, K. Xiong, N. Ji, M. D. Porosoff, J. G. Chen, Theoretical and experimental studies of the adsorption geometry and reaction pathways of furfural over FeNi bimetallic model surfaces and supported catalysts, *Journal of Catalysis*, 317 (2014) 253-262.
- [2] D. Li, M. Koike, L. Wang, Y. Nakagawa, Y. Xu, K. Tomishige, Regenerability of hydrotalcite-derived nickel-iron alloy nanoparticles for syngas production from biomass tar, *ChemSusChem*, 7 (2014) 510-522.
- [3] C. Chan-Thaw, A. Villa, Metal carbides for biomass valorization, *Applied Sciences*, 8 (2018) 259.
- [4] K. Yan, G. Wu, T. Lafleur, C. Jarvis, Production, properties and catalytic hydrogenation of furfural to fuel additives and value-added chemicals, *Renewable and Sustainable Energy Reviews*, 38 (2014) 663-676.
- [5] S. Sitthisa, W. An, D. E. Resasco, Selective conversion of furfural to methylfuran over silica-supported Ni-Fe bimetallic catalysts, *Journal of Catalysis*, 284 (2011) 90-101.
- [6] Z. Jiang, W. Wan, Z. Lin, J. Xie, J. G. Chen, Understanding the role of M/Pt(111) (M = Fe, Co, Ni, Cu) bimetallic surfaces for selective hydrodeoxygenation of furfural, *ACS Catalysis*, 7 (2017) 5758-5765.
- [7] W. S. Putro, T. Kojima, T. Hara, N. Ichikuni, S. Shimazu, Selective hydrogenation of unsaturated carbonyls by Ni-Fe-based alloy catalysts, *Catalysis Science & Technology*, 7 (2017) 3637-3646.
- [8] M. S. Aw, G. Dražić, P. Djinović, A. Pintar, Transition metal pairs on ceria-promoted, ordered mesoporous alumina as catalysts for the CO<sub>2</sub> reforming reaction of methane, *Catalysis Science & Technology*, 6 (2016) 3797-3805.
- [9] N. Laosiripojana, W. Sutthisripok, S. Charojrochkul, S. Assabumrungrat, Conversion of biomass tar containing sulphur to syngas by GdCeO<sub>2</sub> coated NiFe bimetallic-based catalysts, *Applied Catalysis A: General*, 478 (2014) 9-14.
- [10] T. F. Sheshko, Y. M. Serov, Bimetallic systems containing Fe, Co, Ni, and Mn nanoparticles as catalysts for the hydrogenation of carbon oxides, *Russian Journal of Physical Chemistry A*,

86 (2012) 283-288.

[11] J. Petró, A. Bóta, K. László, H. Beyer, E. Kálmán, I. Dódon, A new alumina-supported, not pyrophoric Raney-type Ni-catalyst, *Applied Catalysis A: General*, 190 (2000) 73-86.

[12] Y. Du, H. Chen, R. Chen, N. Xu, Poisoning effect of some nitrogen compounds on nano-sized nickel catalysts in p-nitrophenol hydrogenation, *Chemical Engineering Journal*, 125 (2006) 9-14.

[13] X. Yu, J. Chen, T. Ren, Promotional effect of Fe on performance of Ni/SiO<sub>2</sub> for deoxygenation of methyl laurate as a model compound to hydrocarbons, *RSC Advances*, 4 (2014) 46427-46436.

[14] H. Fang, J. Zheng, X. Luo, J. Du, A. Roldan, S. Leoni, Y. Yuan, Product tunable behavior of carbon nanotubes-supported Ni-Fe catalysts for guaiacol hydrodeoxygenation, *Applied Catalysis A: General*, 529 (2017) 20-31.

[15] E. del Río, D. Gaona, J. C. Hernández-Garrido, J. J. Calvino, M. G. Basallote, M. J. Fernández-Trujillo, J. A. Pérez-Omil, J. M. Gatica, Speciation-controlled incipient wetness impregnation: A rational synthetic approach to prepare sub-nanosized and highly active ceria-zirconia supported gold catalysts, *Journal of Catalysis*, 318 (2014) 119-127.

[16] M. Feyzi, A. A. Mirzaei, Preparation and characterization of FeNi/Al<sub>2</sub>O<sub>3</sub> catalysts for production of light olefins, *Petroleum Chemistry*, 52 (2012) 362-371.

[17] D. Pandey, G. Deo, Promotional effects in alumina and silica supported bimetallic Ni-Fe catalysts during CO<sub>2</sub> hydrogenation, *Journal of Molecular Catalysis A: Chemical*, 382 (2014) 23-30.

[18] S. Hwang, U. G. Hong, J. Lee, J. H. Baik, D. J. Koh, H. Lim, I. K. Song, Methanation of carbon dioxide over mesoporous Nickel-M-Alumina (M = Fe, Zr, Ni, Y, and Mg) xerogel catalysts: effect of second metal, *Catalysis Letters*, 142 (2012) 860-868.

[19] J. van de Loosdrecht, A. M. van der Kraan, A. J. van Dillen, J. W. Geus, Metal-support interaction: Titania-supported nickel-iron catalysts, *Catalysis Letters*, 41 (1996) 27-34.

[20] G. Chieffi, C. Giordano, M. Antonietti, D. Esposito, FeNi nanoparticles with carbon armor as sustainable hydrogenation catalysts: towards biorefineries, *Journal of Materials Chemistry*

A, 2 (2014) 11591.

[21] P. S. Kumbhar, M. R. Kharkar, G. D. Yadav, R. A. Rajadhyaksha, Geometric and electronic effects in silica supported bimetallic nickel copper and nickel iron catalysts for liquid-phase hydrogenation of acetophenone and benzonitrile, *Journal of the Chemical Society-Chemical Communications*, (1992) 584-586.

[22] L. Nie, P. M. de Souza, F. B. Noronha, W. An, T. Sooknoi, D. E. Resasco, Selective conversion of m-cresol to toluene over bimetallic Ni-Fe catalysts, *Journal of Molecular Catalysis A: Chemical*, 388-389 (2014) 47-55.

[23] T. Ishihara, K. Eguchi, H. Arai, Hydrogenation of carbon-monoxide over SiO<sub>2</sub>-supported Fe-Co, Co-Ni and Ni-Fe bimetallic catalysts, *Applied Catalysis*, 30 (1987) 225-238.

[24] M. Andersson, T. Bligaard, A. Kustov, K. Larsen, J. Greeley, T. Johannessen, C. Christensen, J. Nørskov, Toward computational screening in heterogeneous catalysis: Pareto-optimal methanation catalysts, *Journal of Catalysis*, 239 (2006) 501-506.

[25] A. L. Kustov, A. M. Frey, K. E. Larsen, T. Johannessen, J. K. Nørskov, C. H. Christensen, CO methanation over supported bimetallic Ni-Fe catalysts: From computational studies towards catalyst optimization, *Applied Catalysis A: General*, 320 (2007) 98-104.

# **Chapter I**

## Bibliographical study



*This chapter has been adapted as a published review: Ni promotion by Fe: what benefits for catalytic hydrogenation? – D. Shi, R. Wojcieszak, S. Paul, E. Marceau – Catalysts, 9, 451-478 (2019).*

In order to understand how the size, distribution, structure and Fe/Ni atomic ratio of Fe-Ni bimetallic nanoparticles affect the hydrogenation of organic molecules, it is highly important to firstly sum up the “state of the art” on that topic. The properties of supported Fe-Ni nanoparticles in catalytic hydrogenation reactions and the factors influencing the preparation of Fe-Ni bimetallic catalysts will be discussed in details in this chapter. In order to make comparisons easier between the different articles, the formulation of the catalysts described in the literature will be written using a common nomenclature: (% metals content)  $\text{Fe}_x\text{Ni}_{(100-x)}$ , with x and (100-x) corresponding to the respective molar proportions of the two metals in the catalyst.

### I.1. Fe-Ni systems as catalysts for hydrogenation reactions

Since the 1980s, various authors have noted that Fe-Ni bimetallic catalysts are promising candidates for hydrogenation processes, whether based on CO or CO<sub>2</sub> (methanation reaction, Fischer-Tropsch synthesis) or on biomass-derived organic molecules. Figure 1.1 exhibits the number of publications for each hydrogenation reactions dealing with supported Fe-Ni bimetallic catalysts.

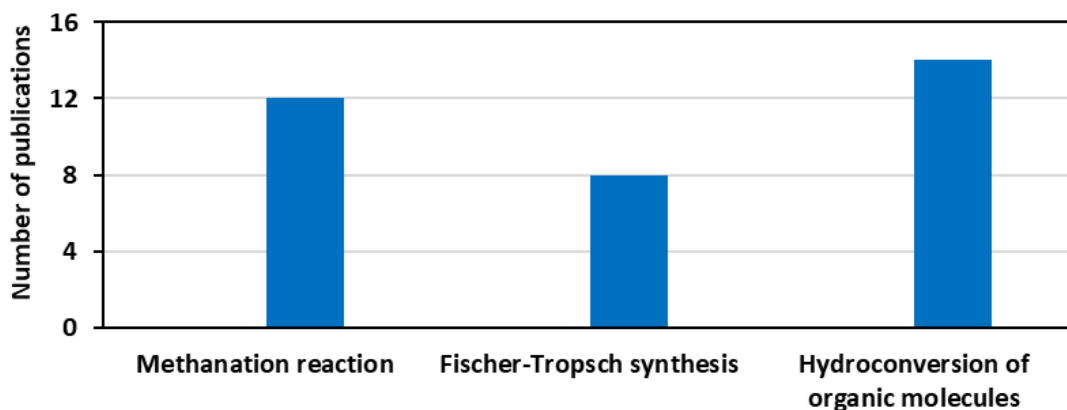


**Figure 1.1.** Number of publications on hydrogenation reactions with Fe-Ni bimetallic catalysts since 1980.

Source: Web of Science, keywords: iron, nickel, hydrogenation

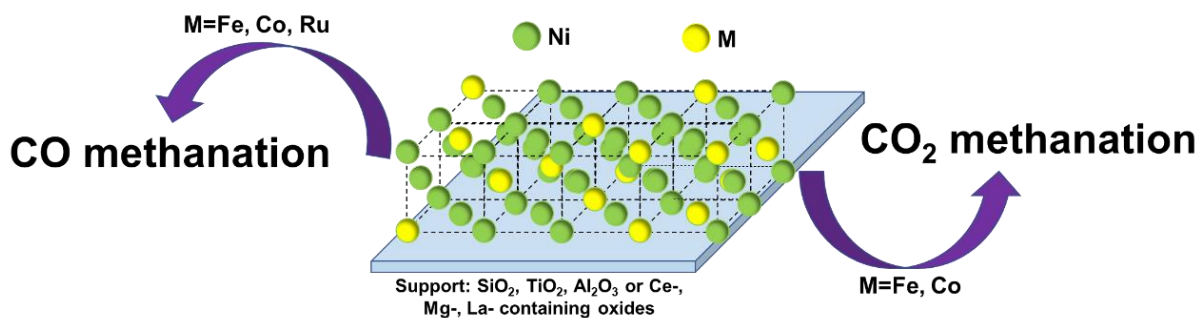
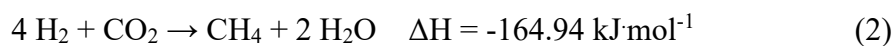
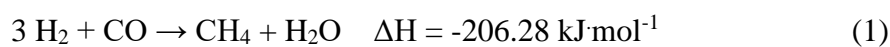


**Figure 1.2.** Bimetallic systems containing Ni used in CO and CO<sub>2</sub> methanation.

### I.1.1. Methanation reactions

CH<sub>4</sub> is the principal component of natural gas, but it can also be produced by hydrogenation of CO or CO<sub>2</sub>, and Ni-based catalysts are known to be effective for this family of reactions [1-4]. However, monometallic Ni catalysts exhibit a poor distribution of metal particles and deactivate under reaction conditions. A second metal has been effectively used as promoter to optimize the properties of monometallic Ni catalysts, as listed in Figure 1.2.

Reactions of CO and CO<sub>2</sub> methanation are described by Equations (1) and (2) [5]:



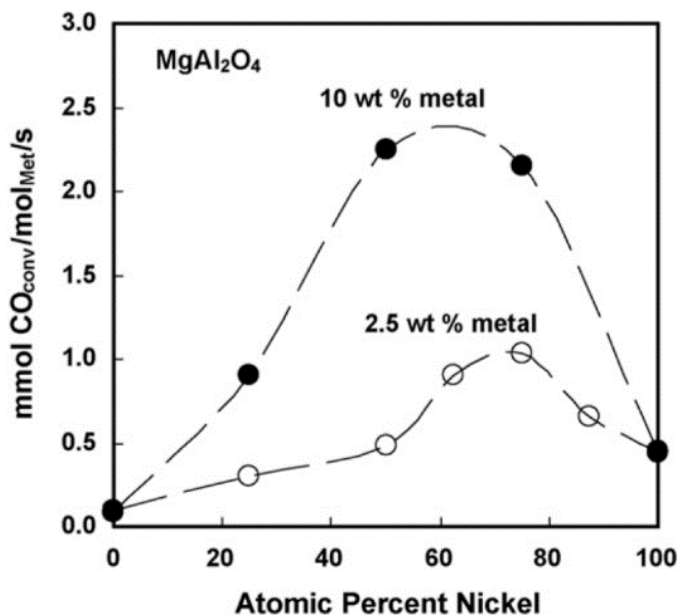


**Figure 1.3.** Measured rates of CO hydrogenation at 225 °C as a function of the Ni content in bimetallic Fe-Ni catalysts supported on MgAl<sub>2</sub>O<sub>4</sub>. Gas composition: 2% CO and 98% H<sub>2</sub>. GHSV = 50000 h<sup>-1</sup>. Reprinted from ref. 6. Copyright 2007 Elsevier

Tian *et al.* [1] showed that bimetallic Fe-Ni/ $\gamma$ -Al<sub>2</sub>O<sub>3</sub> exhibited a higher catalytic activity than a monometallic Ni/ $\gamma$ -Al<sub>2</sub>O<sub>3</sub> catalyst. Under industrial operation conditions (3.0 MPa, H<sub>2</sub>/CO = 3.1), the CO conversion provided by 23.3 wt% Fe<sub>25</sub>Ni<sub>75</sub>/ $\gamma$ -Al<sub>2</sub>O<sub>3</sub> reached 100% and the CH<sub>4</sub> selectivity exceeded 99% in the 300–450 °C temperature range, compared with 23.3 wt% Ni/ $\gamma$ -Al<sub>2</sub>O<sub>3</sub> (conversion of CO: 100%, selectivity to methane: 85%). Also on alumina, Hwang *et al.* [2] have investigated a series of mesoporous nickel-M/alumina xerogel (AX) catalysts, where M is a second metal (40 wt% Ni<sub>75</sub>M<sub>25</sub>/AX, M = Fe, Co, Ce and La). Both the conversion of CO and yield of CH<sub>4</sub> decreased in the order Ni<sub>75</sub>Fe<sub>25</sub>/AX > Ni<sub>100</sub>/AX > Ni<sub>75</sub>Co<sub>25</sub>/AX > Ni<sub>75</sub>Ce<sub>25</sub>/AX > Ni<sub>75</sub>La<sub>25</sub>/AX. This indicates that on mesoporous alumina, Fe also improved the properties of the catalyst compared with monometallic Ni<sub>100</sub>/AX.

Kustov *et al.* [6] found that 10 wt% bimetallic catalysts supported on MgAl<sub>2</sub>O<sub>4</sub> with molar compositions Fe<sub>25</sub>Ni<sub>75</sub> and Fe<sub>50</sub>Ni<sub>50</sub> showed significantly higher activities (conversion of CO: 99.5 and 95.4%, respectively) and selectivities to methane (92.9 and 85.3%, respectively) in comparison with monometallic 10 wt% Ni and 10 wt% Fe catalysts (Ni: conversion of CO: 34.6%, selectivity to methane: 94.2%; Fe: conversion of CO: 4.4%, selectivity to methane:



68.1%) (Figure 1.3). The selectivity to methane increased at higher CO conversion, and with a higher Ni loading in the catalysts. The highest catalytic activity and selectivity to methane were observed for catalyst Fe<sub>25</sub>Ni<sub>75</sub> with a 20 wt% total metals loading (Table 1.1). The same result was obtained by Andersson *et al.* [7], who found that a 10 wt% loading on MgAl<sub>2</sub>O<sub>4</sub> of Fe<sub>25</sub>Ni<sub>75</sub> and Fe<sub>50</sub>Ni<sub>50</sub> (rate of CO removal: 6 and 5.5 mmol CO/mmol metal.s, respectively) exhibited superior activity compared with Fe and Ni (rate: 0 and 2 mmol CO/mmol metal.s, respectively). An explanation has been given by combining catalytic measurements with DFT calculations. Like Co and Ru, the Fe<sub>25</sub>Ni<sub>75</sub> and Fe<sub>50</sub>Ni<sub>50</sub> alloy surfaces are anticipated to be optimum systems in terms of rate of hydrogenation of carbon, and dissociation energy of CO ( $E_{\text{diss}}$ ), used as the main descriptor. Compared with an optimal value of  $E_{\text{diss}} = 0.06$  eV, the calculated gap  $\Delta E_{\text{diss}} = E_{\text{diss}} - E_{\text{diss optimal}}$  for Fe<sub>25</sub>Ni<sub>75</sub> and Fe<sub>50</sub>Ni<sub>50</sub> is lower than 0.25 eV, which is smaller than for Fe (0.9 eV) and Ni (0.4 eV).

**Table 1.1.** Catalytic performances of bimetallic Fe<sub>25</sub>Ni<sub>75</sub> catalysts with different total metal loadings supported on MgAl<sub>2</sub>O<sub>4</sub>. Adapted from ref. 6.

Total metal loading (wt%)	Metal content in the catalyst (wt%)		CO conversion (%)	Selectivity to CH <sub>4</sub> (%)
	Fe	Ni		
2.41	0.53	1.88	24.3	92.8
4.84	1.18	3.66	37.6	93.6
9.79	2.15	7.65	95.8	97.4
15.34	3.76	11.58	98.7	98.3
19.83	4.90	14.93	100.0	99.1
24.01	6.12	17.89	96.3	98.7
30.67	8.04	22.63	2.9	83.0

Gas composition: 2% CO and 98% H<sub>2</sub>. GHSV = 50,000 h<sup>-1</sup>, T = 275 °C.

The influence of the support on the conversion of CO and selectivity to CH<sub>4</sub> has been studied by Jiang *et al.* [8]. 6.15 wt% Fe<sub>6</sub>Ni<sub>94</sub>/Al<sub>2</sub>O<sub>3</sub> (conversion of CO: 4.4%, selectivity to methane: 94%) was found to be more selective than 5.75 wt% Fe<sub>10</sub>Ni<sub>90</sub>/TiO<sub>2</sub> (conversion of CO: 3.8%, selectivity to methane: 43%). However, 5.75 wt% Fe<sub>10</sub>Ni<sub>90</sub>/TiO<sub>2</sub> was more active for the formation of higher hydrocarbons (conversion of CO: 3.8%, selectivity to C<sub>3</sub>-C<sub>5</sub>: 50%). 6.15 wt% Fe<sub>6</sub>Ni<sub>94</sub>/Al<sub>2</sub>O<sub>3</sub> did not show any selectivity to C<sub>3</sub>-C<sub>5</sub>. TiO<sub>x</sub> species on the metal surface

were supposed to serve as a source of OH groups which favor chain-growth through a facilitated elimination of water between growing carbon fragments.

However, it should be noted that the surface composition of the catalyst, which directly determines the catalytic properties, might be different from the nominal composition. Bussière *et al.* [9] found using X-ray photoelectron spectroscopy (XPS) that the Fe/Ni ratio on the surface of a catalyst can change with increasing reduction temperature. For instance, a Fe<sub>50</sub>Ni<sub>50</sub> catalyst possesses a Fe/Ni surface ratio of 10 on the surface after reduction by hydrogen at 200 °C, and the ratio decreases to 1.4 after reduction at 400 °C under hydrogen, because more metallic Ni has come to the surface. The selectivity to methane increased from 65 to 90% at isoconversion. Both Fe and Ni were incompletely reduced during this hydrogen treatment. The total reduction of Fe and Ni required a temperature higher than 400 °C.

**Table 1.2.** Catalytic performances of Ni<sub>86</sub>M<sub>14</sub>/AX catalysts (M = Fe, Zr, Ni, Y and Mg) for methane production from carbon dioxide and hydrogen at 220 °C after 10 h. Adapted from ref. 10.

Catalyst	Conversion (%)		Selectivity (%)				CH <sub>4</sub> yield (%)
	CO <sub>2</sub>	H <sub>2</sub>	C <sub>1</sub>	C <sub>2</sub>	C <sub>3</sub>	CO	
35Ni5FeAX	63.4	68.3	99.5	0.5	0	0	63.1
35Ni5ZrAX	61.6	66.8	99.1	0.8	0.1	0	61.0
35Ni5NiAX	61.1	66.0	99.2	0.7	0.1	0	60.0
35Ni5YAX	58.4	61.9	99.5	0.5	0	0	58.1
35Ni5MgAX	54.2	56.6	99.5	0.4	0.1	0	53.9

Additionally, CO<sub>2</sub> methanation plays an important role in the “power to gas” process and also is an efficient method to produce CH<sub>4</sub> and mitigate CO<sub>2</sub> emissions. In line with their study of CO hydrogenation, Hwang *et al.* [10] have investigated the methanation of CO<sub>2</sub> with a series of mesoporous nickel-M/alumina xerogel (AX) catalysts where M is a second metal (35 wt% Ni<sub>86</sub>M<sub>14</sub>/AX, M = Fe, Zr, Ni, Y and Mg). Both the conversion of CO<sub>2</sub> and yield to CH<sub>4</sub> decreased in the order of Ni<sub>86</sub>Fe<sub>14</sub>/AX > Ni<sub>86</sub>Zr<sub>14</sub>/AX > Ni<sub>100</sub>/AX > Ni<sub>86</sub>Y<sub>14</sub>/AX > Ni<sub>86</sub>Mg<sub>14</sub>/AX, meaning that, as in the case of CO hydrogenation, the Fe-Ni catalyst gave the best results. Detailed data are shown in Table 1.2. Sheshko *et al.* [11] also found that 10 wt% Fe<sub>50</sub>Ni<sub>50</sub>/Al<sub>2</sub>O<sub>3</sub> (yield of methane: 243 μmol/(h·g<sub>active phase</sub>)) exhibited a higher activity than 10 wt% Fe<sub>50</sub>Mn<sub>50</sub>/Al<sub>2</sub>O<sub>3</sub> (yield of methane: 20.8 μmol/(h·g<sub>active phase</sub>)) at 300 °C.

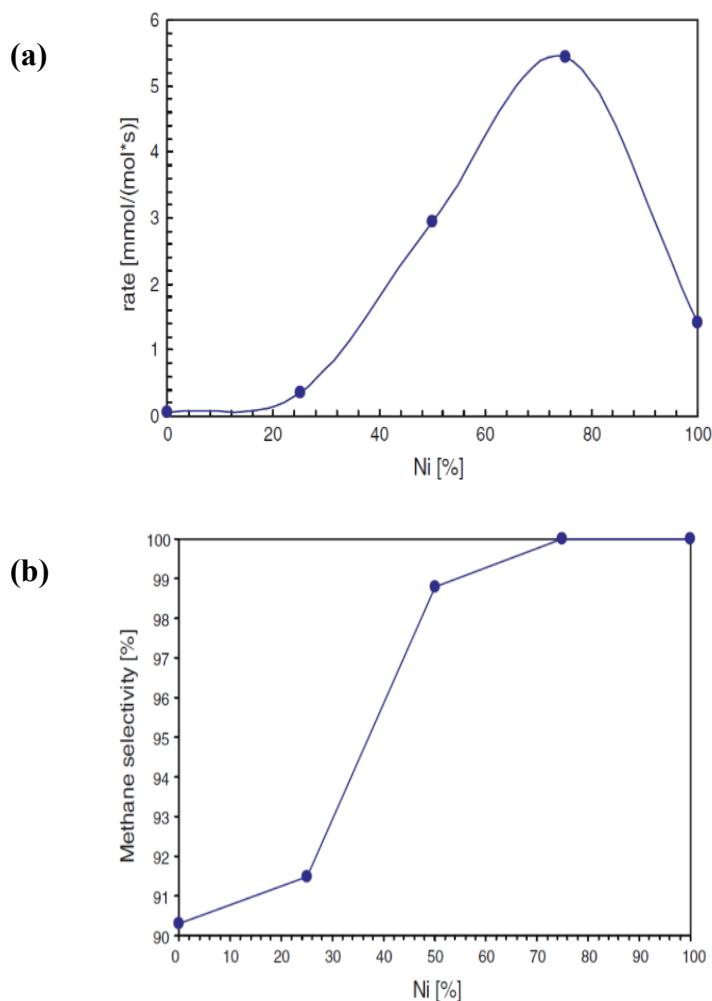


**Figure 1.4.** Measured rate of CO<sub>2</sub> hydrogenation (a) and methane selectivity (b) in a gas containing 2% CO<sub>2</sub> and 2% CO in hydrogen with a total flow of 6 L (STP)/h at 330 °C, as a function of the Ni fraction in 10 wt% Fe-Ni catalysts. Reprinted from ref. 12. Copyright 2007 Springer

The combination of Fe and a small amount of nickel was investigated by Saththawong *et al.* [3]. They showed that adding a low amount of Ni to Fe (15 wt% Fe<sub>98.4</sub>Ni<sub>1.6</sub>/Al<sub>2</sub>O<sub>3</sub>) was required for a reactivity enhancement (conversion of CO<sub>2</sub>: 37.6%, selectivity to CH<sub>4</sub>: 98%) compared with monometallic Fe (conversion of CO<sub>2</sub>: 12.1%, selectivity to CH<sub>4</sub>: 62%). Sehested *et al.* [12] found that a large amount of Ni in Fe-Ni particles (10 wt% Fe<sub>22</sub>Ni<sub>78</sub>/Al<sub>2</sub>O<sub>3</sub>) gave a high conversion of CO<sub>2</sub> and selectivity to methane (Figure 1.4). The 10 wt% Fe<sub>22</sub>Ni<sub>78</sub>/Al<sub>2</sub>O<sub>3</sub> catalyst gave 100% of methane selectivity with the highest rate of CO<sub>2</sub> consumption, and was more active and selective than monometallic Fe or Ni.

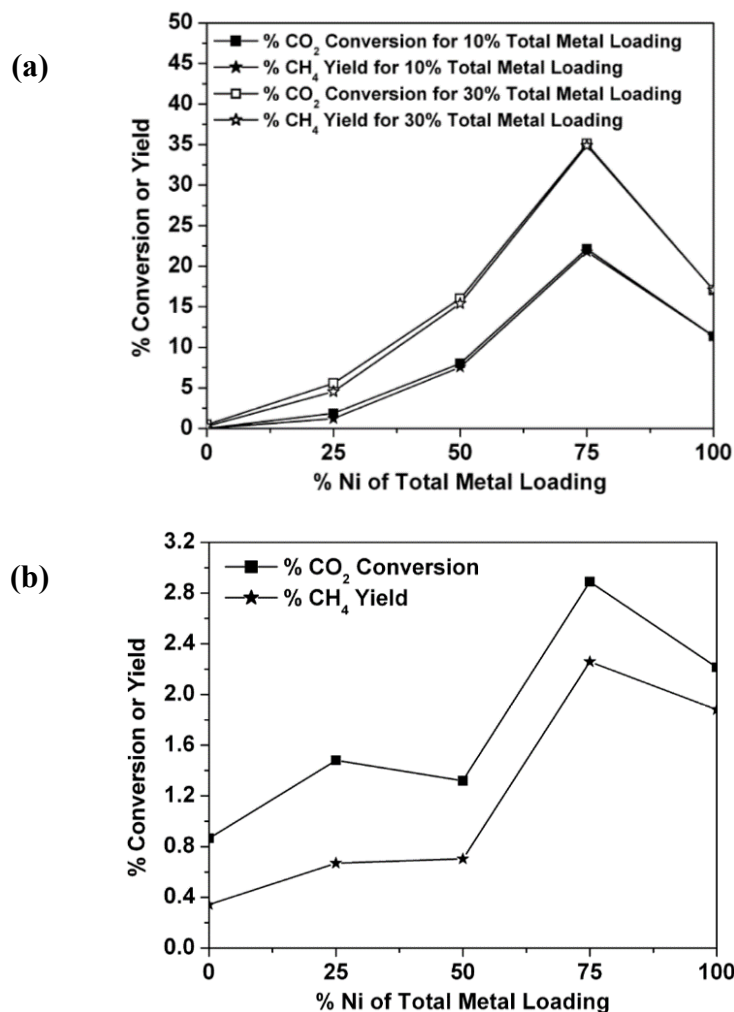


**Figure 1.5.** CO<sub>2</sub> conversion and CH<sub>4</sub> yield for series of 10 and 30 wt% Fe–Ni/Al<sub>2</sub>O<sub>3</sub> catalysts (a) and 10 wt% Fe–Ni/SiO<sub>2</sub> catalysts (b).[4] Copyright 2014 Elsevier

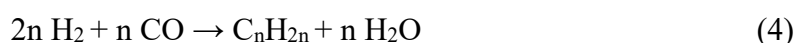
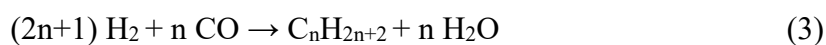
Mutz *et al.* [13] similarly found that a 17 wt% Fe<sub>25</sub>Ni<sub>75</sub>/Al<sub>2</sub>O<sub>3</sub> catalyst produced a higher conversion of CO<sub>2</sub> (80%) and selectivity to methane (99%) compared with 17 wt% Ni/Al<sub>2</sub>O<sub>3</sub> (conversion of CO<sub>2</sub>: 70%, selectivity to CH<sub>4</sub>: 97%). Comparison with monometallic Fe/Al<sub>2</sub>O<sub>3</sub> was not mentioned.

The metal loading and choice of support have also been determined to be important factors to enhance the activity [4]. Here as well, Fe<sub>25</sub>Ni<sub>75</sub> was found to be the optimum composition. 30 wt% Fe<sub>25</sub>Ni<sub>75</sub>/Al<sub>2</sub>O<sub>3</sub> (conversion of CO<sub>2</sub>: 35%, selectivity to CH<sub>4</sub>: 35%) exhibited an enhanced activity compared with 10 wt% Fe<sub>25</sub>Ni<sub>75</sub>/Al<sub>2</sub>O<sub>3</sub> (conversion of CO<sub>2</sub>: 22%, selectivity to CH<sub>4</sub>: 22%), as shown in Figure 1.5a, in connection with the increase in the number of metal

sites. Moreover, 10 wt% Fe<sub>25</sub>Ni<sub>75</sub>/Al<sub>2</sub>O<sub>3</sub> showed a higher activity (conversion of CO<sub>2</sub>: 22%, selectivity to CH<sub>4</sub>: 22%) than a similar catalyst supported on SiO<sub>2</sub> (conversion of CO<sub>2</sub>: 3%, selectivity to CH<sub>4</sub>: 2.2%) (Figure 1.5b). Larger metal particles were formed on SiO<sub>2</sub> (11 nm) compared to Al<sub>2</sub>O<sub>3</sub> (particles could not be detected by XRD meaning that they are smaller than a few nm). It was also supposed that carbonates adsorbed onto Fe<sub>3</sub>O<sub>4</sub> species remaining unreduced on the Al<sub>2</sub>O<sub>3</sub> support and detected by DRIFT can act as reaction intermediates.

### I.1.2. Fischer-Tropsch synthesis

The Fischer–Tropsch synthesis (FTS), discovered by Fischer and Tropsch in the 1920s, has been paid renewed attention in recent years due to the increase of oil prices, decreasing oil reserves and environmental concerns [14-16]. Through FTS, a large variety of carbon-containing resources, coal, natural gas, biomass, can be converted to chemicals and liquid fuels. The principle of the FTS reaction is the strongly exothermic hydrogenation of carbon monoxide (CO) to paraffins and olefins, according to the following chemical equations (3) and (4) [14]:



Among transition metals, Fe, Co and Ru are known to be active for C-C coupling, and the first two metals are the ones that are mostly used industrially due to the high cost and low abundance of Ru [16].

In FTS, Fe–Ni catalysts have been found to provide a high catalytic activity, and a different product distribution from monometallic Fe and Ni catalysts. Li *et al.* [15] showed that Ni-promoted Fe fresh catalysts were mainly composed of  $\alpha$ -Fe<sub>2</sub>O<sub>3</sub> and NiFe<sub>2</sub>O<sub>4</sub>. The addition of nickel improved the dispersion of iron oxides, which led to an increase of the catalyst surface area, and a decrease of the metal oxide crystallite size. The presence of Ni improved the reduction and carburization rates of Fe in H<sub>2</sub> and CO, respectively, while suppressing the formation of iron carbides. The conversion provided by an unsupported Fe<sub>87</sub>Ni<sub>13</sub> catalyst (50%) was more stable with time on stream than that given by the monometallic Fe catalyst (decrease from 65% to 30%). The selectivity to CH<sub>4</sub> and C<sub>2-4</sub> were up to 54.9 and 42.1% at a conversion

of 44.7% for Fe<sub>87</sub>Ni<sub>13</sub>, while monometallic Fe gave 22% of selectivity to CH<sub>4</sub> and 50% of selectivity to C<sub>2</sub>-C<sub>4</sub> at a conversion of 33%.

However, Amelse *et al.* [17], Arai *et al.* [18] and Loosdrecht *et al.* [19] found that for 4.2 wt% Fe<sub>50</sub>Ni<sub>50</sub>/SiO<sub>2</sub> (conversion of CO: 3%, selectivity to C<sub>2</sub>-C<sub>4</sub> olefins/paraffins: 21.3%), 10 wt% Fe<sub>50</sub>Ni<sub>50</sub>/TiO<sub>2</sub> (conversion of CO: 20.5%, selectivity to C<sub>2</sub>-C<sub>4</sub> olefins: 73.9%) and 20 wt% Fe<sub>50</sub>Ni<sub>50</sub>/TiO<sub>2</sub> (conversion of CO: 9.7%, selectivity to C<sub>2</sub>-C<sub>4</sub> olefins: 67%), both CO conversion and selectivity to C<sub>2</sub>-C<sub>4</sub> were higher compared with monometallic 4.58 wt% Ni/SiO<sub>2</sub> (conversion of CO: 2.3%, selectivity to C<sub>2</sub>-C<sub>4</sub> olefins/paraffins: 16.3%), 10 wt% Ni/TiO<sub>2</sub> (conversion of CO: 15.5%, selectivity to C<sub>2</sub>-C<sub>4</sub> olefins: 63.1%) and monometallic 20 wt% Fe/TiO<sub>2</sub> (conversion of CO: 2.6%, selectivity to C<sub>2</sub>-C<sub>4</sub> olefins: 55%). Ishihara *et al.* [20] found that in their experimental conditions, 10 wt% Fe<sub>25</sub>Ni<sub>75</sub>/SiO<sub>2</sub> had the highest CO conversion (16%) in comparison with monometallic 10 wt% Fe/SiO<sub>2</sub> (0%) and 10 wt% Ni/SiO<sub>2</sub> (2%). The best catalytic activities for Fe-Ni/SiO<sub>2</sub> catalysts were correlated with the way NO, used as a probe molecule and characterized by infrared spectroscopy, adsorbed on the surface of the particles. The intensity of the bent-type band for 10 wt% Fe<sub>25</sub>Ni<sub>75</sub>/SiO<sub>2</sub> was stronger than for other compositions. This was interpreted as revealing a higher number of electron-donating surface sites, thought to be more active for CO hydrogenation.

The influence of metal loading on catalytic performance was studied on a TiO<sub>2</sub> support by van de Loosdrecht *et al.* [21]. CO initial conversion increased from 15 to 31% when increasing the Fe<sub>40</sub>Ni<sub>60</sub> loading from 2 to 20 wt%. The amount of carbon deposited per mol of metal was found to be increasing when decreasing the metals loading, leading to deactivation. However, the selectivity to C<sub>3+</sub> increased from 40 to 55% at decreasing loading. TiO<sub>x</sub> (x < 2) species on the surface of the smaller particles at low loading were supposed to globally inhibit CO and H<sub>2</sub> chemisorption, but also to increase the dissociative adsorption of carbon monoxide of the catalyst, and decrease the dissociation of hydrogen. This causes an increase in the ratio between dissociated CO and dissociated hydrogen on the alloy surfaces, leading to more C-C bonding.

Support effects have been studied by Ishihara *et al.* [22] (Table 1.3). Fe-Ni particles supported on TiO<sub>2</sub> exhibited a higher CO conversion than when supported on SiO<sub>2</sub>: 10 wt% Fe<sub>25</sub>Ni<sub>75</sub>/TiO<sub>2</sub> exhibited a 43.2% CO conversion, which is higher than with 10 wt% Fe<sub>25</sub>Ni<sub>75</sub>/SiO<sub>2</sub> (16.5%). Selectivities to C<sub>2</sub><sup>-</sup> - C<sub>5</sub><sup>-</sup> and C<sub>2</sub><sup>-</sup> - C<sub>5</sub><sup>-</sup> were less sensitive to the catalyst composition; however, comparison is not obvious, as data are given at different conversions.

**Table 1.3.** Hydrogenation of carbon monoxide over supported Fe-Ni catalysts. Conditions: T = 250 °C, H<sub>2</sub>/CO/Ar = 62/33/5, GHSV = 0.1 mol/h, P = 10 bar, W<sub>Catalyst</sub> = 1 g. Adapted from ref. 22.

Catalyst	TiO <sub>2</sub> -supported						SiO <sub>2</sub> -supported					
	CO conv./%	Selectivity / % <sup>a</sup>					CO conv./%	Selectivity / % <sup>a</sup>				
		Oxy.	CH <sub>4</sub>	C <sub>2</sub> <sup>-</sup> - C <sub>5</sub> <sup>-</sup>	C <sub>2</sub> <sup>-</sup> - C <sub>5</sub> <sup>-</sup>	C <sub>6</sub> <sup>+</sup>		Oxy.	CH <sub>4</sub>	C <sub>2</sub> <sup>-</sup> - C <sub>5</sub> <sup>-</sup>	C <sub>2</sub> <sup>-</sup> - C <sub>5</sub> <sup>-</sup>	C <sub>6</sub> <sup>+</sup>
Ni	15.5	2.0	36.8	7.2	49.5	6.5	1.6	0	74.7	8.9	16.4	0
Fe	2.2	0	37.5	11.0	51.5	0	0.2	0	58.1	18.5	23.4	0
Fe <sub>25</sub> Ni <sub>75</sub>	43.2	3.1	18.5	13.3	52.9	15.3	16.5	0.3	36.4	10.0	45.0	8.6
Fe <sub>50</sub> Ni <sub>50</sub>	20.5	2.3	20.2	10.6	40.8	28.6	9.8	0.1	38.1	6.8	44.9	10.2
Fe <sub>75</sub> Ni <sub>25</sub>	7.1	0.7	29.3	4.2	62.2	4.3	4.3	0.2	54.1	18.9	27.0	0

<sup>a</sup>Calculations based on carbon number.

C<sub>2</sub><sup>-</sup> - C<sub>5</sub><sup>-</sup>: olefins, C<sub>2</sub><sup>-</sup> - C<sub>5</sub><sup>-</sup>: paraffins, Oxy.: oxygenated compounds

The selective formation of light olefins by FTS is an important issue for the industry. Feyzi *et al.* [16] have shown that with optimal operating conditions (calcination at 260 °C, H<sub>2</sub>/CO ratio = 2/1, GHSV = 3200 h<sup>-1</sup>, total pressure of 3 bar), a 60 wt% Fe<sub>40</sub>Ni<sub>60</sub>/Al<sub>2</sub>O<sub>3</sub> catalyst was more selective to C<sub>2</sub>-C<sub>4</sub> (37.1%) than with H<sub>2</sub>/CO ratios = 1/1 or 3/1 (23 and 25.5%), or with other GHSV. Furthermore, the addition of Ni increased the reducibility of 60 wt% Fe<sub>40</sub>Ni<sub>60</sub>/Al<sub>2</sub>O<sub>3</sub> catalyst (maximum H<sub>2</sub> consumption at 500 °C) compared with a 60 wt% Fe/Al<sub>2</sub>O<sub>3</sub> catalyst (maximum at 600 °C), which suggests that Ni helped to reduce iron at lower temperature.

### I.1.3. Hydrogenation of organic molecules

As shown in Figure 1.1, supported Fe-Ni catalysts have also been investigated for the hydroconversion of organic molecules.

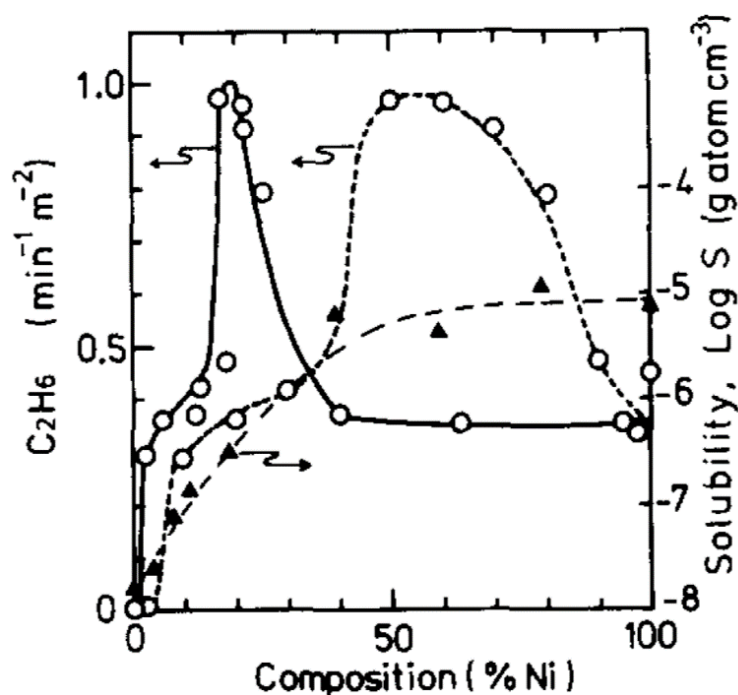


**Figure 1.6.** Catalytic activities in the hydrogenation of ethylene on Fe-Ni catalysts. Activity expressed by surface composition (—○—); Activity expressed by bulk composition (---○---); the triangles show the solubility of hydrogen. Reprinted from ref. 23. Copyright 1986 Elsevier

The hydrogenation of the alkene or alkyne function of ethylene, styrene and phenylacetylene has been studied by Matsuyama *et al.* [23] and Chieffi *et al.* [24]. These reactions can be achieved at low temperature (0, 50 and 50 °C, respectively). The formulations were unsupported  $\text{Fe}_{50}\text{Ni}_{50}$ , 56 wt%  $\text{Fe}_{42}\text{Ni}_{58}$ /cellulose and 56 wt%  $\text{Fe}_{42}\text{Ni}_{58}$ /cellulose, respectively. The reaction temperature should be higher than 100 °C to hydrogenate the aromatic ring. Using 56 wt%  $\text{Fe}_{42}\text{Ni}_{58}$ /cellulose and 25 wt%  $\text{Fe}_{25}\text{Ni}_{75}$ / $\text{CeO}_2$ , respectively, a high activity was achieved for the hydrogenation of  $\alpha$ -terpinene [24] and 2-cyclohexen-1-one [25] at a reaction temperature of 125 °C (conversion of  $\alpha$ -terpinene: 99%, selectivity to 1-isopropyl-4-methylcyclohexene: 56%) or 130 °C (conversion of 2-cyclohexen-1-one: 100%, selectivity to cyclohexanone: 98%).

A relationship between the reactivity and the surface composition, as well as the bulk composition of Fe-Ni alloys, has been studied by Matsuyama *et al.* using the hydrogenation of ethylene [23]. The activity increased gradually in the average composition range 10-40% Ni, where the crystal structure of the bulk is composed of a mixture of *fcc* and *bcc* structures, as



shown in Figure 1.6. The maximum activity was reached for a bulk composition of 50% Ni (pure *fcc*). This corresponded to a surface composition of only 20% Ni. In other words, the concentration of Ni on the surface was always lower, and the concentration of Fe was higher, than in the bulk of the alloy.

Fe-Ni catalysts have also been tested in the hydrogenation of oxygenated molecules (ketones, aldehydes, sugars, acids, esters). The best catalytic activity for the hydrogenation of acetophenone to  $\alpha$ -phenylethanol (optimum formulation: 20 wt% Fe<sub>25</sub>Ni<sub>75</sub>/SiO<sub>2</sub>) [26] was achieved at a reaction temperature of 135 °C, as shown in Figure 1.7.

It was supposed that a charge transfer from Fe to Ni took place on Fe<sub>25</sub>Ni<sub>75</sub> particles, with an increase in electron density of Ni that should lead to increased metal-carbon bonding, and weakening of the carbon-oxygen bond. Chieffi *et al.* [24] have tested the hydrogenation of several oxygenated molecules, including monosaccharides, using a 56 wt% Fe<sub>42</sub>Ni<sub>58</sub>/carbon catalyst, as summarized in Table 1.4.

Hydrogenation of ethyl levulinate [27] was achieved on a 10 wt% Fe<sub>33</sub>Ni<sub>67</sub> catalyst supported on activated carbon, at a reaction temperature of 100 °C (conversion of ethyl levulinate: 100%, selectivity to  $\gamma$ -valerolactone: 99%). The evolution of the catalytic properties with the catalyst formulation is given in Table 1.5. With the increase of Fe content, the conversion and yield increased and reached a maximum for Fe<sub>33</sub>Ni<sub>67</sub>. A further increase led to a decrease of conversion and yield. The optimal formulation was linked to the presence of a maximum amount of Lewis acidic sites characterized by NH<sub>3</sub>-TPD, compared with other Fe-Ni compositions and monometallic Fe and Ni. Lewis acidic sites were supposed to attract and activate the carbonyl group of the ester function, through interactions with the electron pair of the oxygen atom.

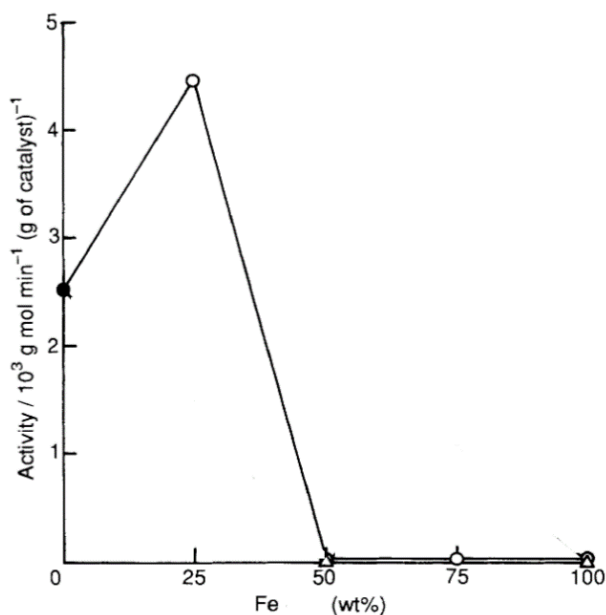


**Figure 1.7.** Activity pattern for 20 wt% Fe-Ni/SiO<sub>2</sub> catalysts in the hydrogenation of acetophenone. Reaction conditions: T = 135 °C, P = 5.9 bar, W<sub>Catalyst</sub> = 150 mg, acetophenone = 15 g, methanol = 45 mL. Reprinted from ref. 26. Copyright 1992 Royal Society of Chemistry

**Table 1.4.** Conversion and selectivity for the hydrogenation of oxygenated molecules by a 56 wt% Fe<sub>42</sub>Ni<sub>158</sub>/carbon catalyst. Conditions: 0.1 M solution in ethanol, <sup>a</sup> 50 bar (H<sub>2</sub>), <sup>b</sup> 10 bar (H<sub>2</sub>), reaction temperature: 150 °C [24].

Substrate	Product	Conversion (%)	Selectivity (%)
Cyclohexanone <sup>a</sup>	Cyclohexanol	84	99
Benzaldehyde <sup>b</sup>	Benzyl alcohol	99	84
Levulinic acid <sup>a</sup>	γ-valerolactone	96	60
Glucose <sup>a</sup>	Sorbitol	99	99
Xylose <sup>a</sup>	Xylitol	99	99

**Table 1.5.** Catalytic performances of Fe-Ni/AC (activated carbon) catalysts for the hydrogenation of ethyl levulinate to γ-valerolactone by H<sub>2</sub>. Conditions: 40 mg catalyst, 100 mg ethyl levulinate, 10 mL water as solvent, 4 MPa H<sub>2</sub>, 100 °C, 6 h, 800 rpm. Adapted from ref. 27.

Entry	Catalysts	Conv. (%)	Yield (%)
1	Ni/AC	53.0	51.7
2	Fe/AC	0	0
3	Fe <sub>17</sub> Ni <sub>83</sub> /AC	91.7	85.9
4	Fe <sub>33</sub> Ni <sub>67</sub> /AC	99.3	99.0
5	Fe <sub>50</sub> Ni <sub>50</sub> /AC	97.1	90.6
6	Fe <sub>67</sub> Ni <sub>33</sub> /AC	78.5	76.2
7	Fe/AC and Ni/AC	59.8	57.3

The hydrogenation of the C≡N bond in nitriles, such as benzonitrile [26], butyronitrile, cinnamitrile and crotonitrile [28] was performed at 150 °C in methanol with 20 wt% Fe<sub>25</sub>Ni<sub>75</sub>/SiO<sub>2</sub> as the optimum formulation. The major final product is the primary amine with some secondary amines. As explained above for the hydrogenation of acetophenone, the reason behind the best catalytic activity of 20 wt% Fe<sub>25</sub>Ni<sub>75</sub>/SiO<sub>2</sub> was assigned to a charge transfer from Fe to Ni.

#### I.1.4. Hydrodeoxygenation of organic molecules

Hydrogenolysis takes place at higher temperatures than hydrogenation reactions presented in the former section. Leng *et al.* [29] showed that 20 wt% Fe<sub>25</sub>Ni<sub>75</sub>/Al<sub>2</sub>O<sub>3</sub> bimetallic catalysts exhibited an excellent activity and selectivity for the hydrodeoxygenation (HDO) of furfuryl alcohol, benzene alcohol and ethyl oenanthatate, at atmospheric pressure and T = 400 °C. The conversions were found to be 100, 95.48 and 97.89%, respectively, and the yield to 2-methylfuran, toluene and heptane were 98.85, 93.49 and 96.11%, respectively.

Fang *et al.* [30] studied the effect of the Fe/Ni atomic ratio for catalysts supported on carbon nanotubes (CNT) on the activity and products distribution in the HDO of guaiacol at 300 °C (Figure 1.8). Monometallic 7 wt% Ni/CNTs exhibited a 79% conversion and 60% selectivity to cyclohexane. A 83.4% selectivity to cyclohexane at 96.8% of conversion was obtained with 7 wt% Fe<sub>17</sub>Ni<sub>83</sub>/CNT. The guaiacol was supposed to be preferentially adsorbed on the surface of oxophilic Fe domains. When increasing the Fe content, the activity became lower and HDO became incomplete, as selectivity was shifted to the production of phenol, such as with 7 wt% Fe<sub>83</sub>Ni<sub>17</sub>/CNT (conversion of guaiacol: 50%, selectivity to phenol: 77%). The HDO of guaiacol requires the dissociation of H<sub>2</sub> on Ni species and the amount of activated hydrogen atoms was considered to be insufficient on Fe-rich particles. The Fe-Ni nanoparticle size and the reduction temperature were also investigated. Increasing the reduction temperature from 400 to 600 °C for Fe-Ni/CNT catalysts increased the size of Fe<sub>17</sub>Ni<sub>83</sub> nanoparticles from 7.7 to 11.2 nm, leading to a decrease of the selectivity to cyclohexane from 85.4 to 55.8%.

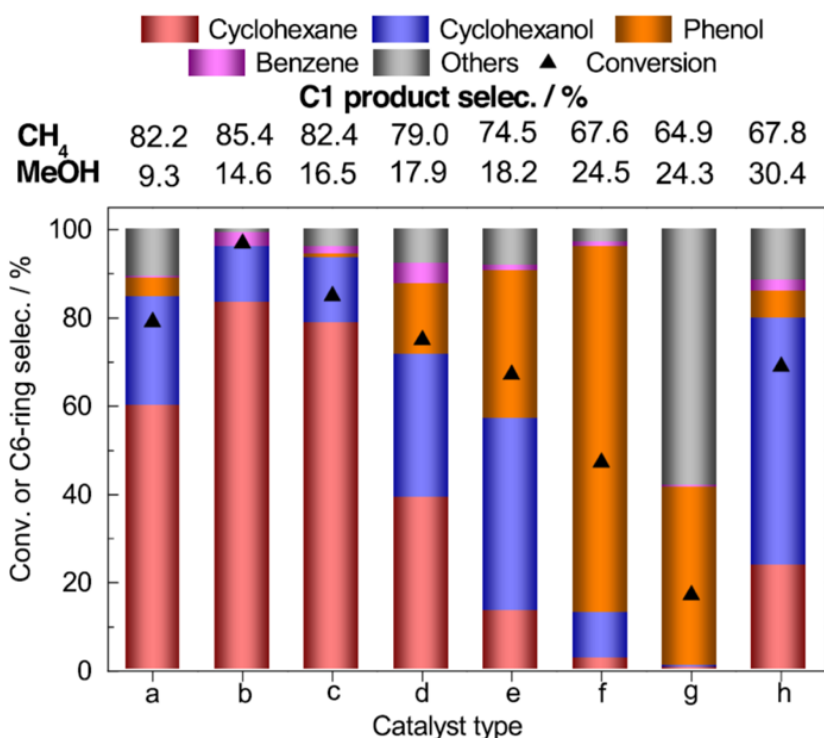


**Figure 1.8.** Catalytic performances of Fe–Ni/CNT catalysts with different Fe/Ni atomic ratios in the hydrodeoxygenation of guaiacol: (a) Ni/CNT, (b) Fe<sub>17</sub>Ni<sub>83</sub>/CNT, (c) Fe<sub>33</sub>Ni<sub>67</sub>/CNT, (d) Fe<sub>50</sub>Ni<sub>50</sub>/CNT, (e) Fe<sub>67</sub>Ni<sub>33</sub>/CNT, (f) Fe<sub>83</sub>Ni<sub>17</sub>/CNT, (g) Fe/CNT, and (h) Ni/CNT + Fe/CNT (Fe/Ni = 1/5). Reaction conditions: WLHSV<sub>GUA</sub> = 6.0 h<sup>-1</sup>, P (H<sub>2</sub>) = 3.0 MPa, H<sub>2</sub>/GUA molar ratio = 50, T = 573 K. Reprinted from ref. 30. Copyright 2017 Elsevier

The effect of Fe content has also been surveyed by Nie *et al.* [31] for the hydrogenolysis of m-cresol. The predominant product for a 15 wt% Ni/SiO<sub>2</sub> catalyst was 3-methylcyclohexanone (conversion of m-cresol: 16.2%, selectivity to 3-methylcyclohexanone: 33.3%), meaning that Ni has a strong affinity for the aromatic ring. Instead, the predominant product was toluene for a 15 wt% Fe<sub>50</sub>Ni<sub>50</sub>/SiO<sub>2</sub> catalyst (conversion of m-cresol: 13.7%, selectivity to toluene: 52.6%), suggesting that oxophilic Fe decreased the interaction with the aromatic ring.

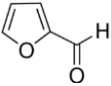
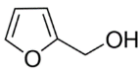
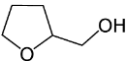
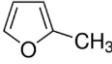
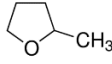
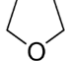
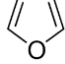
### I.1.5. Hydroconversion of furfural and 5-hydroxymethyl furfural

Results obtained in the hydroconversion of furfural and 5-hydroxymethyl furfural will be presented in this section. Furfural holds a functional aldehyde group (C=O) and a conjugated system of C=C–C=C bonds in the furan ring. Chemical and physical properties of furfural and of its main hydroconversion products are summarized in Table 1.6.

The selective hydrogenation of the aldehyde group leads to furfuryl alcohol (FFA), an intermediate in the production of fine chemicals and synthetic fibers, rubbers and corrosion resistant glass fibers [32-34]. It is also a valuable feedstock for the production of tetrahydrofurfuryl alcohol (THFFA) by hydrogenation of the furan ring, which is a key intermediate for the synthesis of vitamin C, plasticizers, lubricants and lysine. The hydrogenolysis of the C-O bond of the side group leads to a fuel additive, 2-methyl-furan (MF), while decarbonylation leads to furan. 2-methyltetrahydrofuran (MTHF) and tetrahydrofuran (THF) are obtained when the furan ring has been hydrogenated.

The production of FFA with respect to the other products thus lies on the choice of experimental conditions and of a catalyst that hydrogenates the aldehyde function selectively, without hydrogenolysis of the side group and/or hydrogenation of the furan ring.

**Table 1.6.** Chemical and physical properties of furfural and of its main hydroconversion products.

Property	Furfural	FFA	THFFA	MF	MTHF	THF	Furan
Chemical abstract name	Furan-2-carbaldehyde	(Furan-2-yl)methanol	(Oxolan-2-yl)methanol	2-Methylfuran	2-Methyloxolane	Oxolane	Furan
Synonyms	Furfural, Furan-2-Carboxaldehyde, Fural, Furfuraldehyde, 2-furaldehyde, Pyromucic aldehyde	Furan-2-ylmethanol, Furfuryl alcohol, 2-Furanmethanol, 2-Furanmethanol, 2-(Hydroxymethyl)furan	Tetrahydrofurfuryl alcohol, 2-Hydroxymethyl tetrahydrofuran, Tetrahydro-2-furanmethanol	Methylfuran, 2-Methylfuran, 5-Methylfuran, Silvan	2-Methyltetrahydrofuran, 2-Methyl-THF	Tetrahydrofuran, Butylene oxide, Cyclooctamethylene oxide, Diethylene oxide, Tetramethylene oxide	Oxole, 1,4-epoxybuta-1,3-diene, 1,4-epoxy-1,3-butadiene, 5-oxacyclo-1,3-pentadiene
CAS number	98-01-1	98-00-0	97-99-4	534-22-5	96-47-9	109-99-9	110-00-9
Chemical formula	C <sub>5</sub> H <sub>4</sub> O <sub>2</sub>	C <sub>5</sub> H <sub>6</sub> O <sub>2</sub>	C <sub>5</sub> H <sub>10</sub> O <sub>2</sub>	C <sub>5</sub> H <sub>6</sub> O	C <sub>5</sub> H <sub>10</sub> O	C <sub>4</sub> H <sub>8</sub> O	C <sub>4</sub> H <sub>4</sub> O
Molecule structure							
Molecule weight	96.09 g/mol	98.10 g/mol	102.13 g/mol	82.10 g/mol	86.13 g/mol	72.11 g/mol	68.08 g/mol
Description	Colorless oil, almond-like	Colorless liquid, burning odor	Colorless liquid, mild odor	Colorless liquid, chocolate odor	Colorless liquid ether-like odor	Colorless liquid, ether-like odor	Colorless, volatile liquid, ethereal odor
Boiling point	162 °C	170 °C	178 °C	63-66 °C	80.2 °C	66 °C	31.3 °C
Melting point	-37 °C	-29 °C	-80 °C	-87.5 °C	-136 °C	-108.4 °C	-85.6 °C
Solubility	Alcohol: soluble Benzene: soluble Chloroform: soluble Diethyl ether: miscible Water: very soluble	Alcohol: soluble Benzene: soluble Chloroform: soluble Diethyl ether: very soluble Water: miscible	Alcohol: miscible Benzene: miscible Chloroform: miscible Diethyl ether: miscible Water: miscible	Alcohol: soluble Water: insoluble	--	Alcohol: miscible Benzene: very soluble Chloroform: very soluble Water: miscible	Alcohol: very soluble Diethyl ether: very soluble Water: insoluble
Density (25 °C)	1.16 g/mL	1.13 g/mL	1.05 g/mL	0.93 g/mL	0.85 g/mL	0.89 g/mL	0.94 g/mL

**Table 1.7.** Representative catalysts and experimental conditions favoring the hydrogenation of furfural to FFA. Adapted from ref. 35.

No.	Catalyst	Reaction conditions	Conv.(%)	Y <sub>FFA</sub> (%)
1	5% Pt/C	175 °C, 80 bar H <sub>2</sub> , 0.5 h, n-butanol solvent	99.3	47.9
2	5% Pt/C	175 °C, 80 bar H <sub>2</sub> , 0.5 h, n-decanol solvent	94.5	26.3
3	5% Pt/C	150 °C, 20 bar H <sub>2</sub> , 4 h, acetic acid-assisted	41.2	14.4
4	5% Pt/Al <sub>2</sub> (SiO <sub>3</sub> ) <sub>3</sub>	150 °C, 20 bar H <sub>2</sub> , 4 h, acetic acid-assisted	56.9	30.0
5	5% Cu/Al <sub>2</sub> (SiO <sub>3</sub> ) <sub>3</sub>	150 °C, 20 bar H <sub>2</sub> , 4 h, acetic acid-assisted	26.1	7.80
6	5% Ni/Al <sub>2</sub> (SiO <sub>3</sub> ) <sub>3</sub>	150 °C, 20 bar H <sub>2</sub> , 4 h, acetic acid-assisted	23.9	6.2
7	Ni-Ce-B	180 °C, 10 bar H <sub>2</sub> , 3 h, 30 mL ethanol	96.8	N.D.
8	Ni-Fe-B	200 °C, 10 bar H <sub>2</sub> , 4 h, 30 mL ethanol	100	~100
9	Cu <sub>11.2</sub> Ni <sub>2.4</sub> -MgAlO	300 °C, 10 bar H <sub>2</sub> , 90 mL ethanol	89.9	87.0
10	5% Pt/C	175 °C, 30 bar H <sub>2</sub> , 1 h, 20 mL H <sub>2</sub> O solvent, H <sub>3</sub> PO <sub>4</sub> (85 %)	100	27.0
11	5% Ir/TiO <sub>2</sub>	90 °C, 6.2 bar H <sub>2</sub> , n-heptane/ethanol	30	30
12	PtSn/SiO <sub>2</sub>	100 °C, 10 bar H <sub>2</sub> , 8 h, 50 mL 2-propanol	~85	~83
13	1% Pd/SiO <sub>2</sub>	250 °C, H <sub>2</sub> /Feed ratio=25, 1 atm H <sub>2</sub> , TOS=15 min	69	10
14	10% Cu/SiO <sub>2</sub>	230 °C, H <sub>2</sub> /Feed ratio=25, 1 atm H <sub>2</sub> , 5 min	69	67.6
15	2 wt% Pt/TiO <sub>2</sub> /MgO	200 °C, HLSV=2, H <sub>2</sub> /furfural=2 mol/mol	33.6	22.8
16	MoNiB/ $\gamma$ -Al <sub>2</sub> O <sub>3</sub>	80 °C, 50 bar, 3 h, methanol solvent	99.1	90.2
17	Cu-MgO-Cr	200 °C, 6 h, H <sub>2</sub> /furfural=2.5, GHSV=0.05 mol h <sup>-1</sup> g catalyst <sup>-1</sup>	71.6	71.6
18	Cu-Cr	300 °C	60	21
19	Ni <sub>74.5</sub> P <sub>12.1</sub> B <sub>13.4</sub>	250 psi, 80 °C, furfural/ethanol=2 mL/170 mL	~95	~77.9
20	PtSn <sub>0.2</sub> /SiO <sub>2</sub>	100 °C, 10 MPa H <sub>2</sub> , 8 h, 50 mL propanol-2-ol solvent	100	96
21	1 wt% Pt/SiO <sub>2</sub>	100 °C, 10 MPa H <sub>2</sub> , 8 h, 50 mL propanol-2-ol solvent	46	45.5
22	2 wt% Ni/SiO <sub>2</sub>	100 °C, 10 MPa H <sub>2</sub> , 8 h, 50 mL propanol-2-ol solvent	31	23.6
23	Cu-Fe	160 °C, 90 bar H <sub>2</sub> , 5 h	91.0	89.5
24	Cu-Cr	260 °C, 1 bar H <sub>2</sub>	53	51.9
25	Cu/MgO	180 °C, 1 bar H <sub>2</sub> , H <sub>2</sub> /furfural=2.5, GHSV=0.05 mol h <sup>-1</sup> g catalyst <sup>-1</sup>	98	96
26	Cu-Ca/SiO <sub>2</sub>	130 °C, 1 bar H <sub>2</sub> , H <sub>2</sub> /furfural=5, LHSV=0.33 mL h <sup>-1</sup> mL catalyst <sup>-1</sup>	100	99
27	CuLa/MCM-41	140 °C, 1 bar H <sub>2</sub> , H <sub>2</sub> /furfural=5, GHSV=0.087 mol h <sup>-1</sup> g catalyst <sup>-1</sup>	98	> 97
28	Cu-MgO	180 °C, 1 bar H <sub>2</sub> , H <sub>2</sub> /furfural=2.5, GHSV=0.05 mol h <sup>-1</sup> g catalyst <sup>-1</sup>	98	96
29	Cu-Cr/TiO <sub>2</sub>	140 °C, 1 bar H <sub>2</sub> , H <sub>2</sub> /furfural=3, GHSV=0.04 mol h <sup>-1</sup> g catalyst <sup>-1</sup>	90	79.2
30	Pt/TiO <sub>2</sub> -V <sub>2</sub> O <sub>5</sub> -SiO <sub>2</sub>	150 °C, 1 bar H <sub>2</sub> , H <sub>2</sub> /furfural=2, LHSV=2 g h <sup>-1</sup> g catalyst <sup>-1</sup>	87	79.2
31	Ir-ReO <sub>x</sub> /SiO <sub>2</sub>	30 °C, 8 bar H <sub>2</sub> , 6 h, Water solvent	> 99	> 99
32	Cu-Zn-Cr-Zr oxide	170 °C, 20 bar H <sub>2</sub> , 3.5 h, isopropanol solvent	> 99	> 95
33	Raney Ni-CuPMo12	80 °C, 20 bar H <sub>2</sub> , 1 h, ethanol solvent	98	97
34	Co-Mo-B alloy	100 °C, 10 bar H <sub>2</sub> , 3 h, ethanol solvent	> 99	> 99
35	Pt-Sn/SiO <sub>2</sub>	100 °C, 10 bar H <sub>2</sub> , 8 h, isopropanol solvent	90	88.2

36	Ni-Ce-B alloy	80 °C, 10 bar H <sub>2</sub> , 3 h, ethanol solvent	97	~97
37	Ru/C	165 °C, 25 bar H <sub>2</sub> , MTHF solvent	91	42.1
38	Cu:Zn:Cr:Zr(3:2:1:4)	170 °C, 20 bar H <sub>2</sub> , 3.5 h, isopropyl alcohol solvent	100	96
39	Ni-Sn	110 °C, 30 bar H <sub>2</sub> , 1.25 h, isopropanol solvent	72	70
40	Ni-Sn/TiO <sub>2</sub>	110 °C, 30 bar H <sub>2</sub> , 1.25 h, isopropanol solvent	> 99	> 99

In the last decades, the production of FFA obtained from the hydrogenation of furfural has been explored on various metals and in various reaction conditions (Table 1.7) [35]. Most monometallic catalysts have been based on noble metals such as Pt (Entries 1, 2, 10, 15, 21 and 30), Pd (Entries 3, 4 and 13), Ir (Entry 11), and Ru (Entry 37), but non-noble metals such as Ni (Entries 6 and 22) and Cu (Entries 5 and 14) have also been tested. Reaction temperature range was between 150 and 175 °C, sometimes much higher when the metal was not very active (Entry 14, Cu, 230 °C) and sometimes much lower when the metal was very active (Entry 11, Ir, 90 °C). Pressures range was mostly between 10 and 80 bar, and the solvent was often an alcohol (methanol, ethanol, propanol, butanol). However, the reported yield of FFA was very variable and often relatively low for monometallic catalysts (< 50%). For example, a selectivity of only 27% for FFA was obtained at 100% conversion for a Pt catalyst (Entry 10).

Various bimetallic catalysts, such as Ni-Ce (Entry 7), Fe-Ni (Entry 8), Cu-Fe (Entry 23), Cu-Cr (Entry 24) and Ni-Sn (Entry 39), were employed for the hydrogenation of furfural to FFA. Higher conversions (> 90%) and yields (> 80%) were reached compared with monometallic catalysts. For example, a yield of 89.5% at 91% conversion was obtained on a Cu-Fe bimetallic catalyst (Entry 23) at 160 °C, under 90 bar H<sub>2</sub> and after 5 h. Almost 100% FFA at 100% conversion was also obtained with a Ni-Sn catalyst (Entry 23).

Up to now, Fe-Ni bimetallic catalysts have been the object of six articles for the hydroconversion of furfural. Sitthisa *et al.* [36] showed that in the gas phase at 250 °C, furan was the main product of hydroconversion over SiO<sub>2</sub>-supported Ni (conversion of furfural: 98%, yield of furan: 50%). On Fe-Ni bimetallic catalysts, a high conversion was also obtained (96.3% for 7 wt% Fe<sub>29</sub>Ni<sub>71</sub>/SiO<sub>2</sub>), but the yield of 2-methylfuran greatly increased (from 5% for 7 wt% Ni/SiO<sub>2</sub> to 39.1% for 7 wt% Fe<sub>29</sub>Ni<sub>71</sub>/SiO<sub>2</sub>) while the yields of furan decreased (from 50% for



7 wt% Ni/SiO<sub>2</sub>, to 12.1% for 7 wt% Fe<sub>29</sub>Ni<sub>71</sub>/SiO<sub>2</sub>). The yield of FFA slightly increased from 0 for 7 wt% Ni/SiO<sub>2</sub> to 10% for 7 wt% Fe<sub>29</sub>Ni<sub>71</sub>/SiO<sub>2</sub>; it decreased when further increasing the Fe content (conversion of furfural for 7 wt% Fe<sub>50</sub>Ni<sub>50</sub>/SiO<sub>2</sub> < 30%, yield of FFA: 6%). In these experimental conditions, the addition of Fe suppressed the decarbonylation activity of Ni, while promoting both C=O hydrogenation and C-O hydrogenolysis. The effect of Fe was attributed to the increase of the stability of  $\eta^2(\text{C}, \text{O})$ -surface species, by interaction between the O atom of the aldehyde function and the oxophilic Fe atoms. This interaction can also increase the C-O hydrogenolysis properties of the catalyst.

This result was consistent with the work done by Yu *et al.* [37] who used DFT calculations to determine the reaction pathways for furfural over bimetallic Fe-Ni catalysts. They found that furfural was bonded onto the 2.7 wt% Fe<sub>50</sub>Ni<sub>50</sub>/SiO<sub>2</sub> catalyst more strongly through the carbonyl group than onto 2.7 wt% Ni/SiO<sub>2</sub>, since the C-O bond length of adsorbed furfural was longer than that on Ni. Furthermore, 2.7 wt% Fe<sub>50</sub>Ni<sub>50</sub>/SiO<sub>2</sub> reduced the O-M bond distance and increased the C-M bond length compared with 2.7 wt% Ni/SiO<sub>2</sub>. The furan ring was tilted away from the surface. FFA was identified as intermediate product in the HDO reaction.

In the liquid phase (2-propanol), Putro *et al.* [25] obtained a 95% furfural conversion with a 97% selectivity to FFA (reaction conditions: W<sub>CAT</sub> = 200 mg, substrate/Ni = 2; V<sub>iso-PrOH</sub> = 3 mL; P<sub>H2</sub> = 10 bar; T = 150 °C; t = 30 min) with a 20 wt% Fe<sub>25</sub>Ni<sub>75</sub>/Al<sub>2</sub>O<sub>3</sub> catalyst. They found that the higher dispersion of Fe<sub>25</sub>Ni<sub>75</sub> particles on CeO<sub>2</sub>, Al<sub>2</sub>O<sub>3</sub> and TiO<sub>2</sub> supports enhanced the catalyst intrinsic activity (conversion: 99, 95 and 100%, respectively) and selectivity (93, 97 and 91%, respectively) under the reaction conditions given above, compared to unsupported Fe<sub>25</sub>Ni<sub>75</sub> and Ni (conversion: 90% and 100%, selectivity: 92% and 7%). The main product formed with Ni was THFFA (selectivity: 61%). The values were also much higher than those measured on SiO<sub>2</sub>, taeniolite or hydrotalcite supports (conversions: 21, 22 and 42%; selectivities: 95, 77 and 90%), which increased the selectivity to THFFA (5, 23 and 10%), suggesting that layered structures, such as taeniolite and hydrotalcite, were inappropriate for this reaction system. Chieffi *et al.* [24] also found that in ethanol, Fe<sub>42</sub>Ni<sub>58</sub> particles supported on carbon exhibited a high conversion of furfural (99%) and selectivity to FFA (90%).

Li *et al.* [34] found that unsupported Fe<sub>50</sub>Ni<sub>50</sub>-B boride nanoparticles present a much higher activity (conversion: 100%, selectivity to FFA: 100%) than Ni-B (conversion: 55%, selectivity to FFA: 93%). The electrons transferred by Fe to Ni result in the attraction of oxygen from the carbonyl group by electron-deficient Fe, which might weaken and activate the C=O bond  $\pi$ -complexed to Ni atoms, and in turn promote the hydrogenation of the C=O bond.

Using heptane as a solvent, the effect of temperature, pressure, reactant amount, and catalyst loading were investigated by Halilu *et al.* [32] to optimize the reaction conditions. They showed that when increasing the Ni content from 0.05 to 0.5 wt% in a magnetic Ni-Fe<sub>3</sub>O<sub>4</sub>-SiO<sub>2</sub> nanocatalyst (Ni<sup>2+</sup> ions loaded on the surface of a Fe<sub>3</sub>O<sub>4</sub>-SiO<sub>2</sub> core-shell structure), the conversion of furfural increased from 55% to 94% with the selectivity to FFA kept at ~100% in the whole series (T = 250 °C, P<sub>H2</sub> = 20 bar). The Ni-Fe<sub>3</sub>O<sub>4</sub>-SiO<sub>2</sub> (0.51 wt% Ni) nanocatalyst also exhibited a remarkable performance compared with 0.5 wt% Ni/SiO<sub>2</sub>, with a 94.3% conversion of furfural and 100% selectivity of furfuryl alcohol. With 0.5 wt% Ni/SiO<sub>2</sub>, the conversion of furfural was 50%, the selectivity to FFA 25%, and a wide range of products was obtained due to decarbonylation and ring opening reactions, such as furan (selectivity: 48%), butanal (selectivity: 13%), butanol (selectivity: 3%) and butane (selectivity: 11%).

Finally, the selective hydrogenation and hydrogenolysis of a molecule close to furfural, 5-hydroxymethylfurfural, were investigated by Yu *et al.* [38] using carbon nanotube-supported bimetallic Fe-Ni catalysts (Fe-Ni/CNT) with n-butanol as solvent. Monometallic 10 wt% Ni/CNT catalyst showed a high conversion at 110 °C (100%), but a low selectivity to the diol, 2,5-furandimethanol (76.4%). The byproducts of the reaction included decarbonylation (5-methylfurfural), ring hydrogenation (2,5-dimethyltetrahydrofuran), ring opening (1,2-hexanediol), and etherification products. The addition of Fe increased the selectivity to 2,5-furandimethanol (87.7% for 10 wt% Fe<sub>9</sub>Ni<sub>91</sub>/CNT) while keeping the conversion at 100%. 97.5% of selectivity to 2,5-furandimethanol at 100% of conversion could be achieved with 10 wt% Fe<sub>50</sub>Ni<sub>50</sub>/CNT. The products distribution was changed to hydrogenolysis products when the reaction temperature was increased to 200 °C. The main product was 2,5-dimethylfuran (selectivity: 46.3%) for monometallic Ni/CNT catalyst at 100% conversion (selectivity to 2,5-

furandimethanol: 13.4%). After increasing the Fe content up to Fe<sub>33</sub>Ni<sub>67</sub>/CNT, the selectivity to 2,5-dimethylfuran was 91.3% at 100% conversion and no 2,5-furandimethanol was formed. Chieffi *et al.* [24] also found that in ethanol at 150 °C, Fe<sub>42</sub>Ni<sub>58</sub>/carbon possesses superior conversion of 5-hydroxymethylfurfural (99%) and selectivity to 2,5-furandimethanol (88%).

Table 1.8 summarizes the results obtained for the hydrogenation reactions discussed above, including the reaction conditions leading to the best catalytic results, the optimum formulation of the Fe-Ni catalysts (metal content, relative proportions of Fe and Ni and support), the size of Fe-Ni nanoparticles and the preparation methods.

**Table 1.8.** Optimum reaction conditions and formulation of Fe-Ni catalysts for the hydrogenation reactions described in this chapter.

No.	Reaction	Reaction conditions	Optimum formulation of Fe-Ni	Particles size (nm)	Preparation method	Ref.
1	CO methanation	T = 292 °C, H <sub>2</sub> /CO = 15, P <sub>co</sub> = 120 bar, P <sub>H2O</sub> = 30 bar	6.15 wt% Fe <sub>6</sub> Ni <sub>94</sub> /Al <sub>2</sub> O <sub>3</sub>	--	Incipient wetness impregnation	[8]
2	CO methanation	T = 250 °C, H <sub>2</sub> /CO = 49, GHSV = 40000 h <sup>-1</sup> , P = 1 bar, W <sub>Catalyst</sub> = 150 mg	10 wt% Fe <sub>25</sub> Ni <sub>75</sub> /MgAl <sub>2</sub> O <sub>4</sub>	--	Incipient wetness impregnation	[7]
3	CO methanation	T = 250 °C, H <sub>2</sub> /CO = 49, GHSV = 50000 h <sup>-1</sup> , P = 1 bar, W <sub>Catalyst</sub> = 150 mg	10 wt% Fe <sub>50</sub> Ni <sub>50</sub> /Al <sub>2</sub> O <sub>3</sub>	13-15	Incipient wetness impregnation	[6]
4	CO methanation	T = 300 °C, H <sub>2</sub> /CO = 3.1, GHSV = 18000 h <sup>-1</sup> , P = 30 bar, W <sub>Catalyst</sub> = 500 mg, t = 1 h	23.3 wt% Fe <sub>25</sub> Ni <sub>75</sub> /Al <sub>2</sub> O <sub>3</sub>	30	Impregnation	[1]
5	CO methanation	T = 230 °C, H <sub>2</sub> /CO/N <sub>2</sub> = 3/1/1.7, GHSV = 8160 h <sup>-1</sup> , P = 10 bar, W <sub>Catalyst</sub> = 50 mg, t = 10 h	40 wt% Fe <sub>25</sub> Ni <sub>75</sub> /Al <sub>2</sub> O <sub>3</sub>	3.4	Sol-gel method	[2]
6	CO methanation	T = 300 °C, H <sub>2</sub> /CO = 9, t = 10 h	Fe <sub>50</sub> Ni <sub>50</sub>	--	Quenching a fused alloy	[9]
7	CO/CO <sub>2</sub> methanation	T = 300 °C, H <sub>2</sub> / (CO <sub>2</sub> + CO) = 2	10 wt% Fe <sub>50</sub> Ni <sub>50</sub> /Al <sub>2</sub> O <sub>3</sub>	20	Impregnation	[11]
8	CO <sub>2</sub> methanation	T = 330 °C, H <sub>2</sub> /CO/CO <sub>2</sub> = 48/1/1, GHSV = 6 NL/h, P = 1 bar, W <sub>Catalyst</sub> = 150 mg	10 wt% Fe <sub>25</sub> Ni <sub>75</sub> /Al <sub>2</sub> O <sub>3</sub>	--	Incipient wetness impregnation	[12]
9	CO <sub>2</sub> methanation	T = 300 °C, H <sub>2</sub> /CO <sub>2</sub> /Ar = 18/6/1, GHSV = 3600 h <sup>-1</sup> , P = 11 bar, W <sub>Catalyst</sub> = 200 mg, t = 15-16 h	15 wt% Fe <sub>90</sub> Ni <sub>10</sub> /Al <sub>2</sub> O <sub>3</sub>	--	Incipient wetness impregnation	[3]
10	CO <sub>2</sub> methanation	T = 250 °C, H <sub>2</sub> /CO <sub>2</sub> = 24, GHSV = 4800 h <sup>-1</sup> , W <sub>Catalyst</sub> = 150 mg, t = 2 h	30 wt% Fe <sub>25</sub> Ni <sub>75</sub> /Al <sub>2</sub> O <sub>3</sub>	32	Incipient wetness impregnation	[4]
11	CO <sub>2</sub> methanation	T = 220 °C, H <sub>2</sub> /CO <sub>2</sub> /N <sub>2</sub> = 4/1/1.7, GHSV = 9600 h <sup>-1</sup> , P = 10 bar, W <sub>Catalyst</sub> = 50 mg, t = 10 h	40 wt% Fe <sub>12</sub> Ni <sub>88</sub> /Al <sub>2</sub> O <sub>3</sub>	4.4	Sol-gel method	[10]
12	CO <sub>2</sub> methanation	T = 358 °C, H <sub>2</sub> /CO <sub>2</sub> /N <sub>2</sub> = 4/1/5, GHSV = 6000 h <sup>-1</sup> , P = 10 bar, W <sub>Catalyst</sub> = 300 mg, t = 45 h	17 wt% Fe <sub>25</sub> Ni <sub>75</sub> /Al <sub>2</sub> O <sub>3</sub>	4	Deposition-precipitation	[13]

## Chapter I. Bibliographical study

13	Fischer-Tropsch synthesis	T = 250 °C, H <sub>2</sub> /CO = 2.85	4.2 wt% Fe <sub>80</sub> Ni <sub>20</sub> /SiO <sub>2</sub>	--	Incipient wetness impregnation	[17]
14	Fischer-Tropsch synthesis	T = 250 °C, H <sub>2</sub> /CO/Ar = 62/33/5, P = 10 bar, W <sub>Catalyst</sub> = 30 mg	10 wt% Fe <sub>25</sub> Ni <sub>75</sub> /SiO <sub>2</sub>	--	Incipient wetness impregnation	[20]
15	Fischer-Tropsch synthesis	T = 250 °C, H <sub>2</sub> /CO/Ar = 62/33/5, GHSV = 0.1 mol/h, P = 10 bar, W <sub>Catalyst</sub> = 1 g, t = 5 h	10 wt% Fe <sub>25</sub> Ni <sub>75</sub> /TiO <sub>2</sub>	--	Incipient wetness impregnation	[18]
16	Fischer-Tropsch synthesis	T = 250 °C, H <sub>2</sub> /CO/Ar = 62/33/5, GHSV = 0.1 mol/h, P = 10 bar, W <sub>Catalyst</sub> = 1 g	10 wt% Fe <sub>25</sub> Ni <sub>75</sub> /TiO <sub>2</sub>	13.1	Incipient wetness impregnation	[22]
17	Fischer-Tropsch synthesis	T = 250 °C, H <sub>2</sub> /CO = 2, GHSV = 2000 h <sup>-1</sup> , P = 10 bar, W <sub>Catalyst</sub> = 4 g, t = 24 h	Fe <sub>87</sub> Ni <sub>13</sub>	14.3	Co-precipitation	[15]
18	Fischer-Tropsch synthesis	T = 250 °C, H <sub>2</sub> /CO = 2, GHSV = 1800 h <sup>-1</sup> , W <sub>Catalyst</sub> = 350 mg, t = 6 h	5 wt% Fe <sub>40</sub> Ni <sub>60</sub> /TiO <sub>2</sub>	4	Deposition-precipitation	[21]
19	Fischer-Tropsch synthesis	T = 250 °C, H <sub>2</sub> /CO = 2, GHSV = 1800 h <sup>-1</sup> , W <sub>Catalyst</sub> = 350 mg, t = 6 h	20 wt% Fe <sub>40</sub> Ni <sub>60</sub> /TiO <sub>2</sub>	15-20	Deposition-precipitation	[19]
20	Fischer-Tropsch synthesis	T = 260 °C, H <sub>2</sub> /CO = 2, GHSV = 3200 h <sup>-1</sup> , P = 3 bar, W <sub>Catalyst</sub> = 1 g	60 wt% Fe <sub>40</sub> Ni <sub>60</sub> /Al <sub>2</sub> O <sub>3</sub>	--	Sol-gel method	[16]
21	Hydrogenation of ethylene	T = 0 °C, H <sub>2</sub> /Ethylene = 1, P = 2.7×10 <sup>-3</sup> bar, W <sub>Catalyst</sub> = 100 mg	Fe <sub>50</sub> Ni <sub>50</sub>	--	Incipient wetness impregnation	[23]
22	Hydrogenation of styrene	T = 50 °C, C <sub>Styrene</sub> = 0.1 M, P = 10 bar, WHSV = 60 h <sup>-1</sup> , Ethanol as solvent	18 wt% Fe <sub>42</sub> Ni <sub>58</sub> /Carbon	20	Impregnation	[24]
23	Hydrogenation of α-terpinene	T = 125 °C, C <sub>α-terpinene</sub> = 0.1 M, P = 10 bar, WHSV = 60 h <sup>-1</sup> , Ethanol as solvent	18 wt% Fe <sub>42</sub> Ni <sub>58</sub> /Carbon	20	Impregnation	[24]
24	Hydrogenation of 2-cyclohexen -1-one	T = 100 °C, C <sub>2-cyclohexen-1-one</sub> = 0.1 M, P = 10 bar, WHSV = 60 h <sup>-1</sup> , Ethanol as solvent	18 wt% Fe <sub>42</sub> Ni <sub>58</sub> /Carbon	20	Impregnation	[24]
25	Hydrogenation of 2-cyclohexen -1-one	T = 130 °C, 1.1 mmol 2-cyclohexene-1-one (2- cyclohexene-1-one/Ni = 2), P = 10 bar, W <sub>Catalyst</sub> = 200 mg, 3 mL 2-propanol as solvent, t = 15 min	20 wt% Fe <sub>25</sub> Ni <sub>75</sub> /CeO <sub>2</sub>	16	Hydrothermal	[25]
26	Hydrogenation of phenylacetylene	T = 50 °C, C <sub>Phenylacetylene</sub> = 0.1 M, P = 10 bar, WHSV = 60 h <sup>-1</sup> , Ethanol as solvent	18 wt% Fe <sub>42</sub> Ni <sub>58</sub> /Carbon	20	Impregnation	[24]
27	Hydrogenation of nitrobenzene	T = 100 °C, C <sub>Nitrobenzene</sub> = 0.1 M, P = 10 bar, WHSV = 60 h <sup>-1</sup> , Ethanol as solvent	10 wt% Fe <sub>42</sub> Ni <sub>58</sub> /Carbon	20	Impregnation	[24]
28	Hydrogenation of acetophenone	T = 135 °C, P = 5.9 bar, W <sub>Catalyst</sub> = 150 mg, Acetophenone = 15 g, Methanol = 45 ml	20 wt% Fe <sub>25</sub> Ni <sub>75</sub> /SiO <sub>2</sub>	13.2	Incipient wetness impregnation	[26]
29	Hydrogenation of cyclohexanone	T = 150 °C, C <sub>Cyclohexanone</sub> = 0.1 M, P = 50 bar, WHSV = 18 h <sup>-1</sup> , Ethanol as solvent	18 wt% Fe <sub>42</sub> Ni <sub>58</sub> /Carbon	20	Impregnation	[24]
30	Hydrogenation of benzaldehyde	T = 150 °C, C <sub>Benzaldehyde</sub> = 0.1 M, P = 10 bar, WHSV = 60 h <sup>-1</sup> , Ethanol as solvent	18 wt% Fe <sub>42</sub> Ni <sub>58</sub> /Carbon	20	Impregnation	[24]
31	Hydrogenation of butyronitrile	T = 150 °C, P = 34 bar, W <sub>Catalyst</sub> = 1 wt%/Butyronitrile, W <sub>Butyronitrile</sub> = 30 wt%/Methanol	20 wt% Fe <sub>25</sub> Ni <sub>75</sub> /SiO <sub>2</sub>	13.2	Incipient wetness impregnation	[28]
32	Hydrogenation of crotononitrile	T = 150 °C, P = 34 bar, W <sub>Catalyst</sub> = 1 wt%/Crotononitrile, W <sub>Crotononitrile</sub> = 10 wt%/Methanol	20 wt% Fe <sub>25</sub> Ni <sub>75</sub> /SiO <sub>2</sub>	13.2	Incipient wetness impregnation	[28]
33	Hydrogenation of benzonitrile	T = 150 °C, P = 3.4 bar, W <sub>Catalyst</sub> = 240 mg, Benzonitrile = 12.12 g, Methanol = 40 ml	20 wt% Fe <sub>25</sub> Ni <sub>75</sub> /SiO <sub>2</sub>	13.2	Incipient wetness impregnation	[26]

## Chapter I. Bibliographical study

34	Hydrogenation of benzonitrile	T = 150 °C, P = 34 bar, W <sub>Catalyst</sub> = 1 wt%/Benzonitrile, W <sub>Benzonitrile</sub> = 30 wt%/Methanol	20 wt% Fe <sub>25</sub> Ni <sub>75</sub> /SiO <sub>2</sub>	13.2	Incipient wetness impregnation	[28]
35	Hydrogenation of benzonitrile	T = 150 °C, C <sub>Benzonitrile</sub> = 0.1 M, P = 10 bar, WHSV = 60 h <sup>-1</sup> , Ethanol as solvent	18 wt% Fe <sub>42</sub> Ni <sub>58</sub> /Carbon	20	Impregnation	[24]
36	Hydrogenation of cinnamonitrile	T = 150 °C, P = 34 bar, W <sub>Catalyst</sub> = 1 wt%/Cinnamonitrile, W <sub>Cinnamonitrile</sub> = 10 wt%/Methanol	20 wt% Fe <sub>25</sub> Ni <sub>75</sub> /SiO <sub>2</sub>	13.2	Incipient wetness impregnation	[28]
37	Hydrogenation of levulinic acid	T = 150 °C, C <sub>Levulinic acid</sub> = 0.1 M, P = 50 bar, WHSV = 18 h <sup>-1</sup> , Ethanol as solvent	18 wt% Fe <sub>42</sub> Ni <sub>58</sub> /Carbon	20	Impregnation	[24]
38	Hydrogenation of ethyl levulinate	T = 100 °C, 100 mg of ethyl levulinate, P = 40 bar, W <sub>Catalyst</sub> = 40 mg, t = 6 h, 10 mL of deionized water as solvent	10 wt% Fe <sub>33</sub> Ni <sub>67</sub> /AC	7.1	Co-precipitation	[27]
39	Hydrogenation of glucose	T = 150 °C, C <sub>Glucose</sub> = 0.1 M, P = 50 bar, WHSV = 18 h <sup>-1</sup> , Ethanol as solvent	18 wt% Fe <sub>42</sub> Ni <sub>58</sub> /Carbon	20	Impregnation	[24]
40	Hydrogenation of xylose	T = 150 °C, C <sub>Xylose</sub> = 0.1 M, P = 50 bar, WHSV = 18 h <sup>-1</sup> , Ethanol as solvent	18 wt% Fe <sub>42</sub> Ni <sub>58</sub> /Carbon	20	Impregnation	[24]
41	Hydrogenation of furfural	T = 250 °C, H <sub>2</sub> /Furfural = 25, P = 1 bar, W/F = 0.1 h	7.0wt% Fe <sub>25</sub> Ni <sub>75</sub> /SiO <sub>2</sub>	17.1	Incipient wetness impregnation	[36]
42	Hydrogenation of furfural	T = 150 °C, C <sub>Furfural</sub> = 0.1 M, P = 10 bar, WHSV = 60 h <sup>-1</sup> , Ethanol as solvent	18 wt% Fe <sub>42</sub> Ni <sub>58</sub> /Carbon	20	Impregnation	[24]
43	Hydrogenation of furfural	--	2.7 wt% Fe <sub>50</sub> Ni <sub>50</sub> /SiO <sub>2</sub>	2.4	Incipient wetness impregnation	[37]
44	Hydrogenation of furfural	T = 150 °C, 1.1 mmol furfural (Furfural/Ni = 2), P = 30 bar, W <sub>Catalyst</sub> = 200 mg, 3 mL 2-propanol as solvent	20 wt% Fe <sub>25</sub> Ni <sub>75</sub> /Al <sub>2</sub> O <sub>3</sub>	16	Hydrothermal	[25]
45	Hydrogenation of furfural	T = 100 °C, 10 mmol of furfural, P = 10 bar, W <sub>Catalyst</sub> = 1 g, t = 4 h, 30 mL of ethanol as solvent	Fe <sub>36.0</sub> Ni <sub>34.1</sub> B <sub>29.9</sub>	--	--	[34]
46	Hydrogenation of furfural	T = 250 °C, 20 % furfural in heptane, P <sub>H<sub>2</sub></sub> = 20 bar W <sub>Catalyst</sub> = 60 mg	Fe <sub>40.44</sub> Ni <sub>0.51</sub> -O <sub>40.94</sub> Si <sub>18.11</sub>	14.2	Co-precipitation	[32]
47	Hydrogenation of 5-hydroxy methylfurfural	T = 150 °C, C <sub>5-hydroxymethylfurfural</sub> = 0.1 M, P = 10 bar, WHSV = 60 h <sup>-1</sup> , Ethanol as solvent	18 wt% Fe <sub>42</sub> Ni <sub>58</sub> /Carbon	20	Impregnation	[24]
48	Hydrogenation of 5-hydroxy methylfurfural	T = 110 °C, 4 mmol of HMF, P = 30 bar, W <sub>Catalyst</sub> = 5 mg, t = 18 h, 20 mL of n-butanol as solvent	10 wt% Fe <sub>33</sub> Ni <sub>67</sub> /CNT	16.2	Incipient wetness impregnation	[38]
49	Hydrodeoxygenation of m-cresol	T = 300 °C, H <sub>2</sub> / m-cresol = 60 P = 1 bar, W/F = 0.46 h, W <sub>Catalyst</sub> = 30-120 mg	15 wt% Fe <sub>50</sub> Ni <sub>50</sub> /SiO <sub>2</sub>	9.6	Incipient wetness impregnation	[31]
50	Hydrodeoxygenation of guaiacol	T = 300 °C, H <sub>2</sub> /Guaiacol = 50, WLHSV = 6 h <sup>-1</sup> , P = 30 bar, W <sub>Catalyst</sub> = 100 mg	7.0 wt% Fe <sub>17</sub> Ni <sub>83</sub> /CNT	7.7	Co-impregnation	[30]
51	Hydrodeoxygenation of furfuryl alcohol	T = 375 °C, WHSV = 2400 h <sup>-1</sup> , Benzene as solvent	20 wt% Fe <sub>25</sub> Ni <sub>75</sub> /Al <sub>2</sub> O <sub>3</sub>	4.8	Incipient wetness impregnation	[29]
52	Hydrodeoxygenation of benzyl alcohol	T = 375 °C, WHSV = 2400 h <sup>-1</sup>	20 wt% Fe <sub>25</sub> Ni <sub>75</sub> /Al <sub>2</sub> O <sub>3</sub>	4.8	Incipient wetness impregnation	[29]
53	Hydrodeoxygenation of ethyl oenanthane	T = 375 °C, WHSV = 2400 h <sup>-1</sup> , n-decane as solvent	20 wt% Fe <sub>25</sub> Ni <sub>75</sub> /Al <sub>2</sub> O <sub>3</sub>	4.8	Incipient wetness impregnation	[29]

### I.1.6. Conclusions

In summary, in most cases the optimal Fe-Ni formulation for hydroconversion reactions corresponds to a Ni-rich alloy (Fe<sub>50</sub>Ni<sub>50</sub> and richer), and the Fe<sub>25</sub>Ni<sub>75</sub> formulation has been much more reported for different families of reactions. Fe-Ni bimetallic catalysts are more selective than monometallic Ni, which often leads to hydrogenolysis or overhydrogenation side reactions. Four types of possible explanations have been given:

1) *structure of the particles*: *fcc* Fe-Ni alloys exhibit superior catalytic activity compared with *bcc* alloys, and the presence of Ni favors the reduction of Fe compared to monometallic Fe;

2) *amount and nature of the adsorbed species*: the amount of H<sub>2</sub> dissociated on Ni species is not high enough on Fe-Ni systems to promote the deep hydroconversion of the molecules. This is worsened when the proportion of Fe increases, leading to a decrease of activity. Furthermore, a change in the adsorption mode of the organic molecules compared with Ni disadvantages the formation of intermediates leading to decarbonylation, ring-opening or ring-hydrogenation products.

3) *electronic effects*: there is a charge transfer from Fe to Ni, resulting in the attraction of oxygen atoms by electron-deficient Fe, which might weaken and activate CO bonds;

4) *surface sites*: Lewis acidic sites appear with the introduction of Fe (possibly unreduced ions), and they can attract and activate CO bonds through interactions with the electron pair of oxygen atom.

These explanations all involve the structure or the surface of the Fe-Ni systems. However, it could be seen that discussions based on the particles structure may be sometimes lacking, and that only in a few articles the surface of the particles was characterized. In particular, it was shown that the composition of the surface might differ from that of the bulk. Furthermore, Fe-Ni bimetallic catalysts have mostly been prepared by impregnation, and as Table 1.8 shows, this method yields very different metal particles sizes from one article to the other, and sometimes very large ones (range from 2.4 to 30 nm). This means that in order to understand the catalytic properties of Fe-Ni catalysts, the parameters controlling the structure, size and composition of Fe-Ni particles must be investigated.

## I.2. Formation, structure, size and composition of Fe-Ni nanoparticles

The preparation method of Fe-Ni catalysts, the Fe/Ni ratio, the support, the calcination and reduction temperatures, have all an influence on the size of the Fe-Ni nanoparticles, on their structure and on their distribution on the support, which are parameters likely to affect the catalytic activity of the catalyst.

### I.2.1. Preparation methods

Several methods have been used for the preparation of Fe-Ni bimetallic catalysts, principally impregnation. Sol-gel method and deposition-precipitation have seldom been used, but from Table 1.8 it can be seen that they can produce Fe-Ni particles with a size smaller than 8 nm. We will list here the characteristics of these three methods.

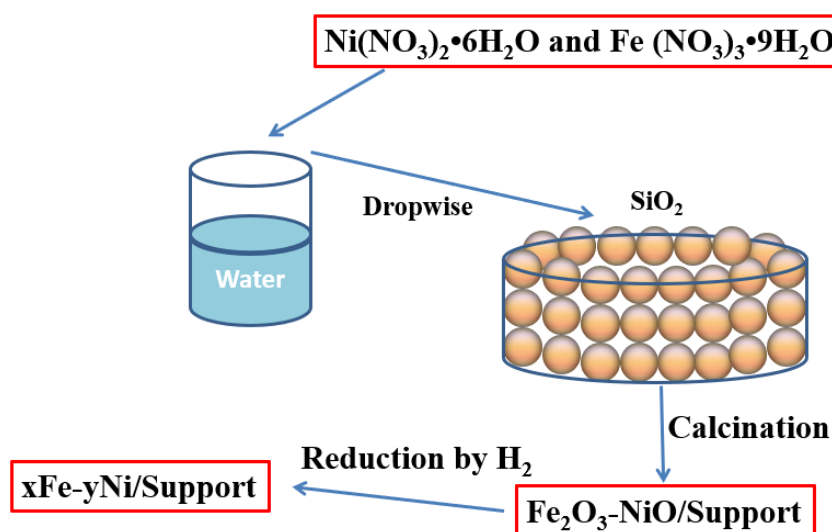


Figure 1.9. Principle of preparation by IWI.

#### I.2.1.1. Incipient wetness impregnation

Incipient wetness impregnation (IWI) is a classical way to prepare catalysts. A thin layer of support is wetted by a metal-containing aqueous solution containing the Fe and Ni precursors (usually nitrates) in the proper Fe/Ni ratio. The volume of the solution is equal to the pore volume of support. After drying, calcination and reduction are essential to obtain reduced Fe-Ni particles on the support, as summarized in Figure 1.9.

**Table 1.9.** Phases detected after calcination, reduction temperature and particle size of Fe-Ni supported nanoparticles after reduction for catalysts prepared by IWI.

Samples	Phases after calcination	Reduction Temp. (°C)	Particle size (nm)	Ref.
Fe-Ni/SiO <sub>2</sub>	Fe <sub>2</sub> O <sub>3</sub> , NiO	300/400	6.5	[22]
	$\alpha$ -Fe <sub>2</sub> O <sub>3</sub> , NiO, $\alpha$ -Fe <sub>2-<math>\zeta</math></sub> Ni $\zeta$ O <sub>3</sub>	425	8.9-12.8	[39]
	Fe <sub>2</sub> O <sub>3</sub> , NiO	450	10	[40]
	NiO	450	7	[41]
	Fe <sub>2</sub> O <sub>3</sub> , NiO	450	9	[26]
	Fe <sub>2</sub> O <sub>3</sub> , NiO	450	--	[42]
	Fe <sub>2</sub> O <sub>3</sub> , NiO	450	9	[28]
	Fe <sub>2</sub> O <sub>3</sub> , NiO	450	16	[36]
	Fe <sub>2</sub> O <sub>3</sub> , NiO	500	11	[4]
	--	800	10	[31]
Fe-Ni/TiO <sub>2</sub>	Fe <sub>2</sub> O <sub>3</sub> , NiO	300/400	13	[22]
	Fe <sub>2</sub> O <sub>3</sub> , NiO	440	5	[9]
	Fe <sub>2</sub> O <sub>3</sub> , NiO	450	10	[31]
Fe-Ni/Al <sub>2</sub> O <sub>3</sub>	NiAl <sub>2</sub> O <sub>4</sub>	400	4.8	[29]
	Fe <sub>2</sub> O <sub>3</sub> , NiO	440/500	4	[43]
	Fe <sub>2</sub> O <sub>3</sub> , NiO	450	--	[44]
	Fe <sub>2</sub> O <sub>3</sub> , NiO	500	--	[12]
	Fe <sub>2</sub> O <sub>3</sub> , NiO	500	13-15	[6]
	Fe <sub>2</sub> O <sub>3</sub> , NiO	500	15	[4]
	Fe <sub>2</sub> O <sub>3</sub> , NiO	800	7	[1]
Fe <sub>2</sub> O <sub>3</sub> , NiO	950	--	[45]	
Fe-Ni/CNTs	Fe <sub>2</sub> O <sub>3</sub> , NiO	400	6.5	[38]
Fe-Ni/CNTs	--	400	5.3	[30]
Fe-Ni/activated carbon (AC)	FeNi, NiFe <sub>2</sub> O <sub>4</sub>	--	--	[46]
Fe-Ni/MgO	Fe <sub>2</sub> O <sub>3</sub> , NiO	450	7	[39]
Fe-Ni/MgO-Al <sub>2</sub> O <sub>3</sub>	Fe <sub>2</sub> O <sub>3</sub> , NiO	500	--	[47]
Fe-Ni/ MgAl <sub>2</sub> O <sub>4</sub>	Fe <sub>2</sub> O <sub>3</sub> , NiO	500	13-15	[6]
Ni/CaO-Fe <sub>2</sub> O <sub>3</sub> -Al <sub>2</sub> O <sub>3</sub>	Fe <sub>2</sub> O <sub>3</sub> , NiO	700	21	[48]



In Table 1.9 are listed Fe-Ni catalysts prepared on different supports by IWI, with the different phases detected after calcination, the reduction temperature and the particle size obtained after reduction.

The phases detected after calcination are usually a mixture of two metal oxides, Fe<sub>2</sub>O<sub>3</sub> and NiO, which have been characterized by XRD and Mössbauer spectroscopy. Particularly, Fe-Ni mixed oxides,  $\alpha$ -Fe<sub>2- $\zeta$</sub> Ni $\zeta$ O<sub>3</sub> and NiFe<sub>2</sub>O<sub>4</sub>, have been identified in two articles [39, 46]. Mössbauer spectroscopy indicated that despite similar iron environments in Fe-Ni/SiO<sub>2</sub> and Fe/SiO<sub>2</sub> oxides ( $\alpha$ -Fe<sub>2</sub>O<sub>3</sub>, also detected by XRD, [39], a difference in the half linewidths of the peaks, significantly broadened for Fe-Ni/SiO<sub>2</sub> compared with Fe/SiO<sub>2</sub>, suggested that at least some iron atoms had nickel nearest neighbors. The oxide was designated as  $\alpha$ -Fe<sub>2- $\zeta$</sub> Ni $\zeta$ O<sub>3</sub>. The low intensities of NiO reflections indicated that most of Ni was in the  $\alpha$ -Fe<sub>2</sub>O<sub>3</sub> rhombohedral phase. NiFe<sub>2</sub>O<sub>4</sub> phase could be identified directly by XRD [46].

In conclusion, IWI does not ensure a complete association of the two metals during the first stages of preparation. Doping of iron oxides by Ni<sup>2+</sup> ions (or possibly of cubic NiO by iron ions) probably occurs but is not obvious to evidence.

The reduction temperature of the oxidic phases ranges between 300 and 500 °C. However, higher reaction temperatures (namely, 950 [45], 800 [1] and 700 °C [48]) were also used in order to totally reduce Fe-Ni oxides. In this case, a large increase of the particle size was observed (up to 21 nm). When mentioned, the particle size varies between 4 and 21 nm, indicating the difficulty of controlling particle size by IWI, calcination and reduction.

Another way to form Fe-Ni particles was presented by Chieffi *et al.* [24]. Carbon-supported Fe-Ni nanoparticles were prepared by carbothermal reduction of a cellulose filter paper impregnated with Fe and Ni salts, at 800 °C for 2 h under nitrogen. The shape and size of cellulose was retained after heat-treatment. The crystalline size of Fe-Ni nanoparticles was 20 nm, as calculated by the Scherrer equation.

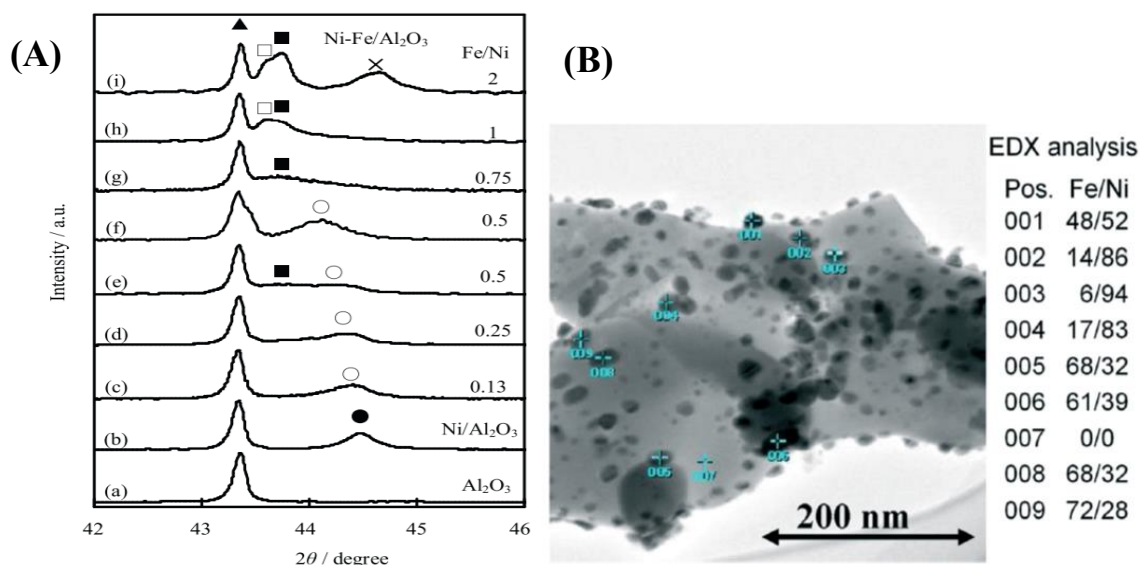


**Figure 1.10.** (A) XRD patterns of Fe-Ni/Al<sub>2</sub>O<sub>3</sub> catalysts reduced at 500 °C for 30 min. (a) Al<sub>2</sub>O<sub>3</sub>, (b) Ni/Al<sub>2</sub>O<sub>3</sub>, (c) Fe-Ni/Al<sub>2</sub>O<sub>3</sub> (Fe/Ni = 0.125), (d) Fe-Ni/Al<sub>2</sub>O<sub>3</sub> (Fe/Ni = 0.25), (e) Fe-Ni/Al<sub>2</sub>O<sub>3</sub> (Fe/Ni = 0.5), (f) Fe-Ni/Al<sub>2</sub>O<sub>3</sub> (Fe/Ni = 0.5) after reduction for 100 min, (g) Fe-Ni/Al<sub>2</sub>O<sub>3</sub> (Fe/Ni = 0.75), (h) Fe-Ni/Al<sub>2</sub>O<sub>3</sub> (Fe/Ni = 1), and (i) Fe-Ni/Al<sub>2</sub>O<sub>3</sub> (Fe/Ni = 2). ● = Ni, ○ = Ni-rich Fe-Ni *fcc* alloy, ▲ = Al<sub>2</sub>O<sub>3</sub>, ■ = FeNi (tetragonal), □ = Fe-rich Fe-Ni *fcc* alloy, × = Fe-rich Fe-Ni *bcc* alloy or α-Fe; (B) TEM image and EDX analysis of a Fe-Ni/Al<sub>2</sub>O<sub>3</sub> catalyst (Fe/Ni = 0.5). Reprinted from ref. 49. Copyright 2011 Elsevier

Another problem with IWI is the varying composition of Fe-Ni particles. Wang *et al.* [49] prepared a series of Fe-Ni catalysts with different Fe/Ni ratios on an Al<sub>2</sub>O<sub>3</sub> support. Several phases coexist, and diffraction peaks are sometimes broad and asymmetric, which may indicate that the composition of the particles is not uniform (Figure 1.10A). The non-uniformity of the composition between Fe-Ni particles has been evidenced by EDX for reduced Fe-Ni/Al<sub>2</sub>O<sub>3</sub> (Fe/Ni = 0.5). The Fe/Ni ratio is in the range 0.06–2.6, indicating the formation of Fe-Ni alloy particles with a wide range of composition. Kumbhar *et al.* [26] also found that 20 wt% Fe<sub>25</sub>Ni<sub>75</sub>/SiO<sub>2</sub> and 20 wt% Fe<sub>50</sub>Ni<sub>50</sub>/SiO<sub>2</sub> both presented a mixture of *fcc* and *bcc* phases, corresponding to different compositions. Unmuth *et al.* [39] showed by Mössbauer spectroscopy that a 4.24 wt% Fe<sub>80</sub>Ni<sub>20</sub>/SiO<sub>2</sub> catalyst possessed particles with two different compositions after reduction at 425 °C, namely, *fcc* phases Fe<sub>62</sub>Ni<sub>38</sub> and *bcc* phases Fe<sub>94</sub>Ni<sub>6</sub>.

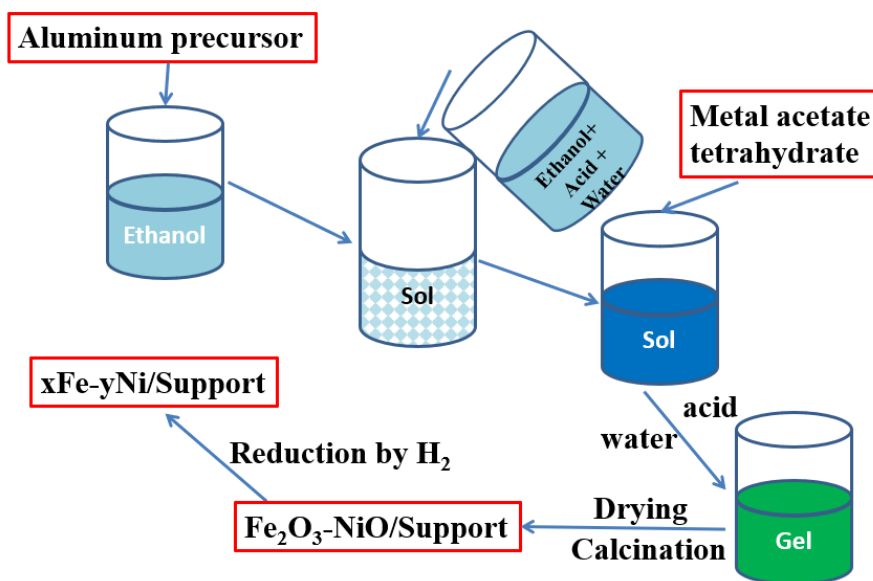


Figure 1.11. Principle of preparation by sol-gel method.

#### I.2.1.2. Sol-gel method

In the sol-gel method (Figure 1.11), a "sol" (a colloidal solution) is formed by adding ethanol and acid to an alkoxide solution (for example, aluminium ethoxide). The system gradually evolves towards the formation of a gel after the addition of Fe and Ni precursors (here, acetate tetrahydrates). Calcination and reduction lead to Fe-Ni alloyed nanoparticles dispersed onto the support.

As is the case for impregnation, phases obtained after calcination are always a mixture of several metal oxides, with some phases involving the support:  $\text{Fe}_2\text{O}_3$ , NiO,  $\text{NiAl}_2\text{O}_4$ ,  $\text{FeAl}_2\text{O}_4$  and  $\text{AlFeO}_3$  (Table 1.10). Spinel formed between metals and support are difficult to reduce, thus leading to a high reduction temperature. However, the particle size mentioned in the literature is about 7 nm, globally smaller than for catalysts prepared by IWI.

**Table 1.10.** Phases detected after calcination, reduction temperature and particle size of Fe-Ni nanoparticles after reduction for catalysts prepared by sol-gel method.

Catalysts	Phases after calcination	Reduction Temp. (°C)	Particles size (nm)	Ref.
Fe-Ni	$\text{NiFe}_2\text{O}_4$ , $\text{AlFeO}_3$ , NiO, $\text{Fe}_2\text{O}_3$ , FeC	400	--	[16]
/ $\text{Al}_2\text{O}_3$	NiO, $\text{NiAl}_2\text{O}_4$ , $\text{FeAl}_2\text{O}_4$	700	7	[10]
	$\text{NiAl}_2\text{O}_4$	700	7	[10]

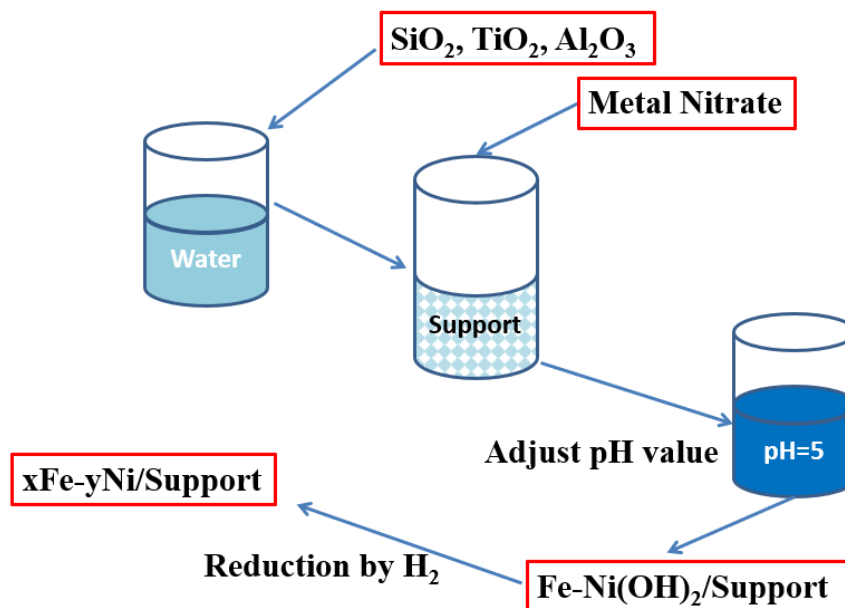


Figure 1.12. Principle of preparation by DP.

### I.2.1.3. Deposition-precipitation

Deposition-precipitation (DP) is a preparation method, which leads to the deposition of a metal compound (for example, a hydroxide) onto the support. Nickel hydroxide should deposit at a pH of around 5.7, iron(III) hydroxide at a pH of around 2.6, and iron(II) hydroxide at a pH of around 6-9. Therefore, unlike what was seen for IWI and the sol-gel method, it can be supposed that an iron(II) salt should be chosen for DP, since nickel hydroxide and iron(II) hydroxide would deposit in the same pH range. During a DP synthesis, the Ni(II) and Fe(II) salts are introduced into an aqueous solution with the support, such as SiO<sub>2</sub>, TiO<sub>2</sub> or Al<sub>2</sub>O<sub>3</sub>. The pH of the solution is increased by addition of a base, till precipitation takes place. Fe-Ni nanoparticles are obtained after reduction in H<sub>2</sub>, summarized in Figure 1.12.

**Table 1.11.** Phases detected after reduction, reduction temperature and particle size of Fe-Ni nanoparticles after reduction for catalysts prepared by DP.

Catalysts	Reduction Temp. (°C)	Phases after reduction	Particles size (nm)	Ref.
Fe-Ni/AC	400	FeNi, Fe <sub>2</sub> O <sub>3</sub> , Fe <sub>3</sub> O <sub>4</sub>	7.1	[27]
Fe-Ni/AC	400	FeNi, Fe <sub>2</sub> O <sub>3</sub> , Fe <sub>3</sub> O <sub>4</sub>	5	[50]
Fe-Ni/Al <sub>2</sub> O <sub>3</sub>	500	FeNi	4	[13]
Fe-Ni/Al <sub>2</sub> O <sub>3</sub> -CeO <sub>2</sub> -ZrO <sub>2</sub>	600	FeNi	15.2	[51]

As we can see, only a few articles have investigated the preparation of Fe-Ni nanoparticles by DP (Table 1.11). The particle size is often smaller (5 nm) than when prepared by IWI and sol-gel methods when the reduction temperature is low, but the metals are not fully reduced. A higher reduction temperature may be necessary because of the phases formed between metal and support, but this may lead to an increase of the particle size (up to 15.2 nm).

Van de Loosdrecht *et al.* [19] prepared Fe-Ni catalysts by using deposition-precipitation of a more unusual precursor, i.e. cyanide complexes, onto a TiO<sub>2</sub> support. A potassium iron cyanide solution was injected into a suspension of TiO<sub>2</sub> with a solution of nickel nitrate kept at a pH of 5, to obtain potassium-containing mixed Fe-Ni cyanide salts. The catalyst was then calcined in air at 300 °C to remove the cyanide ligands. Total reduction of Fe-Ni was reached only at 900 °C according to TPR profiles, because of the formation of a (nickel) iron titanate or a potassium iron titanate. The particle size of the nickel-iron particles after reduction of 900 °C, calculated from XRD data, turned out to be 15-20 nm.

In conclusion, the phases obtained by incipient wetness impregnation and calcination are based on the two monometallic metal oxides, which shows that the two metals are not associated at this stage of the preparation. Doping of the monometallic oxides by the other metal is likely to occur. Phases detected after calcination when the sol-gel method is used are a mixture of monometallic and mixed oxides, some of them involving the support (NiAl<sub>2</sub>O<sub>4</sub>, FeAl<sub>2</sub>O<sub>4</sub>) which are much more difficult to reduce. The particle size obtained by deposition-precipitation is much smaller than that obtained by incipient wetness impregnation and the sol-gel method, but if the reduction temperature increases, the particle size may increase.

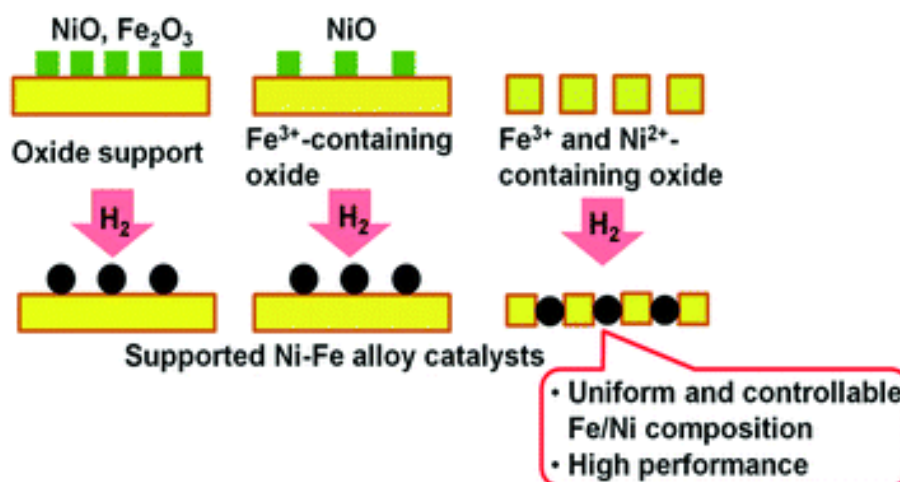


**Figure 1.13.** Formation of Fe-Ni alloyed particles by reducing metal oxides [52]. Copyright 2017 Royal Society of Chemistry

### I.2.2. Reducibility of the oxidic phases to Fe-Ni nanoparticles

The reduction stage is crucial to form Fe-Ni nanoparticles since metal oxides do not bear the active sites for hydrogenation catalysis. Depending on the phase obtained after calcination, there are three routes leading to Fe-Ni nanoparticles (Figure 1.13).

The first route is reduction of (doped) Fe<sub>2</sub>O<sub>3</sub> and NiO obtained after IWI and calcination, as listed in Table 1.8, which is a conventional way to form Fe-Ni alloyed particles. The reducibility of Fe<sub>2</sub>O<sub>3</sub> and NiO is high if the interaction with the surface is weak. Unmuth *et al.* [39] have studied the reducibility of Fe<sub>2</sub>O<sub>3</sub> or NiO on SiO<sub>2</sub> with different temperature rates, as shown in Figure 1.14. In the first case, the  $\alpha$  peak can be assigned to the reduction of Fe<sub>2</sub>O<sub>3</sub> to Fe<sub>3</sub>O<sub>4</sub> at about 320 °C. The  $\beta$  peak can be assigned to the reduction of Fe<sub>3</sub>O<sub>4</sub> to Fe at about 450 °C. Hence, the two stages of reduction for Fe can be summarized as below:



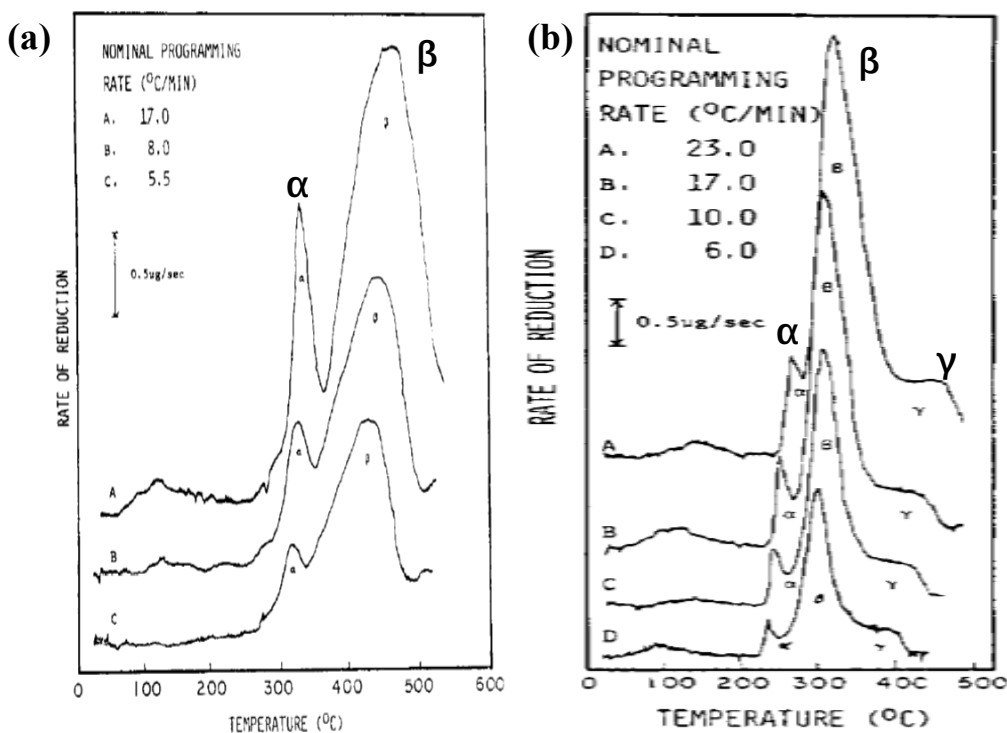


**Figure 1.14.** Temperature-programmed reduction of Fe/SiO<sub>2</sub> (a) and Ni/SiO<sub>2</sub> (b). Reprinted from ref. 39. Copyright 1980 Elsevier

It can be surprising to see that there are three peaks for Ni/SiO<sub>2</sub> reduction. The α peak was assigned to the transformation of a rhombohedral NiO structure to a cubic structure at 250 °C, but this transformation should not involve H<sub>2</sub>. A reduction of residual nitrates is more likely. The β peak can be assigned to the reduction of bulk NiO to Ni at about 300 °C. The shoulder on the β peak, namely γ peak, is thought to be due to very small particles of oxide strongly interacting with silica. Hence, reduction for Ni can be summarized as below:



Therefore, Fe<sub>2</sub>O<sub>3</sub> is more difficult to totally reduce compared with NiO. The effect of the mutual interaction of the two metals on the extent of the reduction of Fe-Ni catalysts is thus important.

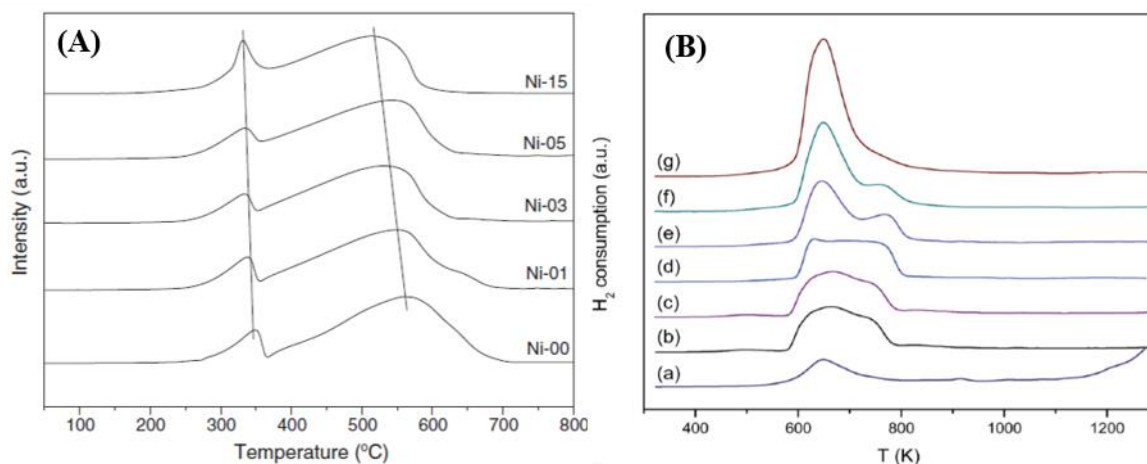


**Figure 1.15.** H<sub>2</sub>-TPR patterns of catalysts Ni-00: Fe; Ni-01: Fe<sub>99</sub>Ni<sub>1</sub>; Ni-03: Fe<sub>97</sub>Ni<sub>3</sub>; Ni-05: Fe<sub>95</sub>Ni<sub>5</sub>; and Ni-15: Fe<sub>87</sub>Ni<sub>13</sub>. Reprinted from ref. 15. Copyright 2014 Elsevier (A); (a) Fe/SiO<sub>2</sub>, (b) Ni/SiO<sub>2</sub>, (c) Fe<sub>6</sub>Ni<sub>94</sub>/SiO<sub>2</sub>, (d) Fe<sub>11</sub>Ni<sub>89</sub>/SiO<sub>2</sub>, (e) Fe<sub>20</sub>Ni<sub>80</sub>/SiO<sub>2</sub>, (f) Fe<sub>33</sub>Ni<sub>67</sub>/SiO<sub>2</sub>, and (g) Fe<sub>50</sub>Ni<sub>50</sub>/SiO<sub>2</sub>. Reprinted from ref. 41. Copyright 2014 Royal Society of Chemistry (B)

Li *et al.* [15] found that the reducibility of unsupported Fe increased when increasing the nickel content introduced by coprecipitation (Figure 1.15A). While the reduction temperature for monometallic Fe was 570 °C, a little shift to 550 °C appeared even for the “Fe<sub>99</sub>Ni<sub>1</sub>” formulation. The reduction temperature for “Fe<sub>87</sub>Ni<sub>13</sub>” was shifted to 510 °C. A dramatic decrease of reduction temperature for Fe-Ni/SiO<sub>2</sub> catalysts compared with Fe/SiO<sub>2</sub> has been investigated by Yu *et al.* [41], as shown in Figure 1.15B. The first peak at 260–510 °C for Fe/SiO<sub>2</sub> could be attributed to the reduction of Fe<sub>2</sub>O<sub>3</sub> to Fe<sub>3</sub>O<sub>4</sub> and the second peak above 930 °C was ascribed to the reduction of Fe<sub>3</sub>O<sub>4</sub> to Fe, but should most likely be attributed to iron silicates. The main reduction peak at about 390 °C for Ni/SiO<sub>2</sub> could be ascribed mainly to the reduction of NiO to Ni. Bimetallic Fe-Ni/SiO<sub>2</sub> precursors containing the same amount of Ni (8 wt%) and increasing amounts of Fe did not display any reduction peaks above 530 °C, implying the simultaneous reduction of iron oxide and nickel oxide.

Reduction of NiO loaded on Fe<sup>3+</sup>-containing oxidic supports is another way to obtain Fe-Ni alloy, as shown in the second example of Figure 1.13. In this case, the oxides exhibit a strong interaction with the support, resulting in a difficult reduction. Ashok *et al.* [48] prepared a Ni/CaO-Fe<sub>2</sub>O<sub>3</sub>-Al<sub>2</sub>O<sub>3</sub> catalyst which was difficult to be totally reduced because of the formation of a spinel, as shown in Figure 1.16. The low-temperature reduction peak ranging



from 350 to 550 °C and centered at 470 °C was attributed to the reduction of  $\text{Fe}_2\text{O}_3$  to  $\text{Fe}_3\text{O}_4$ . The moderate-temperature reduction peak ranging from 550 to 800 °C was assigned to the conversion of NiO species, in interaction with Fe species, to  $\text{Ni}^0$ , and probably to the reduction of  $\text{Fe}_3\text{O}_4$  to Fe. The high-temperature reduction peak from 750 to 1000 °C was attributed to the reduction of Ni species in a  $\text{NiAl}_2\text{O}_4$  spinel because of the strong interaction between Ni species and the support. Catalysts prepared by the sol-gel method have the same reduction problem due to the formation of spinels, as listed in Table 1.10.

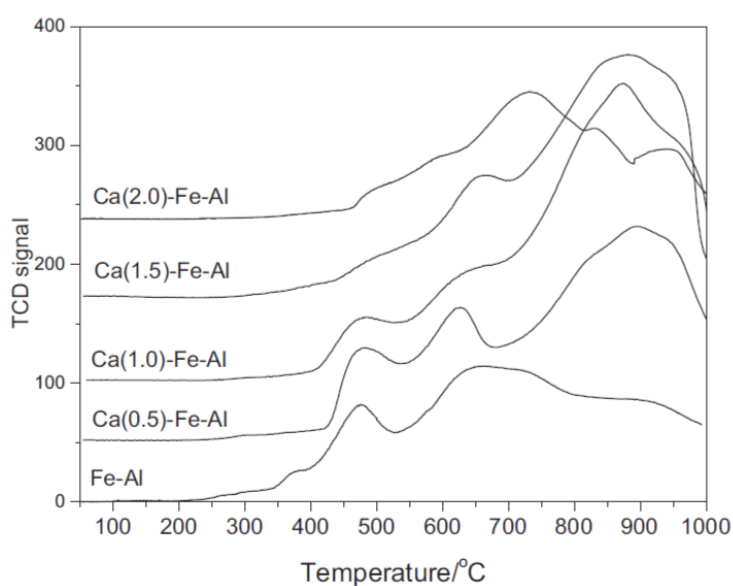


**Figure 1.16.** TPR profiles of freshly calcined  $\text{Ni}/\text{Fe}_2\text{O}_3\text{-Al}_2\text{O}_3$  and  $\text{Ni}/\text{CaO-Fe}_2\text{O}_3\text{-Al}_2\text{O}_3$  catalysts with different contents of Ca. Reprinted from ref. 48. Copyright 2015 Elsevier

Finally, Fe–Ni catalysts can also be formed by the reduction of solid precursors containing both Ni and Fe, such as hydrotalcite-like and perovskite-type compounds, as shown in the third example of Figure 1.13. Fe and Ni can easily substitute the ionic sites in these two types of compounds. Alloyed Fe–Ni particles of small and uniform size can be obtained after reduction because of the random distribution of Fe and Ni in the structure. Oemar *et al.* [53] have studied the reducibility of perovskites containing Fe and Ni to form a Fe–Ni alloy, as shown in Figure 1.17a. No peaks were observed on the TPR profile of  $\text{LaFeO}_3$  catalyst, suggesting that Fe ions formed a very strong interaction with lanthanum oxide in the perovskite structure, and the  $\text{LaFeO}_3$  structure cannot be reduced below 900 °C.

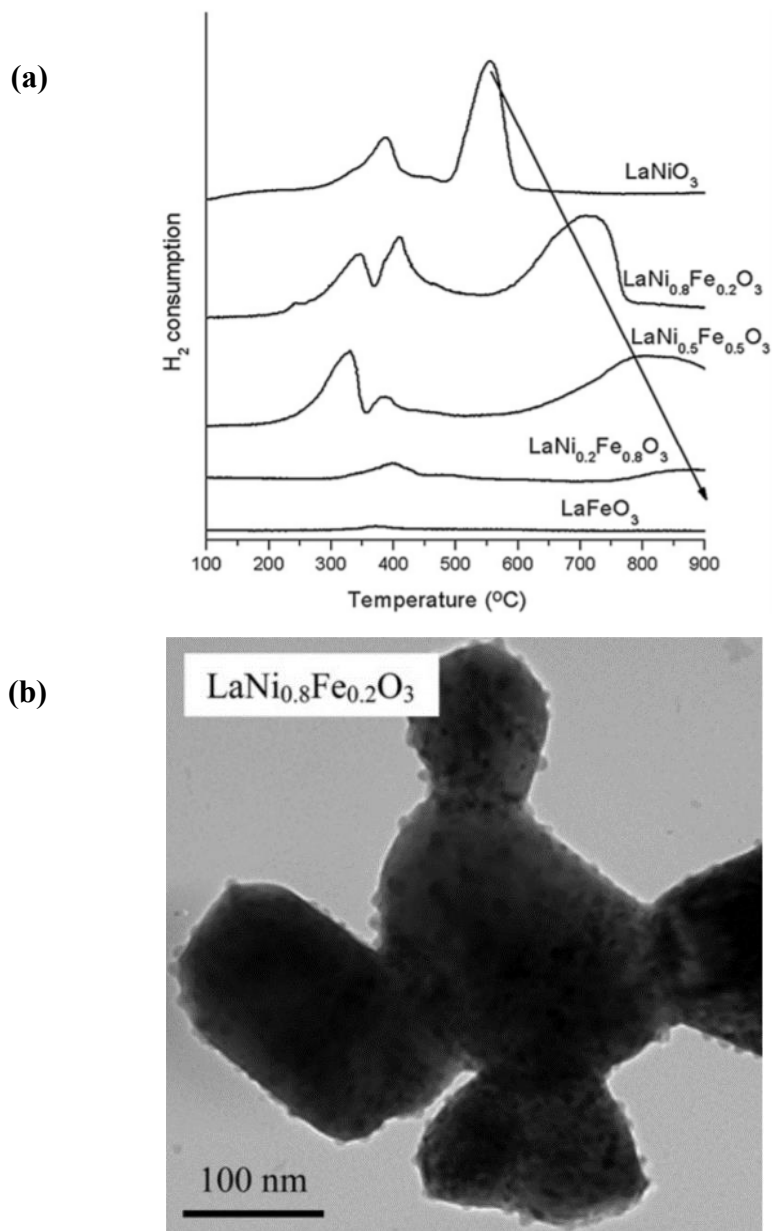


**Figure 1.17.** TPR profile of perovskite catalysts (a) and TEM image of reduced perovskite catalyst (b). Reprinted from ref. 53. Copyright 2013 Elsevier

However, the temperature peak appeared at 850 °C after adding a small amount of Ni ( $\text{LaFe}_{0.8}\text{Ni}_{0.2}\text{O}_3$ ), which indicates that some chemical interaction should exist between Ni and Fe ions inside the structure. The peak shifted to lower temperatures, down to 540 °C, when further increasing the Ni content, meaning that Ni can trigger the reduction of Fe. A TEM image of  $\text{LaNi}_{0.8}\text{Fe}_{0.2}\text{O}_3$  is shown in Figure 1.17b, exhibiting the homogeneity of the Fe-Ni particles over the reduced perovskite, with a particle size of 9.5 nm.

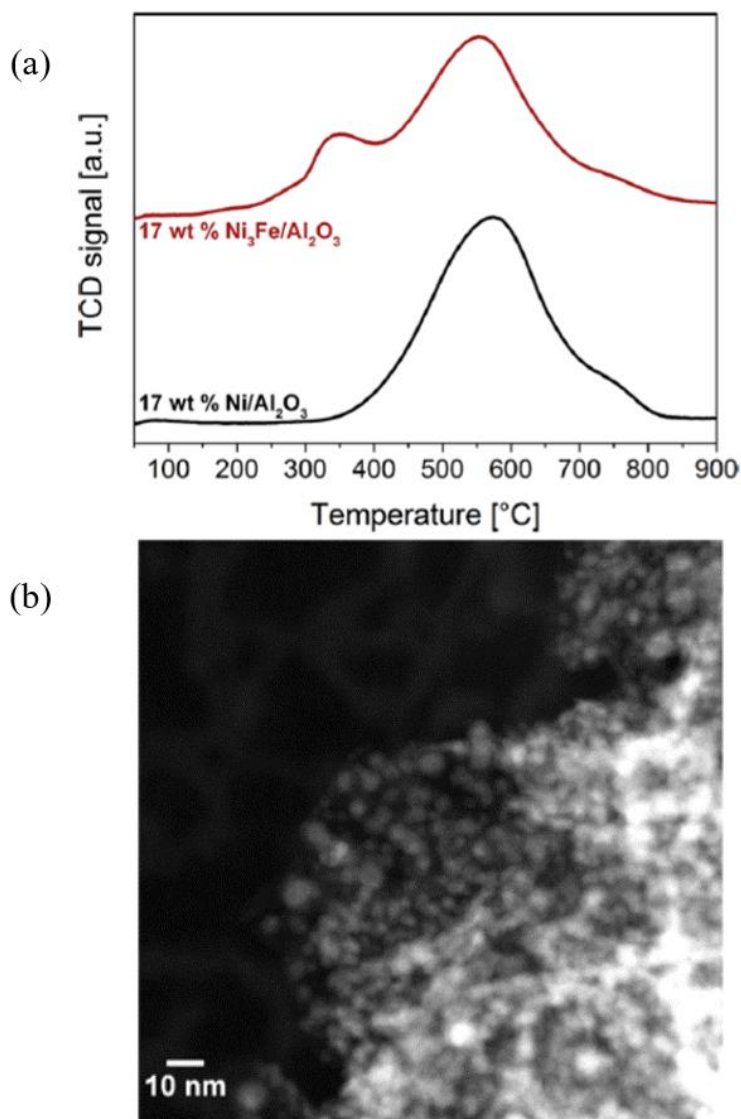


**Figure 1.18.** TPR profile of Fe-Ni/Al<sub>2</sub>O<sub>3</sub> catalysts (a) and STEM image of Fe<sub>25</sub>Ni<sub>75</sub>/Al<sub>2</sub>O<sub>3</sub> catalyst after reduction at 500 °C (b). Reprinted from ref. 13. Copyright 2017 Royal Society of Chemistry

Small particle size and homogeneous distribution of the Fe-Ni particles obtained by this reduction mode could be linked to that obtained by the preparation method of DP. Mutz *et al.* [13] prepared a Fe<sub>25</sub>Ni<sub>75</sub>/Al<sub>2</sub>O<sub>3</sub> catalyst by DP on alumina. The reducibility of the Fe<sub>25</sub>Ni<sub>75</sub>/Al<sub>2</sub>O<sub>3</sub> catalyst was investigated by H<sub>2</sub>-TPR and compared to the profile given by the monometallic Ni catalyst, as shown in Figure 1.18a. The H<sub>2</sub> consumption profile of the Ni catalyst revealed one main peak at 573 °C, referring to the reduction of NiO to metallic Ni. The shoulder around 750 °C could be ascribed to smaller NiO particles exhibiting stronger interactions with the support. The main reduction peak of the Fe<sub>25</sub>Ni<sub>75</sub>/Al<sub>2</sub>O<sub>3</sub> catalyst shifted to lower temperatures (from 573 to 555 °C). The two reduction peaks of Fe<sub>25</sub>Ni<sub>75</sub>/Al<sub>2</sub>O<sub>3</sub> were

assigned to the reduction of  $\text{Fe}_2\text{O}_3$  to  $\text{Fe}_3\text{O}_4$  in the ternary Al-Fe-Ni oxide (350 °C), and to the reduction of  $\text{Fe}_3\text{O}_4$  to Fe and NiO to Ni (555 °C). A narrow size distribution (3.9 nm) was obtained after reduction at 500 °C, with a metal dispersion of 24%, as showed in a STEM image (Figure 1.18b).

In Table 1.12 are listed the different phases detected by XRD after reduction, as a function of the reduction temperature. The higher the reduction temperature, the more Fe-Ni alloy is formed. When the reduction temperature increases to 500 °C, Fe-Ni alloy is formed, though with some remaining unreduced NiO and  $\text{Fe}_3\text{O}_4$  phases (Entries 15 and 18). Even with a further increase (up to 700 °C, for example), some unreduced phases also remain, especially spinels (Entry 22). This indicates that the interaction between metal oxides and support leads to a difficult reduction. Unreduced Fe and Ni species are still remaining even at much higher reduction temperature (900 °C), meaning that the reduction temperature is not the only factor for the reducibility of Fe-Ni alloy, the nature of the support is also the important point. Globally, a  $\text{SiO}_2$  support provides a better reducibility compared with  $\text{Al}_2\text{O}_3$  support, because of the easy formation of spinels on  $\text{Al}_2\text{O}_3$ .

In summary,  $\text{Fe}_2\text{O}_3$  is more difficult to totally reduce to metallic state compared with NiO. Temperature-programmed reduction shows that the reducibility of Fe can be increased when increasing the amount of Ni, but the interpretation of the TPR profiles is more based on the literature than on the experimental characterization of Fe and Ni species.

**Table 1.12.** Detected phases of supported Fe-Ni alloys as a function of the reduction temperature.

No.	FeNi formula	Reduction Temp. (°C)	Phases detected after reduction	Ref.
1	10 wt% Fe <sub>25</sub> Ni <sub>75</sub> /TiO <sub>2</sub>	300/400	FeNi ( <i>fcc</i> ), Fe	[22]
2	10 wt% Fe <sub>25</sub> Ni <sub>75</sub> /TiO <sub>2</sub>	300/400	FeNi ( <i>fcc</i> ), Fe	[22]
3	60 wt% Fe <sub>40</sub> Ni <sub>60</sub> /Al <sub>2</sub> O <sub>3</sub>	400	NiFe <sub>2</sub> O <sub>4</sub> ( <i>bcc</i> ), Ni	[16]
4	5.0 wt% Fe <sub>40</sub> Ni <sub>60</sub> /TiO <sub>2</sub>	400	FeNi ( <i>fcc</i> ), Fe <sup>2+</sup>	[21]
5	4.24 wt% Fe <sub>80</sub> Ni <sub>20</sub> /SiO <sub>2</sub>	425	FeNi ( <i>fcc</i> + <i>bcc</i> )	[39]
6	6.15 wt% Fe <sub>6</sub> Ni <sub>94</sub> /Al <sub>2</sub> O <sub>3</sub>	440	FeNi ( <i>fcc</i> ), Fe <sup>2+</sup>	[8]
7	6.58 wt% Fe <sub>7</sub> Ni <sub>93</sub> /Al <sub>2</sub> O <sub>3</sub> 6.58 wt% Fe <sub>7</sub> Ni <sub>93</sub> /TiO <sub>2</sub>	440/500	FeNi ( <i>fcc</i> ), Fe <sup>2+</sup>	[43]
8	22 wt% Fe <sub>36</sub> Ni <sub>64</sub> /Al <sub>2</sub> O <sub>3</sub>	450	FeNi ( <i>fcc</i> ), $\alpha$ -Fe <sub>2</sub> O <sub>3</sub> , NiFe <sub>2</sub> O <sub>4</sub>	[44]
9	10 wt% Fe <sub>50</sub> Ni <sub>50</sub> /SiO <sub>2</sub>	450	FeNi ( <i>fcc</i> )	[40]
10	20 wt% Fe <sub>25</sub> Ni <sub>75</sub> /SiO <sub>2</sub>	450	FeNi ( <i>fcc</i> ), Fe <sup>2+</sup> , Fe <sup>3+</sup>	[26]
11	10 wt% Fe <sub>50</sub> Ni <sub>50</sub> /SiO <sub>2</sub>	450	FeNi ( <i>bcc</i> + <i>fcc</i> ), Fe <sup>2+</sup>	[42]
12	20 wt% Fe <sub>25</sub> Ni <sub>75</sub> /SiO <sub>2</sub>	450	FeNi ( <i>fcc</i> ), Fe <sup>2+</sup> , Fe <sup>3+</sup>	[28]
13	7.0 wt% Fe <sub>29</sub> Ni <sub>71</sub> /SiO <sub>2</sub>	450	FeNi ( <i>fcc</i> ), Ni, Fe	[36]
14	15 wt% Fe <sub>67</sub> Ni <sub>33</sub> /SiO <sub>2</sub>	450	FeNi ( <i>bcc</i> + <i>fcc</i> )	[31]
15	30 wt% Fe <sub>10</sub> Ni <sub>75</sub> /Al <sub>2</sub> O <sub>3</sub>	500	FeNi ( <i>fcc</i> ), NiO, Fe <sub>3</sub> O <sub>4</sub> , Ni, Fe	[4]
16	10 wt% Fe <sub>50</sub> Ni <sub>50</sub> /Al <sub>2</sub> O <sub>3</sub>	500	FeNi ( <i>fcc</i> )	[6]
17	10 wt% Fe <sub>25</sub> Ni <sub>75</sub> /Al <sub>2</sub> O <sub>3</sub>	500	FeNi ( <i>fcc</i> )	[12]
18	30 wt% Fe <sub>10</sub> Ni <sub>75</sub> /Al <sub>2</sub> O <sub>3</sub>	500	FeNi ( <i>fcc</i> ), NiO, Fe <sub>3</sub> O <sub>4</sub> , Ni, Fe	[4]
19	10 wt% Fe <sub>50</sub> Ni <sub>50</sub> /Al <sub>2</sub> O <sub>3</sub>	500	FeNi ( <i>fcc</i> ), Fe <sup>3+</sup>	[6]
20	10 wt% Fe <sub>50</sub> Ni <sub>50</sub> /MgO-Al <sub>2</sub> O <sub>3</sub>	500	FeNi ( <i>fcc</i> )	[47]
21	1.5 wt% Ni/CaO-Fe <sub>2</sub> O <sub>3</sub> -Al <sub>2</sub> O <sub>3</sub>	700	FeNi ( <i>fcc</i> + <i>bcc</i> ), Fe <sup>x+</sup> , Ni <sup>2+</sup>	[48]
22	40 wt% Fe <sub>25</sub> Ni <sub>75</sub> /Al <sub>2</sub> O <sub>3</sub>	700	FeNi ( <i>fcc</i> ), NiO, Ni, Ni <sub>2</sub> O <sub>3</sub> , NiAl <sub>2</sub> O <sub>4</sub>	[2]
23	40 wt% Fe <sub>12</sub> Ni <sub>88</sub> /Al <sub>2</sub> O <sub>3</sub>	700	FeNi ( <i>fcc</i> ), Ni	[10]
24	Fe <sub>50</sub> Ni <sub>50</sub> /Al <sub>2</sub> O <sub>3</sub>	700	FeNi ( <i>fcc</i> )	[54]
25	10 wt% Fe <sub>50</sub> Ni <sub>50</sub> /[4MgCO <sub>3</sub> ·Mg(OH) <sub>2</sub> ·5H <sub>2</sub> O]	723	FeNi ( <i>fcc</i> ), Fe <sup>2+</sup>	[39]
26	23.3 wt% Fe <sub>25</sub> Ni <sub>75</sub> /Al <sub>2</sub> O <sub>3</sub>	800	FeNi ( <i>fcc</i> )	[1]
27	Fe <sub>25</sub> Ni <sub>75</sub> /Al <sub>2</sub> O <sub>3</sub>	900	FeNi ( <i>fcc</i> ), Fe <sub>2</sub> O <sub>3</sub> , NiO	[45]

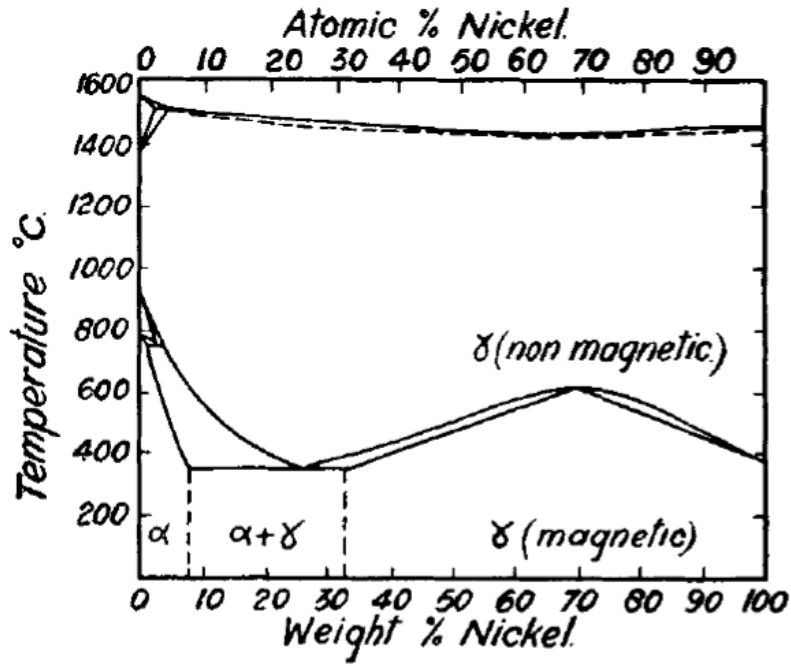


Figure 1.19. Simplified Fe–Ni phase diagram. [55]

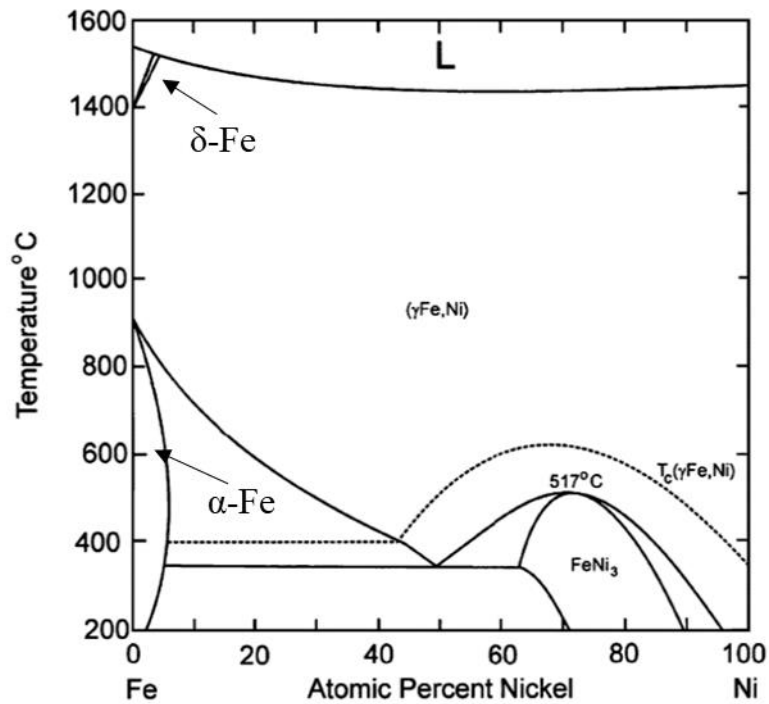


Figure 1.20. Fe–Ni phase diagram involving the presence of definite phases. Reprinted from ref. 6. Copyright 2007 Elsevier

### I.2.3. Influence of the Ni content on the nanoparticles structure

According to the simplified Fe–Ni phase diagram shown in Figure 1.19, the Fe-Ni bulk alloy appears in different structures depending on the Fe/Ni ratio and on the temperature. The  $\alpha$  phase containing less than 8 at% of Ni exhibits the body centered cubic (*bcc*) structure, like metallic Fe, while the  $\gamma$  phase, containing more than 32 at% of Ni, exhibits the face centered cubic (*fcc*) structure, like monometallic Ni. Compositions between 8 and 32 at% lead to a mixture of *bcc* and *fcc* phases after cooling. Except for the lowest Ni contents for which the phase retains the *bcc* structure, the *fcc* phase dominates above 400 °C. Matsuyama *et al.* [23] confirmed that Fe-rich alloys (< 5 at% Ni) exhibit the *bcc* structure, while Ni-rich alloys (> 40 at% Ni) exhibit the *fcc* structure. For a Ni content ranging between 5 and 40 at%, there was a mixture of the two phases (*fcc* and *bcc*). More complex phase diagrams based on the study of meteorites have been published [6, 56]. In the  $\gamma$  domain, they include the existence of compounds of definite composition, such as FeNi<sub>3</sub>, as shown in Figure 1.20.

In the articles in which catalysts were prepared with different Fe and Ni proportions and the structure of the particles was investigated (Table 1.13), variations in terms of structure are often consistent with the phase diagram. For example, Ni-rich alloys exhibit the *fcc* structure, and when the Ni content is lower than 40 at% (“Fe<sub>75</sub>Ni<sub>25</sub>” and “Fe<sub>20</sub>Ni<sub>80</sub>”), a mixture of *bcc* and *fcc* phases was detected. However, it can be noted that in some cases, systems prepared with Ni-rich compositions also present a mixture of phases. No obvious link can be derived between the structure and the average size of the particles.

Finally, as seen in section I.1, the composition of the surface of Fe-Ni particles may not be the same as that of the bulk. In contrast with the bulk structure, little attention has been paid to the surface composition of the nanoparticles, which should present a closer relationship with the catalytic activity. Matsuyama *et al.* [23] found that the maximum catalytic activity for the hydrogenation of ethylene on Fe-Ni alloys was observed for a bulk composition of 40% Ni (*fcc* alloy), but the surface composition was evaluated to be 20% Ni, by detecting  $\beta$ -rays emitted from <sup>63</sup>Ni. More generally, the surface concentration of Ni was always lower than the bulk composition. This suggested that the composition of Fe-Ni alloy was not uniform. Hence,

studies of the effects of both surface and bulk structure on the catalytic activity in hydrogenation reactions on Fe-Ni alloys are essential.

**Table 1.13.** Structure of Fe-Ni nanoparticles and particle size as a function of the Fe/Ni ratio.

Formulation	Structures of Fe-Ni alloy	Particles size (nm)	Ref.
Fe <sub>80</sub> Ni <sub>20</sub>	<i>fcc+bcc</i>	8.9 ( <i>fcc</i> ), 12.8 ( <i>bcc</i> )	[39]
Fe <sub>75</sub> Ni <sub>25</sub>	<i>fcc+bcc</i>	10	[26]
	<i>fcc+bcc</i>	15	[4]
Fe <sub>67</sub> Ni <sub>33</sub>	<i>fcc+bcc</i>	10	[31]
	<i>fcc</i>	6.5	[22]
Fe <sub>50</sub> Ni <sub>50</sub>	<i>fcc+bcc</i>	9	[26]
	<i>fcc</i>	10	[40]
	<i>fcc</i>	10	[36]
	<i>fcc</i>	15	[4]
	<i>fcc</i>	10	[31]
Fe <sub>33</sub> Ni <sub>67</sub>	<i>fcc</i>	10	[31]
Fe <sub>29</sub> Ni <sub>71</sub>	<i>fcc+bcc</i>	10	[36]
Fe <sub>25</sub> Ni <sub>75</sub>	<i>fcc</i>	13	[26]
	<i>fcc</i>	11	[4]
Fe <sub>17</sub> Ni <sub>83</sub>	<i>fcc</i>	12	[36]
Fe <sub>9</sub> Ni <sub>91</sub>	<i>fcc</i>	12	[36]

### I.3. Conclusions

Bimetallic Fe-Ni catalysts are more selective for the hydrogenation of C=C, C=O and C≡N bonds than monometallic Ni, which often leads to hydrogenolysis or overhydrogenation side reactions, in the gas or in the liquid phase. Formulations close to Fe<sub>25</sub>Ni<sub>75</sub>, which have been reported for different families of reaction (hydrogenation of CO and CO<sub>2</sub>, hydroconversion of organic molecules) have often been singled out for their superior activity and selectivity. There are four possible explanations: 1) *fcc* structure of Fe-Ni alloy; 2) suitable amount of H<sub>2</sub> dissociated on Ni species for the Fe-Ni system; 3) charge transfer from Fe to Ni and oxophilic properties of Fe; and 4) unreduced ions acting as Lewis acidic sites. However, the composition of the surface, which might differ from that of the bulk, is only discussed in few articles. Therefore, explanations for the catalytic activity of Fe-Ni alloys are still ambiguous.



In addition, Fe-Ni bimetallic catalysts have mostly been prepared by impregnation which may lead to a poor control of size, structure (*fcc* vs. *bcc*) and composition of the Fe-Ni particles. The deposition-precipitation and sol-gel methods, which have been seldom used, seem to favor a higher homogeneity of the nanoparticles size and composition, but high reduction temperatures may be required to complete the reduction of the two metals, because of the existence of phases between the metals and the support. Fe is reported to be the more difficult of the two metals to reduce totally to the metallic state, but its reducibility seems to be increased with increasing the Ni content. Supports usually used for Fe-Ni catalysts are SiO<sub>2</sub>, TiO<sub>2</sub>, Al<sub>2</sub>O<sub>3</sub> and carbon. Alumina might trap metal ions, and then change the proportion of metals in the nanoparticles compared with the expected formulation. The role of other supports has been demonstrated for some selective hydrogenations, but is difficult to rationalize as they can be accompanied by changes in the particle size or composition.

Therefore, according to the literature, linking the hydrogenation activity to the surface composition of Fe-Ni nanoparticles with homogeneous particle size, structure and composition is needed for further study. Given the limits of incipient wetness impregnation, the deposition-precipitation method has been chosen in this thesis to investigate the synthesis of precisely controlled bimetallic Fe-Ni nanoparticles supported on SiO<sub>2</sub>, and evidence the interplay between Fe and Ni along the different stages of the catalyst preparation. After a complete characterization of the bimetallic nanoparticles, it will be attempted to correlate their bulk and surface composition to their catalytic performances in the conversion of furfural, and in particular to their selectivity to furfuryl alcohol.

**References**

- [1] D. Tian, Z. Liu, D. Li, H. Shi, W. Pan, Y. Cheng, Bimetallic Ni–Fe total-methanation catalyst for the production of substitute natural gas under high pressure, *Fuel*, 104 (2013) 224-229.
- [2] S. Hwang, J. Lee, U. G. Hong, J. C. Jung, D. J. Koh, H. Lim, C. Byun, I. K. Song, Hydrogenation of carbon monoxide to methane over mesoporous nickel-M-alumina (M=Fe, Ni, Co, Ce, and La) xerogel catalysts, *Journal of Industrial and Engineering Chemistry*, 18 (2012) 243-248.
- [3] R. Sathawong, N. Koizumi, C. Song, P. Prasassarakich, Comparative study on CO<sub>2</sub> hydrogenation to higher hydrocarbons over Fe-Based bimetallic catalysts, *Topics in Catalysis*, 57 (2013) 588-594.
- [4] D. Pandey, G. Deo, Promotional effects in alumina and silica supported bimetallic Ni–Fe catalysts during CO<sub>2</sub> hydrogenation, *Journal of Molecular Catalysis A: Chemical*, 382 (2014) 23-30.
- [5] P. Li, F. Yu, N. Altaf, M. Zhu, J. Li, B. Dai, Q. Wang, Two-Dimensional layered double hydroxides for reactions of methanation and methane reforming in C<sub>1</sub> Chemistry, *Materials*, 11 (2018).
- [6] A. L. Kustov, A. M. Frey, K. E. Larsen, T. Johannessen, J. K. Nørskov, C. H. Christensen, CO methanation over supported bimetallic Ni–Fe catalysts: From computational studies towards catalyst optimization, *Applied Catalysis A: General*, 320 (2007) 98-104.
- [7] M. P. Andersson, T. Bligaard, A. Kustov, K. E. Larsen, J. Greeley, T. Johannessen, C. H. Christensen, J. K. Nørskov, Toward computational screening in heterogeneous catalysis: Pareto-optimal methanation catalysts, *Journal of Catalysis*, 239 (2006) 501-506.
- [8] X. Z. Jiang, S. A. Stevenson, J. A. Dumesic, Mössbauer-spectroscopy and methanation kinetics studies of nickel iron alloy particles supported on titania and alumina, *Journal of Catalysis*, 91 (1985) 11-24.
- [9] P. Bussiere, J. L. Duvault, M. Forissier, D. Foujols, C. Mirodatos, V. Perrichon, Relationship between the catalytic properties and surface-composition of a polycrystalline Fe-Ni ribbon, *Applied Catalysis*, 58 (1990) 219-225.

- [10] S. Hwang, U. G. Hong, J. Lee, J. H. Baik, D. J. Koh, H. Lim, I. K. Song, Methanation of carbon dioxide over mesoporous Nickel–M–Alumina (M = Fe, Zr, Ni, Y, and Mg) xerogel catalysts: effect of second metal, *Catalysis Letters*, 142 (2012) 860-868.
- [11] T. F. Sheshko, Y. M. Serov, Bimetallic systems containing Fe, Co, Ni, and Mn nanoparticles as catalysts for the hydrogenation of carbon oxides, *Russian Journal of Physical Chemistry A*, 86 (2012) 283-288.
- [12] J. Sehested, K. E. Larsen, A. L. Kustov, A. M. Frey, T. Johannessen, T. Bligaard, M. P. Andersson, J. K. Nørskov, C. H. Christensen, Discovery of technical methanation catalysts based on computational screening, *Topics in Catalysis*, 45 (2007) 9-13.
- [13] B. Mutz, M. Belimov, W. Wang, P. Sprenger, M. A. Serrer, D. Wang, P. Pfeifer, W. Kleist, J. D. Grunwaldt, Potential of an alumina-supported Ni<sub>3</sub>Fe catalyst in the methanation of CO<sub>2</sub>: impact of alloy formation on activity and stability, *ACS Catalysis*, 7 (2017) 6802-6814.
- [14] J. X. Liu, P. Wang, W. Xu, E. J. M. Hensen, Particle size and crystal phase effects in Fischer-Tropsch catalysts, *Engineering*, 3 (2017) 467-476.
- [15] T. Li, H. Wang, Y. Yang, H. Xiang, Y. Li, Study on an iron–nickel bimetallic Fischer–Tropsch synthesis catalyst, *Fuel Processing Technology*, 118 (2014) 117-124.
- [16] M. Feyzi, A. A. Mirzaei, Preparation and characterization of FeNi/Al<sub>2</sub>O<sub>3</sub> catalysts for production of light olefins, *Petroleum Chemistry*, 52 (2012) 362-371.
- [17] J. A. Amelse, L. H. Schwartz, J. B. Butt, Iron alloy Fischer-Tropsch catalysts. 3. Conversion dependence of selectivity and water-gas shift, *Journal of Catalysis*, 72 (1981) 95-110.
- [18] H. Arai, K. Mitsuishi, T. Seiyama, TiO<sub>2</sub>-supported Fe-Co, Co-Ni and Ni-Fe alloy catalysts for Fischer-Tropsch synthesis, *Chemistry Letters*, (1984) 1291-1294.
- [19] J. van de Loosdrecht, A. J. Vandillen, A. A. Vanderhorst, A. M. Vanderkraan, J. W. Geus, Nickel-iron catalysts prepared by homogeneous deposition-precipitation of cyanide complexes on a titania support, *Topics in Catalysis*, 2 (1995) 29-43.
- [20] T. Ishihara, K. Eguchi, H. Arai, An infrared study of NO SiO<sub>2</sub>-supported Fe, Co and Ni bimetallic alloy catalysts for CO hydrogenation, *Chemistry Letters*, (1986) 1695-1698.

- [21] J. van de Loosdrecht, A. M. van der Kraan, A. J. van Dillen, J. W. Geus, Metal-support interaction: Titania-supported nickel-iron catalysts, *Catalysis Letters*, 41 (1996) 27-34.
- [22] T. Ishihara, K. Eguchi, H. Arai, Hydrogenation of carbon-monoxide over SiO<sub>2</sub>-supported Fe-Co, Co-Ni and Ni-Fe bimetallic catalysts, *Applied Catalysis*, 30 (1987) 225-238.
- [23] M. Matsuyama, K. Ashida, O. Takayasu, T. Takeuchi, Catalytic activities of Ni alloys expressed by surface and bulk compositions, *Journal of Catalysis*, 102 (1986) 309-315.
- [24] G. Chieffi, C. Giordano, M. Antonietti, D. Esposito, FeNi nanoparticles with carbon armor as sustainable hydrogenation catalysts: towards biorefineries, *Journal of Materials Chemistry A*, 2 (2014) 11591.
- [25] W. S. Putro, T. Kojima, T. Hara, N. Ichikuni, S. Shimazu, Selective hydrogenation of unsaturated carbonyls by Ni-Fe-based alloy catalysts, *Catalysis Science & Technology*, 7 (2017) 3637-3646.
- [26] P. S. Kumbhar, M. R. Kharkar, G. D. Yadav, R. A. Rajadhyaksha, Geometric and electronic effects in silica supported bimetallic nickel copper and nickel iron catalysts for liquid-phase hydrogenation of acetophenone and benzonitrile, *Journal of the Chemical Society-Chemical Communications*, (1992) 584-586.
- [27] C. Li, G. Xu, Y. Zhai, X. Liu, Y. Ma, Y. Zhang, Hydrogenation of biomass-derived ethyl levulinate into  $\gamma$ -valerolactone by activated carbon supported bimetallic Ni and Fe catalysts, *Fuel*, 203 (2017) 23-31.
- [28] G. D. Yadav, M. R. Kharkara, Liquid-phase hydrogenation of saturated and unsaturated nitriles-activities and selectivities of bimetallic nickel-copper and nickel-iron catalysts supported on silica, *Applied Catalysis A: General*, 126 (1995) 115-123.
- [29] S. Leng, X. Wang, X. He, L. Liu, Y.e. Liu, X. Zhong, G. Zhuang, J. G. Wang, NiFe/ $\gamma$ -Al<sub>2</sub>O<sub>3</sub>: A universal catalyst for the hydrodeoxygenation of bio-oil and its model compounds, *Catalysis Communications*, 41 (2013) 34-37.
- [30] H. Fang, J. Zheng, X. Luo, J. Du, A. Roldan, S. Leoni, Y. Yuan, Product tunable behavior of carbon nanotubes-supported Ni-Fe catalysts for guaiacol hydrodeoxygenation, *Applied Catalysis A: General*, 529 (2017) 20-31.

- [31] L. Nie, P. M. de Souza, F. B. Noronha, W. An, T. Sooknoi, D. E. Resasco, Selective conversion of m-cresol to toluene over bimetallic Ni–Fe catalysts, *Journal of Molecular Catalysis A: Chemical*, 388-389 (2014) 47-55.
- [32] A. Halilu, T. H. Ali, A. Y. Atta, P. Sudarsanam, S. K. Bhargava, S. B. Abd Hamid, Highly selective hydrogenation of biomass-derived furfural into furfuryl alcohol using a novel magnetic nanoparticles catalyst, *Energy & Fuels*, 30 (2016) 2216-2226.
- [33] L. Liu, H. Liu, W. Huang, Y. He, W. Zhang, C. Wang, H. Lin, Mechanism and kinetics of the electrocatalytic hydrogenation of furfural to furfuryl alcohol, *Journal of Electroanalytical Chemistry*, 804 (2017) 248-253.
- [34] H. Li, H. Luo, L. Zhuang, W. Dai, M. Qiao, Liquid phase hydrogenation of furfural to furfuryl alcohol over the Fe-promoted Ni-B amorphous alloy catalysts, *Journal of Molecular Catalysis A: Chemical*, 203 (2003) 267-275.
- [35] K. Yan, G. Wu, T. Lafleur, C. Jarvis, Production, properties and catalytic hydrogenation of furfural to fuel additives and value-added chemicals, *Renewable and Sustainable Energy Reviews*, 38 (2014) 663-676.
- [36] S. Sitthisa, W. An, D. E. Resasco, Selective conversion of furfural to methylfuran over silica-supported NiFe bimetallic catalysts, *Journal of Catalysis*, 284 (2011) 90-101.
- [37] W. Yu, K. Xiong, N. Ji, M. D. Porosoff, J. G. Chen, Theoretical and experimental studies of the adsorption geometry and reaction pathways of furfural over FeNi bimetallic model surfaces and supported catalysts, *Journal of Catalysis*, 317 (2014) 253-262.
- [38] L. Yu, L. He, J. Chen, J. Zheng, L. Ye, H. Lin, Y. Yuan, Robust and recyclable nonprecious bimetallic nanoparticles on carbon nanotubes for the hydrogenation and hydrogenolysis of 5-hydroxymethylfurfural, *ChemCatChem*, 7 (2015) 1701-1707.
- [39] E. E. Unmuth, L. H. Schwartz, J. B. Butt, Iron alloy Fischer-Tropsch catalysts. 1. Oxidation-reduction studies of the Fe-Ni system, *Journal of Catalysis*, 61 (1980) 242-255.
- [40] G. B. Raupp, W. N. Delgass, Mössbauer investigation of supported Fe and FeNi catalysts. 1. Effect of pretreatment on particle-size, *Journal of Catalysis*, 58 (1979) 337-347.
- [41] X. Yu, J. Chen, T. Ren, Promotional effect of Fe on performance of Ni/SiO<sub>2</sub> for

deoxygenation of methyl laurate as a model compound to hydrocarbons, RSC Advances, 4 (2014) 46427-46436.

[42] C. N. R. Rao, G. U. Kulkarni, K. R. Kannan, S. Chaturvedi, *In situ* Mössbauer and EXAFS investigations of the structural and magnetic-properties of bimetallic Fe-Ni/SiO<sub>2</sub> and Fe-Cu/SiO<sub>2</sub> catalysts, Journal of Physical Chemistry, 96 (1992) 7379-7385.

[43] X. Z. Jiang, S. A. Stevenson, J. A. Dumesic, T. F. Kelly, R. J. Casper, Characterization of NiFe alloy particles supported on titania and alumina – scanning-transmission electron-microscopy, magnetic-susceptibility, Mössbauer-spectroscopy and chemisorption measurements, Journal of Physical Chemistry, 88 (1984) 6191-6198.

[44] D. Huang, M. Ke, X. Bao, H. Liu, Fe-Promoted Ni/Al<sub>2</sub>O<sub>3</sub> thioetherification catalysts with enhanced low-temperature activity for removing mercaptans from liquefied petroleum gas, Industrial & Engineering Chemistry Research, 55 (2016) 1192-1201.

[45] R. Brown, M. E. Cooper, D. A. Whan, Temperature programmed reduction of alumina-supported iron, cobalt and nickel bimetallic catalysts, Applied Catalysis, 3 (1982) 177-186.

[46] X. Lü, Q. Zhang, W. Yang, X. Li, L. Zeng, L. Li, Catalytic ozonation of 2,4-dichlorophenoxyacetic acid over novel Fe–Ni/AC, RSC Advances, 5 (2015) 10537-10545.

[47] N. Laosiripojana, W. Sutthisripok, S. Charojrochkul, S. Assabumrungrat, Conversion of biomass tar containing sulphur to syngas by GdCeO<sub>2</sub> coated NiFe bimetallic-based catalysts, Applied Catalysis A: General, 478 (2014) 9-14.

[48] J. Ashok, S. Kawi, Steam reforming of biomass tar model compound at relatively low steam-to-carbon condition over CaO-doped nickel–iron alloy supported over iron–alumina catalysts, Applied Catalysis A: General, 490 (2015) 24-35.

[49] L. Wang, D. Li, M. Koike, S. Koso, Y. Nakagawa, Y. Xu, K. Tomishige, Catalytic performance and characterization of Ni-Fe catalysts for the steam reforming of tar from biomass pyrolysis to synthesis gas, Applied Catalysis A: General, 392 (2011) 248-255.

[50] Y. Zhai, C. Li, G. Xu, Y. Ma, X. Liu, Y. Zhang, Depolymerization of lignin via a non-precious Ni–Fe alloy catalyst supported on activated carbon, Green Chemistry, 19 (2017) 1895-1903.

- [51] A. G. Bhavani, W. Y. Kim, J. W. Lee, J. S. Lee, Influence of metal particle size on oxidative CO<sub>2</sub> reforming of methane over supported nickel catalysts: effects of second-metal addition, *ChemCatChem*, 7 (2015) 1445-1452.
- [52] K. Tomishige, D. Li, M. Tamura, Y. Nakagawa, Nickel-iron alloy catalysts for reforming of hydrocarbons: preparation, structure, and catalytic properties, *Catalysis Science & Technology*, 7 (2017) 3952-3979.
- [53] U. Oemar, P. S. Ang, K. Hidajat, S. Kawi, Promotional effect of Fe on perovskite LaNi<sub>x</sub>Fe<sub>1-x</sub>O<sub>3</sub> catalyst for hydrogen production via steam reforming of toluene, *International Journal of Hydrogen Energy*, 38 (2013) 5525-5534.
- [54] W. Teunissen, J.W. Geus, Catalyst supports based on encapsulated magnetic metal particles, *Science and Technology in Catalysis*, (1998) 185-190.
- [55] A. J. Bradley D. Sc., A. H. Jay Ph. D., A. Taylor M. Sc., LIII. The lattice spacing of iron-nickel alloys, *The London, Edinburgh, and Dublin Philosophical Magazine and Journal of Science*, Series 7, 23:155 (1937) 545-557.
- [56] S. A. Theofanidis, V. V. Galvita, C. Konstantopoulos, H. Poelman, G. B. Marin, Fe-Based nano-materials in catalysis, *Materials*, 11 (2018).

# Chapter II

Methods: characterization  
techniques and catalytic test





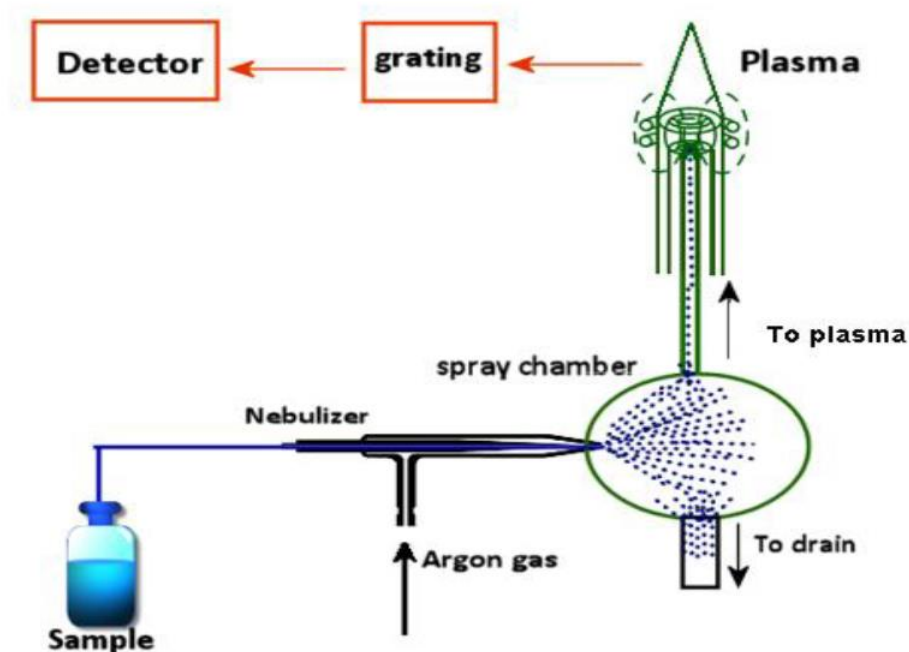


Figure 2.1. Sample introduction into the ICP-OES. [1]

## II.1. Chemical analysis

### II.1.1. Inductively Coupled Plasma Optical Emission Spectroscopy (ICP-OES)

ICP-OES (Inductively Coupled Plasma Optical Emission Spectrometry) is an analytical technique used for the quantitative determination of elements. An inductively coupled plasma produces excited atoms and ions that emit electromagnetic radiations at wavelengths characteristic of each particular element [2].

In this present work, Fe, Ni and Si elemental analysis was performed by inductively coupled plasma-optic emission spectroscopy using a 720-ES ICP-OES spectrometer (Agilent) with axial viewing and simultaneous CCD detection. About 5-7 mg of solid were introduced into 0.5 mL HF and 2 mL aqua regia. The resulting solutions were heated at 110 °C for 3 h, 80 °C for 2 h and then cooled down to room temperature for 48 h. The liquid was then converted in a nebulizer into an aerosol, a small portion of which went to an inductively coupled argon plasma, in which a temperature of approximately 9000 K is attained (Figure 2.1). The analyte

species were detected and quantified with an optical emission spectrometer (OES). Intensity measurements are converted to elemental concentrations by comparison with calibration standards.

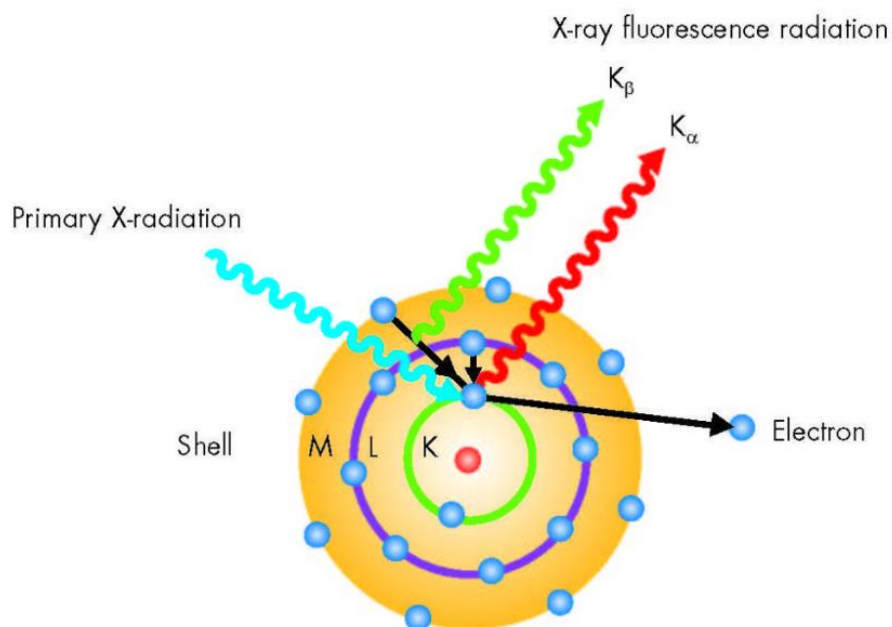


**Figure 2.2.** Principle of XRF. [3]

### II.1.2. X-ray fluorescence (XRF)

X-ray fluorescence spectroscopy (XRF) is one of the most commonly used techniques for studying the elemental composition of materials. X-rays ionize atoms, leaving them in an excited state. In Figure 2.2, one electron from the K shell is emitted after absorption of the primary X-ray radiation. The resultant void is filled by either an electron from the L shell or an electron from the M shell. In the process,  $K_{\alpha}$  and  $K_{\beta}$  radiations are generated, which are characteristic of a given element in the material. The X-ray radiations of different energies that are emitted by the various elements allow their quantification.

In the present work, a M4 Tornado from Bruker was used to estimate the elemental composition of the materials. To obtain accurate quantification of the metals present in the catalysts, each sample was irradiated 30 times. The mean value of the metal content was then determined.

### II.1.3. X-ray Photoelectron Spectroscopy (XPS)

X-ray Photoelectron Spectroscopy (XPS) is a quantitative spectroscopic technique that can be used for the chemical analysis of the surface layers of a material [4]. XPS spectra are obtained by irradiating a material with a beam of X-rays (commonly Al K $\alpha$  or Mg K $\alpha$  radiations) in an ultra-high vacuum environment, while simultaneously measuring the kinetic energy and number of electrons that escape from the top 5 nm of the material being analyzed. The energy and intensity of the emitted photoelectrons allow identifying the elements and determining their surface concentration.

A typical XPS spectrum plots the number of electrons detected versus their binding energy. Each element produces a characteristic set of XPS peaks at characteristic binding energies. The number of detected electrons in each of the characteristic peaks is directly related to the amount of element within the XPS sampling volume. To generate atomic percentage values, each raw XPS signal must be corrected by dividing its signal intensity (number of electrons detected) by a "relative sensitivity factor" (RSF), and normalized over all the elements detected.

In this work, XPS spectra were collected on an Axis UltraDLD "2009" Kratos spectrometer using the monochromatic Al K $\alpha$  radiation ( $h\nu = 1486.6$  eV) as the excitation source. The calibration of the XPS spectra was made using the carbon C 1s reference peak at 284.8 eV. It should be noted that the Fe LMM Auger peak was found not to be interfere strongly with the 2p $_{3/2}$  peak from Ni. However, the Ni LMM Auger peak interfered with the 2p $_{3/2}$  peak from Fe, and it was necessary to take it into account, using reference spectra from Ni compounds, for the integration of the Fe peak.

## II.2. Textural and morphological properties

### II.2.1. Nitrogen physisorption

The Brunauer–Emmett–Teller (BET) model serves as the basis for the measurement of the specific surface area of materials. In 1938, Brunauer, Emmett and Teller (BET) [5] proposed a theory of nitrogen physisorption at -196 °C.

The determination of the  $S_{\text{BET}}$  is based on the BET equation given below (2.1):

$$\frac{1}{v[(p_0-p)]} = \frac{c-1}{v_m c} \left( \frac{p}{p_0} \right) + \frac{1}{v_m c} \quad (2.1)$$

where  $p$  and  $p_0$  are the equilibrium and the saturation pressures of nitrogen at  $-196$  °C, respectively,

$v$  is the quantity of adsorbed nitrogen

$v_m$  is the quantity of adsorbed nitrogen corresponding to a monolayer.

$c$  is the BET constant, which is calculated by the following equation (2.2):

$$c = \exp \left( \frac{E_1 - E_L}{RT} \right) \quad (2.2)$$

$E_1$  is the heat of adsorption for the first layer, and  $E_L$  is that for the second and successive layers. It is equal to the heat of liquefaction.

The BET equation is generally applicable only for relative pressures  $p/p_0$  between 0.05 and 0.35. The BET equation gives a straight line of equation  $y = \alpha x + \beta$ . From the resulting linear plot,  $v_m$  and  $c$  can be calculated as:

$$v_m = \frac{1}{\alpha + \beta} \quad (2.3)$$

$$c = \frac{\alpha}{\beta} + 1 \quad (2.4)$$

The total surface area ( $S_t$ ) is then calculated from the value of  $v_m$  by the equation given below (2.5):

$$S_t = \frac{v_m * N_A}{V_M} \quad (2.5)$$

$N_A$ : Avogadro's constant ( $6.02 * 10^{23}$  mol<sup>-1</sup>)

$V_M$ : volume occupied by 1 mole of the adsorbate gas at STP ( $22414$  cm<sup>3</sup>/mole).

According to these numerical values, the specific surface area  $S_{BET}$  can be expressed by equation (2.6):

$$S_{BET} = \frac{S_t}{m} \quad (2.6)$$

$m$ : mass of the sample, in grams.

In this work,  $N_2$  physisorption isotherms at liquid nitrogen temperature were obtained on a TriStar II Plus gas adsorption analyzer (Micromeritics) after activation at  $150$  °C in vacuum

overnight. The specific surface area was evaluated with the BET model over the range  $p/p_0 = 0.05-0.30$ . The total pore volume was measured from the volume of  $N_2$  adsorbed at  $p/p_0 = 0.95$ .

### II.2.2. *In-situ* / X-ray diffraction (XRD)

X-ray powder diffraction (XRD) is an analytical technique primarily used for phase identification in a crystalline material. A crystal with planes oriented at an angle  $\theta$  to an incident X-ray beam of wavelength  $\lambda$  will diffract the X-rays according to the Bragg's equation (2.7):

$$2d\sin\theta=n\lambda \quad (2.7)$$

where

$n$  is an integer

$\lambda$  is the wavelength of the X-rays

$\theta$  is the angle between the incident rays and the surface of the crystal

$d$  is the corresponding interplanar spacing in the crystal lattice. The measurement of the different values of  $d$  allows identifying the phase.

In this work, X-ray diffraction patterns were recorded in ambient conditions using the Cu  $K\alpha$  radiation ( $\lambda= 1.5418 \text{ \AA}$ ; 40 kV, 30 mA) on a Siemens D5000 diffractometer, with a  $0.05^\circ$  scan step and 2 s time step for  $10-80^\circ$  range. The interpretation of the diffractograms was done using the Diffrac Eva software and by comparison by JCPDS reference files. Finally, the average crystallite size of the metals particles in the catalyst was determined by the Laue-Scherrer formula (2.8):

$$D = \frac{K\lambda}{\beta\cos\theta} \quad (2.8)$$

where

$D$  is the average crystallite size ( $\text{\AA}$ )

$\lambda$  is the wavelength of the X-ray radiation (for Cu  $K\alpha$ ,  $1.5418 \text{ \AA}$ ),

$K$  is Debye-Scherrer's constant = 0.9,

$\beta$  is the peak width at half-maximum intensity (FWHM) (radian),

$\theta$  is the angle of diffraction.

*In-situ* XRD was used to identify phase changes at different temperatures of reduction, without exposure to air. In this study, *in situ* measurements were conducted under H<sub>2</sub> (3%)/N<sub>2</sub> on a D8 Bruker diffractometer equipped with an Anton Paar XRK900 reactive chamber. Data were acquired in the Bragg-Brentano geometry, using the Cu K $\alpha$  radiation (40 kV, 40 mA). Diffractograms were recorded every 25 °C from 50 to 700 °C. A peak from the holder at  $2\theta = 27.2^\circ$  was used for calibration between different experiments. The average size of the metal nanoparticles was evaluated by the Laue-Scherrer equation applied to the (111) reflection.

### II.2.3. (High Resolution) Transmission Electron Microscopy ((HR)TEM)

Bright-field (High Resolution) Transmission Electron microscopy ((HR)TEM) is a microscopy technique in which a parallel high energy electron beam is transmitted through a specimen to form an image generating multiple signals via electron-matter interactions. The specimen is either a thin section, less than 100 nm thick, or a suspension of a powder sample on a grid. A high-resolution image is formed by using both transmitted and scattered beams to form an interference pattern at the image plane of the objective lens. Transmission electron microscopy is a major analytical method used to extract local information at the atomic level on the morphology, structure, size and distribution of metallic nanoparticles, appearing as dark spots contrasting with the support [6].

In this work, TEM observations were made at Lille University and the University of Oxford. The Bright-Field TEM images have been obtained at Lille University by using a Tecnai G2 20 microscope equipped with LaB<sub>6</sub> filament and operating at 200 kV. It is also equipped with an EDX detector and a GATAN CCD camera (Orius SC1000A). The images have been acquired in parallel beam TEM mode. Bright-field TEM has been done at the University of Oxford using a JEOL JEM-2100 microscope fitted with a LaB<sub>6</sub> source.

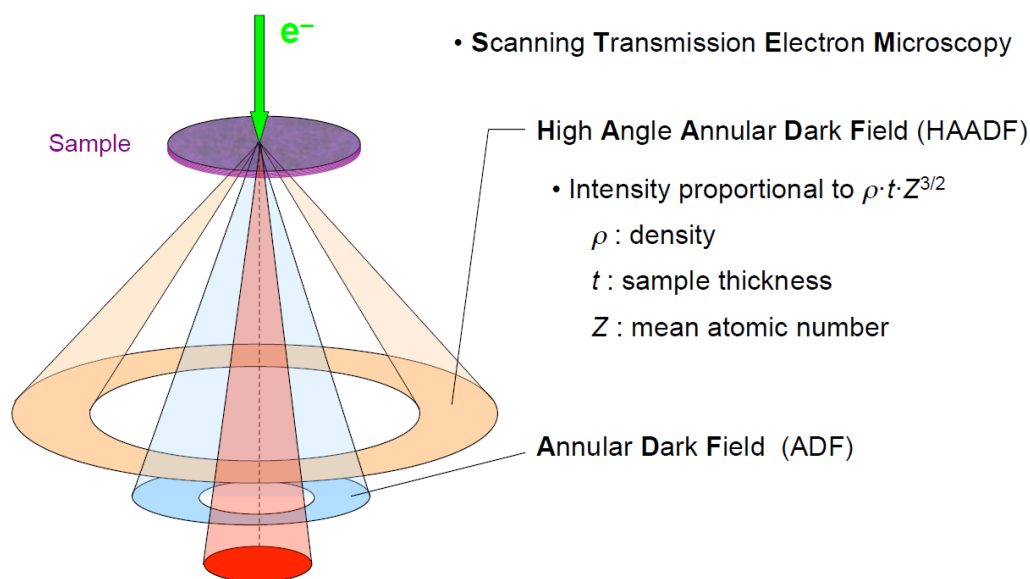


Figure 2.3. Scheme of STEM mode.

#### II.2.4. HAADF/EDX-EELS

In the scanning transmission electron microscopy (STEM) mode, a convergent electron beam is focused to a fine spot which is scanned over the sample using the beam deflection coils of the objective lens, so that the sample is illuminated at each point with the convergent beam parallel to the optical axis. The scanning of the beam across the sample, and the developments done in aberration correction and in the detection systems, make the STEM mode suitable for acquiring analytical signals such as High-angle annular dark-field imaging (incoherent elastic scattering), energy dispersive X-ray (EDX) spectroscopy, or electron energy loss spectroscopy (EELS) (inelastically scattered electrons).

High-angle annular dark-field (HAADF) detectors allow image formation by collecting incoherent elastically scattered electrons at high angles between 40 and 200 mrad (Figure 2.3). With the development of probe aberration correctors, it is possible to form atomic resolution images by using a HAADF detector. This mode of imaging is sensitive to variations in density, to the thickness of the sample and to the atomic number of atoms in the sample ( $\sim Z^{1.7}$ ). Electron-rich zones, such as metallic particles, appear as bright spots against a dark background [7].

Energy dispersive X-ray (EDX) spectroscopy detects the characteristic X-rays that are



emitted by atoms in the sample as they are ionized by the electrons in the beam. The atomic composition of a material can thus be identified, and this technique is particularly sensitive to heavier elements. In the STEM mode, EDX allows elemental mapping of samples at a subnanometric resolution.

Electron energy loss spectroscopy (EELS) is a spectroscopic technique, complementary to EDX, dealing with the analysis of the energy distribution of electrons that have undergone inelastic interaction coming through the specimen. In core-loss spectroscopy ( $> 50$  eV), inner shell electrons are excited to unoccupied levels above the Fermi level, and the EELS signal corresponds to the associated ionization edges that can be used for elemental identification, concentration measurements, mapping of bonding, oxidation state and coordination at an atomic level. The dispersion of the inelastically scattered electrons in a spectrum is done inside a magnetic-prism spectrometer [6, 8].

In this work, EDX was done at the University of Oxford on a JEM-3000F FEGTEM microscope (JEM-3000) fitted with a spherical aberration STEM probe corrector, using a Centurion EDX detector equipped with a super atmospheric thin window (SATW) detector and an INCA processor, for elemental analysis. Electron-beam size was selected to 1.2 nm for EDX point scan measurements on individual particles.

High resolution Scanning Transmission Electron Microscopy has also been performed on the TITAN Themis 300 S/TEM microscope of the Microscopy Platform of Lille University. The TITAN Themis is equipped with: a probe aberration corrector and monochromator, allowing spatial resolution of 65 pm and energy resolution of 100 meV; a super-X windowless 4 quadrant SDD (silicon drift detector) detection system for STEM-EDX mapping and several annual dark field detector; a high resolution post-column GIF, the GATAN's Quantum ERS/966 with 2kx2k Ultrascan 994G camera for EELS spectra acquisition. In order to investigate bimetallic particles, HAADF imaging and EELS have been carried out in the STEM mode for the elemental distribution within the particles. Measurements have been performed with a spot size 9 (corresponding to a spot size of approximately 2.5 Å), a semi-convergence angle between 16 and 21 mrad, and a probe current of approximately 100 pA. For HAADF images, collection

angles have been chosen between 50 and 200 mrad. Dual EELS acquisition has been performed in the spectral imaging mode with a collection angle of 49 mrad, a dispersion of 0.25 eV/ch, a step between 1.5 and 7 Å, and a dwell time between 50 and 200 ms. Alignment of the energy drift has been done on the zero-loss peak. When possible, noise reduction by PCA has been performed on the spectrum images using HyperSpy [9].

### II.2.5. Temperature-programmed reduction (TPR)

Temperature-Programmed Reduction (TPR) is a technique of characterization of oxidized materials. This technique consists in heating the material containing metal ions in a reducing gas mixture, for instance H<sub>2</sub> diluted in He, N<sub>2</sub> or Ar. The concentration of hydrogen in the reducing gas mixture is typically in the 3-17 vol% range [10]. TPR allows estimating the nature of reducible species present in the catalyst, the amount of H<sub>2</sub> required to reduce the material, and reveals the temperature at which the reduction of each species occurs in given conditions of catalyst mass, temperature ramp and flow rate [10].

In this work, all the TPR analyses were performed on an automated AutoChem II 2920 Chemisorption Analyzer from Micromeritics. 100 mg of catalyst were inserted into a glass reactor. The sample was flushed with a mixture gas of 5 vol% H<sub>2</sub> in Ar at room temperature with a flow rate of 50 mL/min. The temperature of the sample was increased linearly at a ramp rate of 7.5 °C/min up to 1000 °C and then kept at this temperature for 0.5 h. The consumption of hydrogen was monitored via a TCD signal converted by use of a calibration factor, to get quantitative information on the species present in the catalyst.

## II.3. Spectroscopic techniques

### II.3.1. Attenuated Total Reflection Infrared spectroscopy (ATR-IR)

In the attenuated total reflection (ATR) mode, the infrared (IR) light travels through an optically dense medium and is totally reflected at the interface with an optically less dense medium. An evanescent field interacts with the sample placed at the interface, making absorption measurements possible. The ATR mode usually does not need any sample

preparation. It allows measurements of interatomic vibrations in solid as well as in liquid samples, including pastes and samples otherwise difficult to handle.

In this study, Attenuated Total Reflection Infra-Red (ATR-IR) spectra were recorded using a Nicolet Magna iS50 spectrometer equipped with a diamond crystal and a DTGS detector (10 scans; resolution: 4  $\text{cm}^{-1}$ ).

### II.3.2. Mössbauer spectroscopy (MössS)

Mössbauer spectroscopy is a versatile technique that can be used to give information about the chemical, structural, magnetic and time-dependent properties of a material. It is based on the discovery of recoilless gamma ray emission and absorption, now referred to as the 'Mössbauer Effect', after its discoverer Rudolph Mössbauer, who first observed the effect in 1957. Mössbauer spectra can easily be recorded in *in situ* conditions, because of the high penetration of gamma rays. The most used isotope for MössS is  $^{57}\text{Fe}$ , which exhibits both a very low-energy gamma ray and a long-lived excited state. The emission or absorption of a gamma ray corresponds to a difference between energy levels in nuclei, that are influenced by their electronic and magnetic environment, which can shift or split these energy levels. Resonance only occurs when the transition energy in the emitting and absorbing nuclei match exactly. The energy of the incident gamma ray, that is produced at a single value by the emitter atom, is varied by accelerating the source with respect to the absorber (Doppler effect).

The energy levels in the absorbing nuclei can be modified by their environment in three main ways: by the Isomer Shift, Quadrupole Splitting and Magnetic Splitting.

. Isomer Shift  $\delta$ : the isomer shift arises due to the non-zero volume of the nucleus and the s-electron density within it. Any difference in the s-electron environment between the source and absorber produces a shift in the resonance energy of the transition. The isomer shift is useful for determining valence states, electron shielding and the electron-drawing power of electronegative groups. For example, the electron configurations for  $\text{Fe}^{2+}$  and  $\text{Fe}^{3+}$  are  $(3d)^6$  and  $(3d)^5$ , respectively. The  $\text{Fe}^{2+}$  ions have less s-electron density at the nucleus due to the greater screening of the d-electrons. They thus have a larger positive isomer shift than  $\text{Fe}^{3+}$  ions.

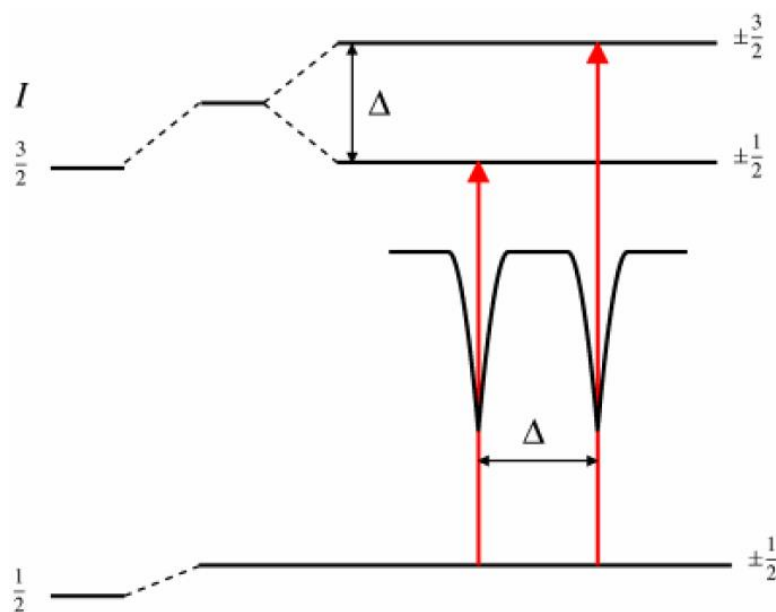


**Figure 2.4.** Quadrupole splitting for a  $I = 1/2$  to  $3/2$  transition. The magnitude of quadrupole splitting,  $\Delta$ , is shown. [11]

. Quadrupole Splitting  $\Delta$ : nuclei in states with an angular momentum quantum number  $I > 1/2$  have a non-spherical charge distribution. This produces a nuclear quadrupole moment. In the presence of an asymmetrical electric field (produced by an asymmetric electronic charge distribution or ligand arrangement), the nuclear energy levels split. The charge distribution is characterized by a single quantity called the electric field gradient. In the case of an isotope with a  $I = 3/2$  excited state, such as  $^{57}\text{Fe}$ , the excited state is split into two substates  $m_I = \pm 1/2$  and  $m_I = \pm 3/2$ . This is shown in Figure 2.4, giving a two line spectrum or 'doublet'.

. Magnetic Splitting: In the presence of a magnetic field, including a magnetic field present inside the material, the nuclear spin moment experiences a dipolar interaction with the magnetic field (Zeeman splitting), which splits the nuclear levels with a spin of  $I$  into  $(2I+1)$  substates. Transitions between the excited state and ground state can only occur where  $m_I$  changes by 0 or 1. For  $^{57}\text{Fe}$ , this gives six possible transitions, giving a sextet as illustrated in Figure 2.5, with the line spacing proportional to  $B_{\text{HF}}$  (total effective magnetic field at the nucleus).

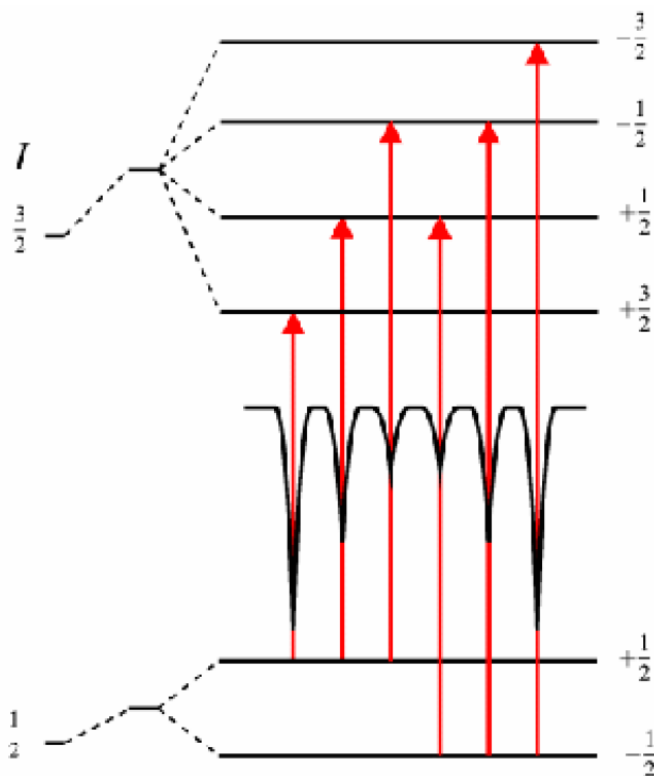


**Figure 2.5.** Magnetic splitting of the nuclear energy levels. [10]

In this work,  $^{57}\text{Fe}$  Mössbauer spectra were measured with a source of  $^{57}\text{Co}$  embedded in a rhodium metal matrix. Measurements were performed in the transmission mode, with the source at room temperature. The measured sample, in the form of a self-supported pellet, was mounted in an *in situ* oven working at controlled temperatures up to 700 °C under diluted  $\text{H}_2$  flow. The gas flow was maintained during cooling to 25 °C for recording of the spectrum at RT. Low temperature spectra (-268 °C) were measured after transferring the sample pellet to a helium gas flow cryostat in an Ar-filled glove box ( $\text{O}_2$ ,  $\text{H}_2\text{O} < 1$  ppm), strictly avoiding any contact with ambient air. The spectrometer was operated with a triangular velocity waveform, and a gas-filled proportional counter was used for the detection of the gamma rays. Velocity calibration was performed with an  $\alpha$ -Fe foil. The isomer shift  $\delta$ , the electric quadrupole splitting  $\Delta$ , the magnetic hyperfine field  $B_{\text{HF}}$ , the linewidth at half maximum  $\Gamma$  and the relative absorption area of the different components were determined by fitting the spectra with the appropriate combinations of Lorentzian profiles.

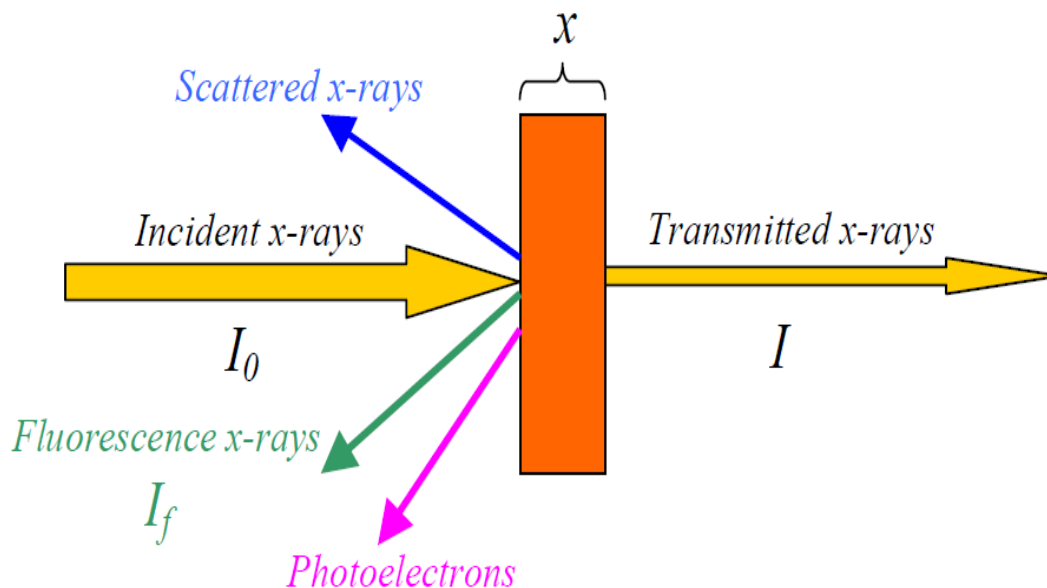


**Figure 2.6.** X-ray absorption spectroscopy in the transmission mode.

### II.3.3. X-ray absorption spectroscopy (XAS)

X-ray absorption spectroscopy (XAS) is used for determining the local geometric and/or electronic structure of matter. The experiment is performed at a synchrotron radiation facility, which provides intense X-ray beams of tunable energy. Like for MössS, the highly penetrating hard X-rays allows using XAS for *in situ* measurements in reactors.

In the transmission mode, a narrow monochromatic X-ray beam of intensity  $I_0$  passing through a sample of thickness  $x$  gets a reduced intensity  $I$  according to the Beer-Lambert expression (2.9):

$$\ln (I_0/I) = \mu x \quad (2.9)$$

where  $\mu$  is the linear absorption coefficient, which depends on the types of atoms and the density  $\rho$  of the material (Figure 2.6). At certain energies, the absorption increases drastically, and gives rise to an absorption edge. Each edge occurs when the energy  $E_0$  of the incident X-ray photon is just sufficient to cause the excitation of a core electron of the absorbing atom to a continuum

state, and to produce a photoelectron. Thus, the energy of the absorbed radiation at an edge corresponds to a binding energy of electrons in the K, L, M, etc., shells, which is specific of the absorbing element. An increase/decrease of the oxidation state shifts the position of the edge to higher/lower energies, respectively. Spectra of metal ions present an intense absorption past the edge called a white line, which is absent from the spectra of the same elements in the metallic state.

An X-ray absorption spectrum is divided into 3 sections: 1) pre-edge ( $E < E_0$ ); 2) X-ray absorption near edge structure (XANES), where the energy of the incident X-ray beam is  $E = E_0 \pm 50$  eV; 3) extended X-ray absorption fine structure (EXAFS), which starts approximately from 50 eV and continues up to 1000 eV above the edge. The oscillations in the EXAFS region are caused by the interaction between the emitted photoelectron and the atoms neighbouring the emitting atom. The Fourier transform of these oscillations yields peaks that are function of the interatomic distance between the emitter atom and its neighbours. A fitting both of the oscillations and of the Fourier transform, based on calculated phase and amplitude functions for a proper emitter-neighbour pair, provides information on the number of neighbouring atoms  $N$  and on their distance  $R$ . The Debye-Waller factor  $\sigma^2$  is associated to the thermal or structural disorder around the emitter atom: an increase of  $\sigma^2$  leads to a decrease of the intensity of the EXAFS oscillations and of the peaks in the Fourier transform.

For this study, time-resolved XAS data were measured in the transmission mode at the ROCK beamline [12] using the SOLEIL home-made Quick-EXAFS monochromator equipped with a Si (111) channel-cut crystal and described in ref. [13]. The channel-cut oscillates with a  $\pm 1.95^\circ$  amplitude around  $14.6^\circ$  and with a frequency of 2 Hz, allowing simultaneous recording of the Fe (7112 eV) and Ni (8333 eV) K-edge spectra in 250 ms. Successive spectra collected with upward Bragg angles during the *in situ* monitoring of catalysts were merged to improve the signal-to-noise ratio, leading to a time resolution of 5 s per spectrum effectively analyzed. Ionization chambers provided by Ohyo Koken Kogyo Co. Ltd. filled with a 2:1 mixture of  $N_2$  and He were used for measurements. The beam size was 2.5 x 0.5 mm. Normalization of spectra was performed by using the Python `normal_gui` graphical interface developed at SOLEIL for

the fast handling of Quick-XAS data. The EXAFS signal extraction and Fourier transformation of the EXAFS spectra were done using the Athena graphical interface software [14]. EXAFS fitting of distances, coordination numbers and Debye–Waller factors was performed with the Artemis interface to IFeFFIT using least-squares refinements [15], firstly checked on NiO, Ni metallic foil and Fe<sub>2</sub>O<sub>3</sub> references. Fourier-transformed EXAFS signals are presented without phase correction.

Temperature-programmed reductions were performed using a dedicated cell [16] connected to the gas-feeding system installed on the ROCK beamline. The cavity of the sample holder (2 mm thick) was filled with the powder catalyst (20 mg) pre-mixed with boron nitride (BN, 10 mg). The *in situ* catalyst reduction was performed by heating the cell from RT to 500 °C under a H<sub>2</sub> (5%)/He flow (50 mL min<sup>-1</sup>) with a heating rate of 5 °C min<sup>-1</sup>, followed by 2 h of isothermal treatment.

#### II.3.4. Chemometric analysis of X-ray absorption spectra

The proportions of the different Fe and Ni species during the successive stages of reduction at the Ni and Fe K edges were determined by a chemometric procedure, the Multivariate Curve Resolution by Alternative-Least Squares (MCR-ALS) methodology [17-19]. MCR-ALS GUI 2.0 developed by the Tauler group [20], and freely available as a Matlab toolbox, was used for MCR-ALS minimization.

In this methodology, XAS spectra are considered to originate from a linear combination of individual spectral components weighted by their abundance at any given temperature. Unlike the more classical linear combination procedure involving reference compounds, no hypothesis on the individual components is initially required in the MCR-ALS procedure. The series of normalized experimental spectra *D* is defined as a matrix resulting from the combination of three matrices: *C* (concentration of the pure components); *S* (normalized XAS spectral of pure components); and *E* (experimental uncertainties), following the matricial equation:

$$D = C S^T + E \text{ (where } S^T \text{ is the transposed matrix of } S) \quad (2.10)$$



The principle of the MCR-ALS analysis is to identify a likely set of concentrations  $C$  (varying along the series) and spectra  $S$  (constant along the series) which can explain the whole set of  $D$ , by iteration and least-squares minimization of the  $E$  matrix. The rank of the matrix (the number of components) is initially determined by Principal Component Analysis. The matrix of concentrations  $C$  contains only positive values and the matrix  $S$  contains only normalized spectral components with a positive absorbance.

XAS spectral components  $S$  are thus extracted by a purely mathematical method, without any initial hypothesis on the nature of the associated compounds. MCR-ALS components can only be validated after checking their chemical meaningfulness by comparison with spectra of compounds already identified in the mixture (as is the case here for nickel), or with plausible models in accordance with the chemistry of the system. The recognized limits of the MCR-ALS method with respect to XAS analysis lie in:

(i) the fact that two spectral components can correspond to the initial and final states of the same chemical species undergoing progressive ordering or disordering with changes of temperature (resulting in changes of the Debye-Waller factor);

(ii) on the opposite, the possible concomitant evolution of two distinct chemical species that appear as merged in a single spectral component.

The EXAFS analysis of components existing at higher temperatures is also challenged by the damping of the oscillations due to an increased Debye-Waller factor.

In Chapter III, a Principal Component Analysis by Singular Value Decomposition (PCA-SVD) was used to estimate the number of chemically relevant components involved in the reduction process at the Fe K edge. A plot of the eigenvalues sorted as a function of components, also named Scree plot, was used for such an estimation, as shown in Figure 2.7. As the components are sorted in order of decreasing contribution to the total variance, the separation between the linearly aligned eigenvalues of the first Principal Components, which are the most important ones, and those belonging to the asymptotic trend are used for the determination of the number of components to consider for the MCR-ALS analysis.

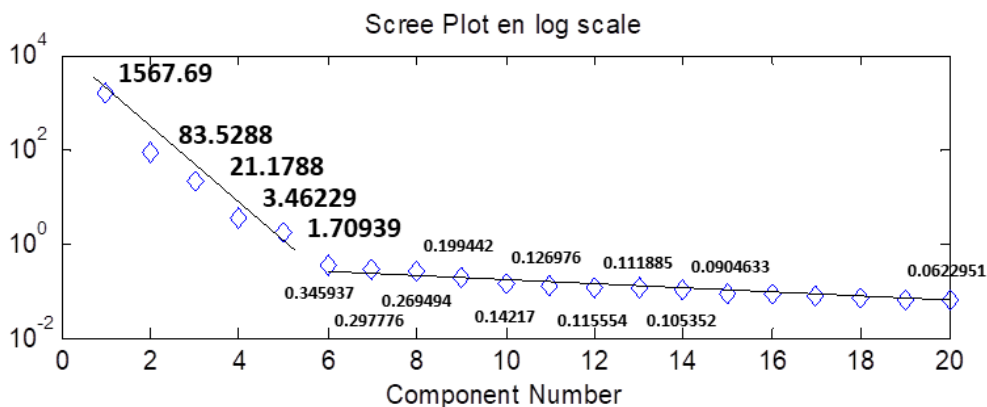


**Figure 2.7.** Scree plot of the eigenvalues sorted as a function of component number.

The Scree plot above displays a break of slope after the 5<sup>th</sup> component, indicating that the important components to retain for explaining most of the variance of the system are the first 5 components, which is a high number that could be questioned. Their meaningfulness was interpreted in accordance with the evolution of the position in energy of the Fe edge, with the simultaneous evolutions observed at the Ni K edge, and through the similarity or shifts of the oscillations and peaks on the Fourier transforms.

## II.4. Catalytic tests

### II.4.1. Materials

The substrate used in the catalytic test was furfural (FF, purity >99%). The solvents used for the reaction was isopropanol. Furfuryl alcohol (FFA, >99%), tetrahydrofurfuryl alcohol (THFFA, >99%), tetrahydrofuran (THF) (>99.9%), methyltetrahydrofuran (MTHF, >99%) and methylfuran (MF, >99%) were used for GC peaks identification and calibration. All the products presented here were purchased from Sigma Aldrich and used as such.

### II.4.2. Experimental set-up

#### II.4.2.1. SPR system presentation

The screening of the catalysts was done on the REALCAT platform in a Screening Pressure Reactor (SPR) system from Freeslate equipped with 24 parallel stainless-steel batch reactors of

6 mL each (Figure 2.8). The stirring in the reactor vessels is ensured by orbital shaking under controlled pressure and temperature conditions. The SPR system operates automatically at temperatures up to 400 °C and pressures up to 50 bar.

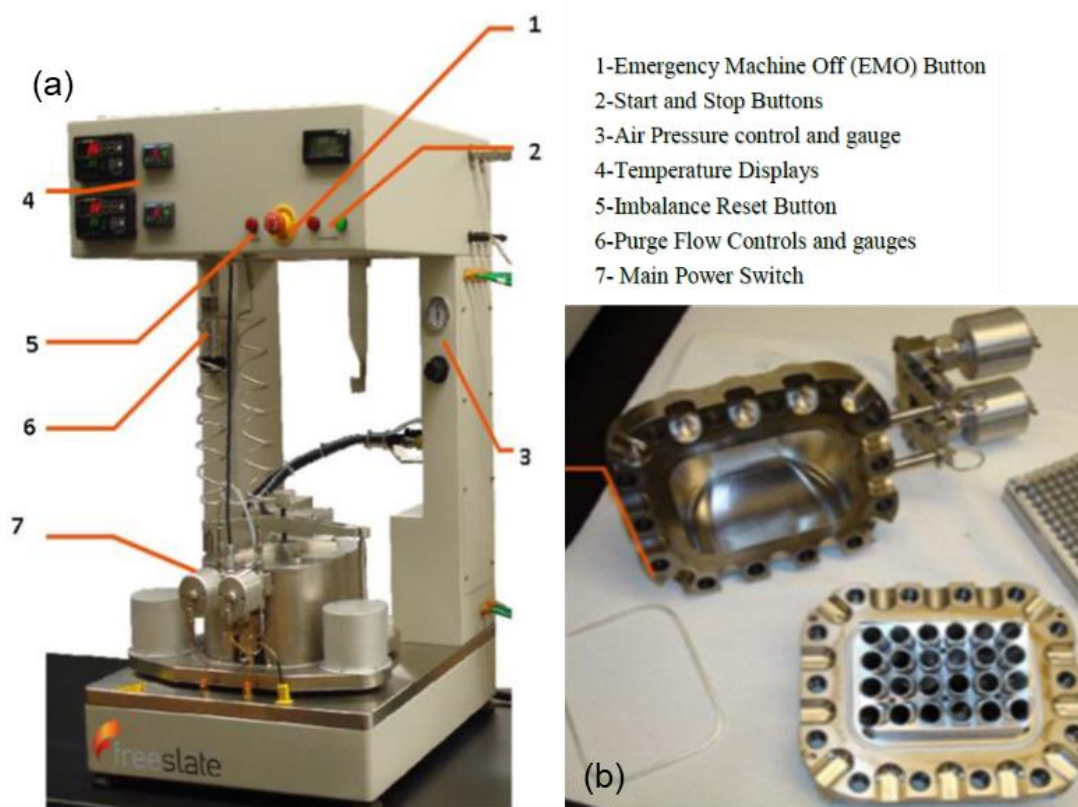


**Figure 2.8.** SPR description (a) and reactors (b).

The SPR is operated via a computer, equipped with Automation Studio and Library Studio softwares that provide a user interface, operational controls, process control and recording, and hardware to communicate with the SPR system. Automation Studio protocols were used to control the experiment, while Library Studio was used to collect and store experimental parameters.

#### II.4.2.2. Description of catalysts activation in H<sub>2</sub>

Due to their low resistance to spontaneous re-oxidation in contact with atmospheric air after reduction, the catalysts were systematically re-reduced under pure hydrogen directly in the SPR prior to the catalytic test.

Firstly, the desired amounts of catalysts were weighed directly into each reactor. Then, the reactor vessel was hermetically sealed and flushed by a gas flow according to the following protocol. The reactors were flushed with N<sub>2</sub> (200 mL/min) at room temperature to remove all the oxygen present. Then, a flow of pure hydrogen (200 mL/min) was flushed for 5 min, prior to gradually increasing the temperature up to 400 °C with a temperature ramp rate of 5 °C/min. This temperature was kept constant for 2 h under hydrogen flow. The reactors were then cooled to 30 °C and flushed with pure N<sub>2</sub> in order to remove the excess of hydrogen. The reactor vessel was hermetically sealed and then transferred to a glove box to be charged with the reagents and solvent without any contact with air. Finally, the hermetically sealed reactor vessel was removed from the glove box and connected to the SPR unit for the catalytic tests.

#### II.4.2.3. Description of the experimental protocol

The inlet and outlet valves of the reactor vessel were opened after connection to the SPR unit. The reactors were flushed with N<sub>2</sub> (200 mL/min) at room temperature for 5 min. Then, a flow of pure hydrogen (200 mL/min) was introduced for 20 min and the pressure was set at 20 bar. The reactors were sealed and the heating was started up to the reaction temperature (150 °C), with a temperature ramp rate of 5 °C/min. When the desired temperature was reached, shaking was turned on (600 rpm). At the end of the reaction, the temperature of the vessel was decreased. When the temperature reached 40 °C, the valves of the reactor vessel were opened and the reactor was flushed with a N<sub>2</sub> gas flow to remove all the gases from the reactor.

**Table 2.1.** GC analytical method parameters.

Injection		
	Injection mode	Split ratio 400
	Temperature	250 °C
	Carrier gas	H <sub>2</sub>
	Pressure	55.5 kPa
	Total flow	609.6 mL/min
	Column flow	1.51 mL/min
Column oven		
	Initial temperature, T <sub>0</sub>	26 °C (4 min)
	Rate-T <sub>1</sub>	25 °C/min-170 °C
	Rate-T <sub>2</sub>	50 °C/min-240 °C (2 min)
	Equilibration time	0.5 min
	Total program time	13.16 min
	Final temperature	240 °C
Detector	FID	
	Temperature	250 °C
	H <sub>2</sub> flow	40 mL/min
	Air flow	400 mL/min

#### II.4.3. Analytical methods

In order to analyze the products obtained after the furfural hydrogenation reaction, Shimadzu GC-2010 Plus and GC-FID-MS-QP2010 Ultra EI gas chromatographs, equipped with a FID detector, a ZB-5MS column (30 m × 0.25 mm × 0.25 μm) and for the latter, with a QP2010 Ultra mass spectrometer, were used. Solutions after reaction were filtered to eliminate the solid, and without further dilution for filtered solutions. It was verified by quantifying acetone that in these experimental conditions, hydrogen transfer from isopropanol to furfural did not occur to a significant extent (less than 3% of converted furfural). The details of the analytical method are presented in Table 2.1.

Furfural (FF), furfuryl alcohol (FFA), tetrahydrofurfuryl alcohol (THFFA), tetrahydrofuran (THF), methyltetrahydrofuran (MTHF) and methylfuran (MF) were used for GC calibration. Each stock solution was prepared with a given amount of compound in 1 mL isopropanol (FF: 1.1 mmol; FFA: 0.6 mmol; THFFA: 0.6 mmol; THF: 0.6 mmol; MTHF: 0.6 mmol). Then, the stock solutions were diluted in isopropanol at 75, 50, 25 10 and 1%

respectively. All the calibration curves have a linear correlation  $> 99.9\%$ .

The conversion of FF, the selectivity and yield in all products were determined by equations (2.11) and (2.12) listed below, respectively. The carbon balance was also determined using (2.12).

$$FF \text{ conversion } (\%) = \frac{n_{FF \text{ initial}} - n_{FF \text{ remaining}}}{n_{FF \text{ initial}}} \times 100 \quad (2.11)$$

$$Selectivity (\%) = \frac{n_i}{n_{FF \text{ initial}} - n_{FF \text{ remaining}}} \times 100 \quad (2.12)$$

$$Carbon \text{ balance } (\%) = \frac{\sum n_i + n_{FF \text{ remaining}}}{n_{FF \text{ initial}}} \times 100 \quad (2.13)$$

where  $n_i$  corresponds to the amount of each product detected: furfuryl alcohol (FFA), tetrahydrofurfuryl alcohol (THFFA), tetrahydrofuran (THF), methyltetrahydrofuran (MTHF), methylfuran (MF), as well as two ethers whose formation and quantification are explained in Chapter V.

## References

- [1] <http://www.chemiasoft.com/chemd/node/52>, accessed February 23, 2017.
- [2] A. Stefansson, I. Gunnarsson, N. Giroud, New methods for the direct determination of dissolved inorganic, organic and total carbon in natural waters by reagent-free ion chromatography and inductively coupled plasma atomic emission spectrometry, *Analytica Chimica Acta*, 582 (2007) 69-74.
- [3] H. Fischer, <http://xrf-spectroscopy.com/>, accessed, February 23, 2017.
- [4] T. Yamashita, P. Hayes, Analysis of XPS spectra of Fe<sup>2+</sup> and Fe<sup>3+</sup> ions in oxide materials, *Applied Surface Science*, 254 (2008) 2441-2449.
- [5] S. Brunauer, P. H. Emmett, E. Teller, Adsorption of gases in multimolecular layers, *Journal of the American Chemical Society*, 60 (1938) 309-319.
- [6] D. B. Williams, C. Barry Carter, *Transmission Electron Microscopy*, Springer-Verlag US, (2009).
- [7] P. Hartel, H. Rose, C. Dinges, Conditions and reasons for incoherent imaging in STEM, *Ultramicroscopy*, 63 (1996) 93-114.
- [8] R. F. Egerton, *Electron Energy-Loss spectroscopy in the Electron Microscope*, Springer US, (2011).
- [9] <https://hyperspy.org/>, Multi-dimensional data analysis.
- [10] J. Zhu, H. Li, L. Zhong, P. Xiao, X. Xu, X. Yang, Z. Zhao, J. Li, Perovskite oxides: preparation, characterizations, and applications in heterogeneous catalysis, *ACS Catalysis*, 4 (2014) 2917-2940.
- [11] [https://www.rsc.org/membership/networking/interestgroups/mossbauerspect/introp\\_art1.asp](https://www.rsc.org/membership/networking/interestgroups/mossbauerspect/introp_art1.asp), Introduction to mössbauer spectroscopy.
- [12] V. Briois, C. La Fontaine, S. Belin, L. Barthe, T. Moreno, V. Pinty, A. Carcy, R. Girardot, E. Fonda, Rock: the new Quick-EXAFS beamline at SOLEIL, *Journal of Physics: Conference Series*, 712 (2016) 012149.
- [13] E. Fonda, A. Rochet, M. Ribbens, L. Barthe, S. Belin, V. Briois, The SAMBA quick-EXAFS monochromator: XAS with edge jumping, *Journal of Synchrotron Radiation*, 19 (2012)

417-424.

- [14] B. Ravel, M. Newville, Athena, artemis, hephaestus: data analysis for X-ray absorption spectroscopy using IFEFFIT, *Journal of Synchrotron Radiation*, 12 (2005) 537-541.
- [15] M. Newville, IFEFFIT: interactive XAFS analysis and FEFF fitting, *Journal of Synchrotron Radiation*, 8 (2001) 322-324.
- [16] C. La Fontaine, L. Barthe, A. Rochet, V. Briois, X-ray absorption spectroscopy and heterogeneous catalysis: Performances at the SOLEIL's SAMBA beamline, *Catalysis Today*, 205 (2013) 148-158.
- [17] W. H. Cassinelli, L. Martins, A. R. Passos, S. H. Pulcinelli, C. V. Santilli, A. Rochet, V. Briois, Multivariate curve resolution analysis applied to time-resolved synchrotron X-ray Absorption Spectroscopy monitoring of the activation of copper alumina catalyst, *Catalysis Today*, 229 (2014) 114-122.
- [18] J. Hong, E. Marceau, A.Y. Khodakov, L. Gaberová, A. Griboval-Constant, J.-S. Girardon, C.L. Fontaine, V. Briois, Speciation of ruthenium as a reduction promoter of Silica-Supported Co catalysts: a time-resolved in situ XAS investigation, *ACS Catalysis*, 5 (2015) 1273-1282.
- [19] A. Rochet, B. Baubet, V. Moizan, C. Pichon, V. Briois, Co-K and Mo-K edges Quick-XAS study of the sulphidation properties of Mo/Al<sub>2</sub>O<sub>3</sub> and CoMo/Al<sub>2</sub>O<sub>3</sub> catalysts, *Comptes Rendus Chimie*, 19 (2016) 1337-1351.
- [20] J. Jaumot, A. de Juan, R. Tauler, MCR-ALS GUI 2.0: New features and applications, *Chemometrics and Intelligent Laboratory Systems*, 140 (2015) 1-12.





# Chapter III

Study of the deposition-  
precipitation and reduction  
processes for Fe-Ni/SiO<sub>2</sub>  
catalysts



*This chapter is partly based on a published article: Bimetallic Fe-Ni/SiO<sub>2</sub> catalysts for furfural hydrogenation: Identification of the interplay between Fe and Ni during deposition-precipitation and thermal treatments – D. Shi et al. – Catal. Today, 334, 162-172 (2019).*

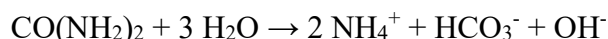
### III.1. Introduction

As we have seen in Chapter I, supported Fe-Ni catalysts have been reported for their activity and selectivity in the hydrogenation of unsaturated organic molecules. However, the control of the size and composition of the bimetallic nanoparticles remains a bottleneck when oxide-supported catalysts are prepared by impregnation, and alternative procedures should be investigated. In this chapter, the deposition-precipitation method has been chosen to synthesize SiO<sub>2</sub>-supported Fe-Ni bimetallic catalysts. The deposition-precipitation method has been thoroughly investigated as a method to prepare well-dispersed monometallic Ni nanoparticles on silica, even at metal loadings as high as 40 wt% [1-4]. Its extension to Fe-based bimetallic nanoparticles raises the question of the association between the two metals upon deposition and thermal treatments. After a selection of proper experimental parameters, the phases formed by deposition-precipitation will be investigated by X-ray diffraction (XRD), Mössbauer spectroscopy (MössS), infrared spectroscopy and X-ray absorption spectroscopy (XAS). Moreover, in order to evidence the interplay between the two metals during the formation of the Fe-Ni particles, the reduction of the samples will be investigated by temperature-programmed reduction (TPR) and *in situ* X-ray absorption spectroscopy.

## III.2. Choice of the experimental parameters for deposition-precipitation and drying

### III.2.1. Choice of the reactants and strategy

The method of deposition-precipitation with urea (DPU) is a preparation method involving the hydrolysis of urea at a temperature of 80 °C or above, to homogeneously generate hydroxide ions within the solution and increase its pH:



The DPU solution containing the metal ions is initially made acidic by the presence of a strong acid. The increase of pH leads to the deposition of the metals over the support, here silica. According to the literature and to the solubility products of iron and nickel hydroxides (pKs  $\text{Fe}(\text{OH})_3 = 38.8$ ;  $\text{Fe}(\text{OH})_2 = 15.1$ ;  $\text{Ni}(\text{OH})_2 = 15.2$  at 25 °C) [5], iron(III) hydroxide should start depositing from a dilute solution at a pH of around 2, whereas nickel(II) hydroxide and iron(II) hydroxide should deposit at a pH of around 6. We will thus have to use iron(II) salts instead of iron(III) nitrate  $\text{Fe}(\text{NO}_3)_3 \cdot 9\text{H}_2\text{O}$  in order to deposit iron and nickel in the same range of pH, and hence avoid the separate precipitation of iron(III) hydroxide. Iron(II) sulfate  $\text{FeSO}_4 \cdot 7\text{H}_2\text{O}$  has been chosen because it is a commercial salt.

In spite of this choice, initial attempts of DPU with nickel nitrate  $\text{Ni}(\text{NO}_3)_2 \cdot 6\text{H}_2\text{O}$  as precursor salt and nitric acid as initial acidifier led to the oxidation of Fe(II) to Fe(III) by nitrate ions upon heating, as evidenced by the change of colour of the suspension from green to orange, and to the separate precipitation of well-crystallized goethite  $\text{Fe}^{\text{III}}\text{O}(\text{OH})$ , from which it was verified that large particles of metallic *bcc* Fe would later grow upon reduction. In order to eliminate oxidizing species, nickel(II) sulfate  $\text{NiSO}_4 \cdot 6\text{H}_2\text{O}$  and sulphuric acid were instead used as reactants, but the preparation still suffered from a lack of reproducibility. Diffraction peaks of Fe(III)-containing layered hydroxysulfate phases, named hydrohonnessite [6-8], were observed after drying ( $2\theta = 8.17, 16.39$  and  $24.69^\circ$ , corresponding to interplanar distances of 1.08, 0.54 and 0.36 nm) (Figure 3.1a), with ulterior formation of large Fe-Ni particles upon reduction (size: 19 nm, using the Scherrer equation) (Figure 3.1b).

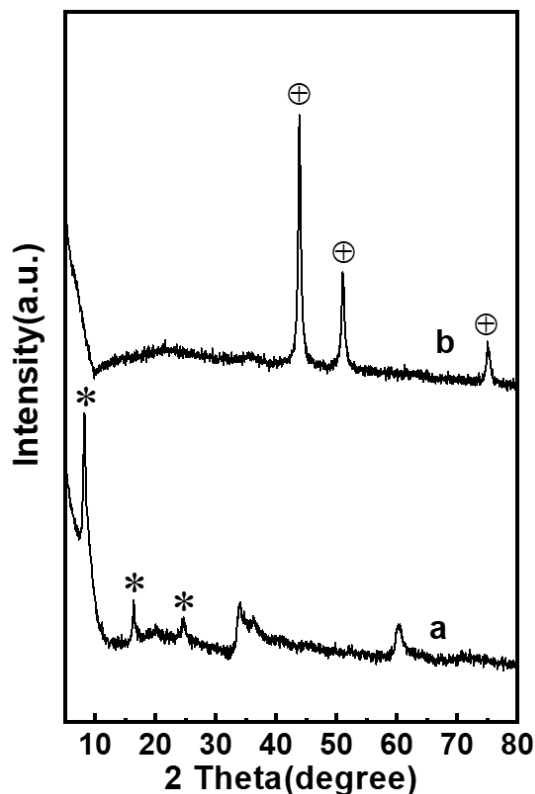


**Figure 3.1.** X-ray diffractograms of  $\text{Fe}_{50}\text{Ni}_{50}/\text{SiO}_2$  prepared without Ar degassing: a) recorded after drying, b) recorded after reduction at 700 °C. (\* hydrohonessite  $[\text{Ni}^{2+}_{8-x} \text{Fe}^{3+}_x (\text{OH})_{16+x}][\text{SO}_4^{2-} \cdot 7\text{H}_2\text{O} \cdot \text{NiSO}_4]$ ; + fcc Fe-Ni alloy).

In order to eliminate oxygen from the gas phase and from the solution, it was then chosen to degas with Ar the suspension containing silica, sulphuric acid, nickel(II) sulfate and urea for 2 h, and to introduce Fe(II) sulfate only after degassing. Ar bubbling was maintained during the whole heating and cooling steps. In these conditions, a plateau corresponding to the deposition of iron and nickel was attained at pH 5.3, which is consistent with the expected pH value, and the suspension remained green. Centrifugation and washing were also carried out with degassed water.

### III.2.2. Description of the preparation procedure

$\text{Fe}_x\text{Ni}_{(100-x)}/\text{SiO}_2$  catalysts (in which  $x$  and  $(100-x)$  represent the relative atomic proportions of the two metals *in the DPU solution*) were thus prepared using a modified procedure originally developed for Ni/SiO<sub>2</sub> catalysts and based on nickel nitrate [1-4].

**Table 3.1.** Mass and volume of reactants used for the preparation of Fe-Ni/SiO<sub>2</sub> catalysts.

Samples <sup>a</sup>	Mass of SiO <sub>2</sub> (g)	Mass of FeSO <sub>4</sub> •7H <sub>2</sub> O (g)	Mass of NiSO <sub>4</sub> •6H <sub>2</sub> O (g)	Mass of urea (g)	Volume of H <sub>2</sub> SO <sub>4</sub> (mL)	Volume of water (mL)
Fe <sub>100</sub> /SiO <sub>2</sub>	1.14	11.7	-	7.56	0.16	150
Fe <sub>75</sub> Ni <sub>25</sub> /SiO <sub>2</sub>	1.14	8.8	2.8	7.56	0.16	150
Fe <sub>60</sub> Ni <sub>40</sub> /SiO <sub>2</sub>	1.14	7.0	4.4	7.56	0.16	150
Fe <sub>50</sub> Ni <sub>50</sub> /SiO <sub>2</sub>	1.14	5.8	5.5	7.56	0.16	150
Fe <sub>40</sub> Ni <sub>60</sub> /SiO <sub>2</sub>	1.14	4.7	6.6	7.56	0.16	150
Fe <sub>25</sub> Ni <sub>75</sub> /SiO <sub>2</sub>	1.14	2.9	8.3	7.56	0.16	150
Fe <sub>10</sub> Ni <sub>90</sub> /SiO <sub>2</sub>	1.14	1.2	9.9	7.56	0.16	150
Ni <sub>100</sub> /SiO <sub>2</sub>	1.14	-	11.0	7.56	0.16	150

a: The two figures represent the relative atomic proportions of the two metals *in the DPU solution*

Sipernat-50 silica (Degussa; surface area, 400 m<sup>2</sup> g<sup>-1</sup>, pore volume, 1.4 cm<sup>3</sup> g<sup>-1</sup>) was used as a support. As stated in the former section, the reactants were iron(II) sulfate heptahydrate (Alfa Aesar, purity: 98%), nickel(II) sulfate hexahydrate (Aldrich, 99%), sulphuric acid (Alfa Aesar, 93-98%) and urea (Alfa Aesar, 99-100%). All reactants were used without further purification.

For the preparation of a Fe<sub>50</sub>Ni<sub>50</sub>/SiO<sub>2</sub> catalyst (here chosen as an example), 150 mL of aqueous solution of 0.84 mol L<sup>-1</sup> urea, 0.01 mol L<sup>-1</sup> H<sub>2</sub>SO<sub>4</sub>, 0.14 mol L<sup>-1</sup> Ni(II) sulfate and 0.14 mol L<sup>-1</sup> Fe(II) sulfate, were mixed with 1.14 g of silica in a three-necked flask allowing Ar bubbling, with the reactants introduced in the order described in the former section. The suspension was continuously stirred and slowly heated to 80 °C, resulting in the decomposition of urea, increase of the pH to 5.3, and deposition-precipitation of metallic compounds onto the silica support. The suspension was kept at 80 °C for 22 h. After cooling to room temperature (RT), the solid was recovered by centrifugation, washed three times with degassed distilled water and dried. Catalysts exhibiting other Fe/Ni proportions were prepared with the appropriate concentrations of Fe(II) sulfate and Ni(II) sulfate using the same procedure as above. Detailed information is listed in Table 3.1. Monometallic Fe<sub>100</sub>/SiO<sub>2</sub> and Ni<sub>100</sub>/SiO<sub>2</sub> catalysts were prepared as references following the same procedure (Ni(II) concentration in solution: 0.28 mol L<sup>-1</sup>).

A reference Co-Ni/SiO<sub>2</sub> system was finally prepared from a solution of Ni(II) nitrate hexahydrate and Co(II) nitrate hexahydrate (Sigma Aldrich, 98%), both 0.14 mol L<sup>-1</sup>, following

the same procedure, as a reference system to support a discussion on metal contents (section III.3.2.).

### III.2.3. Influence of drying on the solids prepared by DPU

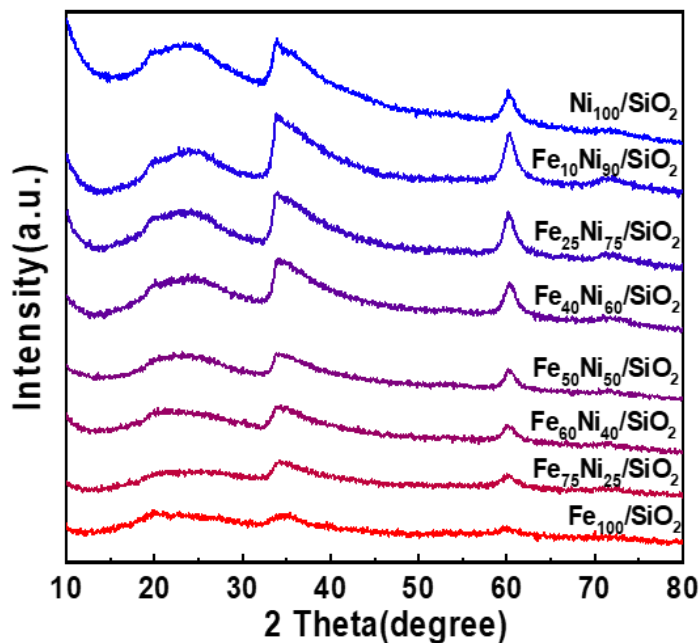
Drying at RT in static ambient air caused a rapid change of colour of the solid, from green to ochre, evidencing the oxidation of Fe(II) to Fe(III) by oxygen from air. The literature shows that such oxidation is prone to happen to Fe(II)-containing layered hydroxides [9-11], but that the presence of Ni(II) ions inhibits their further transformation to Fe<sub>3</sub>O<sub>4</sub> [12, 13]. Drying the solid under Ar flow in the three-necked flask, and storage under Ar, preserved the green colour longer, but oxidation of iron to Fe(III) was nevertheless seen to develop over a period of six weeks. Using XRD and XAS, it was checked that Fe oxidation upon drying and storage had no influence on the structure of the solid formed by DPU, and, by reducing dried solids either kept under Ar or aged in air, it was also verified that, unlike Fe oxidation during DPU, oxidation during storage had no detrimental effect on the formation, nature and size of the reduced Fe-Ni nanoparticles.

## III.3. Characterization of Fe-Ni/SiO<sub>2</sub> samples after drying

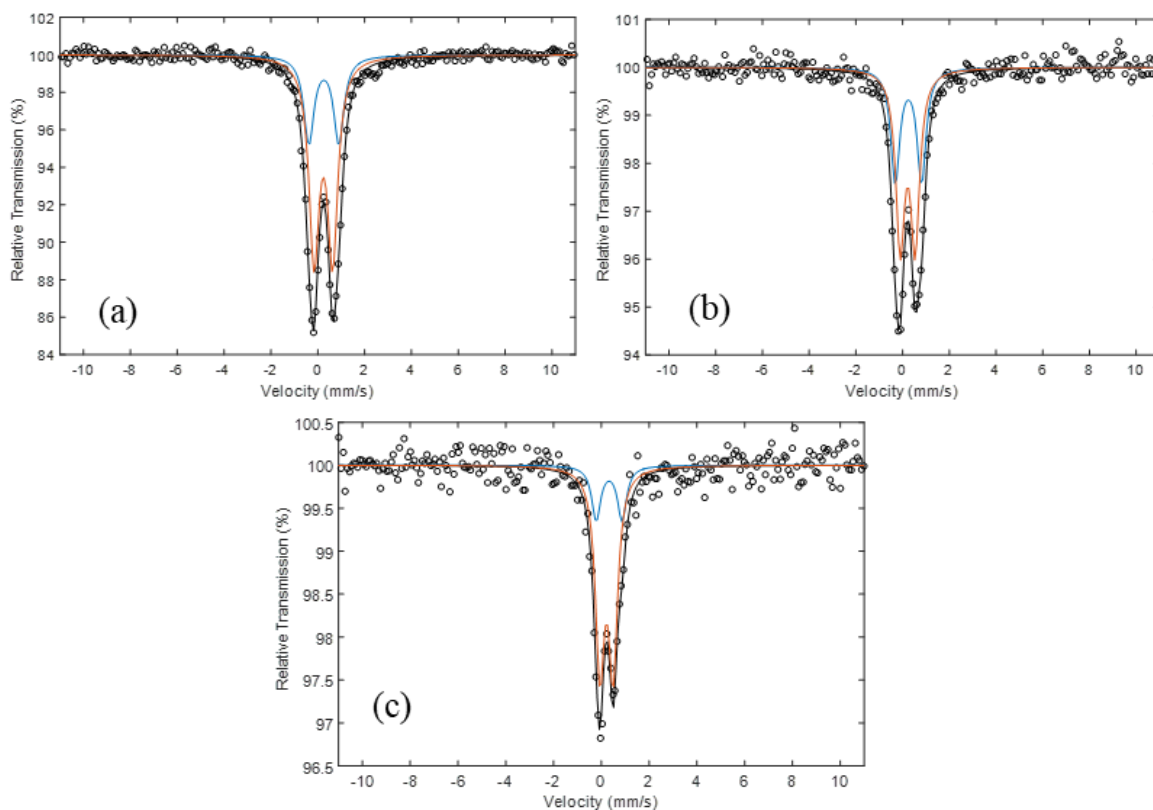
### III.3.1. Speciation of the metal ions

Figure 3.2 shows the XRD patterns of the series of Fe-Ni/SiO<sub>2</sub> samples prepared by DPU, after drying at RT. The XRD patterns exhibit a broad diffraction peak at about 22°, characteristic of amorphous siliceous solids, and a broad asymmetrical line at  $2\theta = 34^\circ$  and a narrow symmetrical one at  $2\theta = 60^\circ$ . As shown in the literature for Ni/SiO<sub>2</sub> catalysts prepared by DPU [1], the latter two peaks can be assigned to structures based on brucitic layers, either M<sup>II</sup>(OH)<sub>2</sub> turbostratic hydroxides or ill-crystallized phyllosilicates. Diffraction peaks for monometallic Fe<sub>100</sub>/SiO<sub>2</sub> were broad and of low intensity, but the peak positions were the same as for Ni-containing samples, suggesting that the same phase was formed.





**Figure 3.2.** XRD patterns of Fe<sub>100</sub>/SiO<sub>2</sub>, Fe<sub>75</sub>Ni<sub>25</sub>/SiO<sub>2</sub>, Fe<sub>60</sub>Ni<sub>40</sub>/SiO<sub>2</sub>, Fe<sub>50</sub>Ni<sub>50</sub>/SiO<sub>2</sub>, Fe<sub>40</sub>Ni<sub>60</sub>/SiO<sub>2</sub>, Fe<sub>25</sub>Ni<sub>75</sub>/SiO<sub>2</sub>, Fe<sub>10</sub>Ni<sub>90</sub>/SiO<sub>2</sub> and Ni<sub>100</sub>/SiO<sub>2</sub>, after drying at room temperature.



**Figure 3.3.** <sup>57</sup>Fe Mössbauer spectra recorded on Fe<sub>75</sub>Ni<sub>25</sub>/SiO<sub>2</sub> (a), Fe<sub>50</sub>Ni<sub>50</sub>/SiO<sub>2</sub> (b) and Fe<sub>25</sub>Ni<sub>75</sub>/SiO<sub>2</sub> (c) after drying (RT). Hyperfine parameters for the fits are listed in Table 3.2.

**Table 3.2.**  $^{57}\text{Fe}$  Mössbauer hyperfine parameters for samples  $\text{Fe}_{75}\text{Ni}_{25}/\text{SiO}_2$ ,  $\text{Fe}_{50}\text{Ni}_{50}/\text{SiO}_2$  and  $\text{Fe}_{25}\text{Ni}_{75}/\text{SiO}_2$  after drying. Spectra were recorded at room temperature (RT, 25 °C).

Sample	Site	$\delta$ (mm.s <sup>-1</sup> )	$\Delta$ (mm.s <sup>-1</sup> )	$\Gamma$ (mm.s <sup>-1</sup> )	Area (%)
$\text{Fe}_{75}\text{Ni}_{25}/\text{SiO}_2$	Fe(III) Oh	0.35(1)	0.78(2)	0.48(1)	67(3)
	Fe(III) Oh	0.37(1)	1.25(3)	0.48(1)	33(3)
$\text{Fe}_{50}\text{Ni}_{50}/\text{SiO}_2$	Fe(III) Oh	0.33(1)	0.65(2)	0.44(2)	64(4)
	Fe(III) Oh	0.36(1)	1.15(3)	0.45(4)	22(5)
$\text{Fe}_{25}\text{Ni}_{75}/\text{SiO}_2$	Fe(III) Oh	0.33(4)	0.55(3)	0.45(4)	78(5)
	Fe(III) Oh	0.43(4)	1.08(8)	0.45(4)	22(5)

$\delta$ : isomer shift;  $\Delta$ : electric quadrupole splitting;  $\Gamma$ : line width at half maximum;  $B_{\text{HF}}$ : magnetic hyperfine field

The speciation of iron ions in this layered structure after drying and exposure to air has first been investigated by  $^{57}\text{Fe}$  Mössbauer spectroscopy (MössS) in three solids. In dried  $\text{Fe}_{75}\text{Ni}_{25}/\text{SiO}_2$ ,  $\text{Fe}_{50}\text{Ni}_{50}/\text{SiO}_2$  and  $\text{Fe}_{25}\text{Ni}_{75}/\text{SiO}_2$ , iron is exclusively present as octahedral Fe(III) ions, as shown by the presence of a quadrupole-split doublet signal centered around an isomer shift of 0.35 mm.s<sup>-1</sup> (Figure 3.3, Table 3.2). The signal recorded at RT is asymmetric and must be fitted with two different contributions, as is often done for ions present in a continuum of environments. Given the relatively narrow range of isomer shifts and quadrupole splittings for octahedral Fe(III), it is virtually impossible to distinguish between Fe(III) oxyhydroxides and silicates [14]. However, the absence of a sextet allows discarding the presence of well-crystallized goethite FeOOH, which is expected to exhibit magnetic order at room temperature [15, 16]. Moreover, the relatively low isomer shift of the narrow doublet, close to that measured for octahedrally coordinated iron in mixed metal Fe-Ni ferrites, suggests the formation of mixed-metal species [17]. The significant changes in the quadrupole splittings, when one compares the three samples that exhibit different metal proportions, as well as the slight decrease of the average isomer shift, suggest that Fe(III) ions are not present in an isolated phase but are co-deposited with Ni(II) ions. Finally, electric quadrupole splittings are noticeably larger here than in well-defined oxyhydroxides and silicates, especially that of the second doublet: this is usually interpreted as the sign of distortions in the chemical environment: distorted octahedra, surface sites, proximity to tetrahedral sites or to divalent cations, such as Ni<sup>2+</sup>, in hydroxides or silicates [12, 15, 18-20].

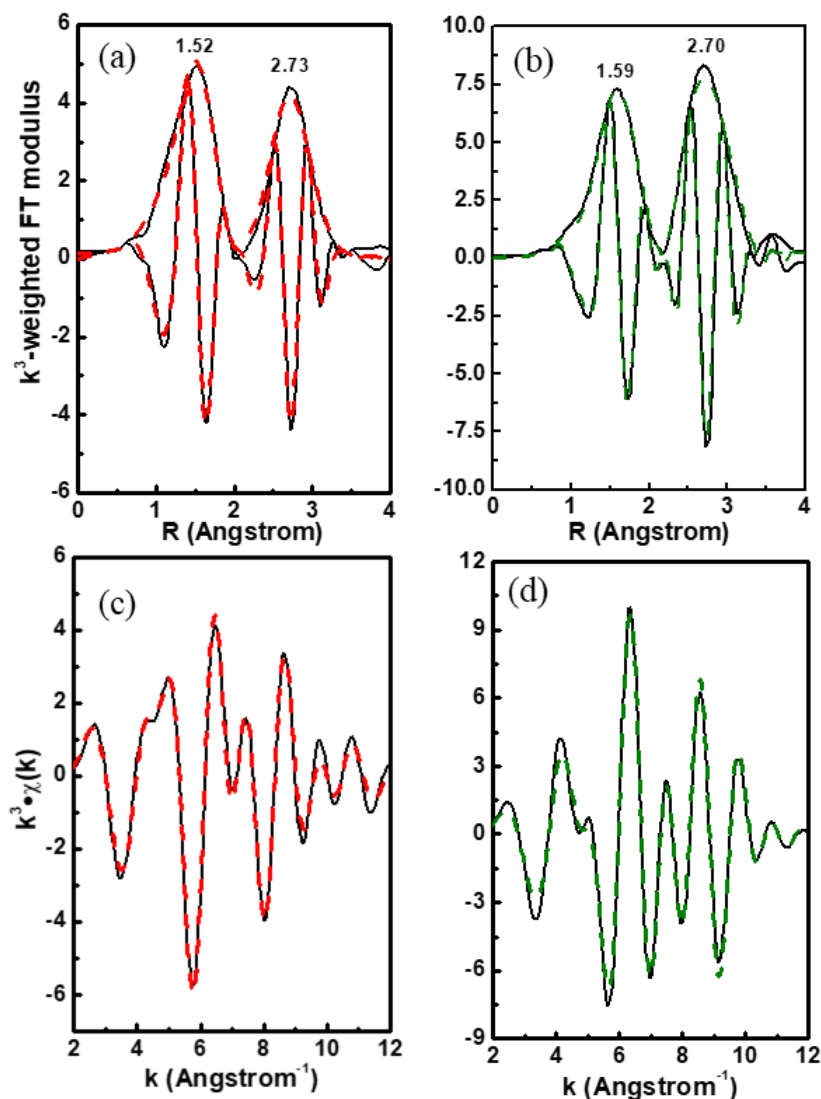


**Figure 3.4.** EXAFS  $k^3$ -weighted Fourier transform moduli and results of  $k^3 \chi(k)$  EXAFS fitting in R-space; EXAFS  $k^3$ -weighted oscillations and results of  $k^3 \chi(k)$  EXAFS fitting in k-space of: dried  $\text{Fe}_{50}\text{Ni}_{50}/\text{SiO}_2$ , a) and c) at the Fe K edge (black: experimental; red: fit), b and d) at the Ni K edge (black: experimental; green: fit). Interatomic distances R are listed in Table 3.3.

Analysis of the EXAFS oscillations recorded both at the Fe and Ni K edges on dried  $\text{Fe}_{50}\text{Ni}_{50}/\text{SiO}_2$  brings more information about the two metal ions. The local environment of both  $\text{Fe}^{3+}$  and  $\text{Ni}^{2+}$  ions is consistent with the octahedral sites of the structures of divalent hydroxides and phyllosilicates, both based on brucitic layers [1] (Figure 3.4, Table 3.3).

**Table 3.3.** Structural parameters determined from the EXAFS analysis of the spectra recorded at RT for the Fe<sub>50</sub>Ni<sub>50</sub>/SiO<sub>2</sub> catalyst after drying.

Sample	Absorbing atom	N, scattering atom	R (Å)	$\sigma^2 \cdot 10^{-3}$ (Å <sup>2</sup> )	R <sub>F</sub> (%)	$\chi^2\nu$
Fe <sub>50</sub> Ni <sub>50</sub> /SiO <sub>2</sub> DPU, dried	Ni	6 O *	2.05 (1)	5 (1)	2.3	1688
		6 Ni *	3.11 (1)	6 (1)		
Fe <sub>50</sub> Ni <sub>50</sub> /SiO <sub>2</sub> DPU, dried	Fe	6 O *	1.99 (1)	11 (1)	0.5	697
		6 Ni *	3.11 (1)	13 (1)		

N: Coordination number, \*: fixed number; R: Distance between absorbing atom and neighbours;  $\sigma$ : Debye-Waller factor; R<sub>F</sub>: reliability factor, which measures the relative misfit with respect to the data;  $\chi^2\nu$ : reduced chi-square, which takes into account the uncertainty level in the data, as well as the number of free parameters allowed to vary in the fit. Simulations were done over  $\Delta k$  range = 3.5-10.5 Å<sup>-1</sup>,  $\Delta R$  = 1-3.4 Å for catalyst before reduction and 1-2.7 Å for catalyst after reduction,  $S_0^2 = 0.75$ ,  $E_0 + \Delta E_0 = 7724 \pm 2$  eV at the Fe K edge, and  $8340 \pm 3$  eV at the Ni K edge.

The first shell is satisfactorily fitted using 6 oxygen atoms ( $R = 1.99$  Å for Fe<sup>3+</sup>,  $R = 2.05$  Å for Ni<sup>2+</sup>), probably in a more distorted symmetry in the case of Fe(III), as shown by the higher value of the Debye-Waller factor. The best fits for the second shell of neighbours involve 6 Ni (or Fe) atoms at  $R = 3.11$  Å, characteristic of edge-sharing octahedra (it must be noted that, due to the closeness of scattering phase and amplitude functions for Fe and Ni, the nature of the second neighbours as backscatterers cannot be unambiguously discriminated by EXAFS). The fit is not significantly improved if one adds Si atoms to the second shell of neighbours: at this stage it is thus impossible to distinguish between hydroxide or phyllosilicate phases. If existing, iron environments involving two very different Fe-Fe distances above 3 Å, as would be encountered in FeOOH phases [19, 21-22], are not predominant, which is in line with MössS results.

### III.3.2. Evolution and composition of the phases deposited during DPU: the Fe<sub>50</sub>Ni<sub>50</sub>/SiO<sub>2</sub> solid

In order to know more about the DPU process, the nature of the deposited phases and the metal proportions were investigated as a function of DPU duration, from 1 to 22 h, for the Fe<sub>50</sub>Ni<sub>50</sub>/SiO<sub>2</sub> system.

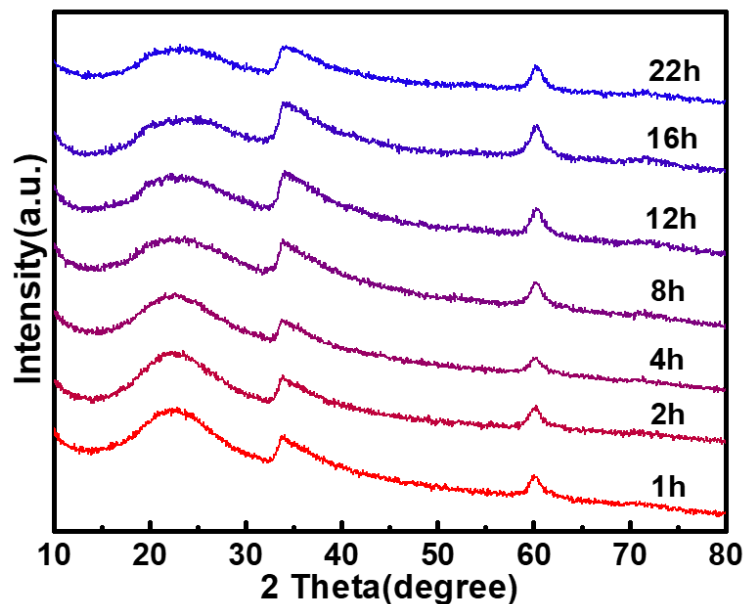


**Figure 3.5.** X-ray diffractograms recorded in ambient conditions on  $\text{Fe}_{50}\text{Ni}_{50}/\text{SiO}_2$  samples prepared with different durations of DPU.

While the X-ray diffractograms do not exhibit major changes besides the gradual broadening of the large halo associated to silica (Figure 3.5), the evolution of ATR-IR bands (Figure 3.6a) reveals that, following the pattern reported for monometallic  $\text{Ni}/\text{SiO}_2$  catalysts [1], brucitic  $\text{M}^{\text{II}}(\text{OH})_2$  phases were first formed during the first 4 h of DPU, then evolved into an ill-crystallized 1:1 phyllosilicate. The structure of a 1:1 phyllosilicate consists of a brucite-type sheet containing different proportion of Ni and Fe ions in octahedral coordination and a sheet containing linked tetrahedral  $\text{SiO}_4$  units, as shown in Figure 3.7. The assignment of the IR bands is based on:

- (1) the progressive growth of the asymmetrical doublet of bands at  $1007$  and  $1083\text{ cm}^{-1}$  ( $\nu(\text{Si-O})$  stretching vibration in a 1:1 phyllosilicate);
- (2) the decrease of the weak asymmetrical  $\nu(\text{Si-OH})$  band originating from silica at  $974\text{ cm}^{-1}$ ;
- (3) the shift and decrease of the intensity of the  $\nu(\text{Si-O})$  vibration band assigned to silica at *ca.*  $800\text{ cm}^{-1}$ ;
- (4) the decrease of the  $\delta(\text{OH})$  band at  $640\text{ cm}^{-1}$ , characteristic of turbostratic  $\text{M}^{\text{II}}(\text{OH})_2$ , between 2 and 4 h,

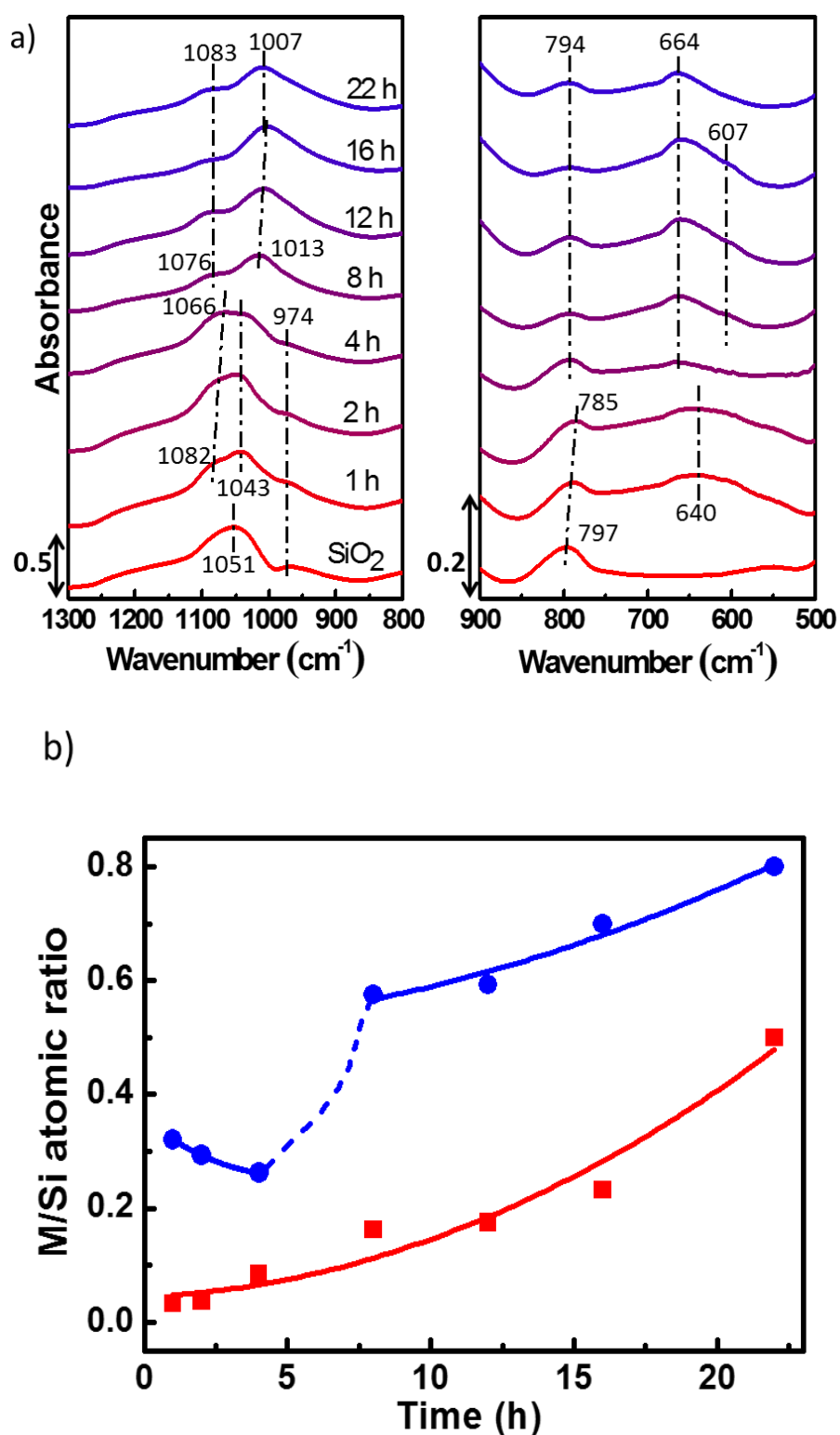


**Figure 3.6.** Evolution as a function of DPU duration: a) of the infrared bands of  $\text{Fe}_{50}\text{Ni}_{50}/\text{SiO}_2$  samples in the  $500\text{-}1300\text{ cm}^{-1}$  region (ATR mode); b) of the Fe/Si (red curve) and Ni/Si (blue curve) atomic ratios measured by ICP.

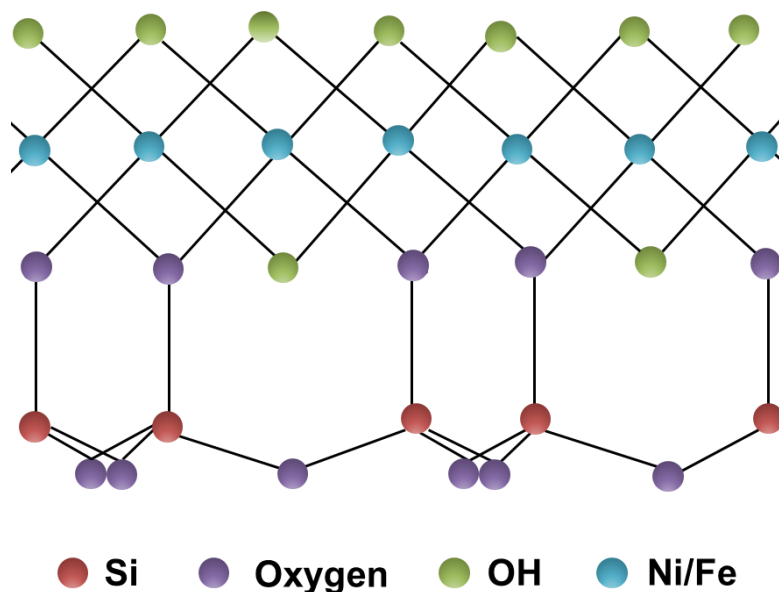


**Figure 3.7.** Projection on the *bc* plane of a layer of 1:1 phyllosilicate, based on ref. 6.

and, (5) from 4 h, the increase of a broad band at  $664\text{ cm}^{-1}$  assigned to a tetrahedral Si-O mode in the 1:1 phyllosilicate structure.

A poor crystallinity or degree of organization of the phyllosilicate phase may explain the absence of Si second-shell neighbours in the EXAFS fits.

ICP measurements indicate that, despite the equimolarity between Fe and Ni in solution, nickel is the main metal initially depositing onto silica as hydroxide during the first hours of DPU (Figure 3.6b). After a moderate drop between 1 and 4 h, the nickel content increases by a two-fold between 4 and 8 h, that is, when the phyllosilicate phase forms by reaction between the metal ions and siliceous species. In contrast, the Fe content steadily increases throughout the process. As a result, a significant excess of nickel with respect to iron is present after 22 h DPU in the dried solid, compared with the atomic proportions in solution: 38 Fe at% and 62 Ni at% are measured by ICP on the solid, corresponding to 42% of the amount of Fe and to 67% of the amount of Ni initially introduced in the DPU solution. The (Fe+Ni)/Si ratio of 1.3 is consistent with a 1:1 phyllosilicate stoichiometry, as the M/Si ratio varies between 1 and 1.5 for phyllosilicates exclusively containing trivalent ( $\text{Si}_2\text{M}^{\text{III}}\text{O}_5(\text{OH})_4$ ) and divalent ( $\text{Si}_2\text{M}^{\text{II}}\text{O}_5(\text{OH})_4$ ) cations, respectively. This result also indicates that shortening the DPU duration would result in an even larger difference of loading between the two metals.

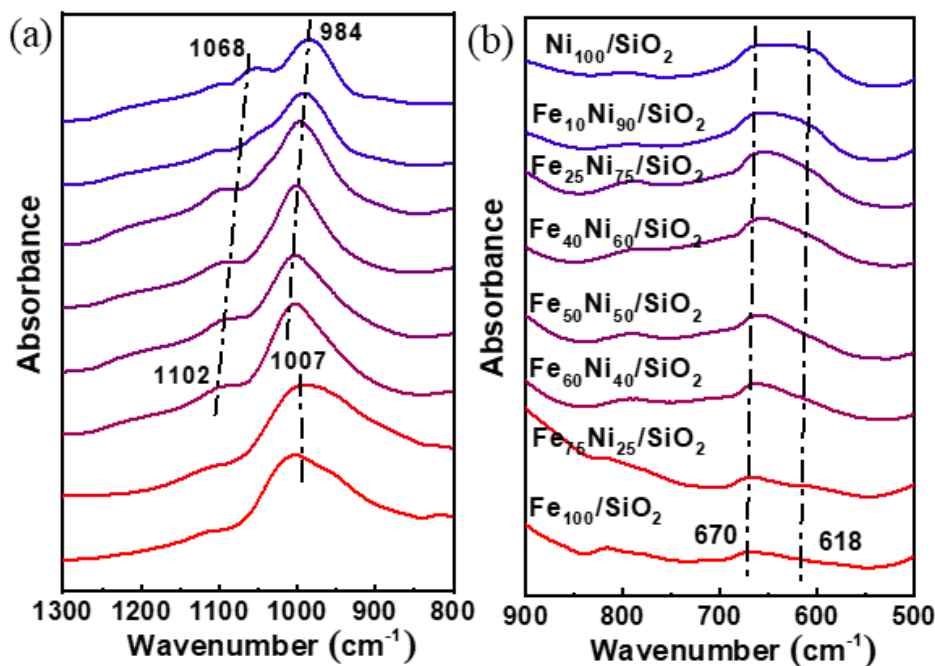


**Figure 3.8.** Infrared bands of Fe-Ni/SiO<sub>2</sub> samples in the 800-1300 cm<sup>-1</sup> region (ATR mode) (a) and in the 500-900 cm<sup>-1</sup> region (ATR mode) (b).

This excess of nickel does not originate from its early introduction in the DPU solution, as the excess was also observed when nickel and iron sulfates were added together in solution after Ar degassing. For the sake of comparison, a reference system was prepared from nickel and cobalt(II) nitrates (proportions in solution: 50 and 50 at%), without degassing and separate introduction of the reactants. The atomic proportions given by EDX measurements (34 Co at%, 66 Ni at%) prove that nickel tends to react with silica preferentially, compared with the other metal.

Finally, no IR band assigned to isocyanates or carbonates was observed in the spectra. A shoulder at 607 cm<sup>-1</sup> could be assigned to sulfate ions (ν<sub>4</sub> vibration mode [23,24]), but it was verified by ICP and XPS that sulfate ions were not detected on the dried solid.

### III.3.3. Nature and composition of the phases deposited during DPU: the Fe<sub>x</sub>Ni<sub>(100-x)</sub>/SiO<sub>2</sub> series

ATR-IR spectra were recorded for the whole series of Fe-Ni/SiO<sub>2</sub> solids prepared by a 22 h DPU process (Figure 3.8). The formation of an ill-crystallized 1:1 phyllosilicate can be confirmed by:



**Table 3.4.** Metal loadings measured by XRF (on the basis of the dualistic formula: Fe.Ni.SiO<sub>2</sub>), and relative molar proportions of Fe and Ni measured by XRF and XPS for samples prepared by DPU.

Samples	Relative proportions in DPU solution		Metal content and relative proportions for catalysts after drying				
			XRF			XPS	
	Fe (%)	Ni (%)	Metal loading (wt%)	Fe (%)	Ni (%)	Fe (%)	Ni (%)
Fe <sub>100</sub> /SiO <sub>2</sub>	100	0	55	100	0	-	-
Fe <sub>75</sub> Ni <sub>25</sub> /SiO <sub>2</sub>	75	25	63	62	38	69	31
Fe <sub>60</sub> Ni <sub>40</sub> /SiO <sub>2</sub>	60	40	49	41	59	49	51
Fe <sub>50</sub> Ni <sub>50</sub> /SiO <sub>2</sub>	50	50	49	30	70	31	69
Fe <sub>40</sub> Ni <sub>60</sub> /SiO <sub>2</sub>	40	60	54	24	76	25	75
Fe <sub>25</sub> Ni <sub>75</sub> /SiO <sub>2</sub>	25	75	55	13	87	13	87
Fe <sub>10</sub> Ni <sub>90</sub> /SiO <sub>2</sub>	10	90	58	6	94	8	92
Ni <sub>100</sub> /SiO <sub>2</sub>	0	100	59	0	100	-	-

(1) the asymmetrical doublet of bands at 1007 and 1102 cm<sup>-1</sup> ( $\nu(\text{Si-O})$  stretching vibration in a 1:1 phyllosilicate), from Fe<sub>100</sub>/SiO<sub>2</sub> to Fe<sub>60</sub>Ni<sub>40</sub>/SiO<sub>2</sub> (Figure 3.8a). These bands shift to lower wavenumbers when increasing the Ni content, suggesting a change in the structure or in the degree of organization of the phyllosilicates. Moreover, the band at 1007 cm<sup>-1</sup> becomes narrower for some Ni-rich samples, and other poorly intense bands appear in the 980-1100 cm<sup>-1</sup> range (Ni<sub>100</sub>/SiO<sub>2</sub>), possibly indicating a higher crystallinity for Ni-rich samples compared with Fe-rich ones;

(2) the increase of intensity of the broad bands at 670 and 618 cm<sup>-1</sup> assigned to a tetrahedral Si-O mode in the 1:1 phyllosilicate structure (Figure 3.8b), which may also indicate a change in the degree of organization of the phyllosilicate.

ICP was first used as an attempt to quantify the metal loadings on the catalysts. However, some solids could not be completely digested at 110 °C, and a higher proportion of hot HF produced gaseous SiF<sub>6</sub>, leading to irreproducible measurements of Si. Therefore, XRF was selected to evaluate both the metal loadings and the metal proportions after drying at 60 °C (Table 3.4). Metal loadings listed in the table will be discussed in section III.3.2. The Ni proportion with respect to Fe was found to be higher than that in the DPU solution for the whole series of solids, in line with what was found for Fe<sub>50</sub>Ni<sub>50</sub>/SiO<sub>2</sub>. This tendency was confirmed

by XPS, which also confirmed the exclusive presence of Fe(III) and Ni(II) ions in all the dried solids ( $2p_{3/2}$  signals at 712.1-712.6 and 856.2-856.5 eV, respectively).

#### III.3.4. Conclusions

The DPU process applied to Fe-Ni/SiO<sub>2</sub> systems according to the procedure described in section III.1 takes place in two successive steps. A combination of characterization techniques (X-ray diffraction, Mössbauer spectroscopy, infrared spectroscopy, X-ray absorption spectroscopy) shows that the early precipitation of Ni(OH)<sub>2</sub> onto silica during the first hours of DPU is followed by the formation of a poorly organized 1:1 phyllosilicate, in which, after drying, Fe<sup>3+</sup> and Ni<sup>2+</sup> ions occupy the octahedral layer. In all the solids, the Ni molar proportion with respect to Fe is higher than the proportion in the DPU solution, because of a preferential reaction of Ni with silica.

### III.4. The process of reduction for Fe-Ni/SiO<sub>2</sub> solids prepared by DPU

#### III.4.1. Speciation of the metals: the Fe<sub>50</sub>Ni<sub>50</sub>/SiO<sub>2</sub> solid

The interplay between the two metals will now be investigated during the reduction process leading to the Fe-Ni nanoparticles, first using Fe<sub>50</sub>Ni<sub>50</sub>/SiO<sub>2</sub> as a reference system.

The temperature-reduction profile of Fe<sub>50</sub>Ni<sub>50</sub>/SiO<sub>2</sub> (after storage in ambient air and drying at 60 °C to eliminate adsorbed water) evidences three main reduction stages (Figure 3.9): a minor one between 270 and 350 °C, and two major ones between 350 and 500 °C, and between 500 and 700 °C, respectively.

To explain the events seen on the TPR profile, the reduction of this sample was monitored simultaneously at the Ni and Fe K edges by *in situ* X-ray absorption spectroscopy up to 500 °C, the upper temperature limit allowed by the XAS set-up (Figure 3.10). The temperature was maintained at 500 °C during 60 min after completion of the temperature ramp.

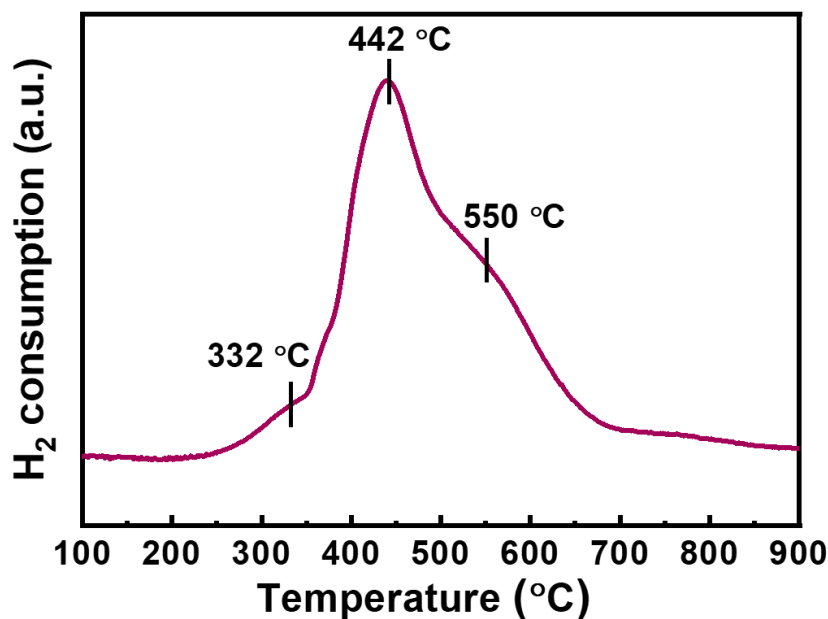


**Figure 3.9.** Temperature-reduction profile of  $\text{Fe}_{50}\text{Ni}_{50}/\text{SiO}_2$  after storage in air and drying at  $60\text{ }^\circ\text{C}$  ( $\text{H}_2$  (5%)/Ar, flow rate:  $50\text{ mL min}^{-1}$ , heating ramp:  $7.5\text{ }^\circ\text{C min}^{-1}$ ).

The evolution of the spectra at the Ni K edge during the reduction process, up to  $500\text{ }^\circ\text{C}$ , is presented on Figure 3.10a. The initial spectrum corresponds to Ni(II) ions in the phyllosilicate phase. Below  $350\text{ }^\circ\text{C}$ , the intensity of the spectrum does not change much, indicating that no reduction happens during this stage. Above  $350\text{ }^\circ\text{C}$ , the intensity of the white line gradually decreases, and the edge and first EXAFS oscillation shift to lower energies, denoting a decrease in the Ni oxidation state and changes in its chemical environment.

The EXAFS analysis of the final state corresponds to metallic *fcc* Ni (Figure 3.11a and b, Table 3.5), as indicated by the shape of the Fourier transform, similar to that of the metal reference, and by the fit of the first shell of neighbours: number of closest neighbours of 11 (12 in a *fcc* structure), and a Ni-Ni distance of  $2.49\text{ \AA}$  consistent with the distance present in metallic Ni.

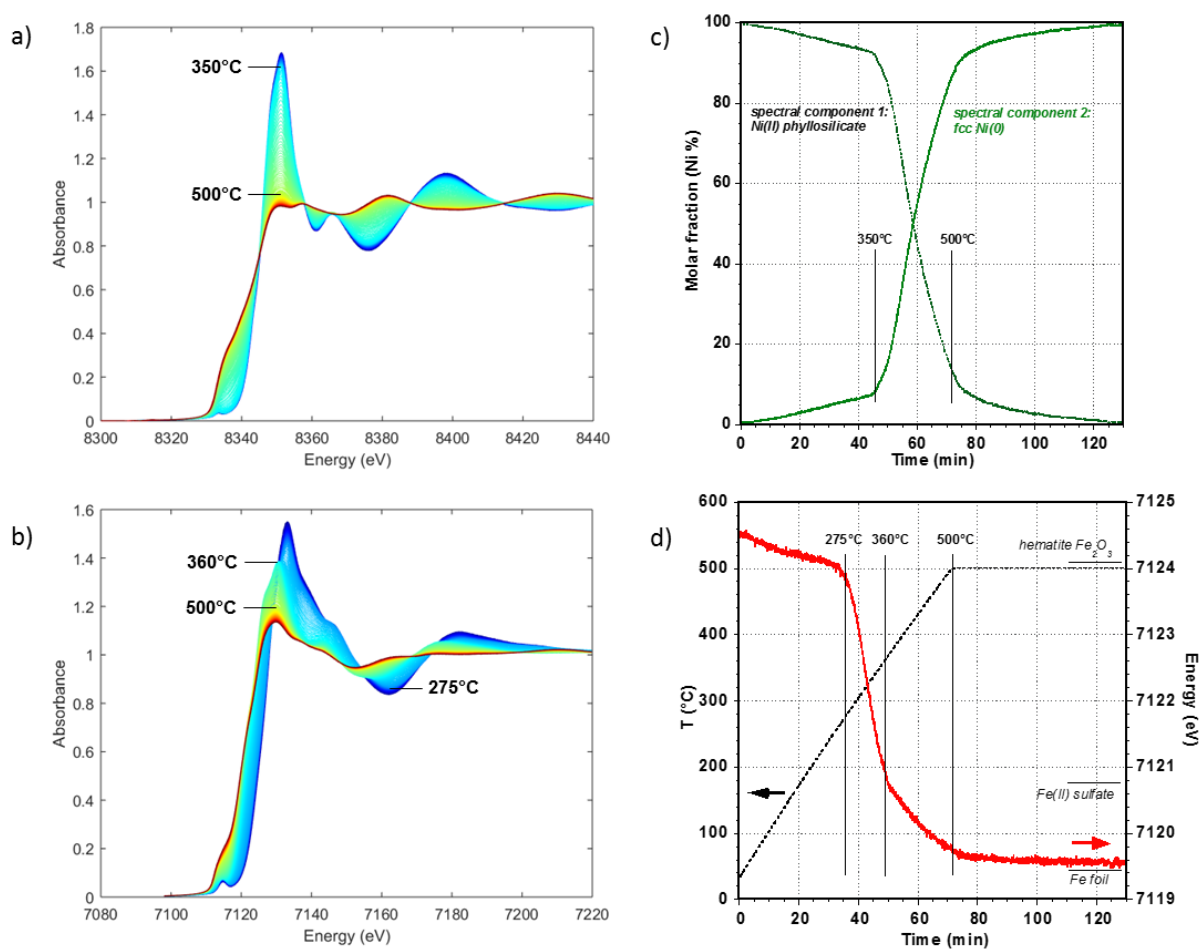


**Figure 3.10.** X-ray absorption spectra recorded during the reduction of  $\text{Fe}_{50}\text{Ni}_{50}/\text{SiO}_2$ : a) at the Ni K edge; b) at the Fe K edge. c) MCR-ALS analysis of Ni reduction. d) Evolution during reduction of the energy at the inflection point of XANES spectra recorded at the Fe K edge. Scales of the x-axes of figures c) and d) are similar.

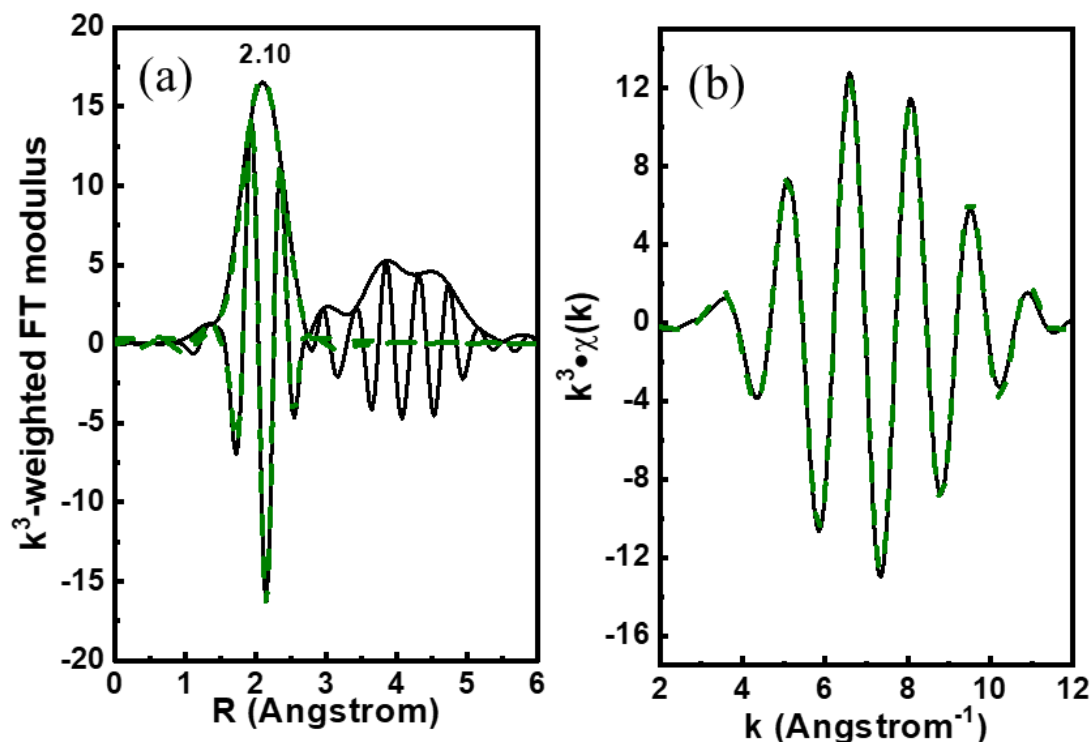


**Figure 3.11.** EXAFS  $k^3$ -weighted Fourier transform moduli and results of  $k^3 \chi(k)$  EXAFS fitting in R-space; EXAFS  $k^3$ -weighted oscillations and results of  $k^3 \chi(k)$  EXAFS fitting in k-space of:  $\text{Fe}_{50}\text{Ni}_{50}/\text{SiO}_2$  after reduction at 500 °C: a and b) at the Ni K edge (black: experimental; green: fit; spectrum recorded at RT). Interatomic distances R are listed in Table 3.5.

**Table 3.5.** Structural parameters determined from the EXAFS analysis of the spectra recorded at RT for the  $\text{Fe}_{50}\text{Ni}_{50}/\text{SiO}_2$  catalyst after reduction at 500 °C.

Sample	Absorbing atom	N, scattering atom	R (Å)	$\sigma^2 \cdot 10^{-3}$ (Å <sup>2</sup> )	R <sub>F</sub> (%)	$\chi^2\nu$
$\text{Fe}_{50}\text{Ni}_{50}/\text{SiO}_2$ reduced at 500 °C	Ni	11 (1) Ni	2.49 (1)	8 (1)	1.1	1067

N: Coordination number, R: Distance between absorbing atom and neighbours;  $\sigma$ : Debye-Waller factor; R<sub>F</sub>: reliability factor, which measures the relative misfit with respect to the data;  $\chi^2\nu$ : reduced chi-square, which takes into account the uncertainty level in the data, as well as the number of free parameters allowed to vary in the fit. Simulations were done over  $\Delta k$  range = 3.5-10.5 Å<sup>-1</sup>,  $\Delta R$  = 1-3.4 Å for catalyst before reduction and 1-2.7 Å for catalyst after reduction,  $S_0^2 = 0.75$ ,  $E_0 + \Delta E_0 = 8340 \pm 3$  eV at the Ni K edge.

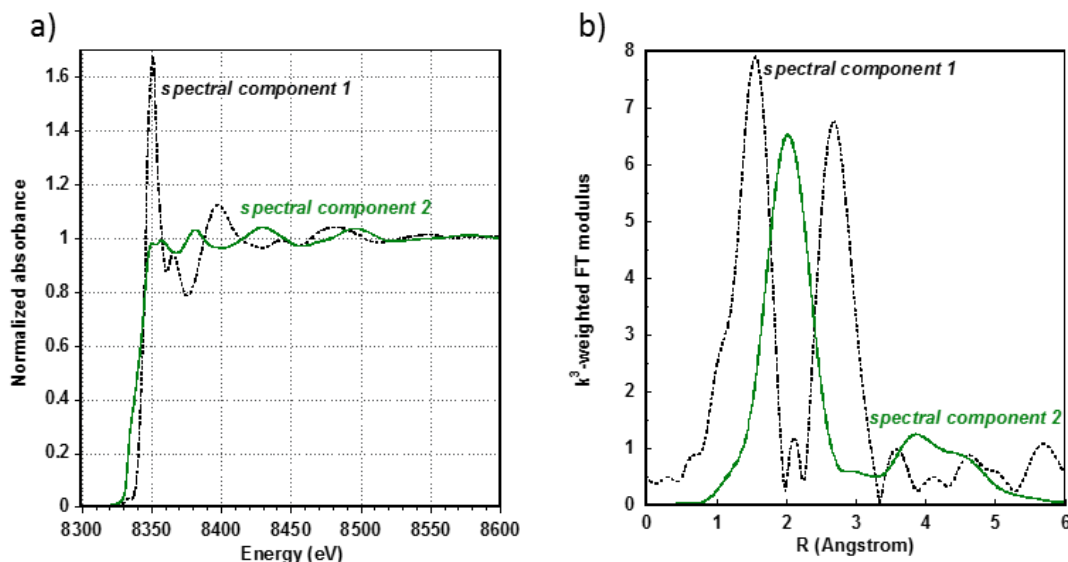


**Figure 3.12.** MCR-ALS spectral contributions to the spectra recorded at the Ni K edge during the reduction of  $\text{Fe}_{50}\text{Ni}_{50}/\text{SiO}_2$ : a) XANES region; b) Fourier transforms.

In order to go deeper into the evolution of nickel spectra, a quantitative analysis by a MCR-ALS procedure required two spectral components only (Figure 3.10c), in line with the presence of a set of isosbestic points (Figure 3.10a). The two extracted components closely recall the experimental spectrum of  $\text{Ni}^{2+}$  ions in the initial phyllosilicate, and that of metallic *fcc* Ni (Figure 3.12). The quantitative analysis shows that the reduction of  $\text{Ni}^{2+}$  ions starts above 350 °C, with an inflection point at 400 °C. Nickel reduction is complete after a plateau of 1h at 500 °C. The absence of an intermediate dehydrated phase in the analysis is justified by the higher temperature range at which nickel phyllosilicate would decompose to NiO (500-600 °C) [4].

The progress of iron reduction, deduced from the spectra recorded at the Fe K edge, is more complex to analyze. The initial spectrum corresponds to oxidized Fe(III) ions in the phyllosilicate phase. It can be seen on Figure 3.10b that there are two main stages. The intensity of the spectrum starts changing above 275 °C, with a shift of the white line and of the edge to lower energies. Between 360 and 500 °C, the two phenomena become more marked, indicating a further decrease of Fe oxidation state. A comparison between the final XANES spectrum and the spectrum of reference metallic Fe shows that the reduction of iron is not complete at the end of the plateau at 500 °C, and the EXAFS signal of the final state could not be satisfactorily

fitted with a limited set of parameters. The lack of isosbestic points indicates that more than 2 components are involved in the reduction.

In order to go deeper into the evolution of iron speciation during reduction, it was chosen in a first approach to follow the decrease in energy of the Fe edge position, correlated to a decrease of the Fe oxidation state (Figure 3.10d). The position in energy of the edge was interpreted with respect to reference compounds: hematite  $\text{Fe}_2\text{O}_3$ , Fe(II) sulfate, Fe foil. This analysis shows that  $\text{Fe}^{3+}$  ions originally present inside the layered structure undergo a fast reduction to  $\text{Fe}^{2+}$  in the 275-350 °C temperature range. A more gradual decrease of the edge value above 350 °C, starting when Ni reduces to the metallic state, can be interpreted as a progressive reduction of  $\text{Fe}^{2+}$  ions to Fe metal.

The MCR-ALS analysis of Fe reduction provides a set of five independent spectral components, that must be interpreted to confirm their validity in terms of chemistry (Figures 3.13 and 3.14).

The white lines of the first two components, that dominate the analysis below 275 °C, are identical, and the EXAFS oscillations are found at the same energies, though damped for the second component.

The third component appears between 275 and 358 °C. The edge energy is lower than that of the first two contributions and, as seen above, this is associated a reduction of iron to the Fe(II) oxidation state (Figure 3.14a). The EXAFS oscillations are similar to those of the first component, though shifted to lower energies (Figure 3.14b). The Fourier transforms of the first three components resemble each other, apart from the decrease of intensity of the peaks possibly due to a temperature-induced increase of the Debye-Waller parameter (Figure 3.14c). The Fourier transform of the third component also differs from those recorded on reference oxides such as  $\text{Fe}_3\text{O}_4$ . This suggests that the set of the first three components is related to the same phase, i.e., the Fe-containing phyllosilicate. It can be supposed that the second component does not correspond to a new species, but mostly reflects an increase of disorder in the phyllosilicate phase with increasing temperature (the results of the fits are globally similar to that of the initial state, except for an increase of the Debye-Waller factors for the second component, Table 3.5 and Figure 3.15).

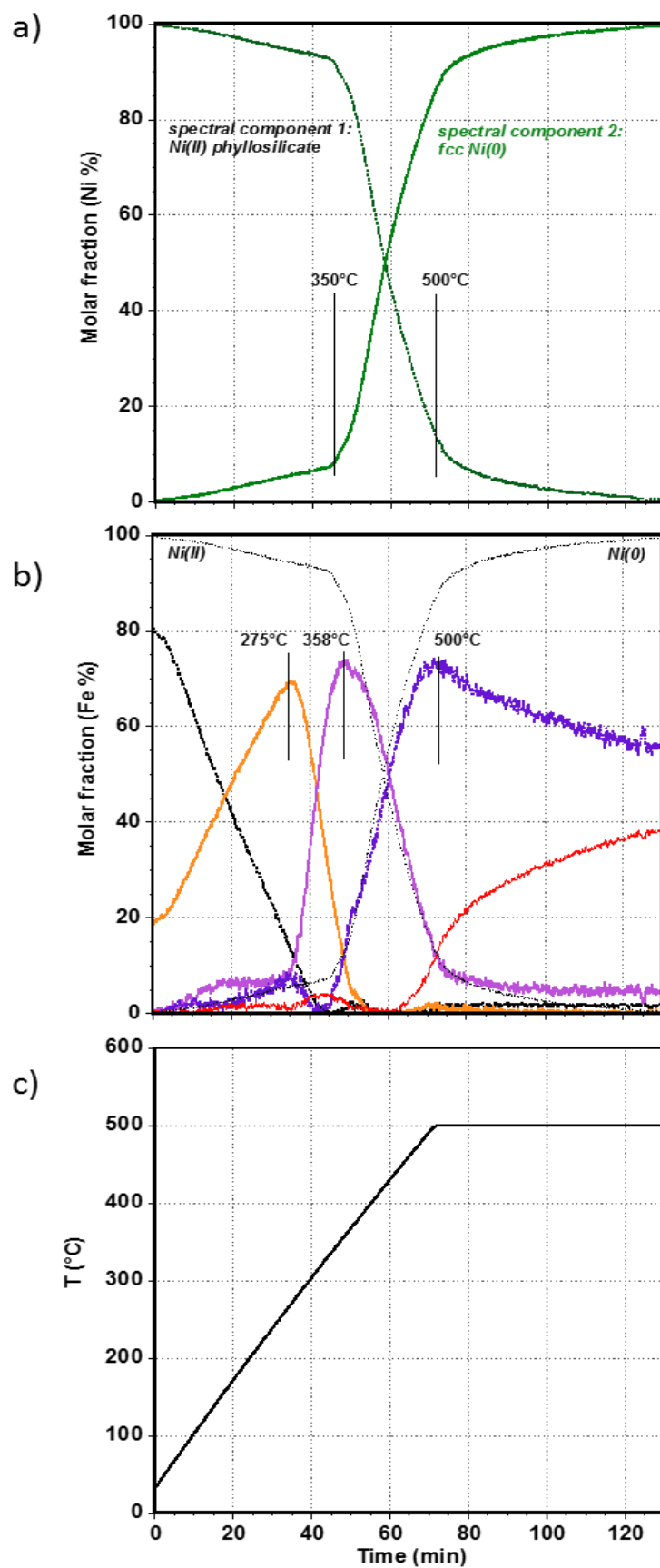


**Figure 3.13.** MCR-ALS analysis of the reduction of  $\text{Fe}_{50}\text{Ni}_{50}/\text{SiO}_2$ : a) at the Ni K edge (cf. Figure 3.10c); b) at the Fe K edge; c) temperature curve as a function of time.



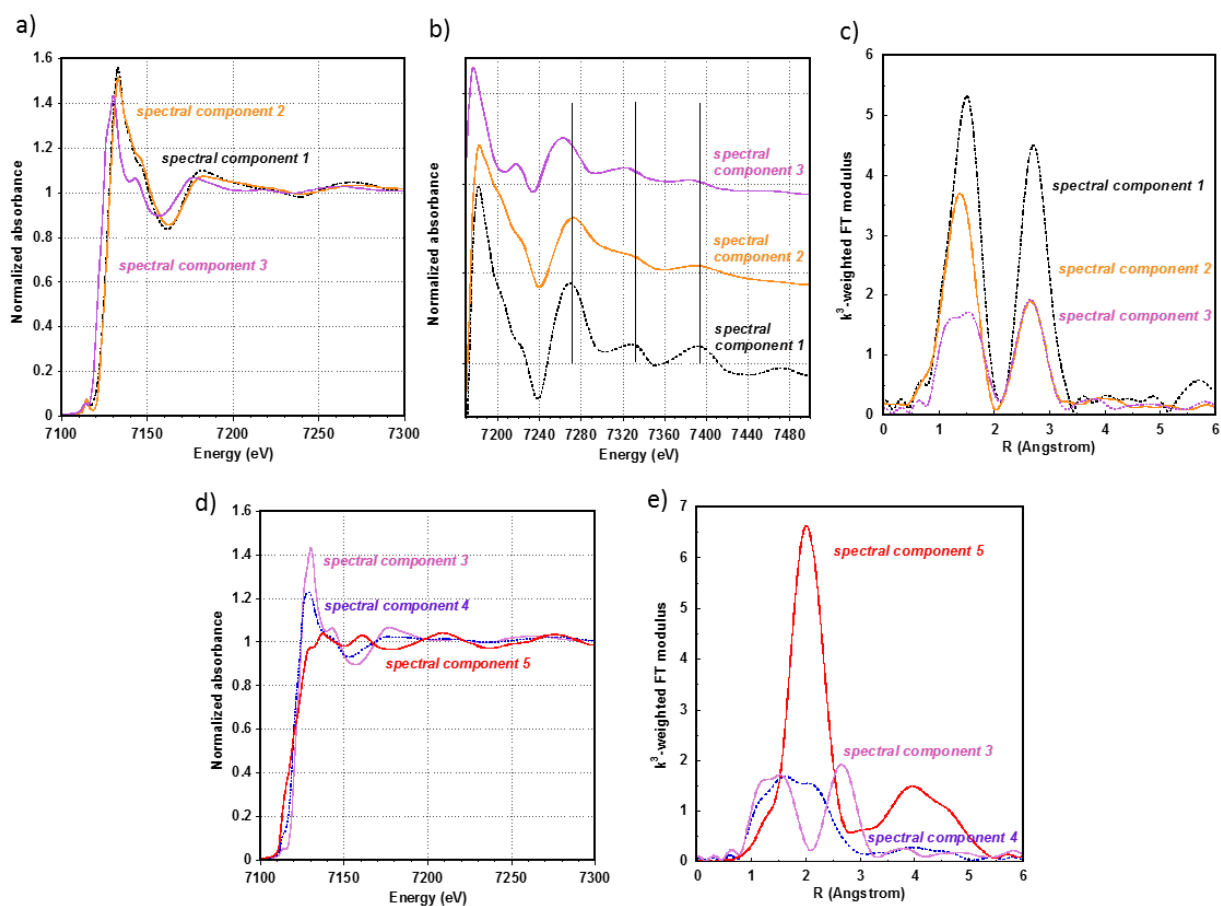


**Figure 3.14.** MCR-ALS spectral contributions to the spectra recorded at the Fe K edge during the reduction of  $\text{Fe}_{50}\text{Ni}_{50}/\text{SiO}_2$ : a) XANES region, b) oscillations (curves shifted upwards) and c) Fourier transforms of spectral components 1, 2 and 3; d) XANES region and e) Fourier transforms of spectral components 3, 4 and 5.

**Table 3.6.** Structural parameters determined from the EXAFS analysis of the two spectral components presented in Figure 3.15.

	Absorbing atom	N, scattering atom	R (Å)	$\sigma^2 \cdot 10^{-3}$ (Å <sup>2</sup> )	R <sub>F</sub> (%)	$\chi^2_{\nu}$
$\text{Fe}_{50}\text{Ni}_{50}/\text{SiO}_2$ DPU, dried (from Table 3.4)	Fe	6 O *	1.99 (1)	11 (1)	0.5	697
		6 Ni *	3.11 (1)	13 (1)		
1st component (black curves, Figure 3.13 and 3.14)	Fe	6 O *	1.99 (1)	9 (1)	1.0	1291
		6 Ni *	3.12 (1)	11(1)		
2nd component (orange curves, Figure 3.13 and 3.14)	Fe	6 O *	1.95 (1)	14 (1)	1.5	1824
		6 Ni *	3.10 (1)	22 (1)		

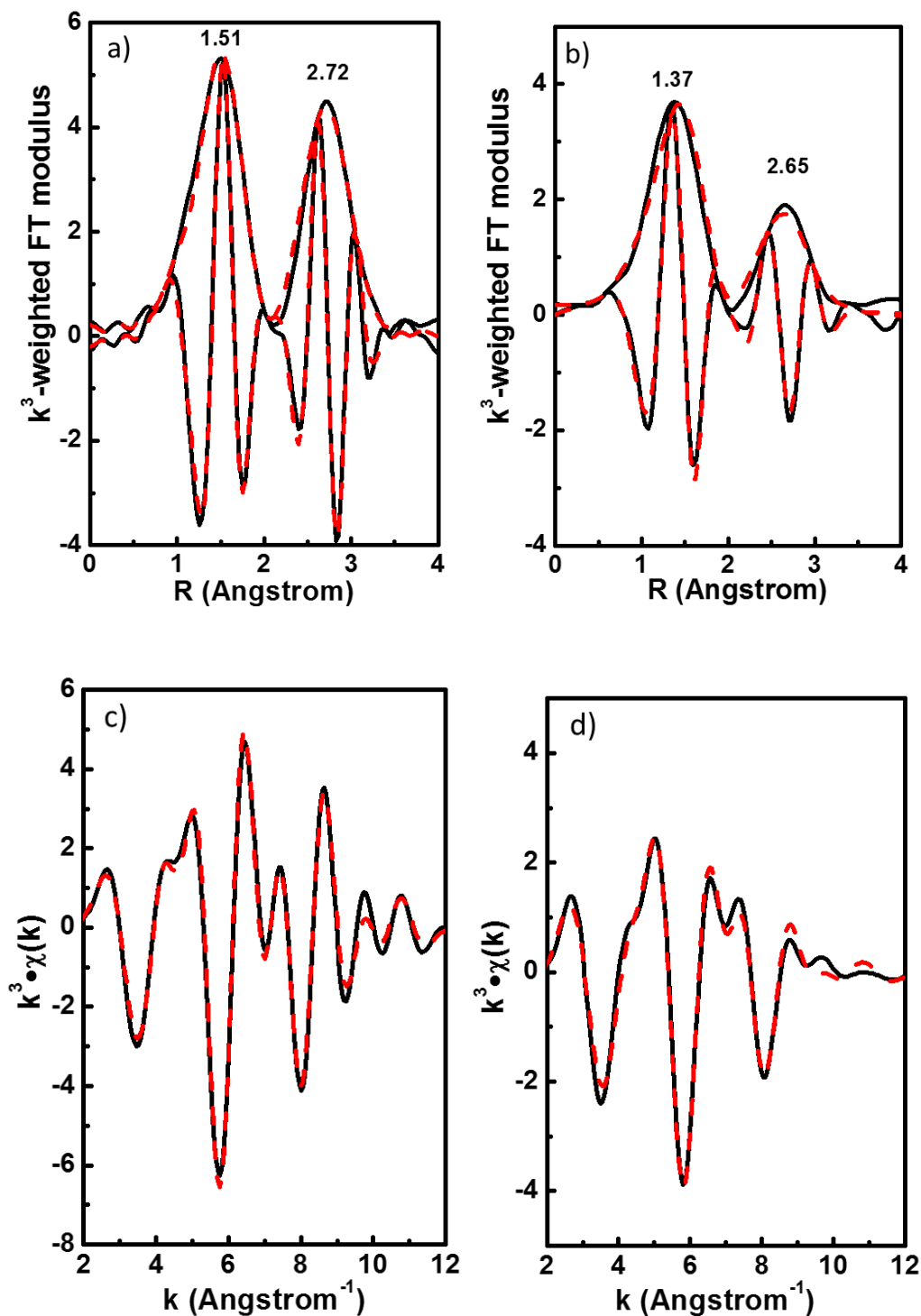


**Figure 3.15.** EXAFS  $k^3$ -weighted oscillations and results of  $k^3 \chi(k)$  EXAFS fitting in R-space of: a) the first component (black, Figure 3.11 and 3.12), b) the second component (orange, Figure 3.11 and 3.12). EXAFS  $k^3$ -weighted oscillations and results of  $k^3 \chi(k)$  EXAFS fitting in  $k$ -space of: c) the first component (black, Figure 3.11 and 3.12), d) the second component (orange, Figure 3.11 and 3.12) Black: experimental; red: fit. Interatomic distances  $R$  are listed in Table 3.6.

The third component would then evidence a reduction of iron to the  $\text{Fe}^{2+}$  state, still in the layered phase. The first event observed on the TPR profile presented above (Figure 3.9) would thus be linked to the reduction of  $\text{Fe}^{3+}$  to  $\text{Fe}^{2+}$ .

The third component starts disappearing when nickel reduction starts (Figure 3.13b), while the fourth component appears exactly in parallel with the formation of metallic nickel. The fourth component could not be identified to a single species. The position in energy of the edge of the fourth component, close to that of the third one, lets one assume that it is associated to  $\text{Fe}^{2+}$  ions, though in a strongly altered environment (Figure 3.14d). The shape of the first peak in the Fourier transform (Figure 3.14e), which seems to contain Fe-O and Fe-Fe (or Fe-Ni) contributions, suggests both the existence of an oxidic phase, and a proximity to metal particles.

The last component, whose weight increases gradually during the plateau at 500 °C, gives a well-defined Fourier transform identical to that of metallic *fcc* Ni (Figure 3.14e). Because monometallic Fe crystallizes in the *bcc* structure, it is interpreted as Fe(0) atoms located in the *fcc* core of Ni-containing nanoparticles.

In view of this last result, the fourth component may be understood as a Fe(II)-containing phase external to the Fe-Ni particles, from which Fe reduces and diffuses into the bimetallic nanoparticles upon increasing temperature and time. These processes, and the concomitant reduction of  $\text{Ni}^{2+}$  to Ni(0), are thus all included in the second reduction stage on the TPR profile (Figure 3.9).

$^{57}\text{Fe}$  Mössbauer spectrometry was implemented in *in situ* conditions to investigate the reduction of iron above 500 °C. Spectra were first recorded at room temperature after reduction at 500 or 700 °C, still under  $\text{H}_2$  atmosphere. The  $^{57}\text{Fe}$  Mössbauer spectrum of the  $\text{Fe}_{50}\text{Ni}_{50}/\text{SiO}_2$  sample reduced at 500 °C (Figure 3.16a, Table 3.7) can be interpreted in terms of three components: two quadrupole split components (isomer shift above 1  $\text{mm}\cdot\text{s}^{-1}$ , red and blue curves), and a singlet (isomer shift close to 0  $\text{mm}\cdot\text{s}^{-1}$ , yellow curve).

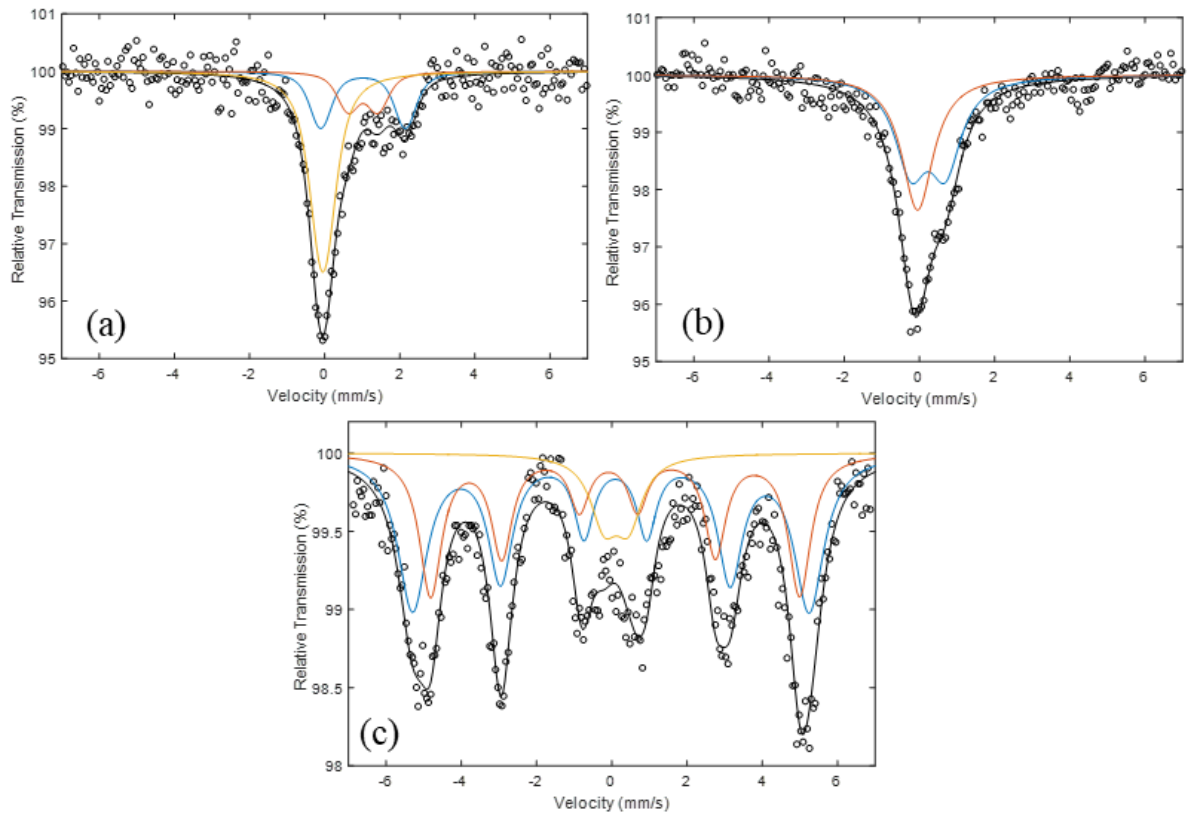


**Figure 3.16.**  $^{57}\text{Fe}$  Mössbauer spectra recorded on  $\text{Fe}_{50}\text{Ni}_{50}/\text{SiO}_2$ : a) after reduction at 500 °C under  $\text{H}_2$  (RT); b) after reduction at 700 °C under  $\text{H}_2$  (RT); c) after reduction at 700 °C under  $\text{H}_2$  (-268 °C).

**Table 3.7.**  $^{57}\text{Fe}$  Mössbauer hyperfine parameters of sample  $\text{Fe}_{50}\text{Ni}_{50}/\text{SiO}_2$  after reduction. Spectra were recorded at room temperature (RT, 25 °C) or low temperature (LT, -268 °C).

Sample	Site	$\delta$ (mm.s $^{-1}$ )	$\Delta$ (mm.s $^{-1}$ )	$\Gamma$ (mm.s $^{-1}$ )	Area (%)	$B_{\text{HF}}$ (T)
$\text{Fe}_{50}\text{Ni}_{50}/\text{SiO}_2$	Fe(II) Oh	1.11(4)	2.25(8)	0.48(4)	26(3)	-
reduced at 500 °C (RT)	Fe(II) Oh	1.12(6)	0.79(8)	0.48(4)	17(3)	-
	Fe(0) in Fe-Ni alloy	0.06(4)	0.00	0.64(9)	57(3)	-
$\text{Fe}_{50}\text{Ni}_{50}/\text{SiO}_2$	Fe(0) in Fe-Ni alloy	0.04(4)	0.00	1.03(4)	43(5)	-
reduced at 700 °C (RT)	Fe(0)	0.35(6)	0.88(8)	1.03(4)	57(3)	-
	Fe(0) in Fe-Ni alloy	0.12(2)	0.00	0.90(1)	62(8)	32.5(4)
reduced at 700 °C (LT)	Fe(0) in Fe-Ni alloy	0.16(2)	0.00	0.60(1)	28(1)	30.1(3)
	Fe(0), non magnetic	0.21(2)	0.67(7)	0.77(8)	10(1)	-

$\delta$ : isomer shift;  $\Delta$ : electric quadrupole splitting;  $\Gamma$ : line width at half maximum;  $B_{\text{HF}}$ : magnetic hyperfine field

The isomer shift of the two quadrupole split components is typical of high-spin Fe(II) ions, confirming the XAS results presented above. Of the two, the component with the larger quadrupole splitting  $\Delta$  (blue curve) is consistent with Fe(II) ions in silicates, since the hyperfine parameters correspond to their typical range [25]. The quadrupole splitting of the second component, however, is too small to correspond to a bulk silicate, and can be attributed to Fe(II) ions in extremely distorted octahedral sites, or to lower coordination numbers.

The third contribution, covering 57% of Fe, consists of a singlet typical of Fe(0), with an isomer shift at  $\delta = 0.06 \text{ mm.s}^{-1}$  slightly more positive than that of iron metal ( $\delta = 0 \text{ mm.s}^{-1}$ ), and in line with what has been reported for Fe-Ni alloys ( $\delta = 0-0.06 \text{ mm.s}^{-1}$  at 25 °C, the value of  $\delta$  increasing with the Ni content [26-28]). The absence of a sextet, that would be linked to the presence of a phase magnetic at RT, suggests that the Fe-Ni nanoparticles may be superparamagnetic at RT, thus exhibiting a size smaller than 10 nm [27-28].

The third reduction event on the TPR profile can be explained by comparing the Mössbauer spectra recorded at 500 and 700 °C, that evidence a progress in the reduction of iron. Reduction at 700 °C (Figure 3.16b and c, Table 3.7) produces a complete modification of the  $^{57}\text{Fe}$  Mössbauer spectrum, which can now be fitted with only two spectral components, a singlet (red curve) and a quadrupole doublet (blue curve). Both components are often observed for reduced, superparamagnetic iron nanoparticles, and are usually attributed to bulk and surface iron atoms, respectively [29]. The singlet at  $\delta = 0.04 \text{ mm.s}^{-1}$  corresponds to Fe(0) in the core of Fe-Ni nanoparticles. Compared with the reduction state at 500 °C, the slight decrease of  $\delta$  from 0.06 to 0.04  $\text{mm.s}^{-1}$  suggests an environment richer in Fe compared with the reduced state at 500 °C [26].

Since the hyperfine parameters of the quadrupole doublet can be confused with those of Fe(III), the same sample was measured at -268 °C after transfer in a helium-flow cryostat. The contribution of the quadrupole split component diminishes much, which would not be the case if a separate Fe(III)-containing phase was present, and the low-temperature spectrum is dominated by a magnetically split contribution, that can be fitted with at least two magnetic sextets (red and blue curves), comprising 90% of total Fe and confirming the presence of small

alloyed nanoparticles that become magnetic at low temperature. The isomer shift, once taken into account the second-order Doppler shift, and the magnetic field of these sextets are in the typical range of Fe(0) in Fe-Ni alloys [30]. Moreover, the two hyperfine fields are close to those measured for *fcc* Fe-Ni alloys in which Ni or Fe is the major metal (29 and 33 T, respectively [31]). In addition to these two components, a minor quadrupole split component, accounting for about 10% of the total resonance area (yellow curve), is still present at the centre of the spectrum. At this stage, it can be interpreted as Fe(0) species not ordered magnetically, either located at the periphery of bimetallic particles, or in highly dispersed monometallic Fe nanoparticles.

In summary, the evolution of the speciation of Fe and Ni for Fe<sub>50</sub>Ni<sub>50</sub>/SiO<sub>2</sub> during reduction can be described as: (1) a Fe(III),Ni(II)-containing phyllosilicate that remains as such up to 275 °C; (2) the reduction of the Fe<sup>3+</sup> ions to Fe<sup>2+</sup> in the phyllosilicate structure between 275 °C and 360 °C; (3) the reduction of Ni<sup>2+</sup> to Ni(0) above 360 °C, triggering the progressive reduction of Fe<sup>2+</sup> ions to the metallic state; (4) the deeper reduction of Fe<sup>2+</sup> ions to the metallic state between 500 and 700 °C, and progressive migration into the core of alloyed Fe-Ni *fcc* nanoparticles.

#### III.4.2. Reducibility of the metals across the Fe<sub>x</sub>Ni<sub>(100-x)</sub>/SiO<sub>2</sub> series, and composition of the Fe-Ni metal nanoparticles

In order to compare the reducibility of the Fe-Ni/SiO<sub>2</sub> systems, the TPR profiles recorded on the solids of the whole Fe-Ni/SiO<sub>2</sub> series (after storage in ambient air and drying at 60 °C to eliminate adsorbed water) are presented on Figure 3.17, including that of Fe<sub>50</sub>Ni<sub>50</sub>/SiO<sub>2</sub> interpreted above. The total H<sub>2</sub> consumption for each sample is listed in Table 3.8. The low value obtained for the monometallic Fe catalyst suggests that iron has not been totally reduced at 900 °C, as seen from the increase of the TCD signal at that temperature.

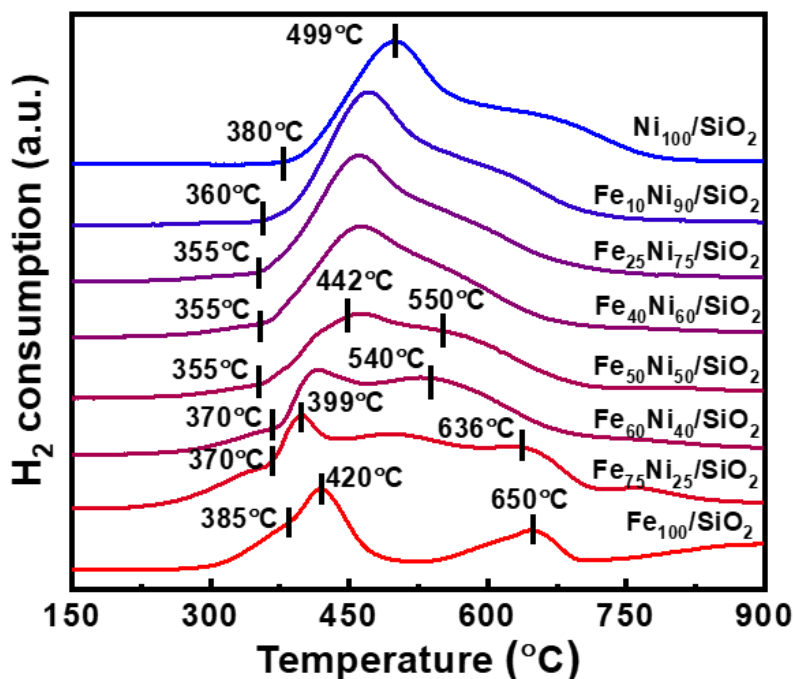


Figure 3.17. TPR profiles of Fe-Ni/SiO<sub>2</sub> samples after drying at 60 °C.

**Table 3.8.** H<sub>2</sub> consumption according to TPR profiles of Fe-Ni/SiO<sub>2</sub> samples dried at 60 °C, and metal loadings in reduced Fe-Ni/SiO<sub>2</sub> catalysts deduced from H<sub>2</sub> consumptions.

Samples	Fe <sub>100</sub> / SiO <sub>2</sub>	Fe <sub>75</sub> Ni <sub>25</sub> / SiO <sub>2</sub>	Fe <sub>60</sub> Ni <sub>40</sub> / SiO <sub>2</sub>	Fe <sub>50</sub> Ni <sub>50</sub> / SiO <sub>2</sub>	Fe <sub>40</sub> Ni <sub>60</sub> / SiO <sub>2</sub>	Fe <sub>25</sub> Ni <sub>75</sub> / SiO <sub>2</sub>	Fe <sub>10</sub> Ni <sub>90</sub> / SiO <sub>2</sub>	Ni <sub>100</sub> / SiO <sub>2</sub>
Amount of consumed H <sub>2</sub> (mmol/g cat)	5.0	7.2	6.8	6.3	6.8	6.2	6.4	6.3
Fe loading in reduced catalyst (wt%)	n.d.	25	17	12	11	5	3	0
Ni loading in reduced catalyst (wt%)	n.d.	16	25	29	35	38	44	47
Total metal loading in reduced catalyst (wt%)	n.d.	41	42	41	46	43	47	47

Globally speaking, the main reduction stages from the Fe<sub>60</sub>Ni<sub>40</sub>/SiO<sub>2</sub> and the Fe<sub>40</sub>Ni<sub>60</sub>/SiO<sub>2</sub> solids can be easily interpreted by comparison with the profile of Fe<sub>50</sub>Ni<sub>50</sub>/SiO<sub>2</sub>. The minor event at 355-370 °C can be assigned to the reduction of Fe<sup>3+</sup> to Fe<sup>2+</sup>. One can note accordingly that, over the whole series, the intensity of this H<sub>2</sub> consumption peak decreases when the Fe

content decreases. The major event at 400-450 °C corresponds to the partial reduction of  $\text{Fe}^{2+}$  to metallic Fe, and to the total reduction of  $\text{Ni}^{2+}$  to metallic Ni at same time. The last stage between 500 and 700 °C corresponds to the total reduction of  $\text{Fe}^{2+}$  to metallic Fe. These three samples present a maximum of reducibility across the series, especially when compared with monometallic Fe and Ni catalysts that complete their reduction at a higher temperature.

The reduction of Fe-rich samples ( $\text{Fe}_{100}/\text{SiO}_2$  and  $\text{Fe}_{75}\text{Ni}_{25}/\text{SiO}_2$ ) must be interpreted differently. For  $\text{Fe}_{100}/\text{SiO}_2$ , the TPR profile shown in Figure 3.17 is consistent with the profile discussed in Chapter I (section I.2.2), indicating that the first reduction peak at 420 °C corresponds to the reduction of a Fe(II)-containing phase to  $\text{Fe}_3\text{O}_4$ , and the second reduction peak at 650 °C corresponds to the reduction of  $\text{Fe}_3\text{O}_4$  to metallic Fe. In this case, the phyllosilicate could be transformed to an oxide, as it is not stabilized by doping with Ni(II) (as discussed in III.2.3). The incomplete reduction event above 750 °C may be due to the presence of difficult-to-reduce iron silicates. The complex profile of  $\text{Fe}_{75}\text{Ni}_{25}/\text{SiO}_2$  may be explained by a global shift of these reduction peaks to lower temperatures, caused by the presence of nickel ions which favour the reduction.

As for the Ni-rich samples ( $\text{Fe}_{25}\text{Ni}_{75}/\text{SiO}_2$  and  $\text{Fe}_{10}\text{Ni}_{90}/\text{SiO}_2$ ), the first two events can be interpreted in the same way as for  $\text{Fe}_{50}\text{Ni}_{50}/\text{SiO}_2$ , but the peak between 550 and 750 °C becomes more intense, and shifts to higher temperature with increasing Ni content. The same can be said of  $\text{Ni}_{100}/\text{SiO}_2$ . This peak cannot be explained any more by the mere reduction of Fe, because the Fe content decreases much, or Fe is not present. For Ni-rich samples, we suggest to correlate this event with a higher degree of organization of the phyllosilicate phase that is less troubled by the presence of co-deposited, and ultimately oxidized during drying, Fe ions.



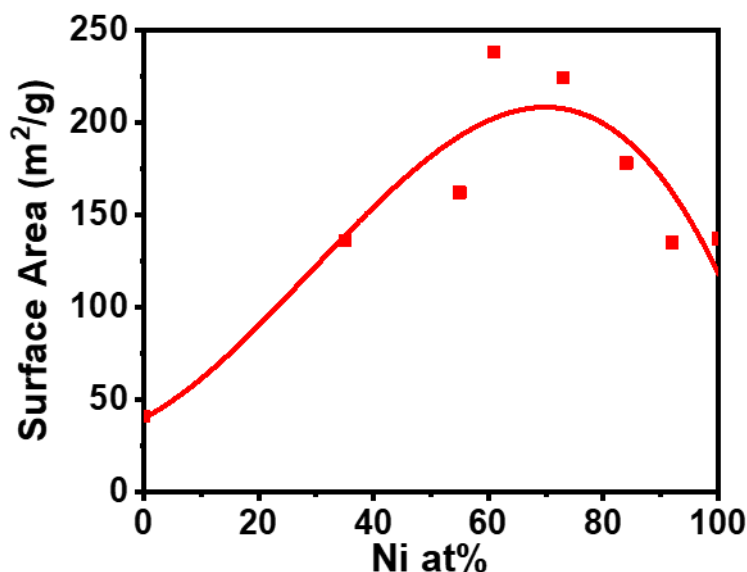


**Figure 3.18.** Evolution of specific surface area with increasing Ni content for Fe-Ni/SiO<sub>2</sub> samples after 700 °C reduction.

In order to validate this hypothesis, Figure 3.18 presents the evolution of the specific surface area of the solids after reduction at 700 °C (calculated using the BET model), as a function of the actual Ni atomic proportion. The specific surface area of Fe-Ni/SiO<sub>2</sub> catalysts first increases when increasing the Ni content. The Fe<sub>50</sub>Ni<sub>50</sub>/SiO<sub>2</sub> catalyst (actual composition: Fe<sub>31</sub>Ni<sub>69</sub>) exhibits the highest surface area, 240 m<sup>2</sup> g<sub>catalyst</sub><sup>-1</sup>, an apparently low value compared with pristine silica, but explained first by the dilution of silica by the presence of the metals, and by the deep transformation of silica during DPU. When further increasing the Ni content, the specific surface area decreases. One can thus suppose that this trend results from an initially higher degree of organization of the phyllosilicate phase in the Ni-rich samples. The evolution of the ATR-IR spectra presented above, with more structured bands in the Ni-rich domain, may also be linked to an increase of crystallinity.

Metals loadings in the reduced bimetallic and monometallic Ni catalysts were estimated from the TPR H<sub>2</sub> consumptions per gram of dried solids, as follows:

- in the dried catalysts undergoing TPR, iron is initially present as Fe<sup>3+</sup>, consuming 1.5 equivalent of H<sub>2</sub>, and nickel as Ni<sup>2+</sup>, consuming 1 equivalent of H<sub>2</sub>
- the molar proportions of iron and nickel are the ones given by XRF, which were

globally confirmed by XPS (Table 3.4). From the TPR total H<sub>2</sub> consumptions per gram of catalyst, and from the proportions of Fe<sup>3+</sup> and Ni<sup>2+</sup>, it is possible to come back to the total amount of metals in 1 g of dried solid, and to the amounts of Fe and Ni

- the composition of the dried solid is approximated as a mixture of Fe(OH)<sub>3</sub>, Ni(OH)<sub>2</sub> and SiO<sub>2</sub>. Knowing the amounts of Fe and Ni in 1 g of dried solid allows estimating the mass of Fe(OH)<sub>3</sub>, Ni(OH)<sub>2</sub>, and, by difference, of SiO<sub>2</sub>
- the composition of the catalyst after reduction is deduced from the masses of Fe, Ni and SiO<sub>2</sub>

The values given in Table 3.8 show that the total metal loadings on the seven catalysts are close in the 41-47 wt% range. They are lower than the metal loadings measured by XRF in the dried catalysts and reported in Table 3.4, on the basis of a Fe.Ni.SiO<sub>2</sub> dualistic formulation: they belonged to the 49-59 wt% range, except for Fe<sub>75</sub>Ni<sub>25</sub>/SiO<sub>2</sub>, for which measurements need to be verified. However, it is not logical that dried solids contain a larger proportion of metals than reduced solids that have undergone dehydration and loss of oxygen. This may be due to an underestimation of Si in the quantification by XRF. XRF measurements should thus be corroborated by a series of ICP measurements. One can however conclude from these series of measurements that the total metal loadings are high, and comprised within an interval of 6-10 wt%.

The formation of metallic nanoparticles was followed by *in situ* X-ray diffraction during reduction under H<sub>2</sub> for the bimetallic and the Ni systems. Diffractograms are presented as a function of temperature on Figure 3.18. Only the diffraction peaks of the phyllosilicate phase are visible up to the 330-400 °C range. In accordance with XAS data obtained on the Fe<sub>50</sub>Ni<sub>50</sub>/SiO<sub>2</sub> system, three diffraction peaks characteristic of *fcc* metal nanoparticles ((111), (200) and (220) reflections) appear in this temperature range and their intensity increases when temperature increases up to 700 °C. No peak related to *bcc* phases is observed (in particular the (200) reflection expected around  $2\theta = 65.0^\circ$ ), even for the Fe-rich systems. The average size of the crystalline domains increases from 3 to 5 nm from 350 to 700 °C. The diffraction peaks attributed to the phyllosilicate phase completely disappear above 500 °C.

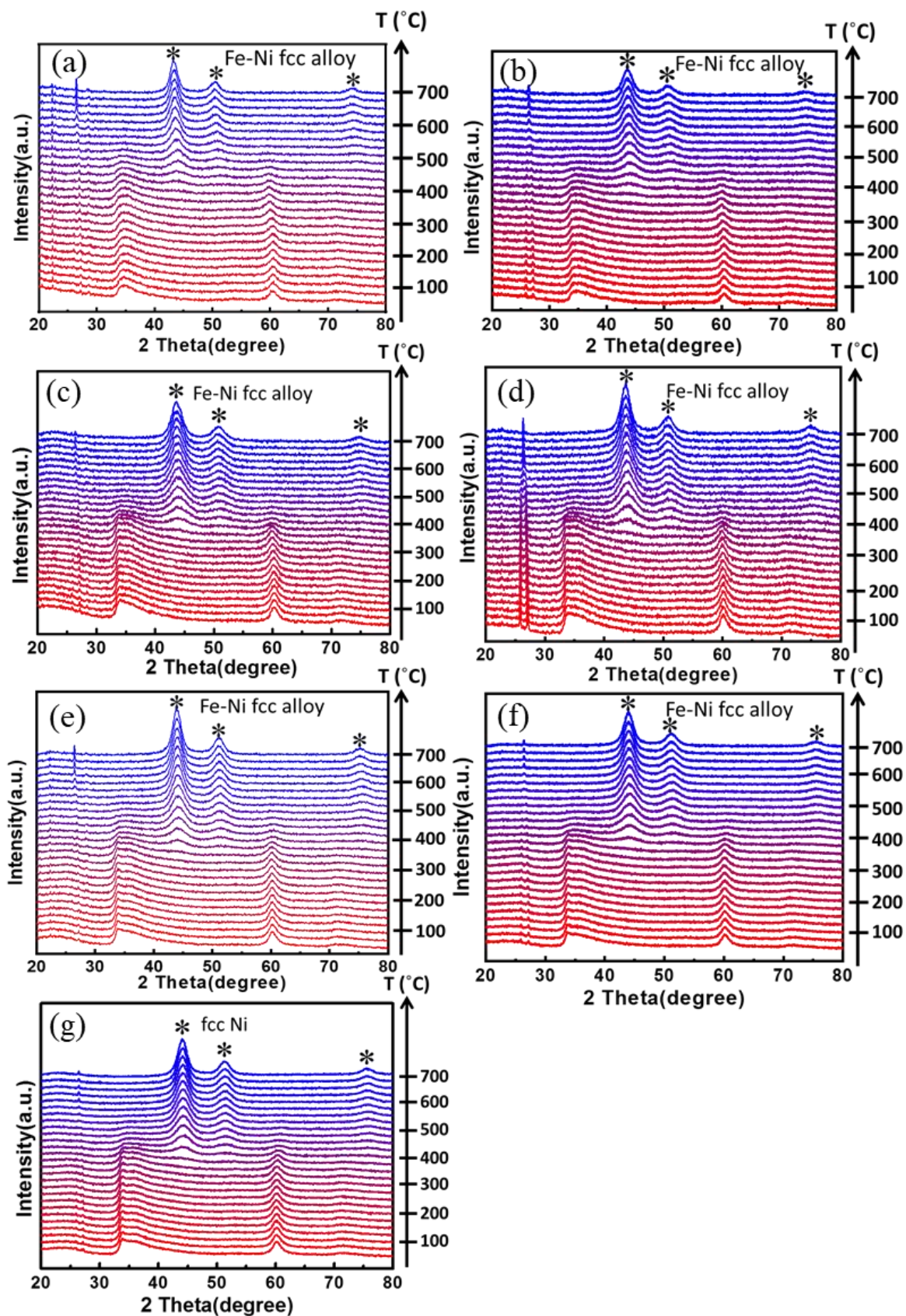


**Figure 3.19.** X-ray diffractograms recorded as a function of temperature during the reduction of a)  $\text{Fe}_{75}\text{Ni}_{25}/\text{SiO}_2$ , b)  $\text{Fe}_{60}\text{Ni}_{40}/\text{SiO}_2$ , c)  $\text{Fe}_{50}\text{Ni}_{50}/\text{SiO}_2$ , d)  $\text{Fe}_{40}\text{Ni}_{60}/\text{SiO}_2$  e)  $\text{Fe}_{25}\text{Ni}_{75}/\text{SiO}_2$  f)  $\text{Fe}_{10}\text{Ni}_{90}/\text{SiO}_2$  and g)  $\text{Ni}_{100}/\text{SiO}_2$  under  $\text{H}_2$  (3%)/ $\text{N}_2$ .

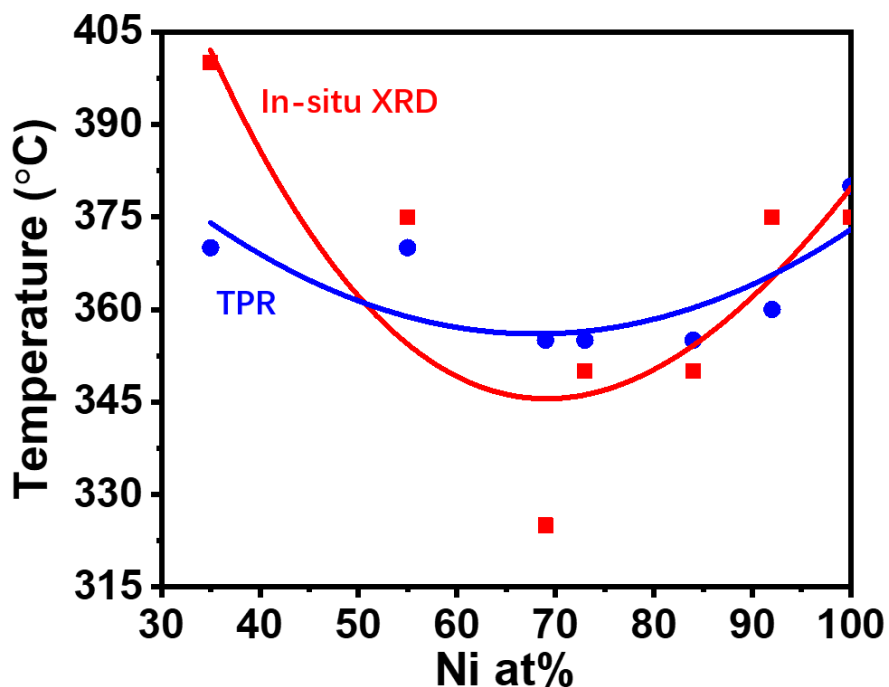


**Figure 3.20.** Temperature at which Fe-Ni metal nanoparticles are first detected by *in situ* XRD (red), and temperature of the limit between the first and the second reduction events seen on the TPR profiles, Figure 3.17 (blue line), as a function of the actual Ni content.

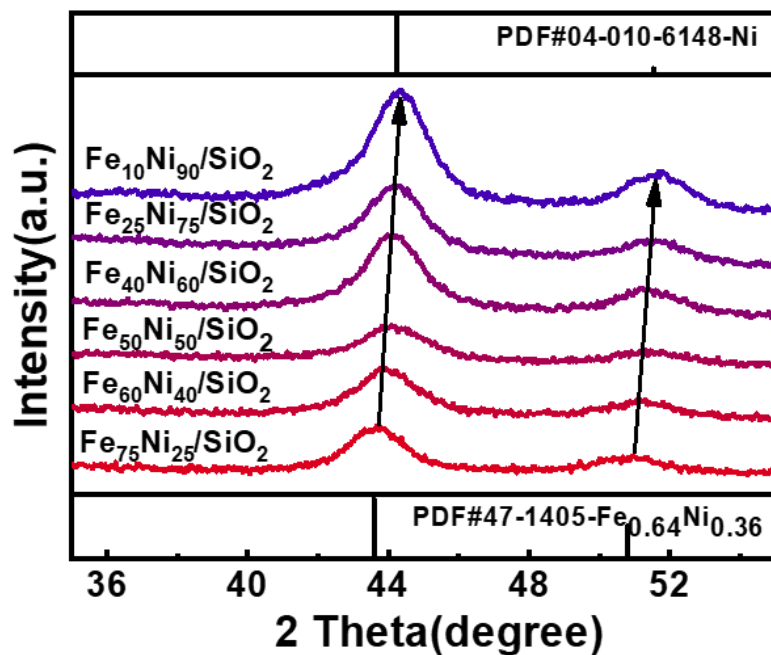


**Figure 3.21.** XRD patterns recorded at RT for Fe-Ni/SiO<sub>2</sub> samples after reduction at 700 °C under 10% H<sub>2</sub>/Ar, and exposure to air.

The starting reduction temperature (defined as the first appearance of (111), (200) and (220) reflections of the Fe-Ni alloys) is plotted as a function of the actual Ni content in Figure 3.20. This temperature decreases when increasing the Ni content up to Fe<sub>50</sub>Ni<sub>50</sub>/SiO<sub>2</sub>, that presents the lowest temperature in the series. Further increasing the Ni content leads to an increase in the temperature of Fe-Ni alloy formation. A comparison can be done with the TPR results. The temperature selected for plotting on Figure 3.19, is the limit between the first reduction event (reduction of Fe<sup>3+</sup> to Fe<sup>2+</sup>) and the second reduction event (reduction of Ni<sup>2+</sup> to Ni(0), triggering the reduction of Fe(II) to Fe(0)), as seen on Figure 3.17. The tendencies are similar, confirming a higher reducibility for systems in the middle of the series (actual Ni proportion: 60-80 at%), and the highest reducibility for the Fe<sub>50</sub>Ni<sub>50</sub>/SiO<sub>2</sub> sample.

XRD reflections can be used to determine the metals proportions in the Fe-Ni nanoparticles. Because the atomic radius of Fe (0.126 nm) is larger than that of Ni (0.124 nm), the unit cell parameter  $a$  of bimetallic *fcc* Fe-Ni alloys is known to decrease linearly with increasing Ni content [32]. Actually, the XRD peaks of the Fe-Ni nanoparticles shift to larger angles (smaller interplanar distances) when their Ni content increases (Figure 3.21). A linear Vegard correlation between  $a$ , measured at RT, and the Ni atomic content was drawn from the JCPDS files of reference Fe-Ni alloys (Figure 3.22); the equation of the linear regression is given above the figure.

Shifts in the position of the reflections when temperature increases (Figure 3.23) can be both due to a change of the composition of the nanoparticles, and to a temperature effect. The temperature effect can be estimated from the shift of the reflections for the solid whose composition does not change, Ni<sub>100</sub>/SiO<sub>2</sub>. After correction from the temperature-induced shifts measured for monometallic Ni<sub>100</sub>/SiO<sub>2</sub>, the positions of the (111) and (200) reflections for the Fe-Ni/SiO<sub>2</sub> solids give access to the values of  $a$  after reduction at 500 °C, at 700 °C, and back at RT, still under H<sub>2</sub> atmosphere (Table 3.9). Through the equation established above, one can then assess the composition of the crystalline core of the particles at each step of the reduction. The latter value of  $a$  is confirmed after measurement back at RT under H<sub>2</sub>. The Fe content at 700 °C is higher than that at 500 °C, meaning that more Fe has been reduced and has migrated

into the core of particles. Moreover, the trends in the evaluation of the composition of the particles at 700 °C remains consistent with those found at room temperature under H<sub>2</sub> after 700 °C. Discrepancies can be due to uncertainties in the estimation of the temperature-induced shift for the measurements carried out at 700 °C.

Phase	JCPDS file	a (nm)
Fe <sub>64</sub> Ni <sub>36</sub>	PDF 00-047-1405	0.35922
Fe <sub>45</sub> Ni <sub>55</sub>	PDF 04-003-2425	0.35758
Fe <sub>40</sub> Ni <sub>60</sub>	PDF 04-004-8867	0.35632
Fe <sub>27</sub> Ni <sub>73</sub>	PDF 04-004-8203	0.35480
Fe <sub>25</sub> Ni <sub>75</sub>	PDF 04-004-6754	0.35525
Fe <sub>18</sub> Ni <sub>82</sub>	PDF 04-003-2245	0.35440
Ni <sub>100</sub>	PDF 04-010-6148	0.35285

$$\text{Ni at \%} = 3393 - 9346 a \text{ (nm)}$$

$$a \text{ (nm)} = 0.36307 - 1.07 \times 10^{-4} \text{ Ni at \%}$$

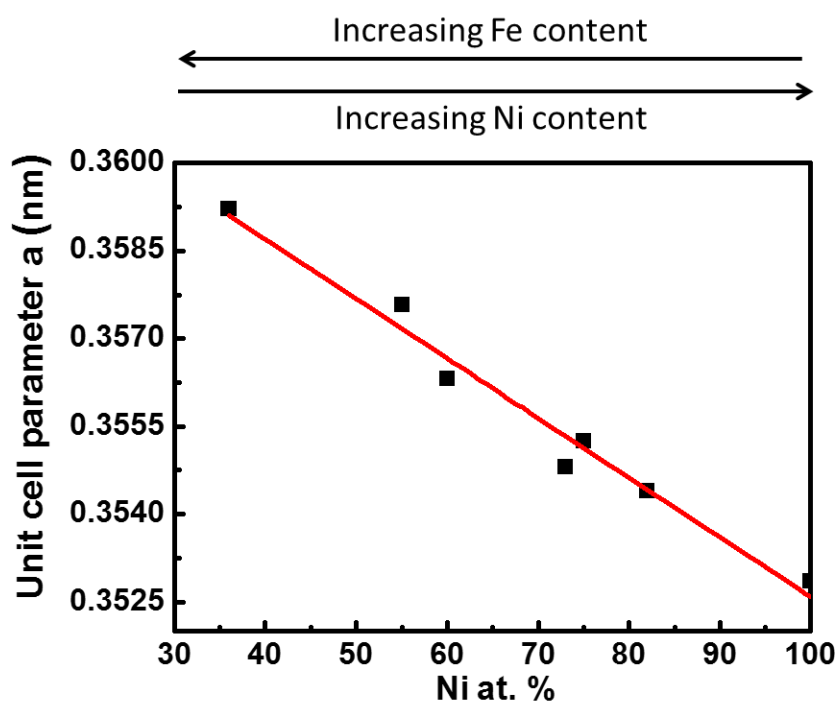


**Figure 3.22.** Correlation between the unit cell parameter *a* of reference Fe-Ni alloys (see table above) and the nickel atomic content.

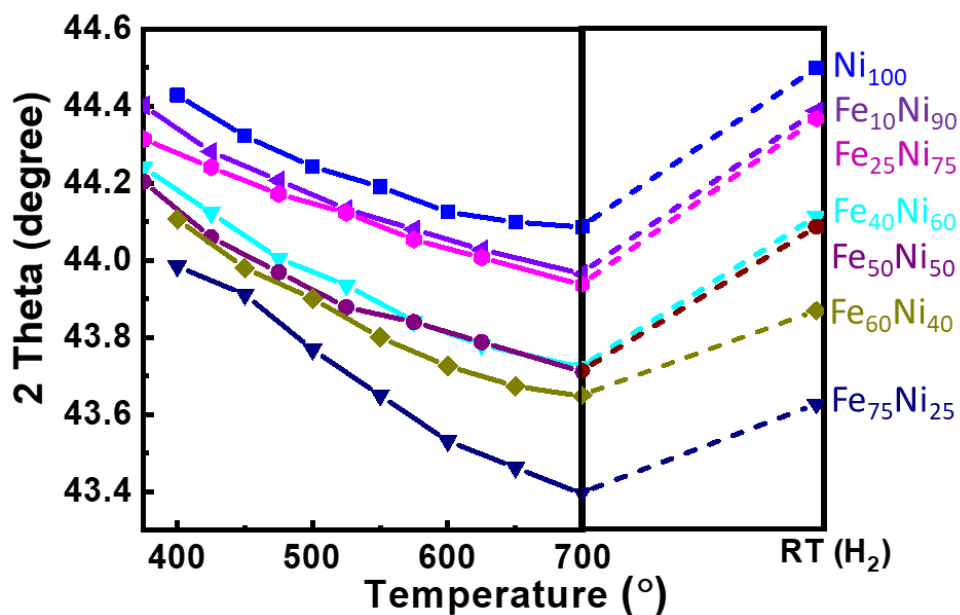


**Figure 3.23.** Evolution of the position of the (111) Bragg reflection for Fe-Ni and Ni nanoparticles on  $\text{Fe}_{75}\text{Ni}_{25}/\text{SiO}_2$ ,  $\text{Fe}_{60}\text{Ni}_{40}/\text{SiO}_2$ ,  $\text{Fe}_{50}\text{Ni}_{50}/\text{SiO}_2$ ,  $\text{Fe}_{40}\text{Ni}_{60}/\text{SiO}_2$ ,  $\text{Fe}_{25}\text{Ni}_{75}/\text{SiO}_2$ ,  $\text{Fe}_{10}\text{Ni}_{90}/\text{SiO}_2$  and  $\text{Ni}_{100}/\text{SiO}_2$  during heating under  $\text{H}_2$  and after cooling to room temperature under  $\text{H}_2$  (RT).

**Table 3.9.** Values of  $a$  and composition of the crystalline core of bimetallic particles assessed through the linear Vegard correlation in Figure 3.21 after correction from a temperature effect, during heating under  $\text{H}_2$  at 500 and 700 °C and after cooling to room temperature under  $\text{H}_2$  (RT).

Samples	At 500 °C		At 700 °C		At room temperature under $\text{H}_2$ after reduction at 700 °C	
	$a$ (nm)	Composition	$a$ (nm)	Composition	$a$ (nm)	Composition
$\text{Fe}_{75}\text{Ni}_{25}/\text{SiO}_2$	0.3579	$\text{Fe}_{32}\text{Ni}_{68}$	0.3609	$\text{Fe}_{54}\text{Ni}_{46}$	0.3591	$\text{Fe}_{63}\text{Ni}_{37}$
$\text{Fe}_{60}\text{Ni}_{40}/\text{SiO}_2$	0.3569	$\text{Fe}_{23}\text{Ni}_{77}$	0.3589	$\text{Fe}_{35}\text{Ni}_{65}$	0.3572	$\text{Fe}_{45}\text{Ni}_{55}$
$\text{Fe}_{50}\text{Ni}_{50}/\text{SiO}_2$	0.3567	$\text{Fe}_{22}\text{Ni}_{78}$	0.3584	$\text{Fe}_{31}\text{Ni}_{69}$	0.3555	$\text{Fe}_{29}\text{Ni}_{71}$
$\text{Fe}_{40}\text{Ni}_{60}/\text{SiO}_2$	0.3564	$\text{Fe}_{18}\text{Ni}_{82}$	0.3583	$\text{Fe}_{30}\text{Ni}_{70}$	0.3553	$\text{Fe}_{27}\text{Ni}_{73}$
$\text{Fe}_{25}\text{Ni}_{75}/\text{SiO}_2$	0.3550	$\text{Fe}_5\text{Ni}_{95}$	0.3566	$\text{Fe}_{15}\text{Ni}_{85}$	0.3534	$\text{Fe}_9\text{Ni}_{91}$
$\text{Fe}_{10}\text{Ni}_{90}/\text{SiO}_2$	0.3548	$\text{Fe}_3\text{Ni}_{97}$	0.3564	$\text{Fe}_{13}\text{Ni}_{87}$	0.3532	$\text{Fe}_8\text{Ni}_{92}$

At this stage, the molar proportions of Fe and Ni in the catalysts from the series have been measured by XRF, XPS and XRD and can be compared. In all cases, more Ni is found to be deposited by DPU than expected, as shown in Figure 3.24. Despite their differences (bulk vs. surface techniques, global composition vs. composition of a crystalline domain), the three methods give similar proportions of Ni, with a good agreement for Ni-rich catalysts, meaning that the data obtained are consistent, and that Ni does react preferentially with silica during the DPU process whatever the proportions in solution.

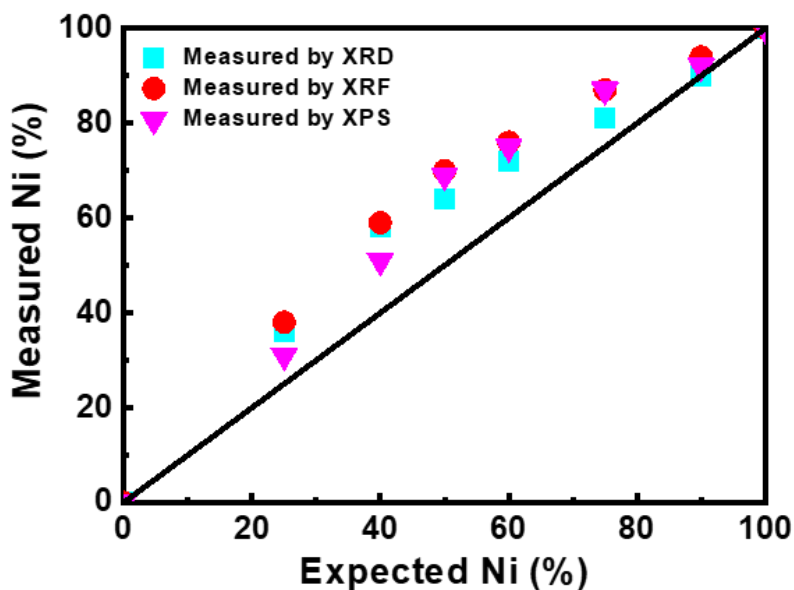


**Figure 3.24.** Actual Fe-Ni composition measured by different characterization methods, compared with the proportion of Ni in the DPU solution.

### III.5. Conclusions

The preparation of bimetallic Fe-Ni/SiO<sub>2</sub> catalysts by deposition-precipitation with urea requires the use of a Fe(II) salt and the absence of oxidizing species such as nitrates or dissolved oxygen. A layered structure best described as an ill-crystallized Fe-containing Ni(II) 1:1 phyllosilicate is formed after 22 h of DPU, with a lower proportion of Fe compared with the composition of the DPU solution, due to a preferential reaction of Ni<sup>2+</sup> ions with silica. The oxidation of Fe<sup>2+</sup> to Fe<sup>3+</sup> upon drying and storage does not challenge the subsequent formation of bimetallic particles upon reduction. Reduction under H<sub>2</sub> proceeds in several stages: (1) reduction of Fe<sup>3+</sup> ions to Fe<sup>2+</sup> above 275 °C; (2) reduction of Ni<sup>2+</sup> to Ni(0) above 350 °C, triggering the progressive reduction of Fe<sup>2+</sup> ions to the metallic state and the formation of *fcc* alloyed Fe-Ni nanoparticles; (3) deeper reduction of Fe<sup>2+</sup> ions between 500 and 700 °C to metallic state. In terms of reduction temperature, the reducibility of the catalyst is maximum for formulations containing a molar proportion of 60-75 at% Ni. Ni increases the reducibility of Fe, but too much Ni leads to a more organized phyllosilicate that is more difficult to reduce. The core composition of Fe-Ni bimetallic particles can be assessed during and after reduction



under H<sub>2</sub> according to the linear Vegard correlation. This confirms the presence of an excess of Ni in the catalyst compared with the metal proportions in solution, and the progressive insertion of Fe into the crystalline core of the Fe-Ni nanoparticles during the last stage of reduction.

## References

- [1] P. Burattin, M. Che, C. Louis, Characterization of the Ni(II) phase formed on silica upon deposition-precipitation, *Journal of Physical Chemistry B*, 101 (1997) 7060-7074.
- [2] P. Burattin, M. Che, C. Louis, Molecular approach to the mechanism of deposition - precipitation of the Ni(II) phase on silica, *Journal of Physical Chemistry B*, 102 (1998) 2722-2732.
- [3] P. Burattin, M. Che, C. Louis, Metal particle size in Ni/SiO<sub>2</sub> materials prepared by deposition-precipitation: Influence of the nature of the Ni(II) phase and of its interaction with the support, *Journal of Physical Chemistry B*, 103 (1999) 6171-6178.
- [4] P. Burattin, M. Che, C. Louis, Ni/SiO<sub>2</sub> materials prepared by deposition-precipitation: Influence of the reduction conditions and mechanism of formation of metal particles, *Journal of Physical Chemistry B*, 104 (2000) 10482-10489.
- [5] S. Sitthisa, W. An, D. E. Resasco, Selective conversion of furfural to methylfuran over silica-supported NiFe bimetallic catalysts, *Journal of Catalysis*, 284 (2011) 90-101.
- [6] T. Yamashita, P. Hayes, Analysis of XPS spectra of Fe<sup>2+</sup> and Fe<sup>3+</sup> ions in oxide materials, *Applied Surface Science*, 254 (2008) 2441-2449.
- [7] E. H. Nickel, J. E. Wildman, Hydrohonessite - a new hydrated Ni-Fe hydroxy-sulfate mineral – its relationship to honessite, carboydite, and minerals of the pyroaurite group, *Mineralogical Magazine*, 44 (1981) 333-337.
- [8] L. H. G. Chaves, J. E. Curry, D. A. Stone, M. D. Carducci, J. Chorover, Nickel incorporation in Fe(II, III) hydroxysulfate green rust: effect on crystal lattice spacing and oxidation products, *Revista Brasileira De Ciencia Do Solo*, 33 (2009) 1115-1123.
- [9] J. M. R. Génin, R. Aïssa, A. Géhin, M. Abdelmoula, O. Benali, V. Ernstsens, G. Ona-Nguema, C. Upadhyay, C. Ruby, Fougerite and Fe<sup>II-III</sup> hydroxycarbonate green rust; ordering, deprotonation and/or cation substitution; structure of hydrotalcite-like compounds and mythic ferrosic hydroxide, *Solid State Sciences*, 7 (2005) 545-572.
- [10] J. M. R. Génin, A. Renard, C. Ruby, M. Abdelmoula, In situ oxidation of green rusts by deprotonation; wet corrosion and passivation of weathering steels, *Journal of Physics:*

Conference Series, 217 (2010) 012095.

[11] X. Wang, F. Liu, W. Tan, X. Feng, L. K. Koopal, Transformation of hydroxycarbonate green rust into crystalline iron (hydr)oxides: Influences of reaction conditions and underlying mechanisms, *Chemical Geology*, 351 (2013) 57-65.

[12] V. Briois, C. La Fontaine, S. Belin, L. Barthe, T. Moreno, V. Pinty, A. Carcy, R. Girardot, E. Fonda, Rock: the new Quick-EXAFS beamline at SOLEIL, *Journal of Physics: Conference Series*, 712 (2016) 012149.

[13] K. W. Chung, Y. T. Kho, K. B. Kim, Oxidation behavior of  $\text{Ni}_x\text{Fe}_{1-x}(\text{OH})_2$  in Cl-containing solution, *Corrosion Science*, 44 (2002) 2757-2775.

[14] F. Menil, Systematic trends of the  $^{57}\text{Fe}$  Mössbauer isomer-shifts in  $(\text{FeO}_n)$  and  $(\text{FeF}_n)$  polyhedra – evidence of a new correlation between the isomer – shift and the inductive effect of the competing bond T-X (- Fe) (where X is O or F and T any element with a formal positive charge), *Journal of Physics and Chemistry of Solids*, 46 (1985) 763-789.

[15] M. L. M. de Carvalho-e-Silva, C. S. M. Partiti, J. Enzweiler, S. Petit, S. M. Netto, S. M. B. de Oliveira, Characterization of Ni-containing goethites by Mössbauer spectroscopy and other techniques, *Hyperfine Interactions*, 142 (2002) 559-576.

[16] M. Usman, M. Abdelmoula, K. Hanna, B. Grégoire, P. Faure, C. Ruby,  $\text{Fe}^{\text{II}}$  induced mineralogical transformations of ferric oxyhydroxides into magnetite of variable stoichiometry and morphology, *Journal of Solid State Chemistry*, 194 (2012) 328-335.

[17] N. A. Halasa, G. Depasquali, H. G. Drickamer, High-pressure studies on ferrites, *Physical Review B*, 10 (1974) 154-164.

[18] E. Murad, U. Schwertmann, The Mössbauer spectrum of ferrihydrite and its relations to those of other iron-oxides, *American Mineralogist*, 65 (1980) 1044-1049.

[19] X. Wang, M. Zhu, L. K. Koopal, W. Li, W. Xu, F. Liu, J. Zhang, Q. Liu, X. Feng, D. L. Sparks, Effects of crystallite size on the structure and magnetism of ferrihydrite, *Environmental Science: Nano*, 3 (2016) 190-202.

[20] F. Baron, S. Petit, M. Pentrak, A. Decarreau, J. W. Stucki, Revisiting the nontronite Mössbauer spectra, *American Mineralogist*, 102 (2017) 1501-1515.

- [21] S. Suzuki, T. Suzuki, M. Kimura, Y. Takagi, K. Shinoda, K. Tohji, Y. Waseda, EXAFS characterization of ferric oxyhydroxides, *Applied Surface Science*, 169 (2001) 109-112.
- [22] C. M. van Genuchten, J. Pena, S. E. Amrose, A. J. Gadgil, Structure of Fe(III) precipitates generated by the electrolytic dissolution of Fe(0) in the presence of groundwater ions, *Geochimica et Cosmochimica Acta*, 127 (2014) 285-304.
- [23] S. Peulon, Electrochemical deposition of thin films of green rusts 1 and 2 on inert gold substrate, *Electrochemistry Communications*, 5 (2003) 208-213.
- [24] A. Zegeye, G. Ona-Nguema, C. Carteret, L. Huguet, M. Abdelmoula, F. Jorand, Formation of hydroxysulphate green rust 2 as a single Iron(II-III) mineral in microbial culture, *Geomicrobiology Journal*, 22 (2005) 389-399.
- [25] H. Brongersma, M. Draxler, M. Deridder, P. Bauer, Surface composition analysis by low-energy ion scattering, *Surface Science Reports*, 62 (2007) 63-109.
- [26] G. B. Raupp, W. N. Delgass, Mössbauer investigation of supported Fe and FeNi catalysts. 1. Effect of pretreatment on particle-size, *Journal of Catalysis*, 58 (1979) 337-347.
- [27] G. B. Raupp, W. N. Delgass, Mössbauer investigation of supported Fe and FeNi catalysts. 2. Carbides formed by Fischer – Tropsch synthesis, *Journal of Catalysis*, 58 (1979) 348-360.
- [28] E. E. Unmuth, L. H. Schwartz, J. B. Butt, Iron alloy Fischer-Tropsch catalysts. 1. Oxidation-reduction studies of the Fe-Ni system, *Journal of Catalysis*, 61 (1980) 242-255.
- [29] F. Bødker, I. Chorkendorff, S. Mørup, Nitrogen chemisorption on  $\alpha$ -Fe nanoparticles studied by in situ Mössbauer spectroscopy, *Zeitschrift für Physik D Atoms, Molecules and Clusters*, 40 (1997) 152-154.
- [30] C. E. Johnson, T. E. Cranshaw, M. S. Ridout, Mössbauer effect in iron alloys, *Proceedings of the Physical Society of London*, 81 (1963) 1079-1090.
- [31] K. Nagorny, S. Bubert, Mössbauer spectroscopic investigations of bimetallic FeCo, FeNi and FeRu model catalysts supported on magnesium-hydroxide carbonate, *Journal of Catalysis*, 108 (1987) 112-134.
- [32] D. Li, M. Koike, L. Wang, Y. Nakagawa, Y. Xu, K. Tomishige, Regenerability of hydrotalcite-derived nickel-iron alloy nanoparticles for syngas production from biomass tar, *ChemSusChem*, 7 (2014) 510-522



# Chapter IV

## Characterization of Fe-Ni/SiO<sub>2</sub> nanoparticles after pre-reduction and during reductive activation



## IV.1. Introduction

Chapter III has presented a macroscopic characterization of the catalysts from the deposition-precipitation process to the end of the reduction stage. The purpose of Chapter IV is to analyze bimetallic Fe-Ni nanoparticles individually after reduction at 700 °C (the "pre-reduction" step) and exposure to air, and to investigate their homogeneity in size, global chemical composition, and chemical composition within each nanoparticle. It will also be verified how the two metals interact with each other upon a new stage of activation in H<sub>2</sub>, as will be done prior to the catalytic reaction (exposed in the next chapter).

## IV.2. Characterization of the Fe-Ni nanoparticles on system Fe<sub>50</sub>Ni<sub>50</sub>/SiO<sub>2</sub>

The supported metal nanoparticles on Fe<sub>50</sub>Ni<sub>50</sub>/SiO<sub>2</sub> were chosen as a first case study, and were investigated at the University of Oxford, before having access to the Titan Themis microscope at Lille University (next section). They were characterized by bright field TEM after reduction at 500 or 700 °C, and exposure of the samples to ambient air (Figure 4.1a and b). After reduction at 500 °C, nanoparticles appeared as evenly distributed over the siliceous support and exhibited an average diameter of 5.1 nm (standard deviation: 0.9 nm), with a high proportion of smaller particles (Figure 4.1a). Agglomeration was not observed after reduction at 700 °C, and the bimetallic nanoparticles were still evenly distributed on the silica substrate despite the high metal loading, with a separation distance of 5 nm on average. The size distribution histogram shows that the average size, 5.4 nm, has only slightly increased between 500 and 700 °C (Figure 4.2b). The standard deviation was 1.3 nm and the size distribution was more symmetrical, with a lower proportion of smaller particles. Particle growth with temperature as evidenced by *in situ* XRD is thus confirmed.



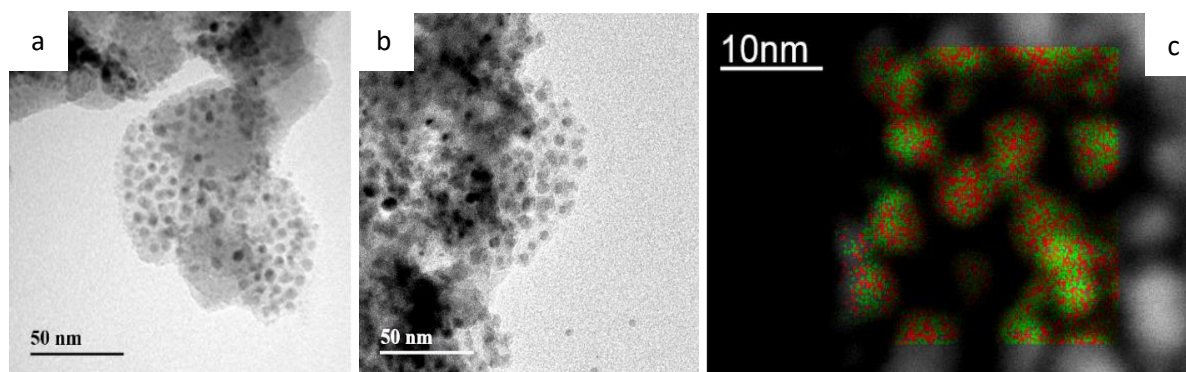


**Figure 4.1.** Left: Bright field TEM micrographs of Fe<sub>50</sub>Ni<sub>50</sub>/SiO<sub>2</sub>: a) after reduction at 500 °C and exposure to air; b) after reduction at 700 °C and exposure to air. Right: c) EDX mapping of Fe<sub>50</sub>Ni<sub>50</sub>/SiO<sub>2</sub> after reduction at 500 °C and exposure to air (Fe: red; Ni: green).

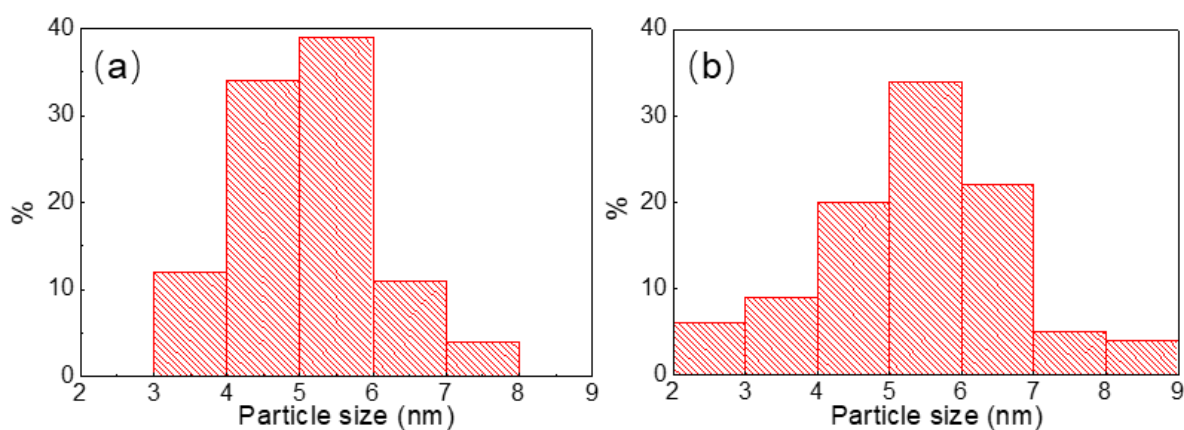


**Figure 4.2.** Particle size distributions measured by TEM for Fe<sub>50</sub>Ni<sub>50</sub>/SiO<sub>2</sub>: a) after reduction at 500 °C and exposure to air; b) after reduction at 700 °C and exposure to air.

The elemental distribution of Fe and Ni was examined by EDX mapping after reduction at 500 °C (Figure 4.1). No metal was detected on bare zones of the support. The composition of 28 individual particles was measured, resulting in an average composition of Fe<sub>31</sub>Ni<sub>69</sub>, and a standard deviation of 8 at% (Table 4.1). This value is in line with the quantifications presented in the former chapter. Both elements were present in every particle and Fe was never the major metal. This indicates that the non-magnetic, non-ordered metallic Fe species detected by *in situ* MössS in Chapter III are presumably a Fe-rich shell surrounding the Fe-Ni core of the nanoparticles.

**Table 4.1.** EDX point scan measurements on 28 individual particles from Fe<sub>50</sub>Ni<sub>50</sub>/SiO<sub>2</sub> reduced at 500 °C and exposed to air.

	Fe at %	Ni at %
	31	69
	29	71
	47	53
	28	72
	41	59
	36	64
	24	76
	39	61
	37	63
	41	59
	16	84
	14	86
	25	75
	38	62
	28	72
	30	70
	39	61
	30	70
	31	69
	19	81
	29	71
	36	64
	25	75
	32	68
	46	54
	19	81
	25	75
	33	67
Average:	31%	69%
Standard deviation for Fe: 8 at%		

In Oxford, it was not possible to perform point scans along the diameter of particles, owing to their small size, or to evidence local metal segregation. Moreover, the comparison with *in situ* measurements presented in Chapter III is not straightforward, as the distribution of the metals may be perturbed by metal oxidation upon exposure to air [1].

### IV.3. Characterization of the Fe-Ni nanoparticles across the Fe-Ni/SiO<sub>2</sub> series

In order to determine the particle size distribution of samples with different Fe/Ni proportions after reduction at 700 °C and exposure to air, bright field TEM was subsequently used at Lille University for Fe<sub>75</sub>Ni<sub>25</sub>/SiO<sub>2</sub>, Fe<sub>60</sub>Ni<sub>40</sub>/SiO<sub>2</sub>, Fe<sub>50</sub>Ni<sub>50</sub>/SiO<sub>2</sub>, Fe<sub>40</sub>Ni<sub>60</sub>/SiO<sub>2</sub>, Fe<sub>25</sub>Ni<sub>75</sub>/SiO<sub>2</sub>, Fe<sub>10</sub>Ni<sub>90</sub>/SiO<sub>2</sub> and Ni<sub>100</sub>/SiO<sub>2</sub>. The corresponding histograms are presented in Figure 4.3, 4.4 and 4.5. The average particle sizes calculated from the histograms are given in

Table 4.2. Narrow size distributions centered on 5-6 nm were found for all the catalysts. The values of the average particle size are consistent with those calculated from the X-ray diffractograms presented in Chapter III (Figure 3.21), using the Scherrer equation.

**Table 4.2.** Average particle size according to X-ray diffraction and from TEM images for bimetallic Fe-Ni/SiO<sub>2</sub> catalysts and monometallic Ni/SiO<sub>2</sub> reduced at 700 °C and exposed to air.

Samples	Average particle size (nm)	
	Measured by XRD	Measured by TEM
Fe <sub>75</sub> Ni <sub>25</sub> /SiO <sub>2</sub>	6	6
Fe <sub>60</sub> Ni <sub>40</sub> /SiO <sub>2</sub>	6	5
Fe <sub>50</sub> Ni <sub>50</sub> /SiO <sub>2</sub>	5	5
Fe <sub>40</sub> Ni <sub>60</sub> /SiO <sub>2</sub>	5	6
Fe <sub>25</sub> Ni <sub>75</sub> /SiO <sub>2</sub>	6	6
Fe <sub>10</sub> Ni <sub>90</sub> /SiO <sub>2</sub>	5	6
Ni <sub>100</sub> /SiO <sub>2</sub>	5	5

The metal dispersion  $D$  (%), which is the ratio between the number of atoms at the surface of the particles and the total number of atoms inside the particles, was calculated for bimetallic catalysts by applying  $97.1/\varnothing$  (nm) to each class of diameter  $\varnothing$  from the histograms in Figure 4.3 and 4.4, assuming that metal particles are hemispherical and that this calculation, usually applied to *fcc* Ni [2, 3], can be extended to *fcc* Fe-Ni alloys. Values of  $D$  (%) range from 16 to 22%. The metal surface area exposed per gram of catalyst is evaluated between 56 to 77 m<sup>2</sup> g<sub>cat</sub><sup>-1</sup>, assuming that one Fe or Ni atom occupies 6.3 Å<sup>2</sup> [2, 3].

The distribution of Fe and Ni for individual Fe-Ni nanoparticles after reduction at 700 °C and exposure to air was also studied by STEM-EELS coupled to HAADF imaging, for Fe<sub>60</sub>Ni<sub>40</sub>/SiO<sub>2</sub>, Fe<sub>50</sub>Ni<sub>50</sub>/SiO<sub>2</sub>, Fe<sub>40</sub>Ni<sub>60</sub>/SiO<sub>2</sub> and Fe<sub>25</sub>Ni<sub>75</sub>/SiO<sub>2</sub> (Figure 4.5-4.8). It reveals that all Fe-Ni nanoparticles possess a core-shell structure, with Fe-Ni alloys in the core, and some Fe-rich phases in a 1-nm thick oxidized shell (characterization by X-ray absorption spectroscopy will be presented in section IV.4). This observation can be linked to the supposed presence of a Fe-rich shell in the reduced particles, which becomes oxidized upon exposure to air. On some pictures (Figure 4.6 and 4.8), it can be seen that the Fe-rich shell has developed on one side of the particles and not all around.

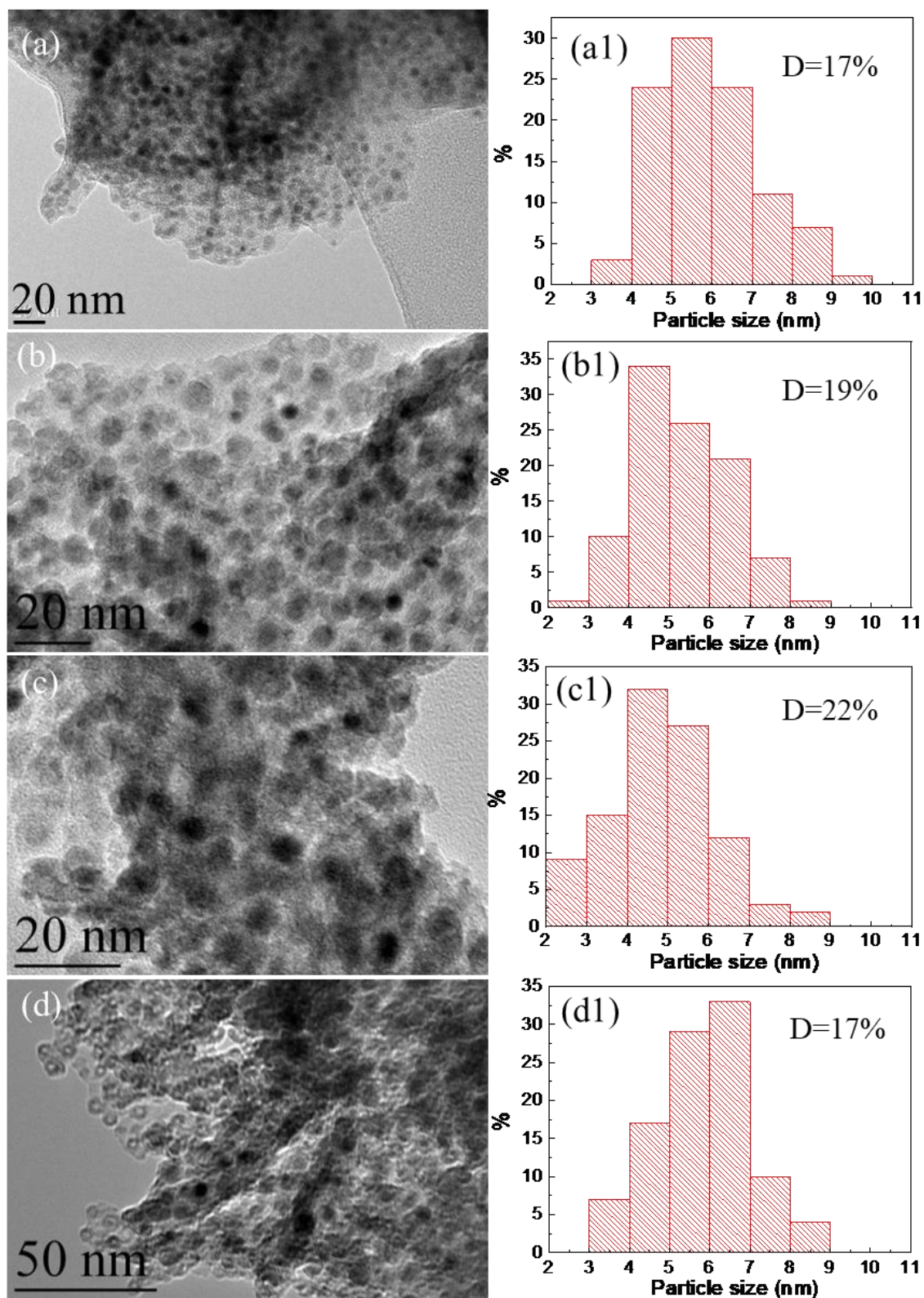


**Figure 4.3.** Bright field TEM micrographs and particle size distributions measured by TEM for Fe<sub>75</sub>Ni<sub>25</sub>/SiO<sub>2</sub> (a and a1), Fe<sub>60</sub>Ni<sub>40</sub>/SiO<sub>2</sub> (b and b1), Fe<sub>50</sub>Ni<sub>50</sub>/SiO<sub>2</sub> (c and c1) and Fe<sub>40</sub>Ni<sub>60</sub>/SiO<sub>2</sub> (d and d1) after reduction at 700 °C and exposure to air.

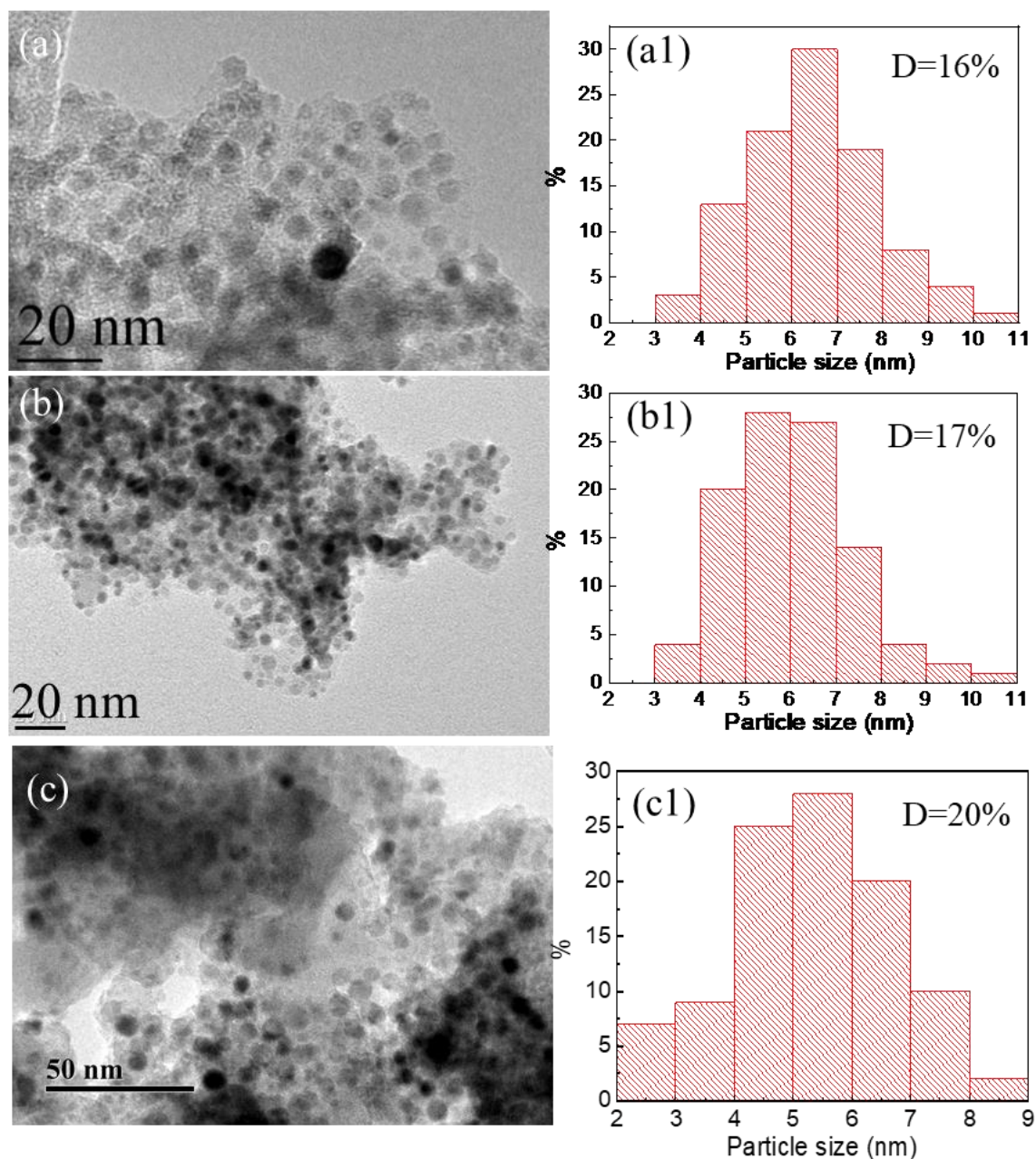


**Figure 4.4.** Bright field TEM micrographs and particle size distributions measured by TEM for Fe<sub>25</sub>Ni<sub>75</sub>/SiO<sub>2</sub> (a and a1), Fe<sub>10</sub>Ni<sub>90</sub>/SiO<sub>2</sub> (b and b1) and monometallic Ni<sub>100</sub>/SiO<sub>2</sub> (c and c1) after reduction at 700 °C and exposure to air.

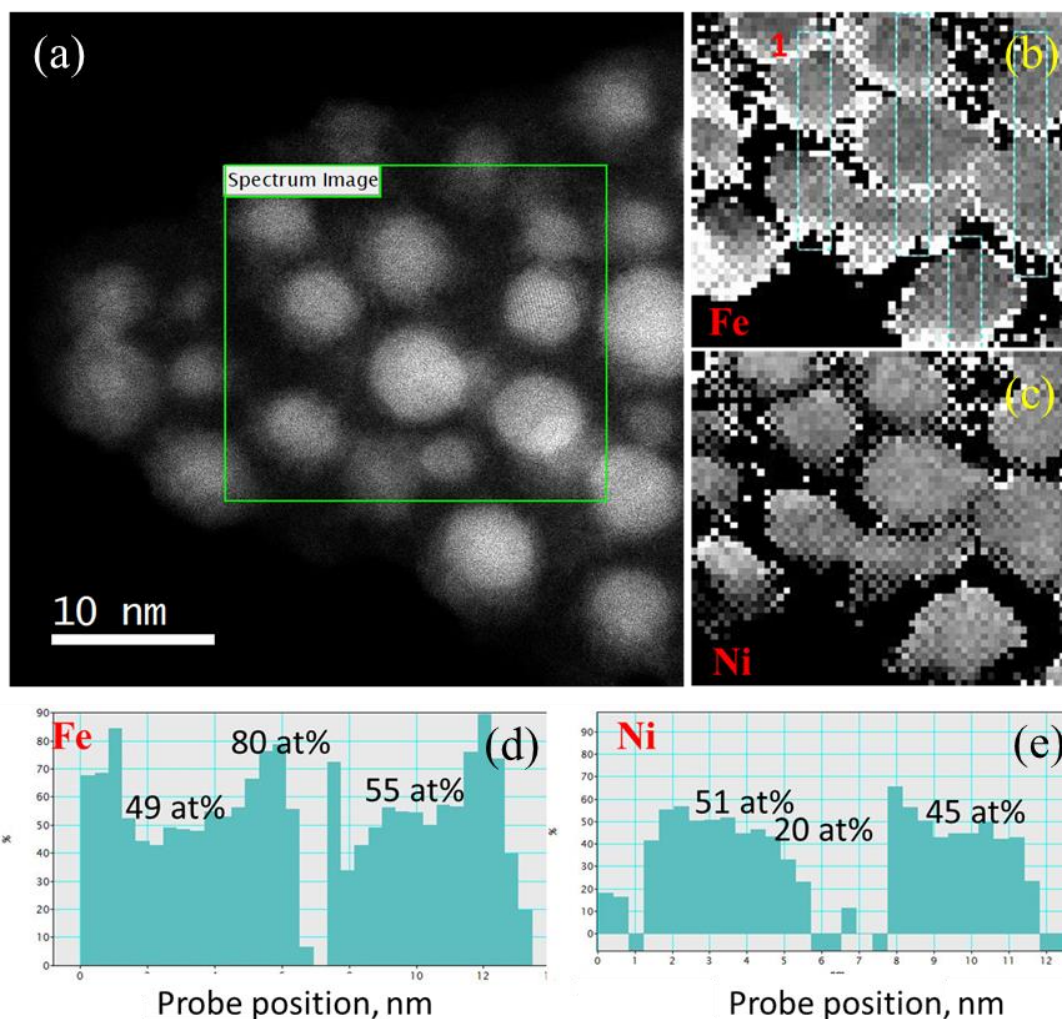


**Figure 4.5.** STEM - HAADF image (a) and relative composition maps for Fe-L<sub>3,2</sub> edge at 708 eV (b) and Ni-L<sub>3,2</sub> edge at Ni-L<sub>3,2</sub> at 855 eV (c) obtained by STEM - EELS mapping for Fe<sub>60</sub>Ni<sub>40</sub>/SiO<sub>2</sub> after reduction at 700 °C and exposure to air. Panels (d) and (e) show extracted relative concentration profiles (indicated with 1 in (b)) for two particles, for Fe (d) and Ni (e). The extraction has been done from the concentration maps from (b) and (c) respectively.

**Table 4.3.** Composition measurements extracted from STEM - EELS mapping of the core of individual particles from Fe<sub>60</sub>Ni<sub>40</sub>/SiO<sub>2</sub> reduced at 700 °C and exposed to air (error bar: +/-5 at%).

	Fe at %	Ni at %
	60	40
	49	51
	55	45
	42	58
	40	60
	42	58
	49	51
	58	42
	45	55
	40	60
Average:	48%	52%
Standard deviation for Fe:	7 at%	

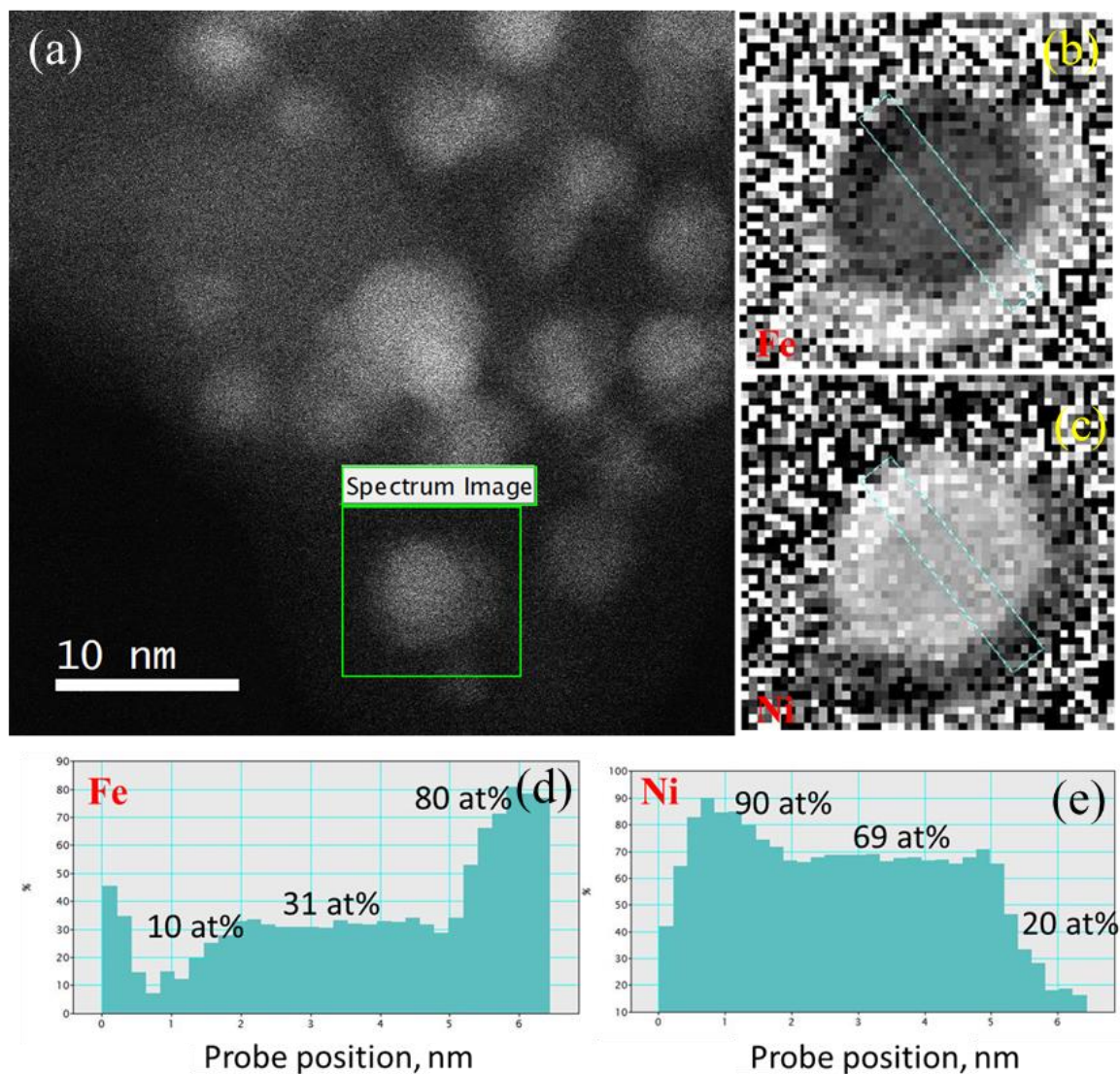


**Figure 4.6.** STEM - HAADF image (a) and relative composition maps for Fe-L<sub>3,2</sub> edge at 708 eV (b) and Ni-L<sub>3,2</sub> edge at Ni-L<sub>3,2</sub> at 855 eV (c) obtained by STEM - EELS mapping for Fe<sub>50</sub>Ni<sub>50</sub>/SiO<sub>2</sub> after reduction at 700 °C and exposure to air. Panels (d) and (e) show extracted relative concentration profiles on particle, for Fe (d) and Ni (e). The extraction has been done from the concentration maps from (b) and (c) respectively.

**Table 4.4.** Composition measurements extracted from STEM - EELS mapping of the core of individual particles from Fe<sub>50</sub>Ni<sub>50</sub>/SiO<sub>2</sub> reduced at 700 °C and exposed to air (error bar: +/-5 at%).

	Fe at %	Ni at %
	21	79
	31	69
	31	69
	60	40
	30	70
Average:	35%	65%
Standard deviation for Fe: 7 at%		

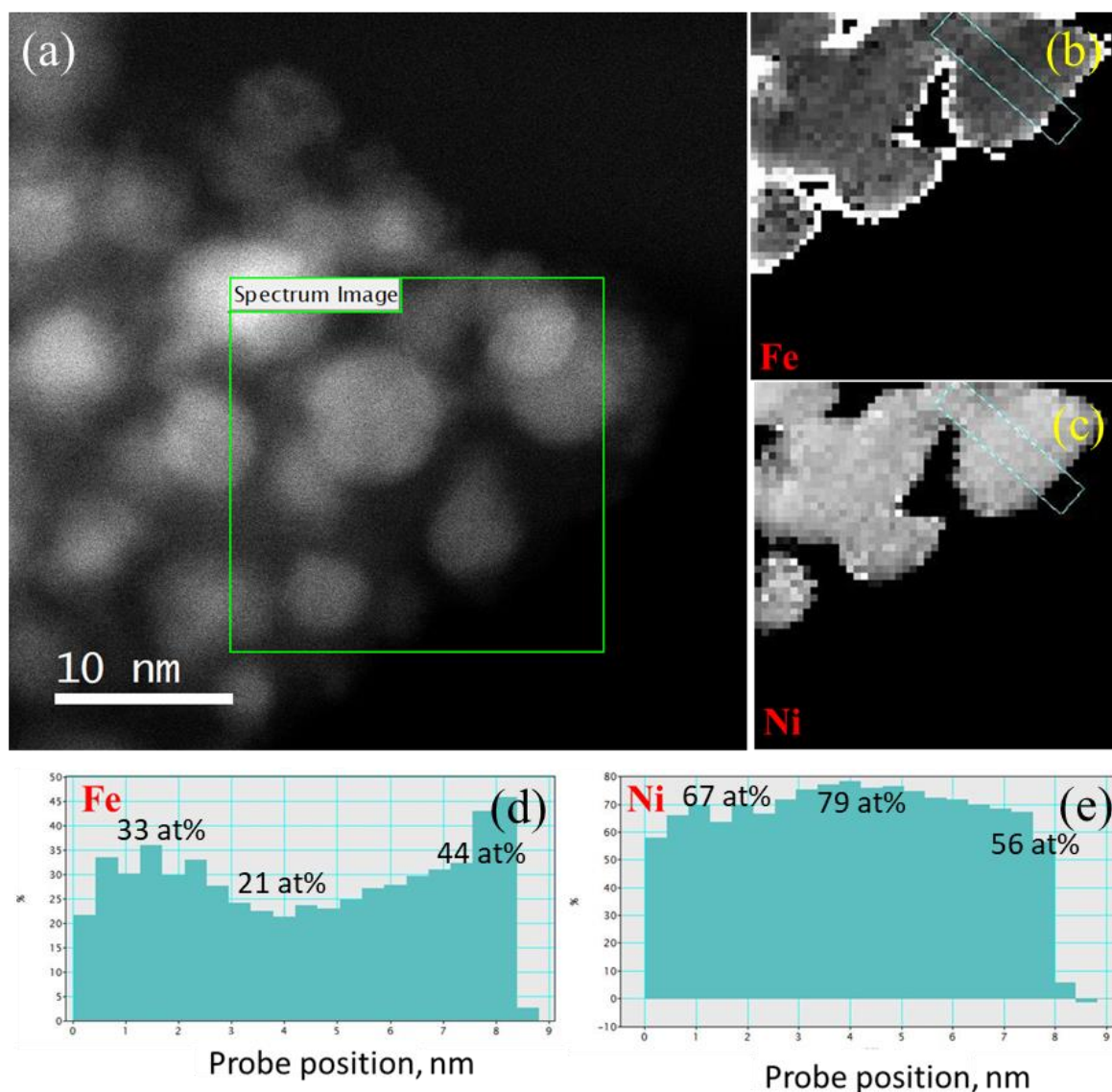


**Figure 4.7.** STEM - HAADF image (a) and relative composition maps for Fe-L<sub>3,2</sub> edge at 708 eV (b) and Ni-L<sub>3,2</sub> edge at Ni-L<sub>3,2</sub> at 855 eV (c) obtained by STEM - EELS mapping for Fe<sub>40</sub>Ni<sub>60</sub>/SiO<sub>2</sub> after reduction at 700 °C and exposure to air. Panels (d) and (e) show extracted relative concentration profiles on particle, for Fe (d) and Ni (e). The extraction has been done from the concentration maps from (b) and (c) respectively.

**Table 4.5.** Composition measurements extracted from STEM - EELS mapping of the core of individual particles from Fe<sub>40</sub>Ni<sub>60</sub>/SiO<sub>2</sub> reduced at 700 °C and exposed to air (error bar: +/-5 at%).

	Fe at %	Ni at %
	21	79
	30	70
	24	76
	25	75
Average:	25%	75%
Standard deviation for Fe: 7 at%		



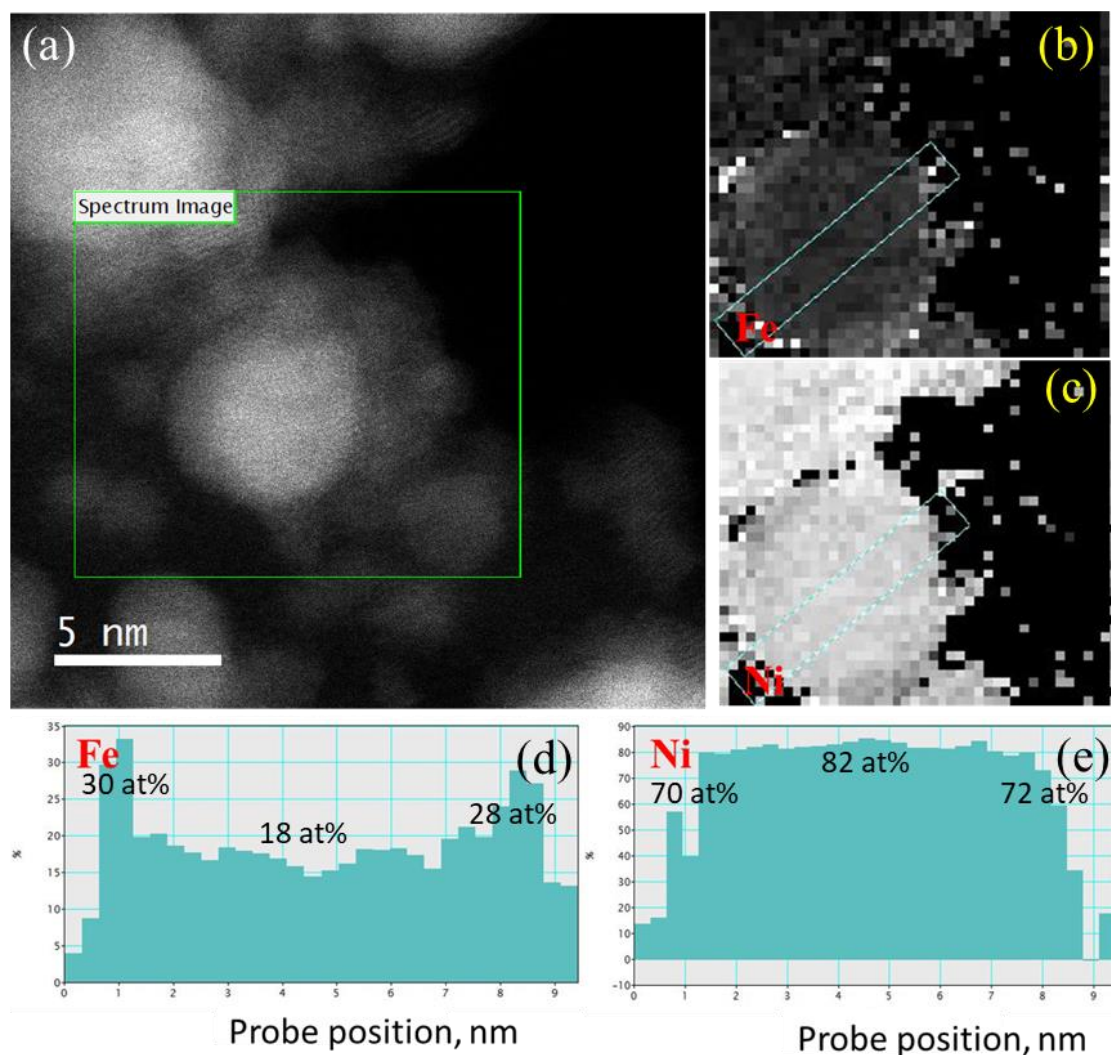


**Figure 4.8.** STEM - HAADF image (a) and relative composition maps for Fe-L<sub>3,2</sub> edge at 708 eV (b) and Ni-L<sub>3,2</sub> edge at Ni-L<sub>3,2</sub> at 855 eV (c) obtained by STEM - EELS mapping for Fe<sub>25</sub>Ni<sub>75</sub>/SiO<sub>2</sub> after reduction at 700 °C and exposure to air. Panels (d) and (e) show extracted relative concentration profiles on particle, for Fe (d) and Ni (e). The extraction has been done from the concentration maps from (b) and (c) respectively.

**Table 4.6.** Composition measurements extracted from STEM - EELS mapping of the core of individual particles from Fe<sub>25</sub>Ni<sub>75</sub>/SiO<sub>2</sub> reduced at 700 °C and exposed to air (error bar: +/-5 at%).

	Fe at %	Ni at %
	6	94
	15	85
	10	90
	15	85
	10	90
	13	87
	14	86
	13	87
	18	82
Average:	12%	88%
Standard deviation for Fe: 7 at%		

The compositions of the core of different particles are given in Tables 4.3-4.6. The average values of composition for Fe and Ni are consistent with the compositions determined by XRD, XRF and XPS, shown in Chapter III (Figure 3.24). The standard deviation is found to be 7 at% in all cases, though it should be noted that some statistical samples are small. This value is consistent with the one presented in the former section (measurements carried out at the University of Oxford), with a larger sampling of particles.

In summary, deposition-precipitation with urea allows a good control of the Fe-Ni particles size (narrow size distribution centered on the same values of 5-6 nm) and corresponding dispersion (16-22%). The composition of individual nanoparticles is consistent with those estimated by XRD, XRF and XPS, and the standard deviation is small in all cases. After exposure to air, the bimetallic nanoparticles possess a Fe-Ni alloy core and a Fe-rich oxidized shell. The enrichment in Fe in the oxidized shell can derive from the presumed Fe-shell evidenced on one sample by Mössbauer spectroscopy in the reduced state. This enrichment can be due to the late reduction of Fe, in line with former interpretations from the literature based on spectroscopic data and on beta emission from radioactive Ni [4-7].

#### IV.4. Evolution of the nanoparticles upon activation in H<sub>2</sub>

Before being used for catalysis, the Fe-Ni/SiO<sub>2</sub> catalysts will be activated under H<sub>2</sub> in order to reduce the oxidic shell. In this section, it will be verified by *in situ* X-ray absorption spectroscopy at the Ni and Fe K edges, at what temperatures the two metal are reduced during this activation step, and if there is an interplay between the two metals, as was seen during the initial reduction process described in Chapter III. Reduction was investigated by synchrotron SOLEIL in the same conditions as in Chapter III, in a dilute hydrogen flow, and in a ramp up to 500 °C.

A chemometric analysis was carried out using the MCR-ALS procedure described in Chapter II, and implemented in Chapter III for the initial reduction process. The catalysts pre-reduced at 700 °C and exposed to air initially contain a mixture of metallic and oxidic Fe and Ni, and not pure phases. A first analysis by MCR-ALS of the experimental spectra recorded at

the Fe K edge did not allow extracting pure, separate components of iron in the oxidized and metallic state. Instead, the chemometric analysis was found to be based on the initial spectrum (mixture of oxidic and reduced iron) and on the final spectrum (reduced iron), without evidencing the possible presence of intermediate species.

To solve this problem, it was chosen to introduce in the matrices of experimental spectra reference spectra characteristic of Fe and Ni only in an oxidized state. The environment of Fe and Ni ions was not known precisely in the oxidized shell. Rather than using the spectrum from a reference salt, it was preferred to use the spectrum of each catalyst after calcination in air, in a muffle oven at 200 °C for 10 h. In these calcined solids, it was supposed that the metals ions would end up in a chemical environment similar to that of the oxidic shell, that is, a mixed Fe-Ni oxide.

The MCR-ALS procedure was then applied only to the XANES region; the EXAFS region will not be considered. Given these approximations, it will not be attempted to discuss a precise quantification of oxidized/metallic Fe or Ni in the initial catalysts. It will only be determined on which temperature range the two metals reduce, and how the reduction process of the two metals takes place with respect to each other.

The MCR-ALS analysis at the Ni K edge yielded only two contributions, the one of oxidized nickel (corresponding to the reference oxidized sample), and the final reduced metal. In contrast, the MCR-ALS analysis at the Fe K edge yielded three components, that can be interpreted as Fe<sup>3+</sup> ions (corresponding to the reference oxidized sample), transforming into Fe<sup>2+</sup> ions as intermediate species, and finally metallic Fe.

For the Fe<sub>75</sub>Ni<sub>25</sub>/SiO<sub>2</sub> catalyst, the reduction of Ni<sup>2+</sup> started at 240 °C, and the metal was completely reduced at 350 °C (Figure 4.9a). Fe<sup>3+</sup> ions started to transform into Fe<sup>2+</sup> ions at 120 °C. At 294 °C, Fe<sup>3+</sup> ions were totally transformed into Fe<sup>2+</sup> ions. When further increasing the reduction temperature, metallic Fe appeared and gradually increased at the expense of Fe<sup>2+</sup> ions. Finally, iron was totally reduced at 500 °C. The reduction process of Ni<sup>2+</sup> to metallic Ni matches well that of the reduction of Fe<sup>3+</sup> to Fe<sup>2+</sup>, and the formation of metallic iron starts at the same time as the formation of metallic Ni. Here as well, Ni can trigger the reduction of Fe,

which is consistent with the mechanism obtained for the pre-reduction step at 700 °C, discussed in Chapter III.

When increasing the Ni content, the tendencies for Fe and Ni reduction are similar to that found for the Fe<sub>75</sub>Ni<sub>25</sub>/SiO<sub>2</sub> catalyst, as shown in Figures 4.9(b-e). However, the start of the reduction of Fe<sup>3+</sup> to Fe<sup>2+</sup> ions shifts to lower temperatures, from 130 °C for Fe<sub>75</sub>Ni<sub>25</sub>/SiO<sub>2</sub> to 60 °C for Fe<sub>25</sub>Ni<sub>75</sub>/SiO<sub>2</sub>. The same tendency is found for the reduction of Fe<sup>2+</sup> ions to metallic Fe, which shifts from 294 °C for Fe<sub>75</sub>Ni<sub>25</sub>/SiO<sub>2</sub> to 182 °C for Fe<sub>25</sub>Ni<sub>75</sub>/SiO<sub>2</sub>. This indicates that increasing the proportion of Ni is beneficial for the reduction of Fe. Nevertheless, the complete reduction of iron to metallic Fe is often not found below 500 °C in these conditions of TPR, which is a higher temperature than for the complete reduction of Ni (complete below 400 °C).

EXAFS signals were recorded at room temperature under H<sub>2</sub>, after activation at 500 °C. The Fourier transforms at the Ni and K edges are presented in Figure 4.10 and will be commented only quantitatively. Whatever the Fe-Ni catalysts, the similar Fourier transforms for the two metals correspond to the metals in *fcc* environments, indicating that the majority of the two metals remain associated in *fcc* alloyed nanoparticles. If upon the reduction of the oxidic shell, Fe had been extracted as *bcc* nanoparticles, the Fourier transform would have been very different (red curve on Figure 4.15b, recorded on a metal foil of Fe).

In summary, the two metals present in the oxidic shell after exposure to air are reduced upon activation under H<sub>2</sub>, and the major part remains associated in the metallic state in alloyed *fcc* nanoparticles. Fe<sup>3+</sup> ions in the oxidic shell first reduce to Fe<sup>2+</sup>. Ni<sup>2+</sup> ions reduce to the metallic state, which provokes the reduction of Fe<sup>2+</sup> to the metallic state, as was the case, though in different phases, during the first reduction process described in Chapter III. The more Ni in the particles, the lower the temperature of reduction of Fe: here again, it is the reduction of Ni that triggers the reduction of Fe to the metallic state. Despite the presence of an excess of Fe in the oxidic shell surrounding Fe-Ni nanoparticles upon exposure to air, Fe does not appear to reduce separately.

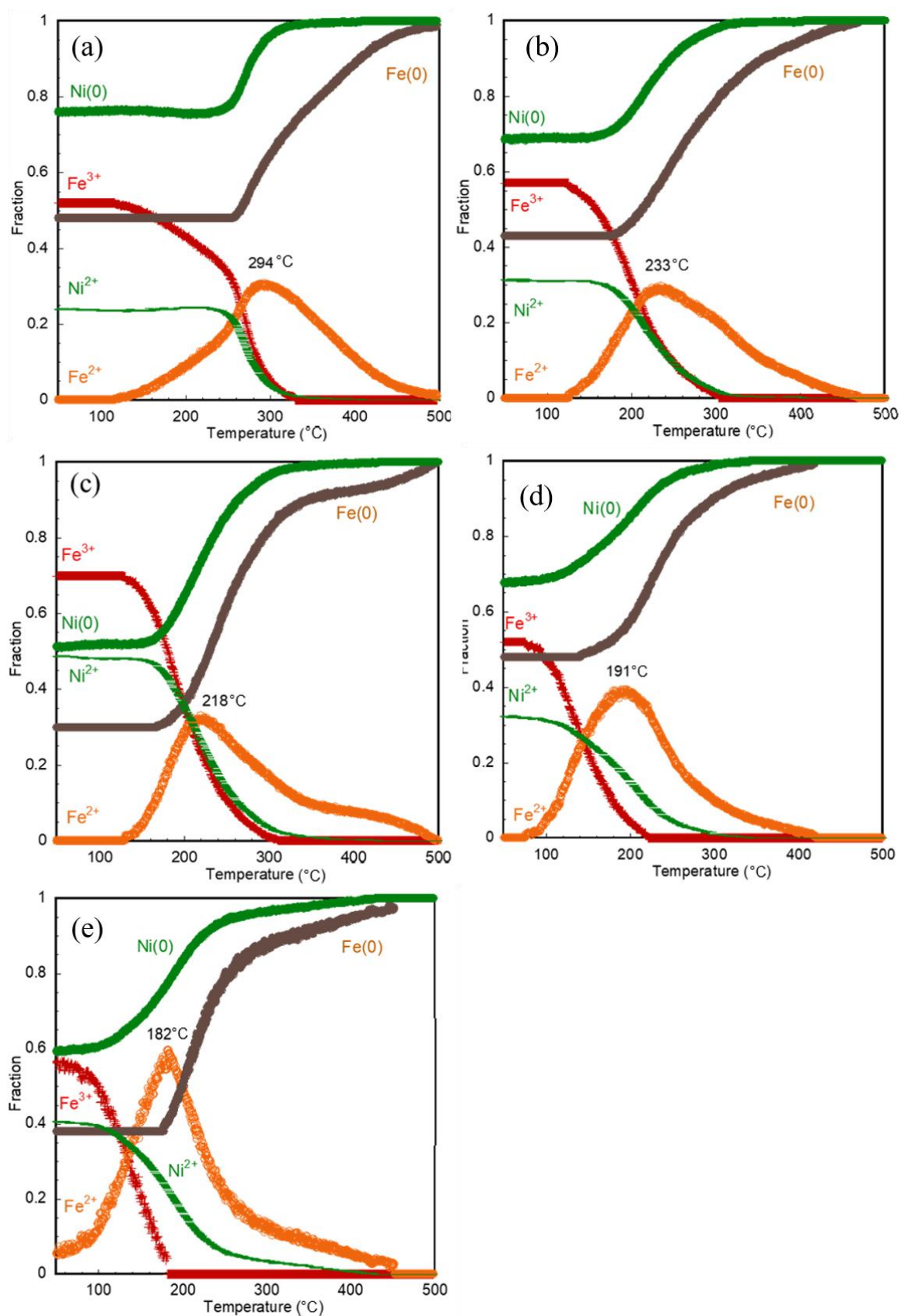


**Figure 4.9.** MCR-ALS analysis of the activation of Fe<sub>75</sub>Ni<sub>25</sub>/SiO<sub>2</sub> (a), Fe<sub>60</sub>Ni<sub>40</sub>/SiO<sub>2</sub> (b), Fe<sub>50</sub>Ni<sub>50</sub>/SiO<sub>2</sub> (c), Fe<sub>40</sub>Ni<sub>60</sub>/SiO<sub>2</sub> (d) and Fe<sub>25</sub>Ni<sub>75</sub>/SiO<sub>2</sub> (e) at the Ni K edge and at the Fe K edge.

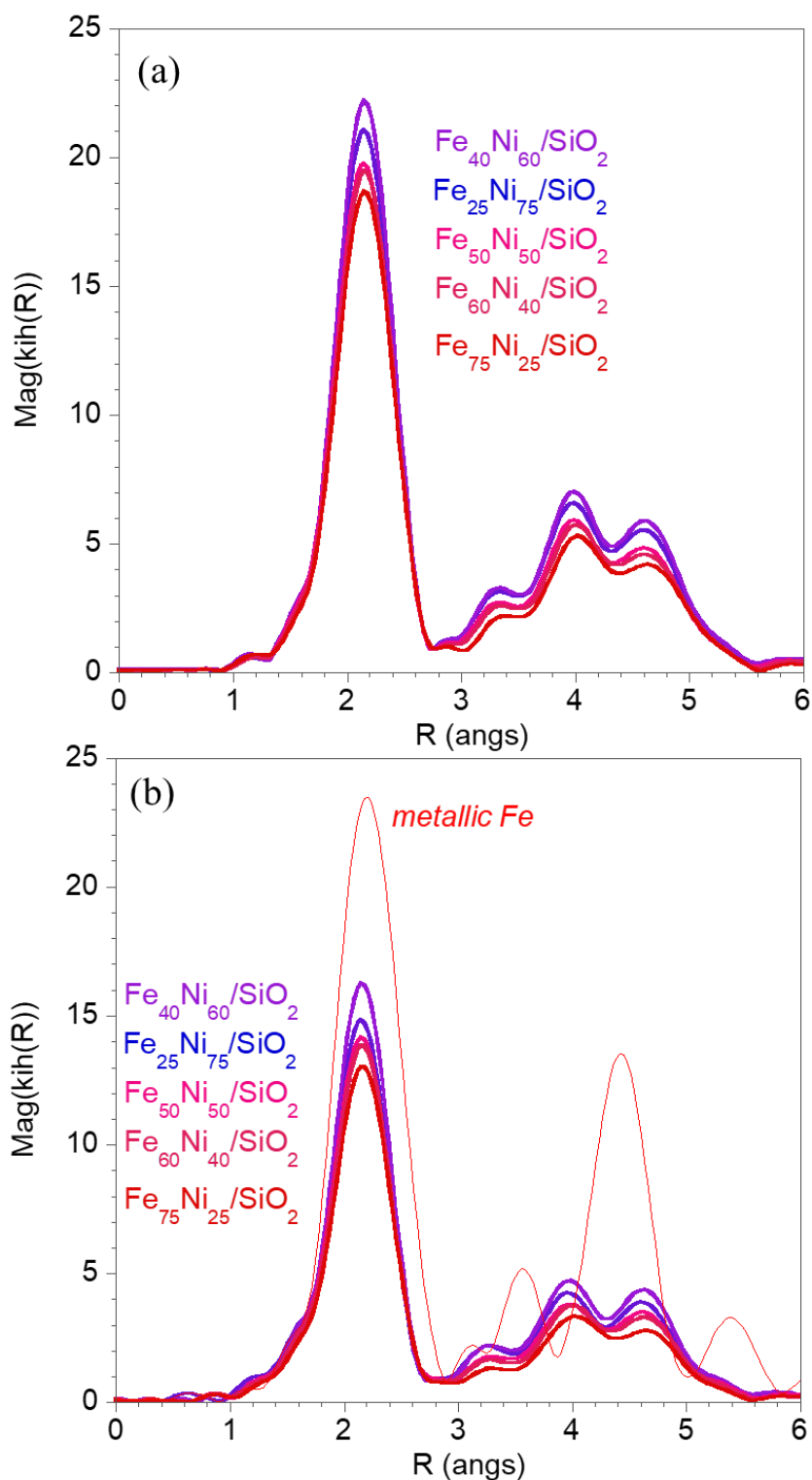


**Figure 4.10.** Fourier transforms of EXAFS signals recorded at room temperature for Fe-Ni/SiO<sub>2</sub> catalysts at the Ni K edge (a) and at the Fe K edge (b) after activation in H<sub>2</sub> at 500 °C.

## IV.5. Conclusions

After reduction at 700 °C and exposure to air, the bimetallic Fe-Ni particles prepared by deposition-precipitation with urea are homogeneous in size, and their average size is close to 5-6 nm. On each catalyst, the composition of the core of the Fe-Ni nanoparticles is consistent with that estimated by XRD, XRF and XPS, and the standard deviation is 7-8 Fe at%. After exposure to air, an oxidized shell is enriched in Fe whatever the catalyst composition. The oxidic shell can be reduced upon activation under H<sub>2</sub> up to 500 °C. Despite the partial segregation upon exposure to air, the major part of the two metals remains associated in the metallic state in alloyed *fcc* nanoparticles.

However, as X-ray absorption spectroscopy is an averaging method dominated by major species, it must be noted that it is not possible to know if a minor amount of metals remains unreduced after activation in H<sub>2</sub>, and if an excess of Fe remains at the surface of the particles, as was the case after the initial reduction at 700 °C. Given the presence of the Fe-enriched shell in the former stages of the catalysts preparation, and the low temperature at which the catalysts will be activated before catalytic test (400 °C), that should prevent a migration of Fe, we will consider that the persistence of the Fe-rich shell at the surface of the nanoparticles is likely after activation under H<sub>2</sub>. This is currently verified by *in situ* Mössbauer spectroscopy, which, as has been seen before, is sensitive to the presence of unreduced Fe<sup>2+</sup> ions and to non-magnetic Fe species in the catalysts. LEIS (Low Energy Ion Scattering) spectra will also be recorded after *in situ* activation under H<sub>2</sub>, in order to estimate, and if it is possible to quantify, the amount of Fe in the surface atomic layers of the nanoparticles.

## References

- [1] B. Mutz, M. Belimov, W. Wang, P. Sprenger, M. A. Serrer, D. Wang, P. Pfeifer, W. Kleist, J. D. Grunwaldt, Potential of an alumina-supported Ni<sub>3</sub>Fe Catalyst in the methanation of CO<sub>2</sub>: impact of alloy formation on activity and stability, *ACS Catalysis*, 7 (2017) 6802-6814.
- [2] A. Gil, A. Diaz, L. M. Gandia, M. Montes, Influence of the preparation method and the nature of the support on the stability of nickel-catalysts, *Applied Catalysis A: General*, 109 (1994) 167-179.
- [3] E. Marceau, A. Löfberg, J. M. Giraudon, F. Négrier, M. Che, L. Leclercq, From Al<sub>2</sub>O<sub>3</sub>-supported Ni(II)-ethylenediamine complexes to CO hydrogenation catalysts: characterization of the surface sites and catalytic properties, *Applied Catalysis A: General*, 362 (2009) 34-39.
- [4] L. Wang, D. Li, M. Koike, S. Koso, Y. Nakagawa, Y. Xu, K. Tomishige, Catalytic performance and characterization of Ni-Fe catalysts for the steam reforming of tar from biomass pyrolysis to synthesis gas, *Applied Catalysis A: General*, 392 (2011) 248-255.
- [5] K. Nagorny, S. Bubert, Mössbauer spectroscopic investigations of bimetallic FeCo, FeNi and FeRu model catalysts supported on magnesium-hydroxide carbonate, *Journal of Catalysis*, 108 (1987) 112-134.
- [6] M. Matsuyama, K. Ashida, O. Takayasu, T. Takeuchi, Catalytic activities of Ni-alloys expressed by surface and bulk compositions, *Journal of Catalysis*, 102 (1986) 309-315.
- [7] T. Mizushima, K. Tohji, Y. Udagawa, M. Harada, M. Ishikawa, A. Ueno, Characterization of silica-supported bimetallic iron-nickel catalysts by EXAFS, *Journal of Catalysis*, 112 (1988) 282-289.





# Chapter V

## Catalytic performances of the Fe-Ni/SiO<sub>2</sub> catalysts in the hydrogenation of furfural



## V.1. Introduction

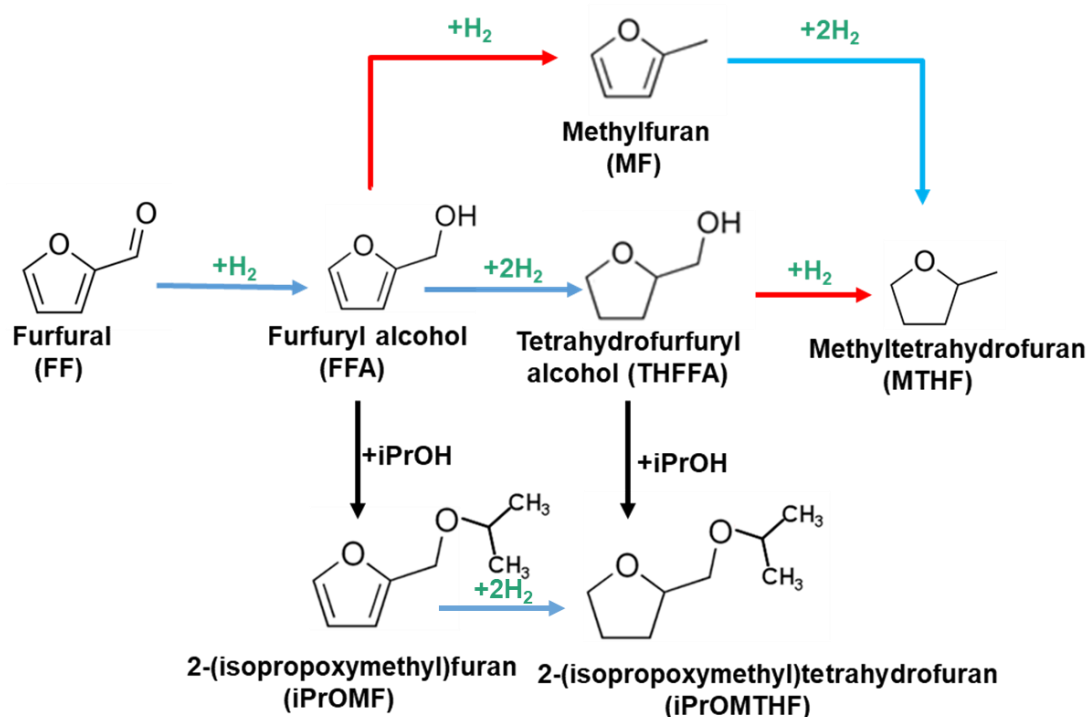
In this chapter, the Fe-Ni/SiO<sub>2</sub> catalysts prepared during this thesis will be tested in the hydrogenation of furfural (FF), a biosourced aldehyde belonging to the family of furanic compounds. Furfuryl alcohol (FFA), which is widely involved in the production of fine chemicals, rubbers and corrosion resistant glass fibers, will be the main target for this reaction of hydrogenation. Therefore, we will determine which Fe-Ni/SiO<sub>2</sub> catalysts are active and selective for the hydrogenation of the unsaturated C=O bond of furfural, while keeping the furan ring intact and avoiding the cleavage of the side-group, and we will try to correlate their catalytic performances with their physicochemical properties.

First, the whole series of Fe-Ni/SiO<sub>2</sub> catalysts prepared by deposition-precipitation, as described in Chapter III, and characterized in the reduced state in Chapter IV, will be tested in the hydrogenation of furfural and compared with the monometallic Ni/SiO<sub>2</sub> catalyst. The way Fe modifies the catalytic activity of nickel will be studied as a function of the Fe and Ni molar proportions, following the furfural conversion and the yield to FFA for different reaction times and masses of catalyst. A comparison between catalysts prepared by deposition-precipitation and by co-impregnation will also be carried out, in terms of reducibility, morphology of the Fe-Ni nanoparticles and catalytic results. We will finally try to explain the catalytic properties of Fe-Ni/SiO<sub>2</sub> catalysts by comparing these results with the characteristics of the nanoparticles presented in Chapter IV.

## V.2. Choice of the solvent and reaction pathways for the hydrogenation of furfural

The solvent has obviously a strong impact on the type of products formed in a liquid-phase reaction. Non-polar organic solvents, such as n-heptane, chlorobenzene and dichloroethane, are more likely to promote the hydrodeoxygenation (HDO) of furfural to methylfuran [1-4]. On the opposite, it has been shown that alcohols (methanol, ethanol, propanol, butanol) are more likely to favor the hydrogenation of the aldehyde group. For example, Chieffi *et al.* [5] found that Ni<sub>58</sub>Fe<sub>42</sub> particles supported on carbon exhibited a high conversion of furfural (99%) and selectivity to FFA (90%) in ethanol. Putro *et al.* [6] obtained a 95% furfural conversion with a

97% selectivity to FFA in isopropanol with a 20 wt% Fe<sub>25</sub>Ni<sub>75</sub>/Al<sub>2</sub>O<sub>3</sub> catalyst. Li *et al.* [7] found that unsupported Fe<sub>50</sub>Ni<sub>50</sub>-B boride nanoparticles present superior activity (conversion: 100%, selectivity to FFA: 100%) in ethanol solution. In this work, isopropanol has been chosen as solvent, to limit side-reactions of FF acetalization.



**Scheme 5.1.** Main products detected in this work in the hydroconversion of furfural, and reaction pathways: blue routes, hydrogenation; red routes: hydrogenolysis of the C-O bond; black routes: etherification with the solvent.

In our reaction conditions, the hydrogenation of furfural has yielded four products that could be identified by comparison of their GC retention times with those of commercial standards: furfuryl alcohol, FFA, resulting from the hydrogenation of the furfural aldehyde function; tetrahydrofurfuryl alcohol, THFFA, resulting from the hydrogenation of the furan ring of FFA; 2-methylfuran, MF, resulting from the hydrogenolysis of the C-O bond of FFA; and 2-methyltetrahydrofuran, MTHF, resulting both from the hydrogenolysis reaction and from the hydrogenation of the furan ring (**Scheme 5.1**).

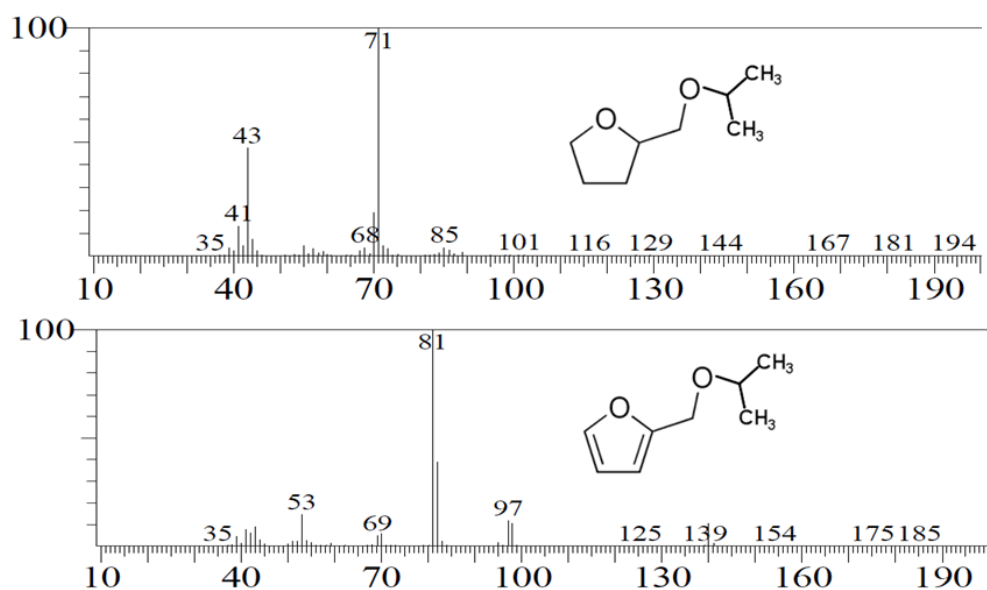


**Figure 5.1.** Mass spectra and identification of the two unknown products formed upon furfural transformation: iPrOMF, bottom; iPrOMTHF, top.

Moreover, two other products were identified by GC/MS, as ethers resulting from reactions between alcohols and the isopropanol solvent (Figure 5.1):

- (i) 2-(isopropoxymethyl)furan, iPrOMF, resulting from the etherification of FFA:  $m/z$  81, furan cycle + CH<sub>2</sub>, C<sub>5</sub>H<sub>5</sub>O; 97, furan cycle + CH<sub>2</sub>O, C<sub>5</sub>H<sub>5</sub>O<sub>2</sub>; 125, furan cycle + CH<sub>2</sub>OCHCH<sub>3</sub>, C<sub>7</sub>H<sub>9</sub>O<sub>2</sub>; 139, molecular peak – H, C<sub>8</sub>H<sub>12</sub>O<sub>2</sub>;
- (ii) 2-(isopropoxymethyl)tetrahydrofuran, iPrOMTHF, resulting from the etherification of THFFA, or from the hydrogenation of iPrOMF:  $m/z$  71, hydrogenated furan cycle, C<sub>4</sub>H<sub>7</sub>O; 85, hydrogenated furan cycle + CH<sub>2</sub>, C<sub>5</sub>H<sub>9</sub>O; 101, hydrogenated furan cycle + CH<sub>2</sub>O, C<sub>5</sub>H<sub>9</sub>O<sub>2</sub>; 129, hydrogenated furan cycle + CH<sub>2</sub>OCHCH<sub>3</sub>, C<sub>7</sub>H<sub>13</sub>O<sub>2</sub>; 144, molecular peak, C<sub>8</sub>H<sub>16</sub>O<sub>2</sub>.

It was verified that the production of each ether was associated to the production of the corresponding alcohol, and not with the amount of furfural in the reaction medium, which allowed discarding the formation of the acetalization product between furfural and two molecules of isopropanol.

GC calibration coefficients for ethers were estimated using the coefficient calculated for FFA or THFFA, multiplied by a factor 8/5 to account for the difference of number of carbon atoms.

### V.3. Choice of the experimental conditions for the hydrogenation of furfural

#### V.3.1. Choice of temperature and hydrogen pressure

In the literature, a reaction temperature of 150 °C has been usually selected for the hydrogenation of furfural to FFA in liquid phase. Chieffi *et al.* [5] found that at 150 °C a high conversion of furfural (99%) and selectivity to FFA (90%) were obtained. Putro *et al.* [6] also found that a 95% furfural conversion with a 97% selectivity to FFA was achieved at 150 °C. A lower reaction temperature always results both in a lower conversion of furfural and in a lower selectivity to FFA. Vetere *et al.* [8] showed that at 100 °C only 46% of the furfural was converted with 45.5% selectivity to FFA. Reyes *et al.* [9] found that 30% of the furfural was converted with 30% selectivity to FFA at 90 °C. Therefore, 150 °C has been chosen as reaction temperature in this work.

The hydrogen pressure in the system can significantly affect the products distribution. A DFT study by Wang *et al.* [10] showed that the product distribution depended on the adsorption energy and conformation of FF on the catalyst, which in turn was driven by the concentration of hydrogen adsorbed on the surface. When increasing the H<sub>2</sub> pressure from 10<sup>-4</sup> to 1 bar, H<sub>2</sub> would cover more completely the surface of the catalyst, and the adsorption energy would slightly decrease compared with that at a lower H<sub>2</sub> surface covering. Furfural adsorbs flatly at a low hydrogen pressure, and in a tilted way, with its carbonyl group interacting with the surface, at high hydrogen pressure. Meanwhile, Li *et al.* [7] showed that 100% conversion of furfural and 100% selectivity to FFA were achieved under 10 bar. Halilu *et al.* [11] obtained 94% conversion of furfural and ~100% of selectivity to FFA under 20 bar.

In initial experiments, a H<sub>2</sub> pressure of 10 bar was selected. However, the loss of solvent from the reactors was higher than 30% because of its volatility. Therefore, increasing the H<sub>2</sub> pressure was necessary. Using 20 bar as reaction pressure, less than 15% of solvent was lost by evaporation, which was considered to be the acceptable limit to exploit the results. 20 bar of H<sub>2</sub> pressure has thus been chosen for the catalytic experiments.

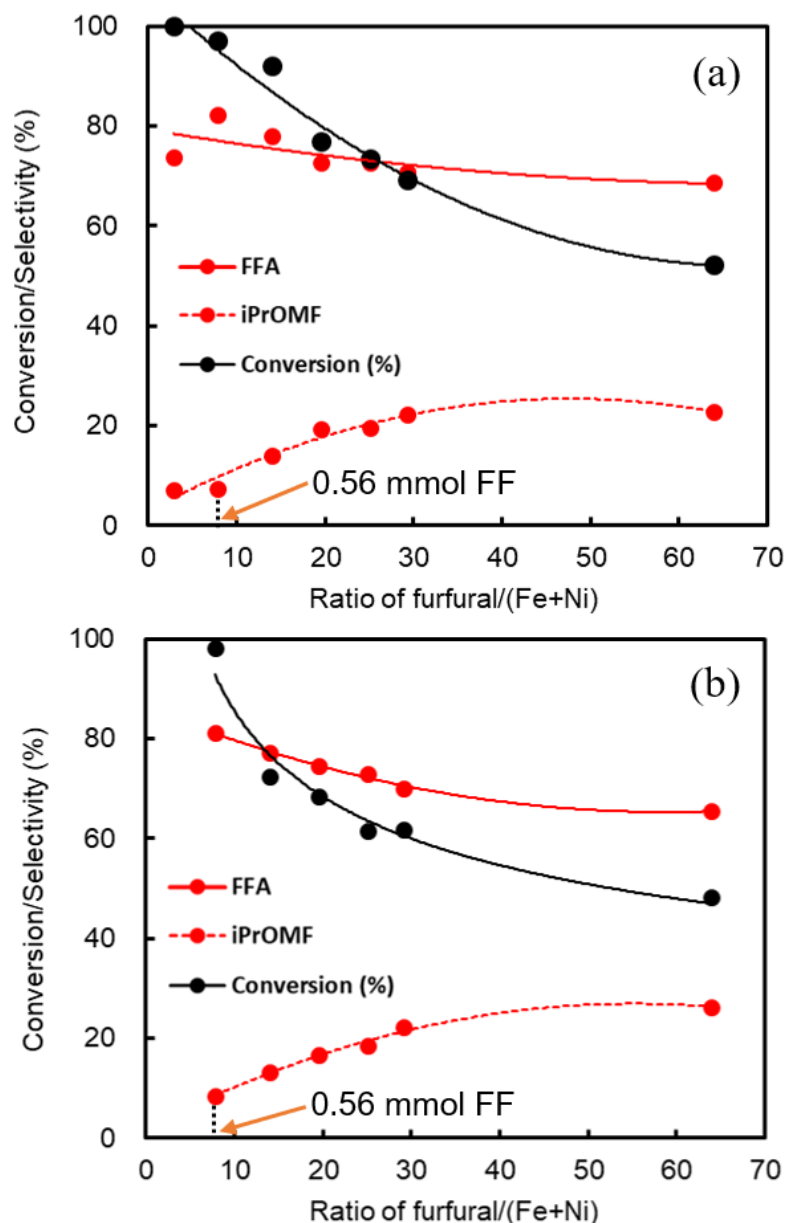


**Figure 5.2.** Conversion and selectivity to FFA and iPrOMF for (a) Fe<sub>50</sub>Ni<sub>50</sub>/SiO<sub>2</sub> and (b) Fe<sub>40</sub>Ni<sub>60</sub>/SiO<sub>2</sub> catalysts as a function of the furfural/(Fe+Ni) molar ratio. Reaction conditions:  $T_{\text{activation}} = 400\text{ }^{\circ}\text{C}$ ,  $T = 150\text{ }^{\circ}\text{C}$ ,  $P(\text{H}_2) = 20\text{ bar}$ , solvent: isopropanol, volume of solution: 1.5 mL,  $m_{\text{catalyst}} = 10\text{ mg}$ ,  $t = 2\text{ h}$ .

### V.3.2. Choice of the ratio between furfural and the catalyst mass

In order to determine the suitable ratio between furfural and the metal catalyst, different concentrations of furfural in isopropanol were used, while the mass of Fe<sub>50</sub>Ni<sub>50</sub>/SiO<sub>2</sub> or Fe<sub>40</sub>Ni<sub>60</sub>/SiO<sub>2</sub> catalysts, formerly reduced at 700 °C and activated in H<sub>2</sub> at 400 °C prior to reaction, was fixed at 10 mg. The conversion of furfural, and selectivity to FFA and to the associated ether, iPrOMF, which are the major products for these catalysts, are plotted as a



function of the furfural/(Fe+Ni) molar ratio in Figure 5.2. The total amount of metals for each of two catalysts was calculated as 0.07 mmol, according to the ICP data, and the amount of furfural increased in the following way: 0.20, 0.56, 1.00, 1.40, 1.80, 2.10 and 4.60 mmol. The same tendencies were found with the two catalysts, in terms of conversion and selectivity. The conversion of furfural decreased from 100 to 50% with an increasing furfural/(Fe+Ni) ratio, while the selectivity to FFA decreased from 80 to 70%, and the selectivity to the ether increased from 7 to 26%. In other words, a higher amount of furfural leads to a higher selectivity to ether in these conditions, and to a lower selectivity to FFA. In order to limit the etherification side-reaction while not using a too low ratio between furfural and catalyst, the amount of furfural was chosen to be 0.56 mmol to evaluate the catalytic activity (see arrows on Figure 5.2).

#### V.4. Description of the set-up

The hydrogenation of furfural was tested using a Screening Pressure Reactor (SPR) system from Freeslate equipped with 24 parallel stainless-steel batch reactors of 6 mL each. Tests were performed at 150 °C under 20 bar H<sub>2</sub> as selected above and a continuous stirring of 600 rpm for all the tests.

The catalysts were weighed and introduced into the reactors, where they would be activated in H<sub>2</sub> in order to totally reduce the nanoparticles which had been oxidized upon exposure to air after reduction at 700 °C. Given the limitations of the catalytic set-up, the activation temperature was limited to 400 °C. In Chapter IV, it was seen that in the conditions of temperature-programmed reduction, Fe was not completely reduced at that temperature. In order to favor the complete reduction of the two metals, and in particular Fe, pure hydrogen was used instead of dilute H<sub>2</sub>, and the catalysts were kept under H<sub>2</sub> during 2 h.

After activation at 400 °C, 1.5 mL of solution was added into each reactor containing the catalyst. In order to avoid the re-oxidation of the catalysts, this step was performed inside a glove-box. The volume of solution was much less than the volume of reactor (6 mL), to leave a free volume to H<sub>2</sub> and to limit the loss of solution during reaction (evaluated by weighing the reactor after reaction). All the solutions tested by GC after reaction were filtered to eliminate the catalysts.

As the amount of FF was fixed at 0.56 mmol, and temperature and pressure were also fixed, the only variables were the catalyst itself, the mass of catalyst, and the reaction time (fixed for a simultaneous run of 24 measurements). As discussed in Chapters III and IV, the Fe-Ni/SiO<sub>2</sub> catalysts prepared by deposition-precipitation present very similar characteristics of metal contents, particle size and metal dispersion. The only major difference between the catalysts for a similar mass introduced in the reactors is thus the metal proportions. A mass of 10 mg of catalyst was first used for varying reaction times, 1, 2 and 4 h. However, it was found that for the most active catalysts, conversion at the shortest time already reached 100%, which did not allow comparison with the less active systems, in particular for an estimation of the initial reaction rate. A significant decrease of the conversion could only be achieved by decreasing both the reaction time and the catalyst mass at the same time, while staying in satisfactory accuracy domains. The following couples of parameters were thus used: 0.5 h, 3 mg; 0.5 h, 5 mg; 1 h, 3 mg; 1 h, 5 mg. It was shown above that at high conversion, the main risk of increasing the furfural/(Fe+Ni) molar ratio was an increase of the selectivity to ether at the expense of the selectivity of FFA. Except for Fe<sub>10</sub>Ni<sub>90</sub>/SiO<sub>2</sub> and Ni<sub>100</sub>/SiO<sub>2</sub>, the production of ether was however found to be limited at the low furfural conversions targeted by a decrease of reaction time and catalyst mass. In these conditions FFA was the main product formed initially.

As a consequence, in the next section, figures will be plotted as a function of the product between reaction time and the mass of catalyst, namely: 1.5 (0.5 h \* 3 mg), 2.5 (0.5 h \* 5 mg), 5 (1 h \* 5 mg), 10 (1 h \* 10 mg), 20 (2 h \* 10 mg) and 40 h.mg (4 h \* 10 mg). As selectivities cannot be compared at identical conversion across the whole catalysts series, given their very different catalytic performances, FF consumption and yields of products will be mostly compared using mmol as unit. The slope of the curves will thus correspond to reaction rates expressed in mmol.mg<sub>cat</sub><sup>-1</sup>.h<sup>-1</sup>.

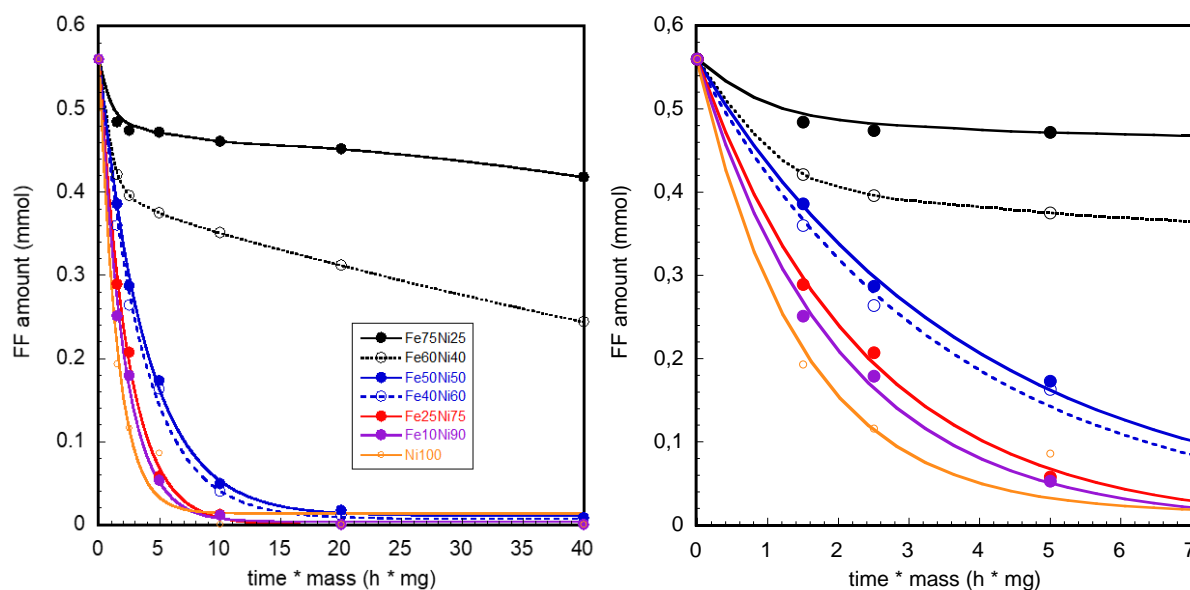


**Figure 5.3.** Furfural consumption for Fe-Ni/SiO<sub>2</sub> catalysts prepared by DP as a function of (time \* mass). Left: whole curves, right: zoom on the shorter time range. Reaction conditions:  $T_{\text{activation}} = 400\text{ }^{\circ}\text{C}$ ,  $T = 150\text{ }^{\circ}\text{C}$ ,  $P(\text{H}_2) = 20\text{ bar}$ , solvent: isopropanol, volume of solution: 1.5 mL,  $m_{\text{catalyst}} = 3 - 10\text{ mg}$ ,  $t = 0.5 - 4\text{ h}$ .

## V.5. Catalytic results

The furfural consumptions provided by bimetallic Fe-Ni/SiO<sub>2</sub> catalysts with various Fe and Ni proportions and by monometallic Ni<sub>100</sub>/SiO<sub>2</sub> prepared by DP were first compared as a function of the (time \* mass) product. It was verified that the monometallic Fe/SiO<sub>2</sub> catalyst did not present any catalytic activity in these experimental conditions.

As shown in Figure 5.3, the FF amount appears to decrease gradually with the increase of (time \* mass) for Fe<sub>75</sub>Ni<sub>25</sub>/SiO<sub>2</sub>, but for this catalyst furfural is not fully consumed in the reaction conditions, even after a few hours. FF consumption as a function of (time \* mass) is faster for Fe<sub>60</sub>Ni<sub>40</sub>/SiO<sub>2</sub>, indicating the improvement of catalytic activity with the increase of the Ni content, but one half of FF remains unconsumed after reaction. A whole consumption is reached when the Ni content is further increased, and monometallic Ni/SiO<sub>2</sub> exhibits the highest initial FF consumption rate.

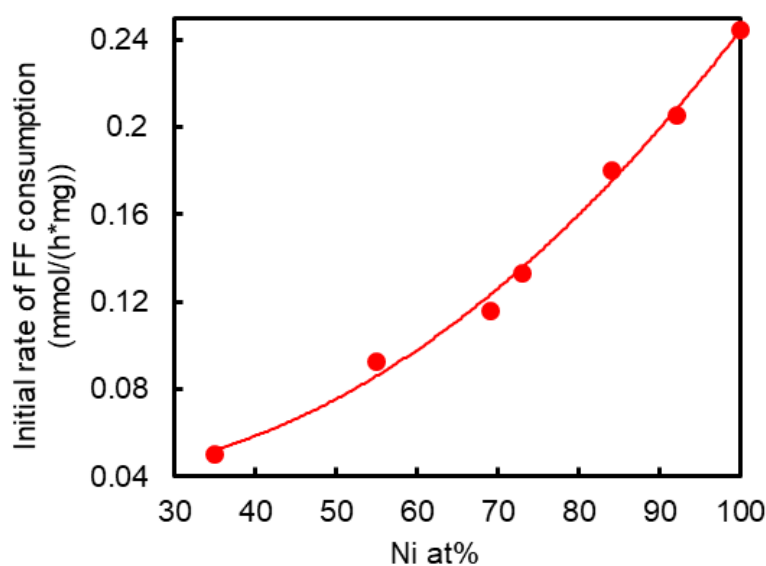


**Figure 5.4.** Initial rate of FF consumption for (Fe-)Ni/SiO<sub>2</sub> catalysts prepared by DP as a function of Ni molar proportion.

The initial rate of FF consumption, calculated from the amount of FF remaining at (time \* mass) = 1.5 h.mg, is plotted in Figure 5.4 as a function of the actual Ni molar proportion measured by XRF in the catalyst. This clearly shows the positive influence of the Ni content on the activity. Therefore, the first conclusion we can propose is that the addition of more Ni in the catalyst formulation favors the hydroconversion of FF.

The carbon balance based on the initial amount of furfural loaded in the reactor was also evaluated as a function of the (time \* mass) product, as shown in Table 5.1. For Fe-rich catalysts (Fe<sub>75</sub>Ni<sub>25</sub>/SiO<sub>2</sub> and Fe<sub>60</sub>Ni<sub>40</sub>/SiO<sub>2</sub>), carbon balances are always lower than 90%. This may be explained by the low consumption of FF and a concentration remaining high in the reaction medium, which results in the adsorption of FF on the surface of the catalysts. In addition, products of degradation not detected by GC can also be responsible for the low carbon balance. Carbon balances higher than 95% are conversely achieved in most tests when increasing the Ni content in the bimetallic catalysts. This indicates that, (i) no major product was left unidentified, and (ii), that the loss of organic molecules by deposition onto the catalyst was minor. Carbon balances slightly higher than 100% for Ni-rich bimetallic catalysts can be explained by the uncertainty in the calibration coefficients for the ethers formed from FFA and THFFA, which, as explained above, were evaluated by comparison with those of the corresponding alcohols.

**Table 5.1.** Carbon balance of Fe-Ni/SiO<sub>2</sub> catalysts prepared by DP after the hydrogenation of furfural as a function of (time \* mass). Carbon balances are calculated by summing the amounts of remaining FF and of produced molecules. Reaction conditions: T<sub>activation</sub> = 400 °C, T = 150 °C, P(H<sub>2</sub>) = 20 bar, solvent: isopropanol, volume of solution: 1.5 mL, m<sub>catalyst</sub> = 3 - 10 mg, t = 0.5 - 4 h.

(time* mass)	Carbon balance (%)						
	Fe <sub>75</sub> Ni <sub>25</sub> / SiO <sub>2</sub>	Fe <sub>60</sub> Ni <sub>40</sub> / SiO <sub>2</sub>	Fe <sub>50</sub> Ni <sub>50</sub> / SiO <sub>2</sub>	Fe <sub>40</sub> Ni <sub>60</sub> / SiO <sub>2</sub>	Fe <sub>25</sub> Ni <sub>75</sub> / SiO <sub>2</sub>	Fe <sub>10</sub> Ni <sub>90</sub> / SiO <sub>2</sub>	Ni <sub>100</sub> / SiO <sub>2</sub>
1.5	90	88	96	93	102	97	102
2.5	89	90	98	98	102	101	102
5	88	84	94	95	92	101	93
10	85	89	94	100	101	101	90
20	85	86	100	101	100	103	93
40	85	91	92	100	100	98	95

The yield of products detected as a function of (time \* mass) has been drawn for each catalyst in Figure 5.5.

For Fe<sub>75</sub>Ni<sub>25</sub>/SiO<sub>2</sub>, the main product is FFA but produced in a very low amount (0.02 mmol), without major change with time. As mentioned above, we can suppose that non-hydrogenated furfural at a high concentration progressively adsorbs on the metal surface, or that polymerization products form, deactivating the active sites. After 4 h of reaction with 10 mg of catalyst, the hydrogenolysis product, MF, appears but also in a very low amount. In other words, Fe<sub>75</sub>Ni<sub>25</sub>/SiO<sub>2</sub> has a very low activity in the hydrogenation of FF.

The amount of FFA produced is higher for Fe<sub>60</sub>Ni<sub>40</sub>/SiO<sub>2</sub>, indicating that more Ni can promote the hydrogenation of the aldehyde function. The production of FFA gradually increases with increasing (time \* mass). Other products, such as the ether iPrOMF, start to appear, but remain very minor.

A further increase of the Ni content (catalyst Fe<sub>50</sub>Ni<sub>50</sub>/SiO<sub>2</sub>) leads to the production of a much larger amount of FFA (0.45 mmol after 2 h of reaction with 10 mg of catalyst), making it the most selective catalyst in the series. FFA is slightly consumed when further increasing the reaction time to 4 h, but remains the major product. This decrease is mainly caused by the etherification reaction to iPrOMF. The amounts of THFFA and MF (maximum amounts: 0.025

mmol and 0.035 mmol) are similar as for Fe<sub>60</sub>Ni<sub>40</sub>/SiO<sub>2</sub>. MTHF, the tertiary product produced by hydrogenation of MF or hydrogenolysis of THFFA, appears but in very small amount.

For the Fe<sub>40</sub>Ni<sub>60</sub>/SiO<sub>2</sub> catalyst, the amount of FFA and evolution with time do not change much compared with Fe<sub>50</sub>Ni<sub>50</sub>/SiO<sub>2</sub>. This catalyst is the second most selective catalyst of the series with respect to FFA. However, the amounts of products from the three types of side-reactions, ether (iPrOMF), THFFA, MF, and from the combination of hydrogenolysis and hydrogenation of the furan ring, MTHF, progressively increase as a function of (time \* mass).

A dramatic impact on the yield of FFA occurs when further increasing the Ni proportion up to Fe<sub>25</sub>Ni<sub>75</sub>/SiO<sub>2</sub>. The amount of FFA increases up to 0.335 mmol with increasing (time \* mass), but it is now rapidly consumed (for time \* mass > 5), mainly by etherification to iPrOMF, that ultimately becomes the dominant product of reaction. The hydrogenolysis of FFA to MF and, to a lesser extent, the hydrogenation of the furan ring of FFA to THFFA, also gradually increase their influence on the products distribution, with final amounts of 0.089 and 0.081 mmol, respectively. Compared to the former catalyst, the production of MTHF also increases but is not dominant yet. The fact that the production of THFFA increases almost linearly without presenting a maximum, whereas the production of MF seems to reach a plateau, suggests that MTHF is mainly produced by the hydrogenation of the ring of MF.

The same tendencies are found with Fe<sub>10</sub>Ni<sub>90</sub>/SiO<sub>2</sub>, with a slightly more rapid consumption of FFA, and slightly lower amounts of ether (iPrOMF) and MF. However, the production of THFFA increases dramatically, and finally becomes the predominant product with iPrOMF. A consequence is the detection of the ether associated to THFFA, iPrOMTHF, which can form either by the etherification of THFFA, now present in large amount, or from the hydrogenation of the furan ring of iPrOMF. In line with the higher activity in the hydrogenation of the furan ring, the amount of MTHF slightly increases compared with the former catalyst. As was the case for Fe<sub>25</sub>Ni<sub>75</sub>/SiO<sub>2</sub>, its production seems to be correlated to the stagnation of the production of MF.

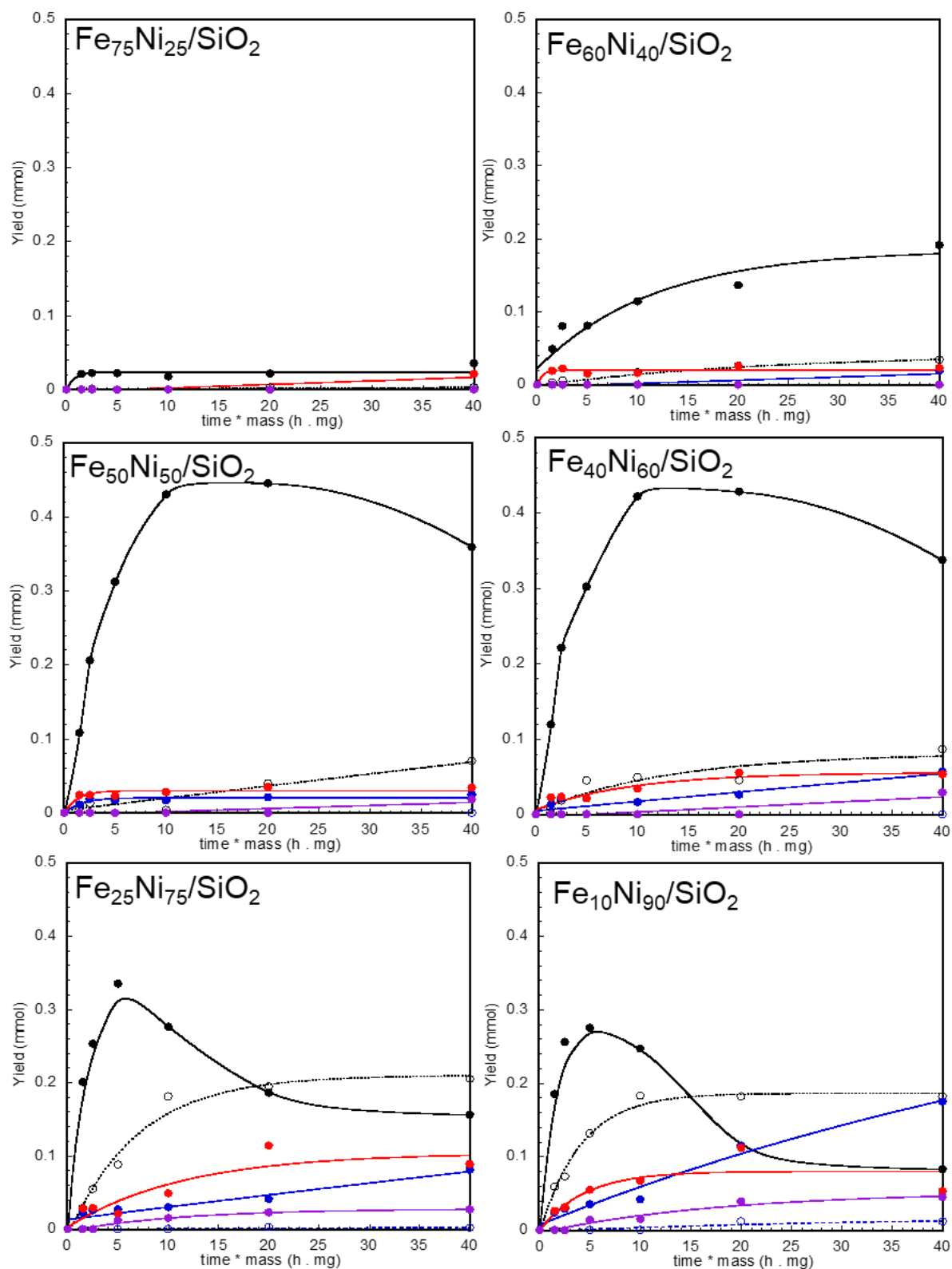


**Figure 5.5.** Yield of products after hydroconversion of FF as a function of (time \* mass) for Fe-Ni/SiO<sub>2</sub> bimetallic catalysts prepared by DP. Black line (—●—): FFA; Black dotted line (---○---): iPrOMF; Blue line (—●—): THFFA; Blue dotted line (---○---): iPrOMTHF; Red line (—●—): MF; Purple line (—●—): MTHF. Reaction conditions: T<sub>activation</sub> = 400 °C, T = 150 °C, P(H<sub>2</sub>) = 20 bar, solvent: isopropanol, volume of solution: 1.5 mL, m<sub>catalyst</sub> = 3 - 10 mg, t = 0.5 - 4 h.

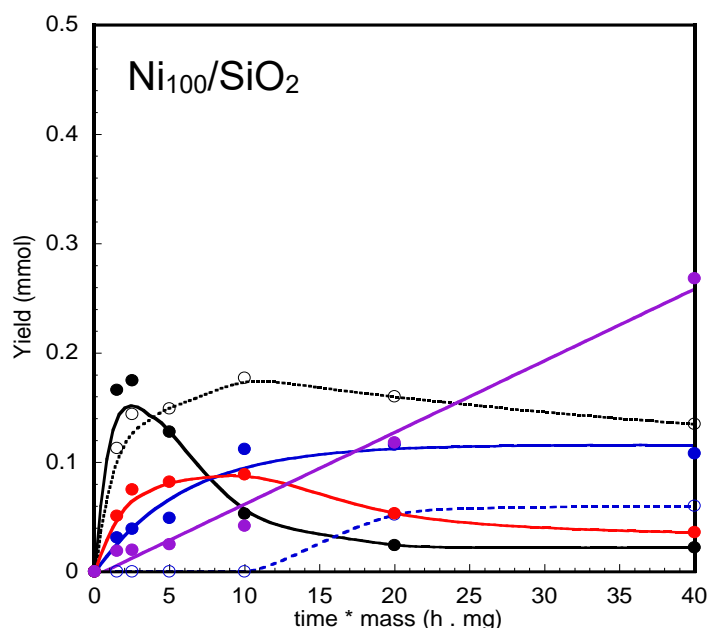


**Figure 5.6.** Yield of products after hydroconversion of FF as a function of (time \* mass) for monometallic Ni/SiO<sub>2</sub> catalyst prepared by DP. Black line (—●—): FFA; Black dotted line (---○---): iPrOMF; Blue line (—●—): THFFA; Blue dotted line (---○---): iPrOMTHF; Red line (—●—): MF; Purple line (—●—): MTHF. Reaction conditions:  $T_{\text{activation}} = 400\text{ }^{\circ}\text{C}$ ,  $T = 150\text{ }^{\circ}\text{C}$ ,  $P(\text{H}_2) = 20\text{ bar}$ , solvent: isopropanol, volume of solution: 1.5 mL,  $m_{\text{catalyst}} = 3 - 10\text{ mg}$ ,  $t = 0.5 - 4\text{ h}$ .

To complete the comparison, monometallic Ni<sub>100</sub>/SiO<sub>2</sub> catalyst exhibits a more complex situation (Figure 5.6). FFA is consumed from (time \* mass) = 2.5 h.mg. The three secondary products initially appear in the following order of decreasing amount: ether (iPrOMF), MF and THFFA. But both MF and iPrOMF are progressively consumed, and only the production of THFFA continues to increase. The associated ether, iPrOMTHF, appears above (time \* mass) = 20 h.mg. In the same line, the hydrogenation of the furan ring leads to a linear increase of the production of MTHF, which finally becomes the dominant product. The clear presence of a maximum for the production of MF confirms that MTHF is mainly formed from MF, but in the present case the production of THFFA reaches a plateau, and THFFA may also contribute to the production of MTHF by hydrogenolysis. In any case, the Ni<sub>100</sub>/SiO<sub>2</sub> catalyst is characterized by its high activity in the hydrogenation of the furan ring, both from FFA and from MF.



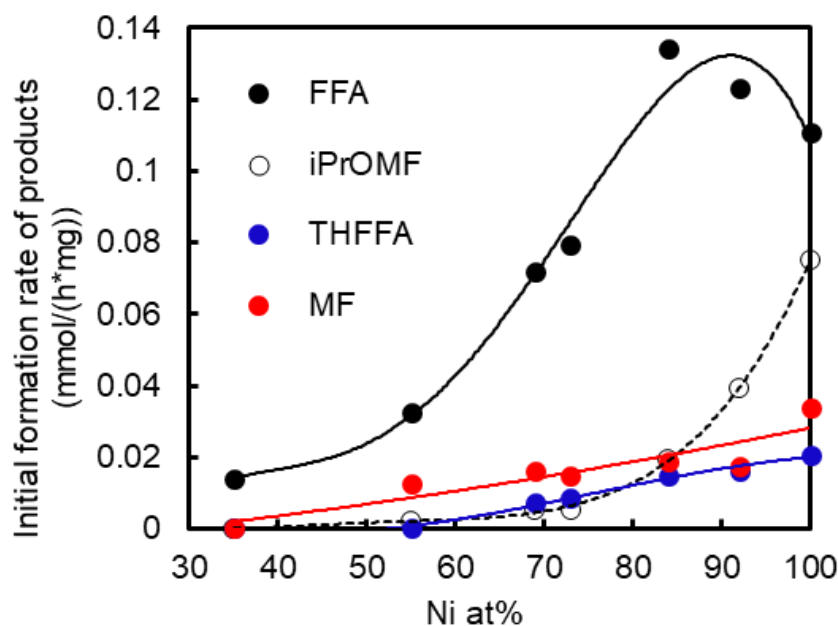


**Figure 5.7.** Initial formation rates of products for (Fe-)Ni/SiO<sub>2</sub> catalysts prepared by DP as a function of actual Ni proportion.

In order to analyze the primary, secondary and tertiary products quantitatively, initial formation rates of those products as a function of Ni proportion are shown in Figure 5.7. The primary product, FFA, is always the main hydrogenation product. The catalyst possess 84 at% of Ni exhibits the highest apparent formation rate of FFA, and it decreases when further increasing the Ni content, as consumption rates become non negligible initially.

The formation rates of iPrOMF, MF and THFFA from FFA also increase with the amount of Ni. FFA is primarily consumed by hydrogenolysis to MF, by a slower second route of etherification to iPrOMF, and by hydrogenation of the furan ring to THFFA, for catalysts possessing a Ni proportion lower than 84 at%. FFA is primarily consumed by etherification to iPrOMF, by a slower second route of hydrogenolysis to MF, and by an even slower hydrogenation of the furan ring to THFFA, for catalysts possessing a Ni proportion higher than 84 at%. It is with these catalysts that a maximum of consumption of FFA is clearly seen, that shifts to shorter (time \* mass) upon increase of the Ni content, as shown in Figures 5.5 and 5.6. When one considers only the secondary reactions of hydroconversion, the hydrogenolysis reaction of FFA to MF is faster than the hydrogenation of the furan ring to THFFA.

A quantitative study of the secondary and tertiary products produced from FFA is shown

in Figure 5.8, for (time \* mass) = 20 h.mg taken as an example. The selectivity to THFFA gradually increases from 3.9 to 22.2% when increasing the proportion of Ni, while the selectivity to MF exhibits a maximum for Fe<sub>25</sub>Ni<sub>75</sub>/SiO<sub>2</sub> (20.3%), and decreases when further increasing the Ni content. Meanwhile, the selectivity to MTHF dramatically increases from 0 to 22.5%. One can then confirm that the production of MTHF mainly comes from the hydrogenation of the furan ring of MF, and much less from the hydrogenolysis of THFFA. The selectivity to iPrOMF exhibits an increase for Fe<sub>25</sub>Ni<sub>75</sub>/SiO<sub>2</sub> (34.7%) compared with Fe<sub>50</sub>Ni<sub>50</sub>/SiO<sub>2</sub> (7.4%), then slightly decreases when further increasing the Ni content. The selectivity to iPrOMTHF is minor (maximum selectivity is 9.9% for monometallic Ni), though it is increasing when increasing the Ni content. Therefore, it is difficult to conclude if iPrOMTHF is mostly produced by etherification of THFFA, or by hydrogenation of the furan ring of iPrOMF. iPrOMF can also be consumed by hydrogenolysis to MF, but a quantitative analysis of the selectivity to MF and iPrOMF cannot allow concluding on this.

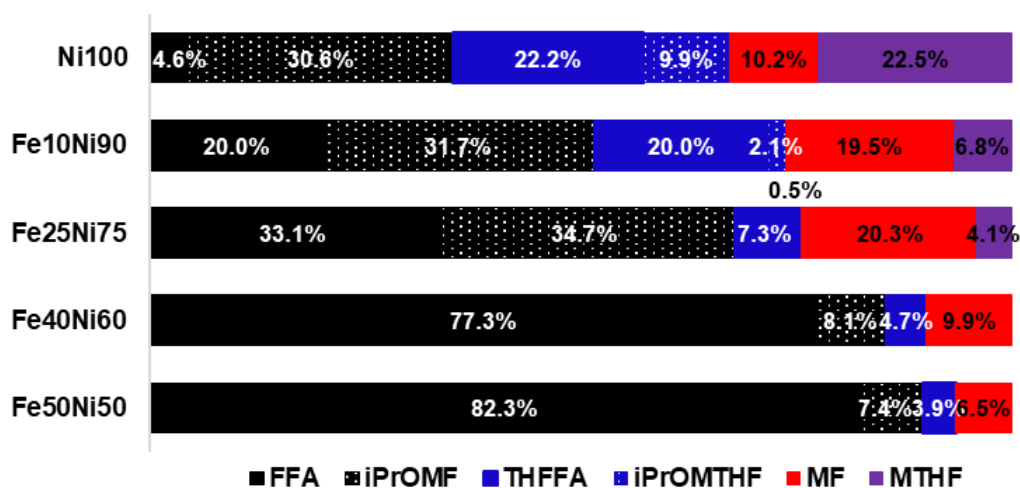


**Figure 5.8.** Selectivity of products in a given (time \* mass) = 20 h.mg for (Fe-)Ni/SiO<sub>2</sub> catalysts prepared by DP. Reaction conditions: T<sub>activation</sub> = 400 °C, T = 150 °C, P(H<sub>2</sub>) = 20 bar, solvent: isopropanol, volume of solution: 1.5 mL.

If one considers that the reduced Fe-Ni nanoparticles are still surrounded by an Fe-enriched shell after activation at 400 °C, one can suppose that the nanoparticles containing 60-75 at% Ni, which presented the best catalytic activity in terms of FF consumption and selectivity to FFA, exhibit at their surface the right balance between Fe and Ni to allow the hydrogenation of furfural while inhibiting side-reactions. It can be explained by the hypotheses that furfural can be bonded onto Fe-rich surfaces more strongly through the carbonyl group than onto Ni surfaces, because of the oxophilic property of Fe with respect to Ni [12, 13], with the furan ring tilted away from the Fe-Ni surface because of the repulsion between the aromatic ring and Fe, preventing its hydrogenation. Too much iron inhibits any reaction of hydrogenation, but too much nickel at the surface of the nanoparticles allow reactions of hydrogenolysis and hydrogenation of the furan ring, as furanic compounds are able to adsorb in a flat mode onto Ni surfaces. While the hydrogenolysis of FFA is favoured with respect to the hydrogenation of the FFA furan ring, the reverse order of reactivity is found when comparing the hydrogenation of the furan ring of MF and the hydrogenolysis of THFFA, in the tertiary reactions. It can be supposed that the adsorption of molecules containing a furan ring, such as MF, is favoured onto Ni, compared with the adsorption of hydrogenated furan rings, as is found in THFFA. The result is the major formation of compounds with a hydrogenated furan ring on the monometallic Ni catalyst (MTHF, THFFA, iPrOMTHF).

In contrast with the other molecules, etherification is usually supposed to happen on unreduced metal ions acting as Lewis acidic centers [14, 15]. As Fe is the last metal to be reduced, including during activation under H<sub>2</sub> prior to reaction (Chapter IV), one could suppose that it is unreduced Fe<sup>2+</sup> ions that act as active sites for etherification side-reactions. However, it has been seen that the initial rate of formation of iPrOMF increases with the amount of Ni in the catalyst, and is the highest on the monometallic Ni catalyst. Unreduced Ni<sup>2+</sup> ions may thus be supposed to be the active sites for etherification as well. The reason why a minority of Ni<sup>2+</sup> ions would remain unreduced, despite the quantitative reduction evidenced by X-ray absorption spectroscopy, may be found in the poorer reducibility of Ni-rich phyllosilicates, compared to Fe-Ni-containing phases (see section III.4.2 of *Chapter III discussing TPR*). This would leave

an increasing amount of Ni<sup>2+</sup> ions from residual silicate phases, apt to catalyze etherification reactions (if we suppose that they are catalyzed by metal ions and not by metallic Ni).

In order to evaluate the stability of the Fe<sub>50</sub>Ni<sub>50</sub>/SiO<sub>2</sub> catalyst prepared by DP, three recycling experiments were conducted in a batch reactor (Figure 5.9). FFA was always the major product after three cycles. However, the conversion of furfural dramatically decreased from 85 to 30%.

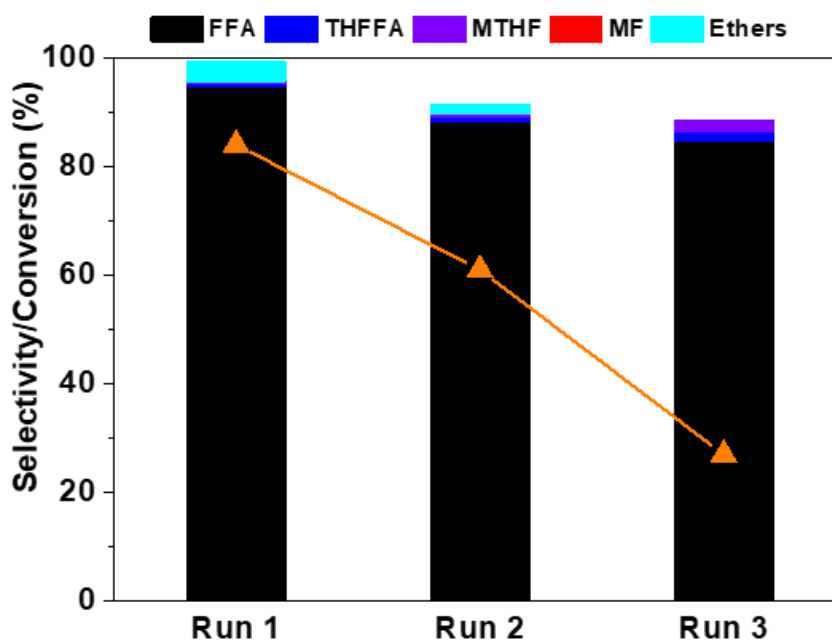


**Figure 5.9.** Reusability of the Fe<sub>50</sub>Ni<sub>50</sub>/SiO<sub>2</sub> catalyst prepared by DP in liquid phase hydrogenation of furfural. Selectivities: vertical bars. Conversion: triangles. Reaction conditions:  $T_{\text{activation}} = 400\text{ }^{\circ}\text{C}$ ,  $T = 150\text{ }^{\circ}\text{C}$ ,  $P(\text{H}_2) = 20\text{ bar}$ , solvent: isopropanol, volume of solution: 24 mL,  $m_{\text{catalyst}} = 174\text{ mg}$ ,  $t = 2\text{ h}$ ,  $n_{\text{FF}}/(n_{\text{Ni}}+n_{\text{Fe}}) = 10$ ,  $C_{0(\text{FF})} = 0.48\text{ mmol/g}$ .

This decrease in activity may be attributed to three possibilities: leaching of the Fe-Ni alloy, a change in Fe-Ni particle size, and a deactivation of active sites on the surface of the catalyst. Verifying the loading of metals after each run by XRF showed that no major leaching of the Fe-Ni alloy happened. Therefore, a growth of the particles size or a deactivation of the active sites should be considered in later studies to explain the loss of conversion.

In summary, increasing the Ni content to a certain extent is beneficial for the activity in terms of FF consumption and yield to FFA. Fe-Ni catalysts containing 60-75 Ni at% favor the hydrogenation of the aldehyde function and provide the highest yield to FFA (0.43 - 0.45 mmol)

because of a faster transformation of FF. However, more Ni progressively favors side-reactions of etherification, hydrogenolysis, and finally hydrogenation of the furan ring, which clearly dominates in the case of the Ni-rich catalysts. MF never becomes the major product because it is consumed by this side-reaction that produces MTHF. The optimum formulation of catalysts for hydrogenation of FF in this work are consistent with the Fe-Ni formulations used in the literature: Fe<sub>42</sub>Ni<sub>58</sub> particles supported on carbon for Chieffi *et al.* [5], a Fe<sub>25</sub>Ni<sub>75</sub>/Al<sub>2</sub>O<sub>3</sub> catalyst for Putro *et al.* [6]. Given that this series of Fe-Ni catalysts were prepared with small and similar particle sizes, narrow size distributions and a narrow range of composition, that Fe-rich shells were detected at the periphery of the nanoparticles, and after comparison with the literature, the catalytic activity can be explained by the hypothesis that the surface of the Fe-Ni nanoparticles exhibits more Fe than the nominal composition, and that Fe-rich surfaces favor the adsorption of the carbonyl group and repel the furan ring. A quantitative analysis of the secondary and tertiary products shows that more nickel both inside and presumably at the surface of the particles would promote hydrogenolysis and hydrogenation of the furan ring. The monometallic nickel catalyst favours both reactions; leading to MTHF as the main product. The formation of ethers, also favoured on Ni-rich catalysts, can be explained by the presence of residual Ni<sup>2+</sup> ions remaining unreduced in silicate phases, and acting as Lewis acidic sites.

## V.6. Comparison with catalysts prepared by impregnation and DP

In order to verify if similar tendencies are observed with Fe-Ni/SiO<sub>2</sub> catalysts prepared following a different procedure, catalysts with different metal proportions were prepared by incipient wetness impregnation (IWI) of silica Sipernat-50, the same support as the one used for DP (pore volume: 1.3 mL/g), by adding the suitable ratio of Fe/Ni precursors (Fe(NO<sub>3</sub>)<sub>3</sub>•9H<sub>2</sub>O and Ni(NO<sub>3</sub>)<sub>2</sub>•6H<sub>2</sub>O) in an impregnation solution. Due to the solubility limitation of metal nitrates (theoretically, the solubility at 20 °C of Fe(NO<sub>3</sub>)<sub>3</sub>•9H<sub>2</sub>O and Ni(NO<sub>3</sub>)<sub>2</sub>•6H<sub>2</sub>O is respectively 13.8 g/10 mL H<sub>2</sub>O [concentration = 3.42 mol/L] and 9.6 g/10 mL H<sub>2</sub>O [concentration = 3.31 mol/L]) [16], a maximum of 20 wt% of metal loading was expected.

In order to determine the actual solubility of Fe(NO<sub>3</sub>)<sub>3</sub>•9H<sub>2</sub>O and Ni(NO<sub>3</sub>)<sub>2</sub>•6H<sub>2</sub>O, tests were carried out before preparing the co-impregnation solutions. During the test, 3 drops of HNO<sub>3</sub> (65-70%) were added into a Fe(NO<sub>3</sub>)<sub>3</sub>•9H<sub>2</sub>O solution (pH = 1), so that the formation of Fe(OH)<sub>3</sub> was avoided. After two measurements at that pH, the actual solubility of Fe(NO<sub>3</sub>)<sub>3</sub>•9H<sub>2</sub>O was found to be 2.63 mol/L, and that of Ni(NO<sub>3</sub>)<sub>2</sub>•6H<sub>2</sub>O 3.31 mol/L at room temperature. Therefore, Ni(NO<sub>3</sub>)<sub>2</sub>•6H<sub>2</sub>O and Fe(NO<sub>3</sub>)<sub>3</sub>•9H<sub>2</sub>O solutions with a concentration of 2.63 mol/L were chosen to prepare the bimetallic co-impregnation solutions with different metal ratios, by mixing complementary volumes of the two solutions. The expected metal loading, 15 wt%, was confirmed by XRF. The metal proportions on the final catalysts were the ones that were targeted when preparing the co-impregnation solutions.

The impregnated support was dried overnight at 60 °C under static air and further calcined for 10 h at 500 °C.

The characterization of the IWI catalysts could not be completed as thoroughly as for the DP catalysts. Therefore, only some elements of comparison are given below, prior to the presentation of the catalysis results. As monometallic Fe is not active in catalysis, this system will not be presented.

#### V.6.1. Comparison of reducibility

In order to determine the reducibility of impregnated catalysts after calcination, temperature-programmed reduction by hydrogen (H<sub>2</sub>-TPR) was conducted, as shown in Figure 5.10. For Fe<sub>75</sub>Ni<sub>25</sub>/SiO<sub>2</sub>, the first peak at 375 °C can be assigned to the reduction of Fe<sup>3+</sup> to Fe<sup>2+</sup> and Ni<sup>2+</sup> to metallic Ni [17, 18]. This interpretation can be supported by the discussion in section I.2.2. Increasing the Ni proportion leads to a shift of reduction peaks towards lower temperatures, then to higher temperatures. The reduction profile for the monometallic Ni sample clearly displays a main reduction peak at 470 °C with a shoulder at lower temperature (370 °C), which corresponds to the reduction of large particles of NiO [19]. The main peak is thus attributed to the reduction of smaller particles of NiO to Ni metal [20]. Between 450 and 570 °C, a broad peak can be assigned to the reduction of Fe<sup>2+</sup> to metallic Fe. It also shifts to

lower reduction temperature and decreases in intensity when increasing the Ni content. For Fe<sub>60</sub>Ni<sub>40</sub>/SiO<sub>2</sub> and Ni-richer catalysts, the reduction is complete at 600 °C. All in all, the H<sub>2</sub> consumption peaks for impregnated samples are located at a lower temperature compared with peaks for DP samples, indicating a higher reducibility.

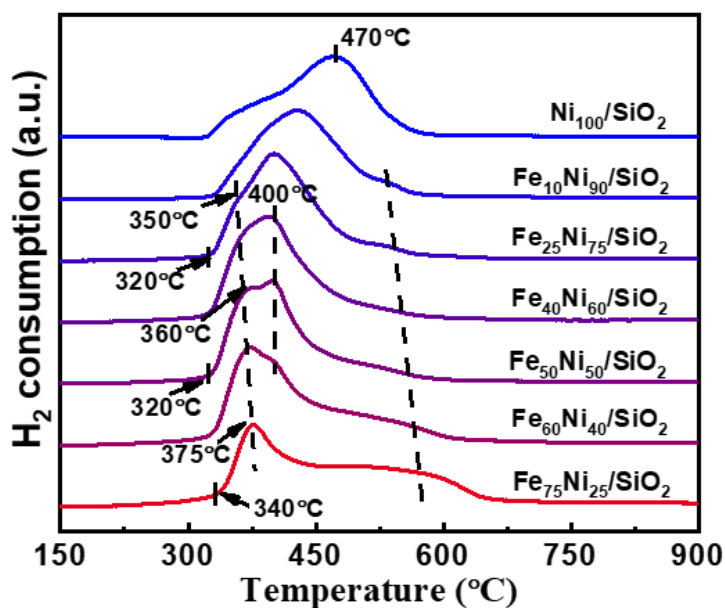


**Figure 5.10.** TPR profiles of Fe-Ni/SiO<sub>2</sub> samples prepared by impregnation, drying at 60 °C and calcination at 500 °C. (The reduction procedure is the same as that used for the DP samples)

#### V.6.2. Comparison of particle size and structure

Figure 5.11 shows the XRD patterns of the samples after reduction at 700 °C and exposure to air. The unit cell parameter  $a$  for each catalyst can be calculated according to peaks position around  $2\theta = 43.7^\circ$  and  $50.9^\circ$ , and the Ni atomic content with respect to Fe can be calculated from  $a$ , according the correlation established in section III.4.2 (Table 5.2). However, results are not straightforward to interpret, as Fe<sub>50</sub>Ni<sub>50</sub>/SiO<sub>2</sub> sample exhibits the highest value of  $a$ , which would correspond to the lowest Ni atomic content. The average particle size calculated by using the Laue-Scherrer equation ranges between 9.5 and 12.8 nm, which is significantly larger than for the particles present on the catalysts prepared by DP.

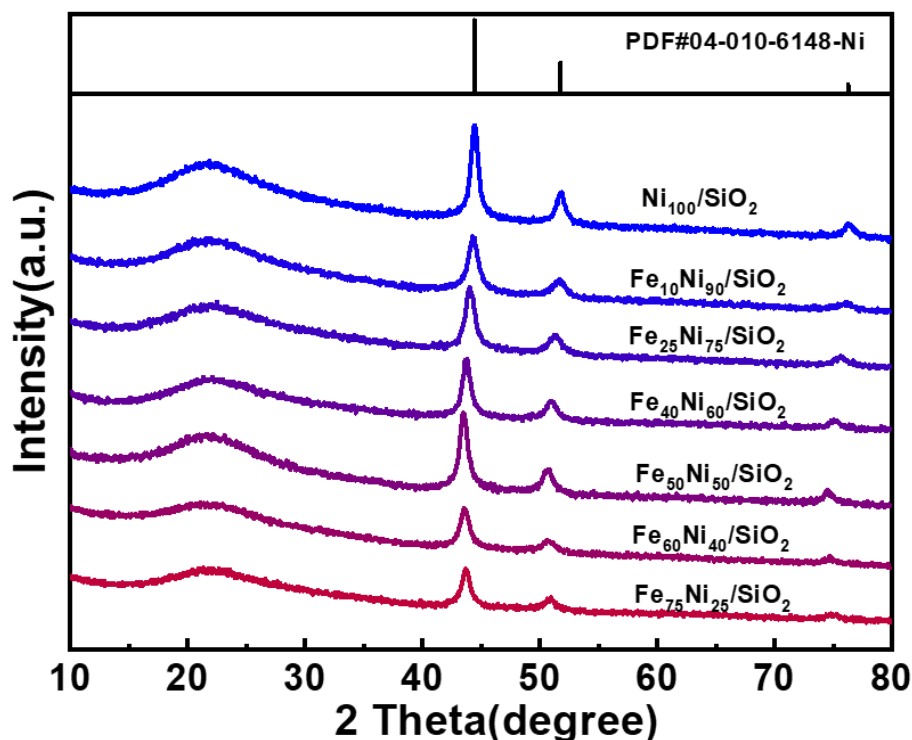


**Figure 5.11.** XRD patterns for Fe-Ni/SiO<sub>2</sub> samples prepared by impregnation and calcined at 500 °C, reduced at 700 °C under 10% H<sub>2</sub>/Ar.

**Table 5.2.** Unit cell parameter a, Ni atomic proportion evaluated from a, and average particle size of catalysts prepared by impregnation, after reduction under 700 °C and exposure to air.

Samples	Fe <sub>75</sub> Ni <sub>25</sub> / SiO <sub>2</sub>	Fe <sub>60</sub> Ni <sub>40</sub> / SiO <sub>2</sub>	Fe <sub>50</sub> Ni <sub>50</sub> / SiO <sub>2</sub>	Fe <sub>40</sub> Ni <sub>60</sub> / SiO <sub>2</sub>	Fe <sub>25</sub> Ni <sub>75</sub> / SiO <sub>2</sub>	Fe <sub>10</sub> Ni <sub>90</sub> / SiO <sub>2</sub>	Ni <sub>100</sub> / SiO <sub>2</sub>
a (nm)	0.3582	0.3592	0.3600	0.3581	0.3557	0.3534	0.3528
Ni at%	45	36	28	47	69	90	100
Size (nm)	12.2	10.4	12.0	12.0	10.7	9.5	12.8

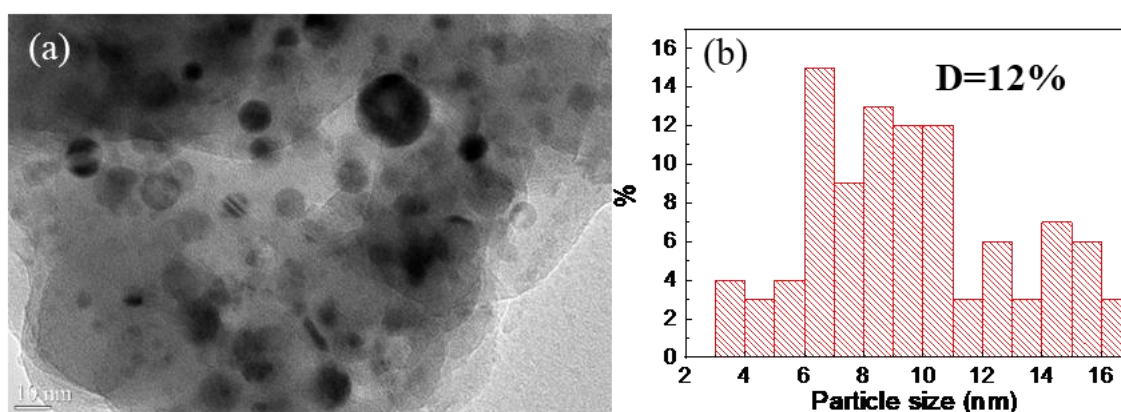


**Figure 5.12.** Bright field TEM micrographs (a) and particle size distribution measured by TEM (b) for Fe<sub>50</sub>Ni<sub>50</sub>/SiO<sub>2</sub>-IWI-700 prepared by impregnation, after reduction at 700 °C and exposure to air.



The metal nanoparticles on Fe<sub>50</sub>Ni<sub>50</sub>/SiO<sub>2</sub>-IWI-700 were characterized by bright field TEM after reduction at 700 °C, and exposure of the samples to ambient air (Figure 5.12a). The particle size distribution of reduced Fe-Ni nanoparticles is broad, with a co-existence between particles smaller and larger than 15 nm, in line with the XRD results (Figure 5.12b). The metal dispersion calculated from the size histogram is 12%, less than the dispersion of 16-22% calculated for the DP catalysts.

The structure of the Fe-Ni nanoparticles after reduction and exposure to air, and the distribution of Fe and Ni for individual particles were also surveyed for Fe<sub>50</sub>Ni<sub>50</sub>/SiO<sub>2</sub> by high-resolution transmission electron microscopy (HRTEM) and electron energy loss spectroscopy (EELS) (Figure 5.13). The Fe-Ni nanoparticles that have been analyzed all present the nominal proportions of Fe and Ni, whatever their size, except for an enrichment in Fe at their periphery, as was observed after exposure to air on the DP catalysts. This casts doubt on the possibility to extract the Ni proportion from XRD results for catalysts prepared by impregnation.

From this set of observations, we will thus suppose that catalysts prepared by impregnation and reduction at 700 °C differ from DP catalysts by three features:

- Their total metal content, limited by the solubility of the metal precursors in the impregnation solution.
- As can be expected from the impregnation procedure, metal proportions that correspond to the proportions initially introduced in the solution.
- A broader particle size histogram, with an associated lower metal dispersion. No variations of metal contents between individual particles were evidenced in the sample investigated by HRTEM.

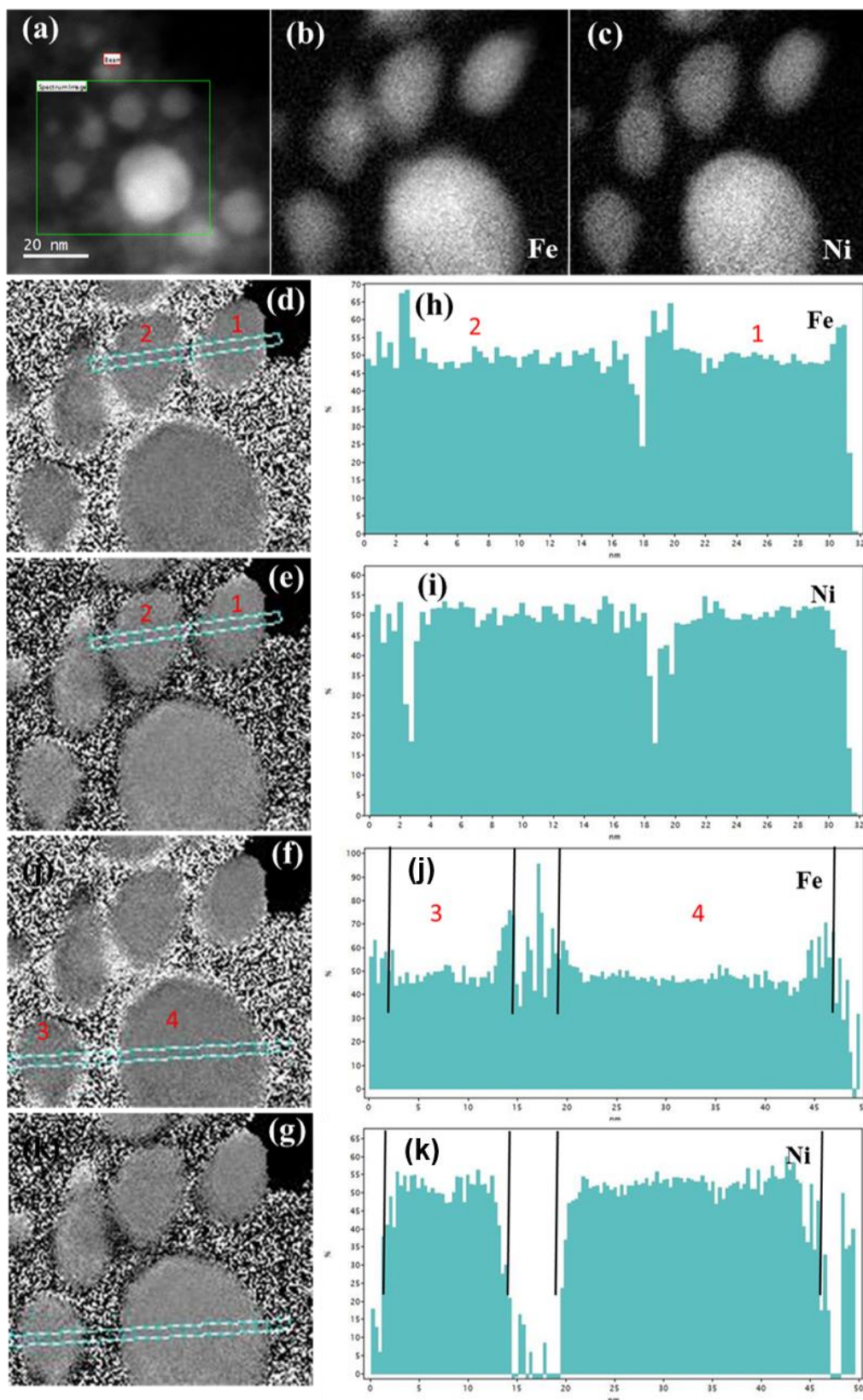


**Figure 5.13.** STEM - HAADF image (a), Fe-L<sub>3,2</sub> edge at 708 eV (b), Ni-L<sub>3,2</sub> edge at Ni-L<sub>3,2</sub> at 855 eV (c), and relative composition maps (d - g) obtained by STEM - EELS mapping for Fe<sub>50</sub>Ni<sub>50</sub>/SiO<sub>2</sub>-IWI-700 after reduction at 700 °C and exposure to air. Panels (h - k) show extracted relative concentration profiles on particles, for Fe (h and j) and Ni (i and k). The extraction has been done from the concentration maps from (d) to (g) respectively.

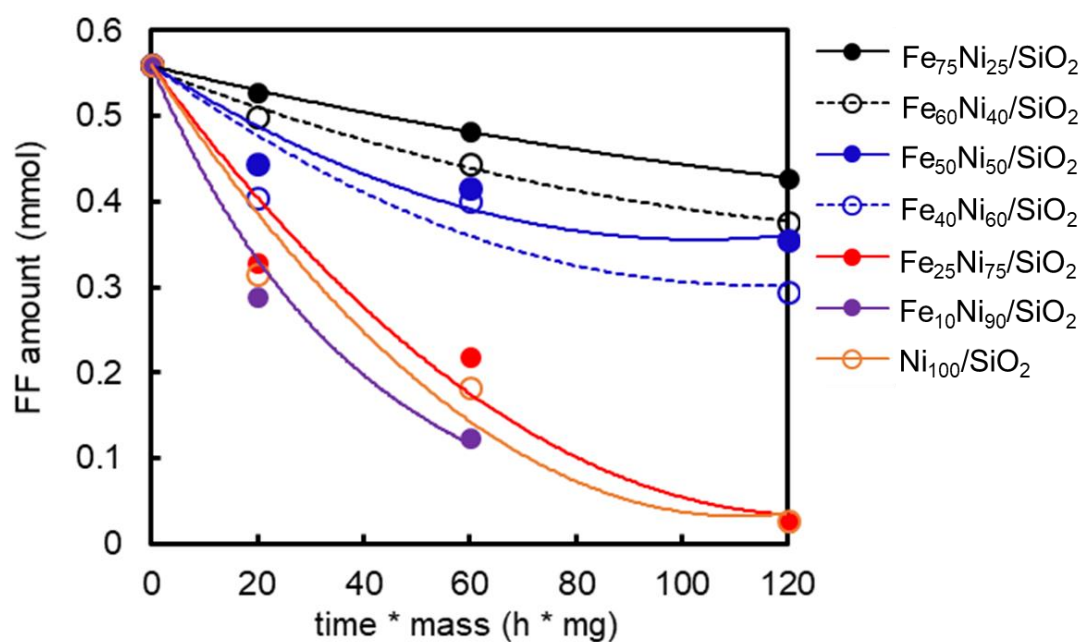


**Figure 5.14.** FF consumption of Fe-Ni/SiO<sub>2</sub> and Ni/SiO<sub>2</sub> catalysts prepared by impregnation and pre-reduction at 700 °C as a function of (time \* mass), in the hydrogenation of furfural. Reaction conditions: T<sub>activation</sub> = 400 °C, T = 150 °C, P(H<sub>2</sub>) = 20 bar, solvent: isopropanol, volume of solution: 1.5 mL, m<sub>catalyst</sub> = 10 - 30 mg, t = 2 - 4 h.

**Table 5.3.** Carbon balance of Fe-Ni/SiO<sub>2</sub> catalysts prepared by impregnation with pre-reduction at 700 °C, as a function of (time \* mass). Reaction conditions: T<sub>activation</sub> = 400 °C, T = 150 °C, P(H<sub>2</sub>) = 20 bar, solvent: isopropanol, volume of solution: 1.5 mL, m<sub>catalyst</sub> = 10 - 30 mg, t = 2 - 4 h.

(time* mass)	Carbon balance (%)						
	Fe <sub>75</sub> Ni <sub>25</sub> / SiO <sub>2</sub>	Fe <sub>60</sub> Ni <sub>40</sub> / SiO <sub>2</sub>	Fe <sub>50</sub> Ni <sub>50</sub> / SiO <sub>2</sub>	Fe <sub>40</sub> Ni <sub>60</sub> / SiO <sub>2</sub>	Fe <sub>25</sub> Ni <sub>75</sub> / SiO <sub>2</sub>	Fe <sub>10</sub> Ni <sub>90</sub> / SiO <sub>2</sub>	Ni <sub>100</sub> / SiO <sub>2</sub>
20	95	93	93	92	97	93	92
60	92	92	92	94	92	90	92
120	89	84	85	86	93	-	91

### V.6.3 Comparison of catalytic activity

FF consumptions were compared as a function of (time \* mass) for monometallic Ni/SiO<sub>2</sub> and bimetallic Fe-Ni/SiO<sub>2</sub> catalysts prepared by impregnation. Catalysts were pre-reduced at 700 °C, and underwent a second stage of reduction at 400 °C prior to reaction, to counter the effect of transfer in air. Experiments were carried out with masses of IWI catalysts of 10 or 30 mg (three times more than the maximum mass of 10 mg used with DP catalysts) in order to take the lower metal loading into account. As shown in Figure 5.14, the FF amount decreases gradually with the increase of (time \* mass) for Fe<sub>75</sub>Ni<sub>25</sub>/SiO<sub>2</sub>. The consumption rate globally increases when the Ni content increases, with some uncertainty for the Ni-rich catalysts owing to a missing measurement.

The carbon balance based on the initial amount of furfural loaded in the reactor was also evaluated as a function of the (time \* mass) product, as shown in Table 5.3. Most of carbon balances are always higher than 90%, but compared with the DP catalysts, they are all lower than 100%. The few values lower than 90% can be explained by the existence of products of degradation which are not detected by GC.

The yield of products is plotted as a function of (time\*mass) for each catalyst in Figure 5.15 and 5.16. In all cases, the dominant product is FFA, with an increasing production rate up to Fe<sub>25</sub>Ni<sub>75</sub>/SiO<sub>2</sub>. MF and TFFA are always minor products, but the production of THFFA increases when one reaches 90 or 100% Ni in the catalyst. In summary, Fe-Ni/SiO<sub>2</sub> catalysts prepared by impregnation favour the hydrogenation of the aldehyde group instead of side-reactions of etherification, hydrogenolysis and hydrogenation of the furan ring, resulting in a high selectivity to FFA. Fe<sub>25</sub>Ni<sub>75</sub>/SiO<sub>2</sub> catalyst possesses the highest activity in terms of FF consumption (0.53 mmol) and yield of FFA (0.44 mmol). As seen above, the most selective catalysts from the DP series, Fe<sub>50</sub>Ni<sub>50</sub>/SiO<sub>2</sub> and Fe<sub>40</sub>Ni<sub>60</sub>/SiO<sub>2</sub>, also possessed a similar Ni content (69 and 73 at%).

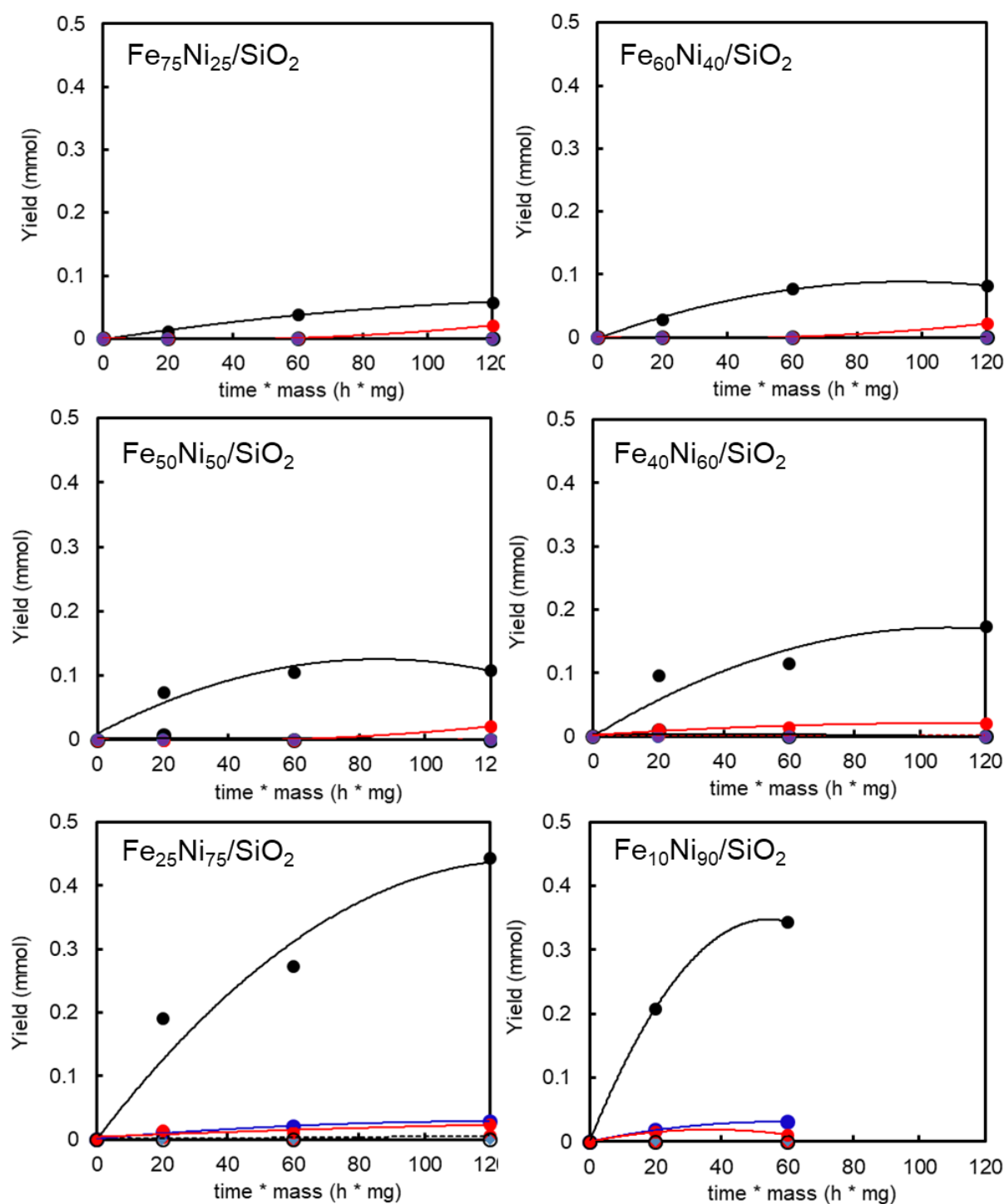


**Figure 5.15.** Yield of products after hydrogenation of FF as a function of (time \* mass) for Fe-Ni/SiO<sub>2</sub> bimetallic catalysts prepared by impregnation and pre-reduction at 700 °C. Black line (●): FFA; Black dotted line (⊙): iPrOMF; Blue line (●): THFFA; Red line (●): MF. Reaction conditions: T = 150 °C, T<sub>activation</sub> = 400 °C, P(H<sub>2</sub>) = 20 bar, solvent: isopropanol, volume of solution: 1.5 mL, m<sub>catalyst</sub> = 10 - 30 mg, t = 2 - 4 h.

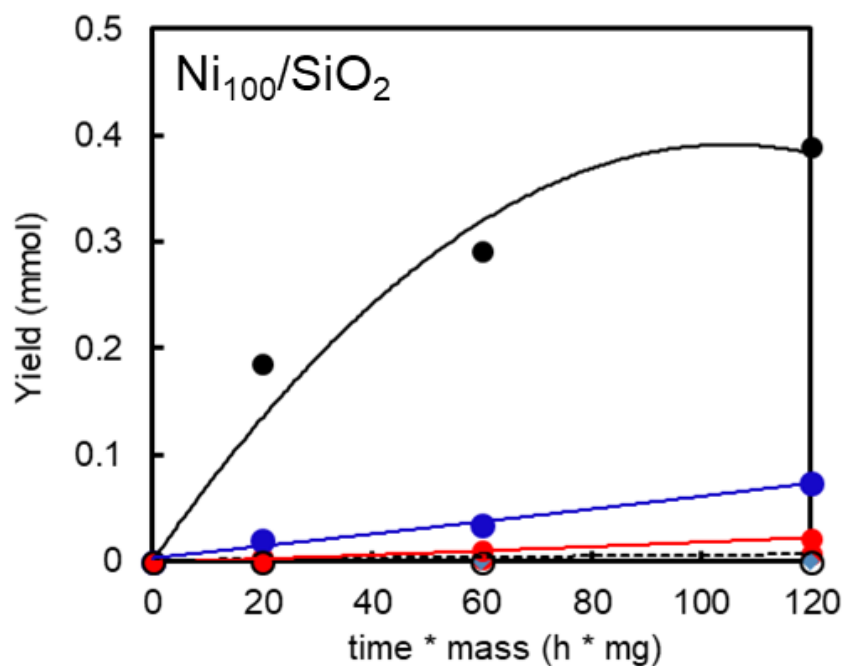


**Figure 5.16.** Yield of products after hydrogenation of FF as a function of (time \* mass) for monometallic Ni/SiO<sub>2</sub> catalyst prepared by impregnation and pre-reduction at 700 °C. Black line (—●—): FFA; Black dotted line (---○---): iPrOMF; Blue line (—●—): THFFA; Red line (—●—): MF. Reaction conditions: T = 150 °C, T<sub>activation</sub> = 400 °C, P(H<sub>2</sub>) = 20 bar, solvent: isopropanol, volume of solution: 1.5 mL, m<sub>catalyst</sub> = 10 - 30 mg, t = 2 - 4 h.

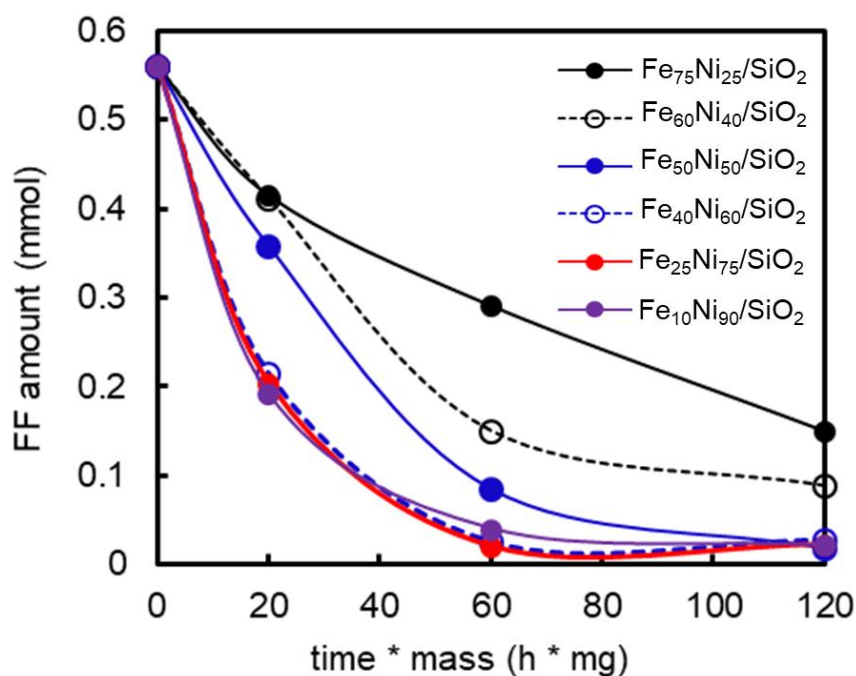


**Figure 5.17.** FF consumption of Fe-Ni/SiO<sub>2</sub> and Ni/SiO<sub>2</sub> catalysts prepared by impregnation, without pre-reduction at 700 °C, as a function of (time \* mass), in the hydrogenation of furfural. Reaction conditions: T = 150 °C, T<sub>activation</sub> = 400 °C, P(H<sub>2</sub>) = 20 bar, solvent: isopropanol, volume of solution: 1.5 mL, m<sub>catalyst</sub> = 10 - 30 mg, t = 2 - 4 h.

It was attempted to investigate the influence of the pre-reduction stage at 700 °C on the catalytic activity of impregnated catalysts. Catalysts prepared by impregnation and calcined at 500 °C were directly activated at 400 °C under H<sub>2</sub>, prior to reaction, without intermediate pre-reduction.

The FF consumption rate is higher compared with impregnated catalysts pre-reduced at 700 °C (Figure 5.17). Fe<sub>40</sub>Ni<sub>60</sub>/SiO<sub>2</sub>, Fe<sub>25</sub>Ni<sub>75</sub>/SiO<sub>2</sub> and Fe<sub>10</sub>Ni<sub>90</sub>/SiO<sub>2</sub> catalysts exhibit a full consumption of FF after 4 h of reaction. Moreover, the yield of FFA for Fe-rich catalysts is higher than that obtained with the corresponding catalysts pre-reduced at 700 °C, such as Fe<sub>75</sub>Ni<sub>25</sub>/SiO<sub>2</sub>, Fe<sub>60</sub>Ni<sub>40</sub>/SiO<sub>2</sub>, and Fe<sub>50</sub>Ni<sub>50</sub>/SiO<sub>2</sub>, as shown in Figure 5.18. Fe<sub>40</sub>Ni<sub>60</sub>/SiO<sub>2</sub> provides the highest yield of FFA (0.46 mmol) with MF and THFFA as very minor products. When the Ni content is further increased, the amount of FFA decreases slightly, and hydrogenolysis and hydrogenation of furan ring reactions start to appear. However, the hydrogenation of the furan ring to THFFA becomes dominant only after 4 h with Fe<sub>10</sub>Ni<sub>90</sub>/SiO<sub>2</sub>, confirming that Ni favours this side-reaction. The study of monometallic Ni/SiO<sub>2</sub> cannot provide useful information because data are lacking after 4 h of reaction.

The carbon balance as a function of the (time \* mass) product is shown in Table 5.4. Most of carbon balances are lower than those obtained for impregnated catalysts with a pre-reduction at 700 °C. The high selectivity of these catalysts is thus counterbalanced by a lower carbon balance.

In the absence of characterization data, it is difficult to derive a correlation with the nanoparticles structure. One can only suppose that the particles sintering is lesser than after reduction at 700 °C, the metal dispersion is higher, and that Fe may not be fully reduced, given the reduction temperature of 400 °C and the TPR profile, leading to an excess of reduced Ni in the particles compared with the nominal formulation. The increase of dispersion would explain the higher rate of FF consumption compared with catalysts pre-reduced at 700 °C, while the partial reduction of Fe and a proportion of reduced Ni higher than expected would explain the fact that, apparently, it is catalysts containing less than 70 at% Ni that present the highest selectivity in FFA. In any case, we can see that among all the catalysts tested in the present work, it is these catalysts, and especially Fe<sub>40</sub>Ni<sub>60</sub>/SiO<sub>2</sub>, that provide both the highest yield of FFA and the lowest yields in side-products.

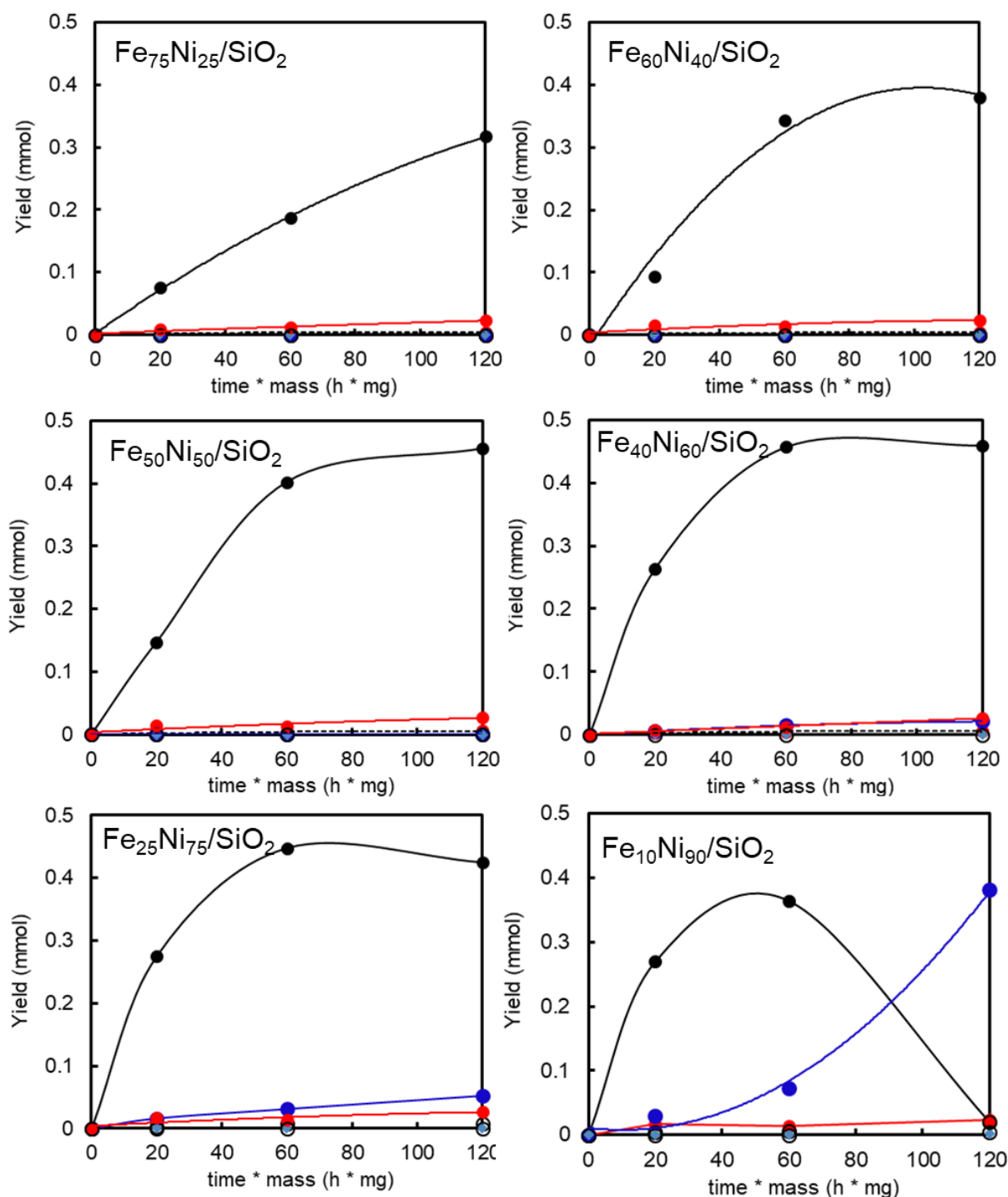


**Figure 5.18.** Yield of products after hydrogenation of FF as a function of (time \* mass) for Fe-Ni/SiO<sub>2</sub>-IWI bimetallic catalysts prepared by impregnation, without pre-reduction at 700 °C. Black line (—●—): FFA; Black dotted line (---⊖---): iPrOMF; Blue line (—●—): THFFA; Red line (—●—): MF. Reaction conditions: T = 150 °C, T<sub>activation</sub> = 400 °C, P(H<sub>2</sub>) = 20 bar, solvent: isopropanol, volume of solution: 1.5 mL, m<sub>catalyst</sub> = 10 - 30 mg, t = 2 - 4 h.



**Table 5.4.** Carbon balance of Fe-Ni/SiO<sub>2</sub> catalysts prepared by impregnation without pre-reduction at 700 °C after the hydrogenation of furfural as a function of (time \* mass). Reaction conditions: T<sub>activation</sub> = 400 °C, T = 150 °C, P(H<sub>2</sub>) = 20 bar, solvent: isopropanol, volume of solution: 1.5 mL, m<sub>catalyst</sub> = 10 - 30 mg, t = 2 - 4 h.

(time* mass)	Carbon balance (%)					
	Fe <sub>75</sub> Ni <sub>25</sub> /SiO <sub>2</sub>	Fe <sub>60</sub> Ni <sub>40</sub> /SiO <sub>2</sub>	Fe <sub>50</sub> Ni <sub>50</sub> /SiO <sub>2</sub>	Fe <sub>40</sub> Ni <sub>60</sub> /SiO <sub>2</sub>	Fe <sub>25</sub> Ni <sub>75</sub> /SiO <sub>2</sub>	Fe <sub>10</sub> Ni <sub>90</sub> /SiO <sub>2</sub>
0	88	92	92	87	91	90
60	87	90	89	90	91	87
120	87	87	89	95	93	85

In conclusion, the expected Fe and Ni atomic proportions for impregnated catalysts are close to the nominal ratios, and in the only sample studied by TEM the composition of individual nanoparticles also corresponds to the nominal composition without large deviations. The average size of Fe-Ni particles calculated by XRD ranges from 9 to 13 nm, which is much larger than for DP catalysts, and moreover with a broader size distribution. As was found for DP catalysts, upon exposure to air, the Fe-Ni alloy nanoparticles possess a core-shell structure with Fe-rich phases in the oxidized shell. The reducibility of samples prepared by impregnation is higher than that of those prepared by DP. Impregnated Fe-Ni/SiO<sub>2</sub> samples pre-reduced at 700 °C and activated at 400 °C prior to reaction show that increasing the Ni content is beneficial for the activity in terms of FF consumption and yield to FFA. The Fe-Ni/SiO<sub>2</sub> catalyst containing 75 Ni at% favors the hydrogenation of the aldehyde function and provides the highest yield to FFA (0.44 mmol). This composition is similar to that found for the most selective DP catalysts. Among impregnated Fe-Ni/SiO<sub>2</sub> samples which were not pre-reduced at 700 °C, it is the Fe-Ni/SiO<sub>2</sub> catalyst containing 60 at% Ni presents the highest selectivity in FFA (0.44 mmol). This may be due to the partial reduction of Fe at 400 °C, and to a proportion of reduced Ni higher than expected.

## V.7. Conclusions

A series of Fe-Ni/SiO<sub>2</sub> catalysts prepared by deposition-precipitation were evaluated in the hydrogenation of furfural under a given set of reaction conditions: isopropanol as solvent, reaction temperature at 150 °C, H<sub>2</sub> pressure of 20 bar, reaction time ranging from 0.5 to 4 h and mass of catalyst ranging from 3 to 10 mg. The consumption of furfural and yield of furfuryl alcohol increases when increasing the Ni content, and Fe-Ni catalysts containing 60-75 Ni at% provide the highest yield of FFA in these experimental conditions. A similar result is obtained for catalysts prepared by co-impregnation, that differ by a larger average particle size and presumably a lower dispersion. More Ni progressively favors side-reactions of etherification (possibly through the presence of residual Ni<sup>2+</sup> ions in unreduced silicate phases), hydrogenolysis and finally hydrogenation of the furan ring. In a first approach the activity of the Fe-Ni catalysts can be correlated to the proportion of Ni. However, upon exposure to air, Fe-Ni/SiO<sub>2</sub> alloyed nanoparticles prepared both by DP and co-impregnation possess a core-shell structure, with Fe-richer phases in the oxidized shell, and a discrepancy between the global composition and the surface composition of the nanoparticles can be expected. On Fe-Ni catalysts containing 60-75 at% Ni, an adequate balance between an excess of Fe and a minority of Ni at the surface of the nanoparticles, that favors the adsorption of furfural via the aldehyde function and repels the furan ring, may limit secondary reactions of hydrogenolysis and hydrogenation of the furan ring linked to Ni-rich surfaces. The high reducibility of these catalysts would also avoid the presence of residual unreduced Ni<sup>2+</sup> metal ions apt to catalyze secondary reactions of etherification.

## References

- [1] G. Giorgianni, S. Abate, G. Centi, S. Perathoner, S. van Beuzekom, S. H. Soo-Tang, J. C. Van der Waal, Effect of the solvent in enhancing the selectivity to furan derivatives in the catalytic hydrogenation of furfural, *ACS Sustainable Chemistry & Engineering*, 6 (2018) 16235-16247.
- [2] R. Albilali, M. Douthwaite, Q. He, S. H. Taylor, The selective hydrogenation of furfural over supported palladium nanoparticle catalysts prepared by sol-immobilisation: effect of catalyst support and reaction conditions, *Catalysis Science & Technology*, 8 (2018) 252-267.
- [3] R. Ma, X. P. Wu, T. Tong, Z. J. Shao, Y. Wang, X. Liu, Q. Xia, X. Q. Gong, The critical role of water in the ring opening of furfural alcohol to 1,2-pentanediol, *ACS Catalysis*, 7 (2016) 333-337.
- [4] S. Iqbal, X. Liu, O. F. Aldosari, P. J. Miedziak, J. K. Edwards, G. L. Brett, A. Akram, G. M. King, T. E. Davies, D. J. Morgan, D. K. Knight, G. J. Hutchings, Conversion of furfuryl alcohol into 2-methylfuran at room temperature using Pd/TiO<sub>2</sub> catalyst, *Catalysis Science & Technology*, 4 (2014) 2280-2286.
- [5] G. Chieffi, C. Giordano, M. Antonietti, D. Esposito, FeNi nanoparticles with carbon armor as sustainable hydrogenation catalysts: towards biorefineries, *Journal of Materials Chemistry A*, 2 (2014) 11591.
- [6] W. S. Putro, T. Kojima, T. Hara, N. Ichikuni, S. Shimazu, Selective hydrogenation of unsaturated carbonyls by Ni-Fe-based alloy catalysts, *Catalysis Science & Technology*, 7 (2017) 3637-3646.
- [7] H. Li, H. Luo, L. Zhuang, W. Dai, M. Qiao, Liquid phase hydrogenation of furfural to furfuryl alcohol over the Fe-promoted Ni-B amorphous alloy catalysts, *Journal of Molecular Catalysis A: Chemical*, 203 (2003) 267-275.
- [8] V. Vetere, A. B. Merlo, J. F. Ruggera, M. L. Casella, Transition metal-based bimetallic catalysts for the chemoselective hydrogenation of furfuraldehyde, *Journal of the Brazilian Chemical Society*, 21 (2010) 914-920.
- [9] P. Reyes, D. Salinas, C. Campos, M. Oportus, J. Murcia, H. Rojas, G. Borda, J. L. G. Fierro, Selective hydrogenation of furfural on Ir/TiO<sub>2</sub> catalysts, *Quimica Nova*, 33 (2010) 777-780.

- [10] S. Wang, V. Vorotnikov, D. G. Vlachos, Coverage-induced conformational effects on activity and selectivity: hydrogenation and decarbonylation of furfural on Pd(111), *ACS Catalysis*, 5 (2014) 104-112.
- [11] A. Halilu, T. H. Ali, A. Y. Atta, P. Sudarsanam, S. K. Bhargava, S. B. Abd Hamid, Highly selective hydrogenation of biomass-derived furfural into furfuryl alcohol using a novel magnetic nanoparticles catalyst, *Energy & Fuels*, 30 (2016) 2216-2226.
- [12] L. Nie, P. M. de Souza, F. B. Noronha, W. An, T. Sooknoi, D. E. Resasco, Selective conversion of m-cresol to toluene over bimetallic Ni-Fe catalysts, *Journal of Molecular Catalysis A: Chemical*, 388-389 (2014) 47-55.
- [13] S. Sitthisa, W. An, D. E. Resasco, Selective conversion of furfural to methylfuran over silica-supported NiFe bimetallic catalysts, *Journal of Catalysis*, 284 (2011) 90-101.
- [14] A. B. Merlo, V. Vetere, J. F. Ruggera, M. L. Casella, Bimetallic PtSn catalyst for the selective hydrogenation of furfural to furfuryl alcohol in liquid-phase, *Catalysis Communications*, 10 (2009) 1665-1669.
- [15] M. Koehle, R. F. Lobo, Lewis acidic zeolite Beta catalyst for the Meerwein-Ponndorf-Verley reduction of furfural, *Catalysis Science & Technology*, 6 (2016) 3018-3026.
- [16] M. C. Iliuta, K. Thomsen, P. Rasmussen, Modeling of heavy metal salt solubility using the extended UNIQUAC model, *Aiche Journal*, 48 (2002) 2664-2689.
- [17] E. E. Unmuth, L. H. Schwartz, J. B. Butt, Iron alloy Fischer-Tropsch catalysts. 1. Oxidation-reduction studies of the Fe-Ni system, *Journal of Catalysis*, 61 (1980) 242-255.
- [18] X. Yu, J. Chen, T. Ren, Promotional effect of Fe on performance of Ni/SiO<sub>2</sub> for deoxygenation of methyl laurate as a model compound to hydrocarbons, *RSC Advances*, 4 (2014) 46427-46436.
- [19] H. Fang, J. Zheng, X. Luo, J. Du, A. Roldan, S. Leoni, Y. Yuan, Product tunable behavior of carbon nanotubes-supported Ni-Fe catalysts for guaiacol hydrodeoxygenation, *Applied Catalysis A: General*, 529 (2017) 20-31.
- [20] B. Mutz, M. Belimov, W. Wang, P. Sprenger, M. A. Serrer, D. Wang, P. Pfeifer, W. Kleist, J. D. Grunwaldt, Potential of an alumina-supported Ni<sub>3</sub>Fe catalyst in the methanation of CO<sub>2</sub>: impact of alloy formation on activity and stability, *ACS Catalysis*, 7 (2017) 6802-6814.



# General conclusions and perspectives



Iron (Fe) and nickel (Ni) are two non-noble metals that can be used as efficient catalysts for the hydrogenation of organic molecules. Whereas monometallic Ni is known to be active in catalytic hydrogenation, but also to favor unwanted side-reactions of hydrogenolysis and ring opening, bimetallic Fe-Ni catalysts have been reported to exhibit interesting properties for the selective hydrogenation of oxygenated functions. However, Fe-Ni bimetallic catalysts are often prepared by co-impregnation, which is a simple procedure, but which has been reported to lead to a poor control of the bimetallic particle composition, structure and size. This has made it difficult to link the composition of Fe-Ni nanoparticles and catalytic activities. The purpose of this PhD has been to prepare SiO<sub>2</sub>-supported Fe-Ni bimetallic nanoparticles of homogeneous structure, size and composition, and to evidence the interplay between the two metals, in order to unambiguously link the molar proportions of Fe and Ni within the particles and the composition at their surface with their catalytic performances. Furfural, a bio-sourced molecule of commercial importance, which holds a furan ring and an aldehyde group, has been chosen to evaluate the hydrogenation ability of these catalysts, especially toward the selective formation of furfuryl alcohol.

Based on the literature for the preparation of Ni/SiO<sub>2</sub> catalysts, deposition-precipitation with urea has been selected as the method to prepare the Fe-Ni/SiO<sub>2</sub> catalysts. In order to avoid the separate precipitation of Fe(III)-containing phases at low pH, Fe(II) and Ni(II) sulfates have been selected as precursor salts, and the whole synthesis has been carried out under inert gas Ar, to remove any source of oxidation. Iron ions nevertheless oxidize to Fe(III) during drying and storage, though without consequence on the ulterior formation of the Fe-Ni nanoparticles. Deposition-precipitation results in the formation of a poorly crystalline (Fe(III),Ni(II))-containing 1:1 phyllosilicate, with an excess of Ni compared with the metal proportions in solution. *In situ* X-ray diffraction, X-ray absorption spectroscopy, Mössbauer spectroscopy and temperature-programmed reduction show that Fe-Ni alloyed nanoparticles form upon three stages of reduction between 275 and 700 °C: (1) reduction of Fe(III) ions to Fe(II) in the phyllosilicate phase; (2) destruction of the phyllosilicate phase and reduction of Ni(II) to Ni(0), which triggers the progressive reduction of Fe(II) ions to the metallic state and the formation of face-centred cubic (*fcc*) Ni-rich bimetallic particles; (3) completion of the reduction of Fe(II)



ions and migration to the core of the Fe-Ni nanoparticles. In terms of reduction temperature, the reducibility of the catalyst is optimal for formulations containing a molar proportion of 60-75 at% Ni. Ni increases the reducibility of Fe, but too much Ni leads to a more organized phyllosilicate that is more difficult to reduce.

The particles size and composition of the *fcc* Fe-Ni nanoparticles have been characterized by HRTEM-EELS-EDX after reduction at 700 °C for six Fe-Ni actual formulations: Fe<sub>65</sub>Ni<sub>35</sub>, Fe<sub>45</sub>Ni<sub>55</sub>, Fe<sub>31</sub>Ni<sub>69</sub>, Fe<sub>27</sub>Ni<sub>73</sub>, Fe<sub>16</sub>Ni<sub>84</sub>, Fe<sub>8</sub>Ni<sub>92</sub>. In all cases, the size distribution of the nanoparticles is narrow, in the 4-7 nm range, with an average size of 5-6 nm, and metal dispersions are close to 20%. The global composition measured on individual particles exhibits a small standard deviation of only 7-8 at%. Upon exposure to air, the nanoparticles possess a core-shell structure, with an outer oxidic shell enriched in Fe. This excess of Fe may derive from the late reduction of this metal during the formation of the nanoparticles. As shown by *in situ* X-ray absorption spectroscopy, the two metals can be reduced back to the metallic state in dilute H<sub>2</sub> below 500 °C. As was the case during the initial reduction process, Ni helps to reduce Fe: the higher the proportion of Ni, the lower the temperature at which the reduction of Fe to the metallic state starts.

The six Fe-Ni/SiO<sub>2</sub> bimetallic catalysts and a monometallic Ni/SiO<sub>2</sub> catalyst prepared according to the same method and displaying the same characteristics of particle size and dispersion have been tested in the hydrogenation of furfural in isopropanol at 150 °C under 20 bar of H<sub>2</sub>, after activation in pure H<sub>2</sub> at 400 °C to reduce the oxidic shell. The furfural consumption rate increases with the Ni content. Fe-Ni catalysts containing a molar proportion of 60-75 Ni at% provide the highest yield of furfuryl alcohol. This tendency is confirmed using Fe-Ni/SiO<sub>2</sub> catalysts prepared by co-impregnation of Fe(III) and Ni(II) nitrates, which in this work have been found to differ from the catalysts prepared by deposition-precipitation by their broader particle size distribution (up to 15 nm) and lower metal dispersion. More Ni progressively favors the consumption of furfuryl alcohol via three parallel secondary reactions: etherification with the isopropanol solvent, possibly catalyzed by nickel ions that remain unreduced in silicate phases after activation; hydrogenolysis of the C-O bond yielding 2-methylfuran; and hydrogenation of the furan ring, which dominates the reactivity of the

monometallic Ni/SiO<sub>2</sub> catalyst.

The comparison between the six Fe-Ni/SiO<sub>2</sub> catalysts is facilitated by the homogeneity of the Fe-Ni nanoparticles in structure, size and global composition. The specificities of the Fe<sub>31</sub>Ni<sub>69</sub>/SiO<sub>2</sub> and Fe<sub>27</sub>Ni<sub>73</sub>/SiO<sub>2</sub> catalysts with respect to their high selectivity and yield in furfuryl alcohol are explained on the one hand by an optimum reducibility, on the other hand by the major presence of oxophilic Fe and by an adequate Fe/Ni balance at the surface of the particles, which presumably favor the adsorption of furfural via the aldehyde group and not via the furan ring, and tone down the hydrogenating properties of Ni, at least by a dilution effect.

For the continuation of the project, it would be important to carry out additional characterizations to link the surface composition of the Fe-Ni nanoparticles to their catalytic properties in the hydrogenation of furfural. Low-energy ion scattering (LEIS) spectroscopy is an analytical tool that provides information on the atomic composition of the outer surface, and can be chosen to quantify the amount of iron located at the surface of the nanoparticles after pre-reduction at 700 °C and activation by H<sub>2</sub> at 400 °C before catalytic test. On the other hand, *in situ* Mössbauer spectroscopy can also be used to identify the initial proportion of Fe<sup>3+</sup> ions in the oxidized shell, and the degree of Fe reduction after activation at 400 °C in conditions similar to those of the catalytic test. This will allow refining the quantitative aspects of the MCR-ALS analysis process applied to the activation step.

Characterizations for Fe-Ni/SiO<sub>2</sub> catalysts prepared by impregnation should be completed in order to finish the comparison with deposition-precipitation samples. For example, STEM-EELS can be used for the characterization of Fe-rich or Ni-rich samples after reduction at 700 °C and exposure to air, in order to know if the composition of individual particles is homogeneous and consistent with the nominal compositions. Furthermore, the composition for samples prepared with and without pre-reduction at 700 °C should be verified so as to explain the discrepancies of their catalytic activity.

Finally, the stability of the most active and selective Fe-Ni catalysts should be verified and spent catalysts should be characterized, in order to confirm the absence of metal leaching during catalytic test, and to explain the origin of the loss of conversion observed in the preliminary tests.



# Scientific production



## Publications:

1. Dichao Shi; Qifeng Yang; Christi Peterson; Anne-Félicie Lamic-Humblot; Jean-Sébastien Girardon; Anne Griboval-Constant; Lorenzo Stievano; Moulay T. Sougrati; Valérie Briois; Paul A. J. Bagot; Robert Wojcieszak; Sébastien Paul and Eric Marceau\*. Bimetallic Fe-Ni/SiO<sub>2</sub> catalysts for furfural hydrogenation: identification of the interplay between Fe and Ni during deposition-precipitation and thermal treatments. *Catalysis Today* **2019**, 334, 162-172.
2. Dichao Shi; Robert Wojcieszak; Sébastien Paul and Eric Marceau\*. Ni promotion by Fe: what benefits for catalytic hydrogenation. *Catalysts* **2019**, 9 (5), 451.

## Conferences:

1. Oral: *Influence of the formulation of bimetallic Fe-Ni/SiO<sub>2</sub> catalysts on the conversion of furfural to furfuryl alcohol* - Dichao Shi,\* Robert Wojcieszak, Anne-Sophie Mamede, Anne-Félicie Lamic-Humblot, Sébastien Paul, Eric Marceau - *Gecat 2018*, Tregunc, France, 22-25 May **2018**.
2. Oral: *Bimetallic Fe-Ni/SiO<sub>2</sub> catalysts: identification of the interplay between Fe and Ni during the preparation of well-defined Fe-Ni nanoparticles* - Dichao Shi, Qifeng Yang, Christi Peterson, Anne-Félicie Lamic-Humblot, Jean-Sébastien Girardon, Anne Griboval-Constant, Anne-Sophie Mamede, Maya Marinova, Valérie Briois, Paul A. J. Bagot, Robert Wojcieszak, Sébastien Paul, Eric Marceau\* - *12th International Symposium on the Preparation of Heterogeneous Catalysts (PREPA12)*, Louvain-la-Neuve, Belgium, 8-12 July **2018**.
3. Poster: *Bimetallic Fe-Ni/SiO<sub>2</sub> catalysts for furfural hydrogenation: respective roles of Fe and Ni* - Dichao Shi, Jean-Sébastien Girardon, Anne Griboval-Constant, Anne-Sophie Mamede, Robert Wojcieszak,\* Sébastien Paul, Eric Marceau, Anne-Félicie Lamic-Humblot, Maya Marinova, Valérie Briois, Lorenzo Stievano, Moulay T. Sougrati - *ISGC 2019, International Symposium on Green Chemistry*, La Rochelle, France, 13-17 May **2019**.

4. Oral: *Identification of the interplay between Fe and Ni in bimetallic Fe-Ni/SiO<sub>2</sub> catalysts for furfural hydrogenation* - Dichao Shi,\* Jean-Sébastien Girardon, Anne Griboval-Constant, Anne-Sophie Mamede, Robert Wojcieszak, Sébastien Paul, Eric Marceau, Anne-Félicie Lamic-Humblot, Maya Marinova, Valérie Briois, Lorenzo Stievano, Moulay T. Sougrati - *EuropaCat 2019*, Aachen, Germany, 18-23 August **2019**.

Titre: Synthèse contrôlée de catalyseurs bimétalliques Fe-Ni/SiO<sub>2</sub> pour l'hydrogénation du furfural: mise en évidence des rôles de Fe et Ni

Les catalyseurs bimétalliques Fe-Ni ont été mentionnés comme présentant des propriétés intéressantes pour l'hydrogénation sélective des fonctions oxygénées. Le but de cette thèse est de préparer des nanoparticules bimétalliques Fe-Ni supportées sur SiO<sub>2</sub>, de structure, de taille et de composition homogènes, et de mettre en évidence les interactions entre les deux métaux, pour relier la présence de Fe et de Ni, dans les particules et à leur surface, aux performances catalytiques. Le furfural a été choisi pour évaluer la capacité en hydrogénation de ces catalyseurs. La méthode choisie pour préparer les catalyseurs Fe-Ni/SiO<sub>2</sub> est le dépôt-précipitation à l'urée. Afin d'éviter la précipitation séparée de phases contenant Fe(III), les sulfates de Fe(II) et Ni(II) ont été sélectionnés comme sels précurseurs, et la synthèse entière a été menée sous un gaz inerte, Ar. Néanmoins, les ions fer s'oxydent en Fe(III) pendant le séchage et le stockage. Le dépôt-précipitation résulte en la formation d'un phyllosilicate 1:1 faiblement cristallisé contenant des ions Fe(III) et Ni(II), avec un excès de Ni comparé aux proportions des métaux en solution. Les nanoparticules d'alliage Fe-Ni se forment au travers de trois étapes de réduction entre 275 et 700 °C: (1) réduction des ions Fe(III) en Fe(II) dans la phase phyllosilicate; (2) destruction de la phase phyllosilicate et réduction de Ni(II) en Ni(0), qui provoque la réduction progressive des ions Fe(II) à l'état métallique et la formation de particules bimétalliques cubique faces centres (cfc) riches en Ni; (3) achèvement de la réduction des ions Fe(II) et migration vers le coeur des nanoparticules Fe-Ni. Ni augmente la réductibilité de Fe, mais trop de Ni conduit à un phyllosilicate mieux organisé qui est plus difficile à réduire. La taille et la composition des particules cfc Fe-Ni ont été caractérisées par HRTEM-EELS-EDX après réduction à 700 °C, pour six formulations Fe-Ni: Fe<sub>65</sub>Ni<sub>35</sub>, Fe<sub>45</sub>Ni<sub>55</sub>, Fe<sub>31</sub>Ni<sub>69</sub>, Fe<sub>27</sub>Ni<sub>73</sub>, Fe<sub>16</sub>Ni<sub>84</sub>, Fe<sub>8</sub>Ni<sub>92</sub>. La distribution en taille est étroite, dans l'intervalle 4-7 nm, et les dispersions métalliques sont proches de 20%. La composition globale mesurée sur des particules individuelles présente un écart-type de seulement 8 at%. Après exposition à l'air, les nanoparticules possèdent une structure coeur-coquille, avec une couche externe oxydée enrichie en Fe. Cet excès de Fe, aussi observé par spectroscopie Mössbauer, peut provenir de la réduction tardive de ce métal durant la formation des nanoparticules. Les six catalyseurs Fe-Ni/SiO<sub>2</sub> ont été testés dans l'hydrogénation du furfural en phase liquide à 150 °C sous 20 bar de H<sub>2</sub>, après activation sous H<sub>2</sub> à 400 °C. La vitesse de consommation du furfural augmente avec la teneur en Ni. Les catalyseurs Fe-Ni contenant une proportion molaire de 60-75 Ni at% fournissent le rendement le plus élevé en alcool furfurylique. Cette tendance est confirmée en utilisant des catalyseurs Fe-Ni/SiO<sub>2</sub> préparés par co-imprégnation de nitrates de Fe(III) et Ni(II). Davantage de Ni favorise progressivement la consommation de l'alcool furfurylique selon trois réactions secondaires parallèles: éthérification avec le solvant isopropanol; hydrogénolyse de la liaison C-O; et hydrogénation du cycle furanique, qui domine la réactivité du catalyseur monométallique Ni/SiO<sub>2</sub>. La comparaison des six catalyseurs Fe-Ni/SiO<sub>2</sub> est facilitée par l'homogénéité des nanoparticules Fe-Ni en structure, taille et composition globale. Les spécificités des catalyseurs Fe<sub>31</sub>Ni<sub>69</sub>/SiO<sub>2</sub> et Fe<sub>27</sub>Ni<sub>73</sub>/SiO<sub>2</sub> quant à leur sélectivité et à leur rendement élevés en alcool furfurylique sont expliquées d'une part par une réductibilité optimale, d'autre part par la présence majoritaire du Fe oxophile et par un rapport Fe/Ni adéquat à la surface des particules, qu'on peut supposer favoriser l'adsorption du furfural par le groupe aldéhyde et non par le cycle furanique, et affaiblir les propriétés hydrogénantes du Ni au moins par un effet de dilution.

Mots clés: Catalyseurs bimétalliques, Hydrogénation, Furfural

Title: Controlled synthesis of bimetallic Fe-Ni/SiO<sub>2</sub> catalysts for furfural hydrogenation: evidencing the roles of Fe and Ni

Bimetallic Fe-Ni catalysts have been reported to exhibit interesting properties for the selective hydrogenation of oxygenated functions. The purpose of this PhD is to prepare SiO<sub>2</sub>-supported Fe-Ni bimetallic nanoparticles of homogeneous structure, size and composition, and to evidence the interplay between the two metals, in order to unambiguously link the presence of Fe and Ni within the particles and at their surface with their catalytic performances. Furfural has been chosen to evaluate the hydrogenation ability of these catalysts. Deposition-precipitation with urea has been selected as the method to prepare the Fe-Ni/SiO<sub>2</sub> catalysts. In order to avoid the separate precipitation of Fe(III)-containing phases, Fe(II) and Ni(II) sulfates have been selected as precursor salts, and the whole synthesis has been carried out under inert gas Ar. Iron ions nevertheless oxidize to Fe(III) during drying and storage. Deposition-precipitation results in the formation of a poorly crystalline (Fe(III),Ni(II))-containing 1:1 phyllosilicate, with an excess of Ni compared with the metal proportions in solution. Fe-Ni alloyed nanoparticles form upon three stages of reduction between 275 and 700 °C: (1) reduction of Fe(III) ions to Fe(II) in the phyllosilicate phase; (2) destruction of the phyllosilicate phase and reduction of Ni(II) to Ni(0), which triggers the progressive reduction of Fe(II) ions to the metallic state and the formation of face-centred cubic (*fcc*) Ni-rich bimetallic particles; (3) completion of the reduction of Fe(II) ions and migration to the core of the Fe-Ni nanoparticles. Ni increases the reducibility of Fe, but too much Ni leads to a more organized phyllosilicate that is more difficult to reduce. The particles size and composition of the *fcc* Fe-Ni nanoparticles have been characterized by HRTEM-EELS-EDX after reduction at 700 °C for six Fe-Ni formulations: Fe<sub>65</sub>Ni<sub>35</sub>, Fe<sub>45</sub>Ni<sub>55</sub>, Fe<sub>31</sub>Ni<sub>69</sub>, Fe<sub>27</sub>Ni<sub>73</sub>, Fe<sub>16</sub>Ni<sub>84</sub>, Fe<sub>8</sub>Ni<sub>92</sub>. The size distribution of the nanoparticles is narrow, in the 4-7 nm range, and metal dispersions are close to 20%. The global composition measured on individual particles exhibits a standard deviation of only 8 at%. Upon exposure to air, the nanoparticles possess a core-shell structure, with an outer oxidic shell enriched in Fe. This excess of Fe, also observed by Mössbauer spectroscopy, may derive from the late reduction of this metal during the formation of the nanoparticles. The six Fe-Ni/SiO<sub>2</sub> catalysts have been tested in the liquid phase hydrogenation of furfural at 150 °C under 20 bar of H<sub>2</sub>, after activation in H<sub>2</sub> at 400 °C. The furfural consumption rate increases with the Ni content. Fe-Ni catalysts containing a molar proportion of 60-75 Ni at% provide the highest yield of furfuryl alcohol. This tendency is confirmed using Fe-Ni/SiO<sub>2</sub> catalysts prepared by co-imprégnation of Fe(III) and Ni(II) nitrates. More Ni progressively favors the consumption of furfuryl alcohol via three parallel secondary reactions: etherification with the isopropanol solvent; hydrogenolysis of the C-O bond; and hydrogenation of the furan ring, which dominates the reactivity of the monometallic Ni/SiO<sub>2</sub> catalyst. The comparison between the six Fe-Ni/SiO<sub>2</sub> catalysts is facilitated by the homogeneity of the Fe-Ni nanoparticles in structure, size and global composition. The specificities of the Fe<sub>31</sub>Ni<sub>69</sub>/SiO<sub>2</sub> and Fe<sub>27</sub>Ni<sub>73</sub>/SiO<sub>2</sub> catalysts with respect to their high selectivity and yield in furfuryl alcohol are explained on the one hand by an optimum reducibility, on the other hand by the major presence of oxophilic Fe and by an adequate Fe/Ni balance at the surface of the particles, which presumably favor the adsorption of furfural via the aldehyde group and not via the furan ring, and tone down the hydrogenating properties of Ni, at least by a dilution effect.

Key words: Bimetallic catalysts, Hydrogenation, Furfural